



Modelling, Analysis and Optimisation of a Molten Carbonate Fuel Cell with Direct Internal Reforming (DIR-MCFC)

**Modellierung, Analyse und Optimierung
einer Schmelzkarbonatbrennstoffzelle mit
direkter interner Reformierung (DIR-MCFC)**

Der Fakultät für Verfahrens- und Systemtechnik der Otto-von-Guericke-Universität Magdeburg zur Erlangung des akademischen Grades

**Doktoringenieur
(Dr.-Ing.)**

am 06. Juli 2004 vorgelegte Dissertation

von Dipl.-Ing. Peter Heidebrecht

Danksagung

Die vorliegende Dissertation ist ein Ergebnis meiner 3½-jährigen Mitarbeit am Lehrstuhl für Systemverfahrenstechnik an der Otto-von-Guericke Universität Magdeburg. Allerdings verdanke ich das Gelingen dieser Arbeit einer Anzahl von Menschen, die auf vielfältigste Art und Weise dazu beigetragen haben.

An erster Stelle sei Professor Dr.-Ing. Kai Sundmacher gedankt, der mir dieses interessante Thema zur Verfügung gestellt und mich während dieser Zeit betreut hat. Seine offene und diskussionsbereite Art in fachlichen Gesprächen, seine präzise und analytische Denkweise sowie die Freiräume, die er mir in meiner Arbeit eingeräumt hat, gehören zu den exzellenten Rahmenbedingungen, die ich während dieser Zeit in Anspruch nehmen durfte.

Auch möchte ich Herrn Dipl.-Ing. Joachim Berndt als treibender Kraft im Hintergrund dafür danken, daß er gemeinsam mit Professor Sundmacher und Herrn Dipl.-Ing. Huppmann dieses Forschungsprojekt ermöglichte und mit all seiner Energie und seinem Know-how voranbringt.

Ebenso gilt mein Dank Herrn Professor Keil von der Universität Hamburg und Herrn Professor Specht von der Universität Magdeburg für die Begutachtung dieser Arbeit.

Mehr als Dank gebührt meinem häufigsten fachlichen Gesprächspartner während dieser Zeit, meiner Frau Alexandra. Ohne ihr geduldiges Zuhören, ihr inhaltliches Interesse und ihre ermutigenden Worte wäre diese Arbeit nicht das, was sie heute ist.

Schließlich geht ein großes Dankeschön an alle meine Kollegen, die mir so oft ihre Unterstützung gewährt haben, als sei dies eine Selbstverständlichkeit. Ich schätze diesen Zusammenhalt, der weit mehr als nur kollegial ist, sehr. Namentlich möchte ich nur einige erwähnen: Matthias Gundermann, der in seiner leisen und zuverlässigen Art oftmals Ruhe in die Dinge brachte; Nancy Eckstein, die so manches möglich machte, was nicht möglich schien; Michael Mangold, der stets für meine Fragen zu ProMoT/Diva da war; Frank Steyer und Richard Hanke, die mir mit viel mehr als nur dem Korrekturlesen dieser Arbeit geholfen haben.

Es liegt in der Natur der Sache, daß ich nicht alle diejenigen erwähnen kann, denen ich Dank schulde. Diese Freunde und Kollegen mögen mir dieses verzeihen in dem Wissen, daß es meine Wertschätzung für ihre Unterstützung in keiner Weise schmälert.

Magdeburg, im Juni 2004

Table of Contents

List of symbols.....	VII
Zusammenfassung.....	XI
1 Introduction.....	1
1.1 Working principle and technical features of the MCFC.....	2
1.2 MCFC models in the scientific literature.....	6
1.3 Scope of this work.....	9
2 Modelling of MCFCs.....	11
2.1 The 2D reference model.....	13
2.1.1 General considerations and assumptions.....	13
2.1.2 Dimensionless numbers.....	15
2.1.3 Model equations.....	18
2.1.3.1 Anode channel.....	19
2.1.3.2 Catalytic combustion chamber.....	23
2.1.3.3 Reversal chamber.....	25
2.1.3.4 Cathode channel.....	26
2.1.3.5 Electrode pores.....	28
2.1.3.6 Solid phase.....	30
2.1.3.7 Electric potential field.....	32
2.1.3.8 Reaction kinetics.....	34
2.1.3.9 Thermodynamics.....	37
2.2 Model parameters.....	39
2.2.1 Definition of standard values.....	39
2.2.2 Parameter values.....	41
2.2.3 Time constants in MCFC.....	45
2.3 Physically-chemically reduced model.....	46
2.3.1 Assumptions.....	46
2.3.2 Model equations.....	47
2.4 Steady state anode model.....	50
2.4.1 Assumptions.....	50
2.4.2 Model equations.....	51
2.4.3 Steady state anode model extensions.....	55
2.5 Concluding remarks on MCFC modelling.....	56
3 Conceptual system design based on the steady state anode model.....	58
3.1 The conversion diagram.....	58
3.2 Comparison of reforming strategies.....	62
3.3 Anode cascades.....	64

3.4 Anode gas recycle.....	68
3.5 Concluding remarks on fundamental system design.....	70
4 Simulation results of the reduced model.....	71
4.1 Numerical solution of the reduced model.....	71
4.2 Steady state results.....	72
4.3 Transient cell behaviour at load change.....	85
4.4 Parameter analysis.....	95
4.4.1 Parametric sensitivity of the current-voltage curve.....	95
4.4.2 Parametric sensitivity under base case conditions.....	101
4.5 Concluding remarks on simulation results.....	102
5 Optimisation based on the reduced model.....	104
5.1 Optimisation of input parameters.....	104
5.1.1 Objective function and constraints.....	104
5.1.2 Optimisation results.....	105
5.2 Optimisation of reforming catalyst distribution.....	108
5.2.1 Objective function and constraints.....	109
5.2.2 Optimisation results.....	109
5.2.3 Effect of catalyst distribution on other load cases.....	114
5.3 Concluding remarks on optimisation.....	115
6 Conclusions and outlook.....	116
Appendix.....	118
A.1 Derivation of the anode channel balance equations in dimensional form.....	118
A.2 Transformation of model equations into dimensionless form.....	123
A.3 Spatial discretisation of the model equations.....	125
A.4 Potential field models.....	128
A.5 Kinetics of the reduction reaction.....	134
A.6 Parameter values of the base case configuration.....	138
A.7 Cited literature.....	142

List of symbols

Symbol table 1: Symbols of dimensionless variables and parameters

Latin symbols

A_i		Coefficients of heat capacity polynomial of component i
Arr_j	$= \frac{E_{A,j}}{RT^\theta} = \frac{\text{Activation energy}}{\text{Characteristic energy}}$	Arrhenius number of reaction j
c	$= \frac{c}{t^\theta t^\theta / \phi^\theta} = \frac{\text{Charge capacity}}{\text{Characteristic charge capacity}}$	Surface related charge capacity
c_p	$= \frac{\tilde{c}_p}{R} = \frac{\text{Heat capacity}}{\text{Characteristic heat capacity}}$	Molar heat capacity
$c_{p,s}$	$= \frac{d_s \cdot \rho_s \cdot c_s}{d_a \cdot c_i^\theta \cdot R} = \frac{\text{Heat capacity solid}}{\text{Characteristic heat capacity gas phase}}$	Heat capacity solid phase
Da_j	$= \frac{r^\theta L_1 L_2}{G^\theta} = \frac{\text{Characteristic reaction rate}}{\text{Characteristic convection rate}}$	Damköhler number of reaction j
D_i	$= \frac{\tilde{D}_i p^\theta}{G^\theta / L_1 L_2} = \frac{\text{Mass exchange rate gas / pore}}{\text{Characteristic exchange flow density}}$	Mass transport coefficient of component i
F	$= \frac{3.5}{4.2} = \frac{\text{Characteristic feed}}{\text{Characteristic current}}$	Dimensionless Faradaic constant
f_{blower}	$= \frac{\tilde{P}_{blower}}{G^\theta} = \frac{\text{Blower power}}{\text{Characteristic convective flow}}$	Blower power coefficient
$h_{f,i}$	$= \frac{\tilde{h}_{f,i}}{RT^\theta}$	Enthalpy of formation of component i
I_{cell}	$= \frac{\tilde{I}_{cell}}{I^\theta} = \frac{\text{Cell current}}{\text{Characteristic current}}$	Total cell current
i	$= \frac{\tilde{i}}{i^\theta} = \frac{\text{Current density}}{\text{Characteristic current density}}$	Current density
K_j		Equilibrium constant of reaction j
l_2	$= \frac{L_2}{L_1} = \frac{\text{Cathode channel length}}{\text{Anode channel length}}$	Geometric aspect ratio
n_i	$= \frac{\tilde{n}_i L_1 L_2}{G^\theta} = \frac{\text{Mass exchange flux density}}{\text{Characteristic convective flow density}}$	Mass exchange flux density of component i
n_j		Number of electrons transferred in electrochemical reaction j
P	$= \frac{\tilde{P}}{P^\theta} = \frac{\text{Electric power}}{\text{Characteristic electric power}}$	Electric power
Pe_s	$= \frac{G^\theta R}{h_s \lambda_s} = \frac{\text{Convective heat transport}}{\text{Conductive heat transport}}$	Peclet number
Q_m	$= \frac{\tilde{Q}_m}{G^\theta RT^\theta} = \frac{\text{Heat exchange flow}}{\text{Characteristic convective heat flow}}$	Heat exchange flux
q	$= \frac{\tilde{q}}{g^\theta RT^\theta} = \frac{\text{Heat exchange flow density}}{\text{Characteristic convective heat flow density}}$	Heat exchange flux density

q_s	$= \frac{\tilde{q}_s L_1 L_2}{G^\theta RT^\theta} = \frac{\text{Heat source density}}{\text{Characteristic convective heat flow density}}$	Heat source density
r_j	$= \frac{\tilde{r}_j}{r_j^\theta} = \frac{\text{Reaction rate}}{\text{Characteristic reaction rate}}$	Reaction rate of reaction j
R_{back}	$= \frac{\Gamma_{back}}{\Gamma_{c,out}} = \frac{\text{Cathode recycle flow rate}}{\text{Cathode outlet flow rate}}$	Cathode recycle ratio
$s_{f,i}$	$= \frac{\tilde{s}_{f,i}}{R}$	Entropy of formation of component i
S/C		Steam to carbon ratio
St	$= \frac{k}{g^\theta \cdot c_p^\theta} = \frac{\text{Characteristic heat exchange}}{\text{Characteristic convective heat transport}}$	Stanton number
St_m	$= \frac{k_m \cdot F_m}{g^\theta \cdot c_p^\theta} = \frac{\text{Characteristic heat exchange}}{\text{Characteristic convective heat transport}}$	Stanton number of the reversal chamber
U_{cell}	$= \frac{\tilde{U}_{cell}}{\phi^\theta} = \frac{\text{Cell voltage}}{\text{Characteristic electric potential}}$	Cell voltage
V	$= \frac{\tilde{V}}{V^\theta} = \frac{\text{Volume}}{\text{Characteristic volume}}$	Volume
Y_{fuel}	$= \frac{\tilde{I}}{G_{feed} \cdot x_{CH_4,feed} \cdot 8 \tilde{F}} = \frac{\text{Total cell current}}{\text{Anode feed}}$	Fuel utilisation

Greek symbols

$\alpha_{j,\pm}$		Transition factors for reaction j
Γ	$= \frac{G}{G^\theta} = \frac{\text{Molar flow}}{\text{Standard molar flow}}$	Total molar flow
γ	$= \frac{g}{g^\theta} = \frac{\text{Molar flow density}}{\text{Characteristic molar flow density}}$	Molar flow density
$\Delta \phi_{j,0}$	$= \frac{\Delta \phi_{j,0}^\sim}{\phi^\theta} = \frac{\text{Equilibrium electric potential difference}}{\text{Characteristic electric potential}}$	Equilibrium potential difference of reaction j
$\Delta_R g_j^0$	$= \frac{\Delta_R \tilde{g}_j^0}{RT^\theta}$	Standard free (Gibbs) enthalpy of reaction j
$\Delta_C h_i^0$	$= \frac{\Delta_C \tilde{h}_i^0}{RT^\theta}$	Standard combustion enthalpy of component i
$\Delta_R h_j^0$	$= \frac{\Delta_R \tilde{h}_j^0}{RT^\theta}$	Standard enthalpy of reaction j
$\Delta_R s_j^0$	$= \frac{\Delta_R \tilde{s}_j^0}{R}$	Standard entropy of reaction j
ζ_d	$= \frac{z_d}{L_d} = \frac{\text{Spatial coordinate}}{\text{Characteristic channel length}}$	Spatial coordinate
η	$= \frac{\text{Power yield}}{\text{Power invested}}$	Electric efficiency
ϑ	$= \frac{T}{T^\theta} = \frac{\text{Temperature}}{\text{Standard temperature}}$	Temperature
κ_e	$= \frac{k_e \cdot \phi^\theta}{i^\theta} = \frac{\text{Characteristic ion flow density}}{\text{Characteristic current density}}$	Ion conductivity
λ_{air}		Air number

$\nu_{i,j}$		Stoichiometric coefficient of component i in reaction j
$\bar{\nu}_j$		Total mole change in reaction j
$\nu_{i,Cj}$		Stoichiometric coefficient of component i in combustion reaction of component j
$\bar{\nu}_{Cj}$		Total mole change in combustion reaction of component j
ξ_j		Extent of reaction j
τ	$= \frac{t}{t^\theta} = \frac{\text{time}}{\text{Characteristic residence time}}$	Time
φ_i	$= \frac{p_i}{p^\theta} = \frac{\text{Partial pressure}}{\text{Standard pressure}}$	Partial pressure of component i
ϕ	$= \frac{\tilde{\phi}}{\phi^\theta} = \frac{\text{Electric potential}}{\text{Characteristic electric potential}}$	Electric potential
X_i	$= x_i$	Mole fraction of component i
ψ	$= \vartheta$	Integration variable, temperature

Symbol table 2: Indexes

Lower Indexes

0	Initial condition
\pm	Forward / backward reaction
a	Anode gas phase
ac	Anode catalyst, anode electrode
air	Burner air
as	Anode / solid phase exchange
b	Burner
$back$	Cathode recycle
c	Cathode gas phase
cc	Cathode catalyst, cathode electrode
cs	Cathode / solid phase exchange
i	Chemical species, component
in	Inlet
j	(usually) chemical reaction
l	Chemical species, component
m	Reversal chamber
out	Outlet
s	Solid phase

Upper Indexes

0	Thermodynamic standard
θ	System specific standard
\sim	Dimensional variable

Symbol table 3: Dimensional parameters

Latin symbols

\tilde{c}	Charge capacity	$C \cdot V^{-1} \cdot m^{-2}$
\tilde{D}_i	Mass transport coefficient of component i	$mol \cdot m^{-2} \cdot s^{-1} \cdot Pa^{-1}$
$E_{A,j}$	Activation energy of reaction j	$J \cdot mol^{-1}$
F_m	Heat exchange surface of reversal chamber	m^2
G	Molar flow	$mol \cdot s^{-1}$
g	Mass flow density	$mol \cdot m^{-2} \cdot s^{-1}$
h_{alc}	Height	m
$\tilde{h}_{f,i}$	Enthalpy of formation of component i	$J \cdot mol^{-1}$
\tilde{I}	Total cell current	A
\tilde{i}	Current density	$A \cdot m^{-2}$
k_e	Ion conductivity of electrolyte	$m^{-1} \cdot \Omega^{-1}$
k^h	Heat exchange coefficient	$W \cdot m^{-2} \cdot K^{-1}$
L_k	Cell size in direction k	m
\tilde{n}_i	Mass exchange flux density	$mol \cdot m^{-2} \cdot s^{-1}$
\tilde{P}	Power	W
p	Pressure	Pa
\tilde{q}	Heat flux density	$W \cdot m^{-2}$
\tilde{Q}_m	Heat flux of reversal chamber	W
\tilde{q}_s	Heat source density solid	$W \cdot m^{-3}$
R	Gas constant	$J \cdot mol^{-1} \cdot K^{-1}$
\tilde{r}_j	Reaction rate of reaction j	$mol \cdot m^{-2} \cdot s^{-1}$
$\tilde{s}_{f,i}$	Entropy of formation of component i	$J \cdot mol^{-1} \cdot K^{-1}$
T	Temperature	K
t	Time	s
\tilde{U}_{cell}	Cell voltage	V
u_a	Gas velocity	$m \cdot s^{-1}$
\tilde{V}	Volume	m^3
x_i	Mole fraction of component i	1
z_k	Spatial coordinate k	m

Greek symbols

$\Delta \tilde{\phi}_{j,0}$	Standard potential difference of reaction j	V
$\Delta_R \tilde{g}_j^0$	Standard free (Gibbs) reaction enthalpy of reaction j	$J \cdot mol^{-1}$
$\Delta_C \tilde{h}_i^0$	Standard combustion enthalpy of component i	$J \cdot mol^{-1}$
$\Delta_R \tilde{h}_j^0$	Standard reaction enthalpy of reaction j	$J \cdot mol^{-1}$
$\Delta_R \tilde{s}_j^0$	Standard reaction entropy of reaction j	$J \cdot mol^{-1} \cdot K^{-1}$
λ_s	Thermal conductivity	$W \cdot m^{-1} \cdot K^{-1}$
$\tilde{\phi}$	Electric potential	V

Zusammenfassung

Ziel der vorliegenden Arbeit ist die Erstellung einer Hierarchie von mathematischen Modellen einer einzelnen Schmelzkarbonatbrennstoffzelle (MCFC). Diese Modelle dienen unterschiedlichen Zwecken in den Bereichen Systementwurf, Optimierung und Anlagensteuerung. Zunächst wird ein Referenzmodell in dimensionslosen Kennzahlen als oberstes Element der Hierarchie formuliert. Dieses Modell berücksichtigt eine Reihe von physikalischen und chemischen Phänomenen und basiert auf Stoff- und Energiebilanzen. Neben der Beschreibung der Vorgänge in der Brennstoffzelle selbst werden in diesem Modell auch ein katalytischer Nachbrenner und eine Umlenkammer zwischen Anoden- und Kathodenkanal beschrieben. Mit Hilfe dieses Modells wird nicht nur die Zellspannung als Resultat der vorgegebenen Eingangsgrößen beschrieben, sondern es ermöglicht auch eine örtlich und zeitlich verteilte Beschreibung von Konzentrations- und Temperaturprofilen. Das Referenzmodell dient hauptsächlich als Ausgangspunkt zur Herleitung weiterer maßgeschneiderter Modelle für die jeweiligen Anwendungen. In dieser Arbeit werden zwei dieser Modelle hergeleitet und ihre Anwendungen demonstriert: Das physikalisch reduzierte Modell und das stationäre Anodenmodell.

Das örtlich eindimensionale, isotherme stationäre Anodenmodell ist auf die Beschreibung der grundlegenden Zusammenhänge zwischen dem Reformierungs- und dem Oxidationsprozess ausgerichtet. Gemeinsam mit dem dazugehörigen Umsatzdiagramm kann dieses Modell zur Synthese von MCFC-Systemen eingesetzt werden, da es einen raschen Vergleich unterschiedlicher Konfigurationen mittels graphischer und numerischer Methoden ermöglicht. Darüber hinaus bietet das Umsatzdiagramm einen intuitiven Einblick in das Zusammenspiel von Reformierung und Oxidation. Exemplarisch werden drei Anwendungen gezeigt: Der Vergleich von Reformierungskonzepten, die Verschaltung von Brennstoffzellen in Kaskaden und die Anwendung einer Anodengasrückführung. Das stationäre Anodenmodell belegt, daß auch in hochkomplexen Systemen wie der MCFC elementare Zusammenhänge mit einfachen Mitteln darzustellen sind.

Die Anwendungen des physikalisch reduzierten Modells liegen in anderen Bereichen. Dieses dynamische, örtlich zweidimensionale Modell ermöglicht die Simulation von stationären Zuständen und dynamischen Übergängen des Systems. Somit dient es zum Einen zur quantitativen Voraussage des Systemverhaltens, andererseits lassen sich daraus auch qualitative Einsichten in die Zusammenhänge innerhalb einer MCFC ableiten. Für den sicheren Betrieb der Zelle ist die Temperaturverteilung von höchster Bedeutung, sie muß innerhalb eines zulässigen Bereiches liegen. Diese ergibt sich aus dem Zusammenwirken von endothermen und exothermen Reaktionen, Wärmeleitung in den festen Bauteilen der Zelle und dem Wärmeaustausch mit den durch die Kanäle strömenden Gasen und kann mit Hilfe des physikalisch reduzierten Modells im voraus berechnet werden. In dynamischen

Szenarien wie dem in dieser Arbeit gezeigten Lastwechsel werden die unterschiedlichen Zeitkonstanten des Systems deutlich. Extrem schnelle Ladungsvorgänge an den elektrochemischen Doppelschichten laufen innerhalb von Mikrosekunden ab, Konzentrationen in den Gaskanälen ändern sich in wenigen Sekunden, während das Temperaturfeld sich nur langsam über einen Zeitraum von mehreren Stunden ändert.

Basierend auf dem physikalisch reduzierten Modell werden Optimierungen durchgeführt. Dabei sind zum einen die Betriebsbedingungen – Gasmenge, Zusammensetzung und Luftmenge – so einzustellen, daß ein maximaler Wirkungsgrad erreicht wird und gleichzeitig Nebenbedingungen bezüglich des Temperaturfeldes und der Zellspannung erfüllt werden. In den vorhergehenden stationären Simulationen wird die kühlende Wirkung des endothermen Reformierungsprozesses deutlich. Diese gezielt einzusetzen ist Gegenstand einer weiteren Optimierung. Dabei wird der Reformierungskatalysator derart örtlich verteilt, daß eine Vergleichmäßigung des Temperaturfeldes erreicht wird und somit letztendlich eine der Wirkungsgrad der Zelle gesteigert werden kann.

Zur Zeit werden diese Modelle experimentell validiert, um die Übertragbarkeit der hier erzielten Ergebnisse zu gewährleisten. Erst wenn dies geschehen ist, lassen sich auch die Optimierungsergebnisse auf reale MCFCs übertragen und dort überprüfen. Augenblicklich werden Arbeiten durchgeführt, die darauf abzielen, ein mathematisch reduziertes Modell als weiteres Element der Modellhierarchie abzuleiten. Dieses wird im wesentlichen als Grundlage für den Entwurf von Zustandsbeobachtern und Optimalsteuerungen eingesetzt werden.

If I have seen further than others, it is by
standing upon the shoulders of giants.

Sir Isaac Newton

Der Zwerg sieht weiter als der Riese, auf
dessen Schultern er steht.

Prof. Bernhard Zimmermann

1 Introduction

Fuel cells are an upcoming technique for efficient and low-pollution generation of electric energy. Their high efficiency is based on the transformation of chemical into electric energy in one single step, instead of taking the detour over the transformation into heat, then pressure, afterwards kinetic energy and finally electric energy. Fuel cells by themselves are not the final answer to the question of a sustainable zero-emission energy cycle, but they promise to use available resources more effectively and will probably become a valuable piece in a future puzzle of sustainable energy supply [1].

Among the various types of fuel cells, the high temperature molten carbonate fuel cell (MCFC) has drawn increasing attention of scientists and engineers both in industry and academia during the last two decades. During this time, many problems concerning effective and durable materials, catalyst degradation, reaction kinetics, stack production and system integration have been dealt with. As a result, MCFCs are produced and operated as field test facilities today. Although the technical feasibility of the MCFC-principle and its high efficiency are proven, there are still some issues remaining to attain economic viability. These issues are about cost minimisation in the production process on the one hand and yield maximisation during the cells' operating phase.

The last mentioned are manifold: System optimisation calculations reveal feasible system designs which improve cell performance and durability. Ideal operating conditions must be found to achieve the highest possible system performance and sophisticated control strategies allow to switch the system from one load condition to a very different point in the shortest time, regarding all relevant material related constraints and limitations. The basis for the development of all these features is the appropriate modelling of the system which is the focus of this work.

In the following chapters, after a short introduction into the principle and the state of the art concerning MCFCs (this chapter), their modelling is extensively discussed (Chapter 2). There the reader finds a reference model together with two additional models, both derived from the first one. The models start with the highest level of complexity and proceed to rather simple and small equation sets. The chapters after that take the same route in the

other direction: Chapter 3 deals with simple, but fundamental thoughts on the combination of reforming and oxidation reactions. Chapter 4 shows the simulation capabilities of the second model and Chapter 5 finally demonstrates the applicability of the model to optimisation calculations. The Appendix contains a literature index, a table of symbols and several derivations, whose extent is too large to be included in the regular chapters.

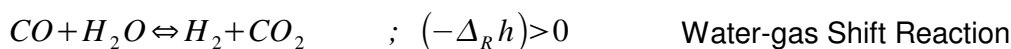
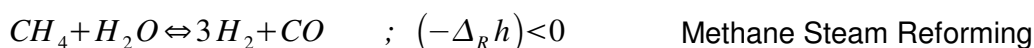
1.1 Working principle and technical features of the MCFC

The working principle of an MCFC is shown in Figure 1.1. It basically consists of three layers, which are the porous anode and cathode electrodes and the electrolyte between these two. The metallic parts of the electrodes possess a certain electric conductivity, although they are far from being good conductors. Their thickness is only a few hundred micrometers. Nickel based alloys are frequently used for the anode electrode, while nickel oxide is the preferred material for the cathode electrode. These materials serve as catalysts for the electrochemical reactions inside the electrode pores.

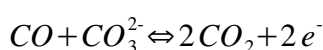
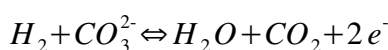
The electrolyte between these two is an eutectic carbonate salt mixture (e.g. Li_2CO_3 / K_2CO_3), which is liquid at the operating temperature of about 600°C . It is held in place by capillary forces in a porous matrix based on alloys with aluminium oxide, for example LiAlO_2 . The layer is about as thick as the electrodes and is a fairly good conductor of carbonate ions. At the same time, this layer is a very good isolator against uncharged molecules like hydrogen or oxygen. The electrolyte is also present in the electrodes, where a part of the pores is flooded with it.

The chemical reactants of both electrodes are supplied by gas channels. The anode channel contains an additional porous catalyst for the reforming of the feed gas.

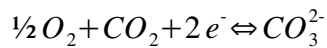
In Figure 1.1 a mixture of methane and water is used as anode fuel gas. Upon entrance in the anode channel, these reactants undergo several reactions on the reforming catalyst, of which the methane steam reforming reaction and the water-gas shift reaction are the most important. The products of these reactions are primarily hydrogen, carbon monoxide and carbon dioxide. The concept of hydrogen production inside the anode channel is known as Direct Internal Reforming (DIR). Although the Water-gas Shift Reaction is slightly exothermic, the overall reforming process is endothermic.



Hydrogen and carbon monoxide migrate into the anode electrode and react electrochemically, consuming carbonate ions from the electrolyte and producing free electrons on the electrode:



The anode exhaust gas consists of unreformed feed gas, reforming products and oxidation products. It is mixed with air and then fed into a catalytic combustion chamber, where all combustible species are completely oxidised. Intentionally air in stoichiometric excess is used here, so that some oxygen is left in the burner exhaust gas. This mixture is then fed into the cathode channel. Here carbon dioxide and oxygen react on the electrode producing new carbonate ions in the electrolyte and consuming electrons from the cathode electrode:



The cathode exhaust gas leaves the system. The sum of the oxidation reactions with the reduction reaction corresponds to the combustion reaction of hydrogen to water or carbon monoxide to carbon dioxide, respectively. A part of their reaction enthalpy is transformed into electric energy, the rest is released as heat.

Driven by gradients in concentration and electric potential, the carbonate ions migrate through the electrolyte from the cathode towards the anode electrode. The surplus electrons on the anode are transferred to the cathode electrode, where electrons are missing, via an electric consumer, where they can perform useful electric work.

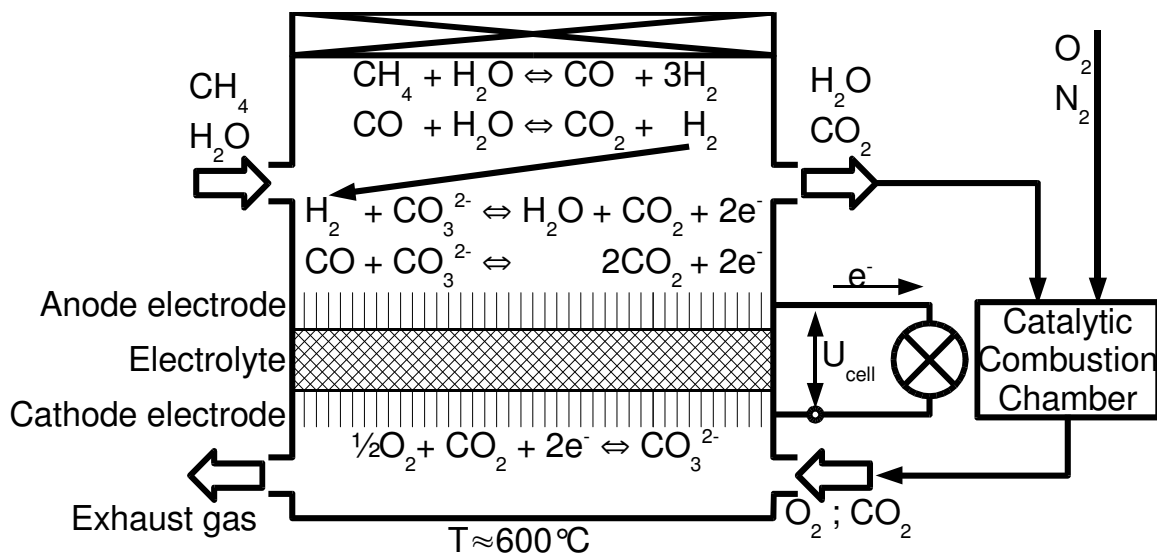


Figure 1.1: Working principle of an DIR-MCFC (Molten Carbonate Fuel Cell with Direct Internal Reforming).

Compared to other types of fuel cells, the MCFC offers a number of advantages. Because of the high operating temperature, the electrochemical reactions are sufficiently fast without cost-intensive noble metal catalysts like platinum. The nickel and nickel oxide catalysts applied here are not only cheaper, they are also less poisonous to handle. Most important is the fact that they are not sensitive to carbon monoxide, which is a major problem in the field of the platinum based PEMFC (Polymer Electrolyte Membrane Fuel Cells). In MCFC, carbon monoxide is not only harmless, it is even a useful educt for the production of electric power. Nevertheless, sulphur in concentrations above a few ppm in the feed gas quickly degrades the catalysts in MCFCs and therefore has to be avoided. The high temperature and the

insensitivity against carbon monoxide allow the realisation of the direct internal reforming concept. The direct integration of the endothermic reforming reaction, which produces hydrogen, with the exothermic oxidation, which consumes hydrogen, elegantly solves the heating problem with reforming and the cooling problem with the electrochemical reactions. Also, it overcomes the equilibrium limitation of the reforming process via the continuous consumption of its reaction product. All this offers the chance for a very compact and highly efficient system design. Chapter 3 of this work treats these matters in more detail.

The insensitivity against carbon monoxide makes the system useful for a large variety of fuels. Among natural gas, which certainly is the ideal feed gas for this system, other gas mixtures containing hydrogen, carbon monoxide or other short chained hydrocarbons are feasible. Possible options include bio gas, converter gas, landfill gas, waste gas from chemical processes (for example in the refining industries) and coal gas.

Due to its high operating temperature, the MCFC not only produces electric energy, but also high temperature waste heat which can be used for additional power production via a micro turbine, for the generation of high pressurised steam or for adsorption cooling. The advantage over conventional processes, which also combine electricity and heat production, is the ratio between both products. Many applications require more electric power than heat, a demand which many conventional processes can not fulfill. The MCFC with its electric system efficiency of about 50% fits these requirements better. If necessary, the cell can also be operated with lower efficiency, providing more heat and less electricity.

The flexibility of the MCFC with respect to fuels and to the form of energy supplied opens a wide spectrum of applications, most of them stationary. Distributed power supply in residence areas, electric power, heat and cold supply in large facilities like hospitals or office towers, also power and steam supply in industrial buildings are only a few examples for this.

Besides these advantages, the MCFC also has some drawbacks. Due to its low current density (typically at about 120 mA/cm²), the power density of this fuel cell type is about ten times lower than that of a PEMFC (usually above 1000mA/cm²). This prohibits any applications where space or weight is a crucial factor. Due to this low power density, the installation costs per installed unit of electric power can hardly beat the costs of today's conventional processes. This problem is expected to be more than compensated during the system's life time by the outstanding electric efficiency.

Since 1990, the MTU CFC Solutions GmbH in Ottobrunn, Germany, (a company of the MTU Friedrichshafen, which belongs to the Daimler-Chrysler group, and the RWE company) is working on the realisation of the MCFC principle. They have developed a system with 250 kW electric power called the "HotModule" (Figure 1.2). Its stack consists of 342 cross flow cells and it features direct internal reforming (DIR) and also indirect internal reforming (IIR). In Figure 1.3 the anode channels run from the bottom of the stack to its top, where air is added to the anode exhaust gas. A catalytic combustion chamber is installed on top of the stack. There the gas is completely oxidised and enters a space, the reversal chamber, from

where it flows into the cathode channels, going from the left to the right side of the stack. For reasons of temperature homogenisation, a part of the cathode exhaust gas is recycled and added to the anode exhaust gas in front of the burner.

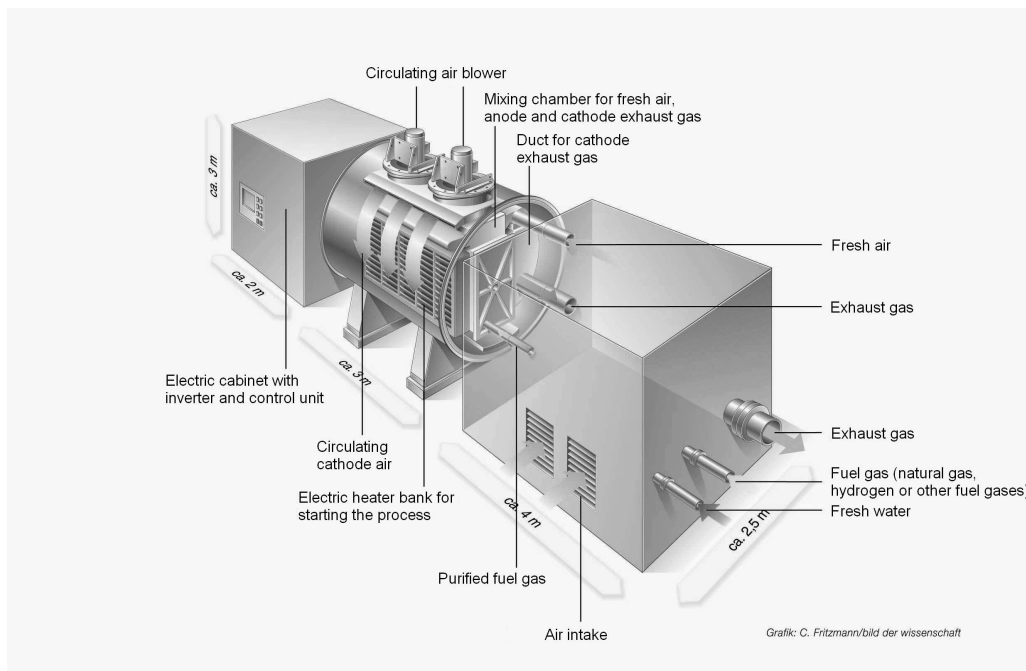


Figure 1.2: Scheme of the HotModule. The three parts of the system are shown: the electric converter system, the cell vessel and the media supply.

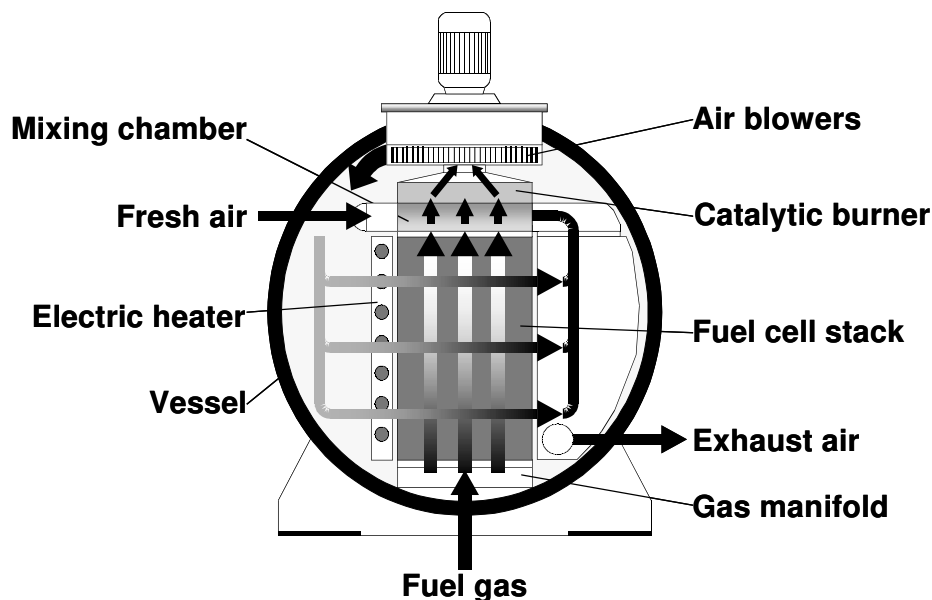


Figure 1.3: Working principle of the HotModule.

The name of the HotModule was chosen to highlight the fact that all hot cell parts are assembled in just one single vessel. Further devices are assembled in the so-called media supply. Here a desulphuriser with activated carbon, a heat exchanger and a humidifier, an external prereformer and several heat exchangers serve for the pre-treatment of the fuel gas. Within this work the focus is on the cell stack vessel, the media supply is not treated.

The first HotModule pilot plant was installed in 1997 in Dorsten, Germany, and was operated for a total of 1500 h [2]. A second plant was installed at the university in Bielefeld. It reliably ran for two years and was shut down intentionally for post-test analysis. During 2001 to 2003, more than 20 plants were installed in Germany, Europe, Japan and the US in various applications as a field trial [3]. With some stacks already having accumulated more than 3 years of operation time, the HotModule has not only proven its technical feasibility, but also demonstrated an unsurpassed electric system efficiency of 47%. Besides the regular maintenance of the sulphur filter, the system requires little attention. After the operating life time of the cell stack, it can easily be replaced by a new cell stack without much effort and with only a few days downtime.

Since October 2002, a HotModule plant is operated at the university hospital in Magdeburg, Germany by the "IPF Heizkraftwerksbetriebsgesellschaft Magdeburg GmbH" (short: IPF). The HotModule is part of the hospital's supply with electricity, heat and cold. It is equipped with a number of thermocouples, mass flow measuring devices and a chromatograph. In a collaboration with the IPF company, data from this HotModule is available for our research work.

Today, while further field trial plants are being installed, the MTU CFC Solutions GmbH is setting up facilities for series production of HotModules. The planned market entry is 2005/2006. As a further aim the development of systems of different power classes is in sight.

1.2 MCFC models in the scientific literature

Although the HotModule has proven to run reliably and with high efficiency, certain optimisation potentials remain to be explored. Due to limited possibilities for measurements, some states inside the stack like concentrations, current density and temperature are not well known. Thus most times the stack is probably not being operated at its optimum point. A better understanding of the cell interior is the basis for the optimisation of the operating conditions. In addition to the operation of the system, improved system design can increase safety, efficiency and profitability.

Not only at steady state operation, but especially in dynamic situations like load changes or the start-up phase, the cell behaviour is not well understood. As a consequence, the system is controlled based on empirical know-how which mainly aims at the safe operation of the system. The development of control strategies can do much to shorten load change times, while ensuring the safety of the system.

When discussing economic issues, the cell life cycle is important. Depending on the application and its specific demands, the cell operation can be optimised with respect to monetary aspects. Also, the automated online detection of stack failures and catalyst

degradation is of interest, because it allows to precisely plan the replacement of old cell stacks.

An indispensable prerequisite for the realisation of all the improvements mentioned is the mathematical modelling of the HotModule, being the major topic of this work. The models have to meet the various demands of the tasks mentioned before.

The beginnings of mathematical modelling of MCFC date back to the 1980's. Wolf and Wilemski [4] have published a number of papers on MCFC, one of which describes a complete two-dimensional steady state model for a single cross flow cell. It is based on the balances of mass and enthalpy and distinguishes the anode and cathode gas phase as well as one lumped solid phase. The methane steam reforming and the water-gas shift reaction in the anode channel are assumed to be in equilibrium, the pressure in both gas phases is assumed constant. The model is potentiostatic, which means that the cell voltage is given as an input variable. The current density is calculated from the actual cell voltage diminished by the open circuit voltage and some empirical functions for the activation overvoltage depending on local temperature and concentrations.

Many papers published later on by other authors are similar to the paper of the above mentioned authors. Yoshida et al. [5] compare various gas flow types for MCFC using a three-dimensional model. It only features the water-gas shift reaction, and the assumption of spatially constant cell voltage is used to derive an equation which allows to operate the model in a galvanostatic mode. Bosio, Costamagna and Parodi [6] set up another two-dimensional steady state model, in which the water-gas shift reaction is described via reaction kinetics.

Koh, Kang and Lim [7] have published a three-dimensional model with the assumption of locally constant current density, which simplifies their equations considerably. Contrary to most other models, momentum balances are considered here in order to estimate the pressure drop in an MCFC stack.

The influence on the MCFC cell in the presence of an Indirect Internal Reforming channel (IIR) is investigated by Park et al. [8]. Their two-dimensional model features a kinetically limited methane steam reforming reaction and a water-gas shift reaction in equilibrium. In order to simulate the temperatures in more detail, additional layers are introduced regarding the temperature of the separator plates and in the IIR channel. Again, a uniform current density is assumed and the cell voltage is calculated from the Nernst equation combined with some functions for the electrochemical activation overpotentials.

A transient, spatially concentrated model of an MCFC with indirect internal reforming is presented by Lukas et al. [9, 10]. It is also based on balances of mass and energy and considers reforming reactions inside the anode channel. This model is applied for the development of cycling control of MCFC plants. Therefore the set of model equations has to be rather small and thus the spatial distribution of states is not considered.

Contrary to these models, which are all based on conventional balances of mass and enthalpy, other approaches to simulate fuel cells have been made. Shen, Cao and Zhu [11] use neural network structures to simulate the nonlinear behaviour of a stack. This method may have the advantage of a comparably small number of equations and thereby a shorter computation time.

Among the other types of fuel cells, the solid oxide fuel cell (SOFC), is most similar to an MCFC. Its major issue is about temperature distribution and it also features internal reforming. Thus the methods of SOFC models could be transferred to MCFC modelling. Achenbach [12] has published a transient three-dimensional model for a SOFC stack including reforming reactions and empirical resistance functions for the anode and cathode electrode. Ferguson et al. [13], Iwata et al. [14] and Nagata et al. [15] have published further steady state models of various dimensions, with kinetics similar to those of Achenbach. Aguiar et al. [16] apply the kinetics from Achenbach on a one dimensional SOFC with an indirect internal reforming channel attached to it. Another transient model is presented by Petruzzi et al. [17] for a three-dimensional stack, but only water-gas shift reaction is included.

An uncounted number of zero-dimensional, that is locally concentrated, models have been published during the last two decades. As their number is far too large and their specifications are more or less similar to their multi-dimensional counterparts, these are not discussed here.

The special features of the models mentioned here are summarised in Table 1.1. Considering the intention of the modelling within this work, which is to supply models for system optimisation and optimal control design, the models available from the literature are not sufficient due to various reasons. Only the few transient models ([9, 10, 11]) are suitable for control development, and the available transient models for MCFC are either spatially concentrated or their parameters lack physical meaning, but physical interpretation of parameters is a precondition for useful system optimisation. Other models do not allow to calculate a current density distribution ([7, 8]), which is vital for the simulation of the temperature distribution, so they are not suitable for cell design optimisation. A few models consider the cell voltage as an input parameter ([4, 6]), but the HotModule is operated in a galvanostatic mode. The possibility to easily extend an existing model to include additional reactions and chemical components, say ethane and its reforming reactions, is severely limited in many models ([4], [12], [13]). Finally, none of the models in the literature features a catalytic combustion chamber between anode outlet and cathode inlet. Even though single tasks like optimisation and control development can be achieved with some of the available models, they are hardly comparable with each other, and each would require to be fitted to the Hotmodule. All these reasons lead to the necessity to develop a new model which fulfills all these demands.

Table 1.1: Survey of the main features of selected MCFC models in literature in chronological order.

Authors	Year	FC-type	Transient	Dim	Based on	Reforming
Wolf & Wilemski [4]	1983	MCFC	Steady state	2	Balances	MSR: Eq. WGSR: Eq.
Yoshiba et al. [5]	1998	MCFC	Steady state	3	Balances	WGSR: Kin.
Bosio et al. [6]	1999	MCFC	Steady state	2	Balances	WGSR: Kin.
Koh et al. [7]	2001	MCFC	Steady state	3	Balances	WGSR: Eq.
Park et al. [8]	2002	MCFC	Steady state	2	Balances	MSR: Kin. WGSR: Eq.
Lukas et al. [9], [10]	2002	MCFC	Transient	0	Balances	MSR: Kin. WGSR: Eq. IIR
Shen et al. [11]	2002	MCFC	Transient	N.N.	Neural network	-
Achenbach [12]	1994	SOFC	Transient	3	Balances	MSR: Kin. WGSR: Eq.
Ferguson et al. [13]	1996	SOFC	Steady state	3	Balances	MSR: Kin. WGSR: Eq.
Iwata et al. [14]	2000	SOFC	Steady state	2	Balances	-
Nagata et al. [15]	2001	SOFC	Steady state	1	Balances	MSR: Kin. WGSR: Eq.
Aguiar et al. [16]	2002	SOFC	Steady state	1	Balances	MSR: Kin. WGSR: Eq. IIR
Petruzzi et al. [17]	2003	SOFC	Transient	3	Balances	WGSR: Eq.

Eq.: Reaction at chemical equilibrium

Kin.: Reaction rate described by reaction kinetics

MSR: Methane steam reforming reaction

WGSR: Water-gas shift reaction

IIR: Indirect internal reforming

1.3 Scope of this work

Because of the broad range of different requirements on the modelling for optimisation, control development and other tasks, a family of cell models is required, each customised to the respective purpose. The base of this hierarchy of models is the reference model, which is introduced and discussed in Chapter 2. This model has the highest level of detail of all models. It is not necessarily applicable, but rather serves as a common basis for all other models. This approach ensures the comparability of the different models. Two of these models derived from the reference equations are also presented in Chapter 2 and their usage is demonstrated in the subsequent chapters. In Chapter 3, the basic interrelations between reforming and oxidation are examined using a very simple anode model. A specific diagram associated with this model not only gives clear insight into the advantages and the

behaviour of DIR, but also allows for fundamental investigations of system design. In Chapter 4, the results of a slightly reduced model are presented together with a parameter sensitivity analysis. Chapter 5 presents the application of this reduced model to detailed optimisations of operating conditions and to system optimisation with respect to the spatial distribution of the reforming catalyst.

Within this work, model parameters are calculated whenever possible. In other cases, they are approximated or adjusted so that the simulation results are reasonable and roughly comply with what is measured in the HotModule. Further tasks like the implementation of the media supply into the modelling and the optimisation, a detailed system optimisation or the development of model based control strategies would definitely exceed the frame of this work and are therefore currently being studied by others.

Data aequatione quotcunque fluentes quantitates involvente fluxiones invenire et vice versa.

Sir Isaac Newton

2 Modelling of MCFCs

The purposes of the modelling efforts of this work are manifold: understanding the principles of MCFC system behaviour, performing steady state optimisations with hundreds of iterations and finally developing control strategies for steady states and dynamic scenarios. These aims require very different mathematical models of varying detail level and complexity, each solvable with reasonable numerical effort. In order to minimise modelling effort and to ensure the comparability between all models it is useful to first establish a high level reference model and from it derive all other models that may be required for any specific task. The hierarchy of the three models presented within this chapter is shown in Figure 2.1. Mangold et al. [18] have derived an additional model of this hierarchy by means of mathematical model reduction, but this model is not treated here.

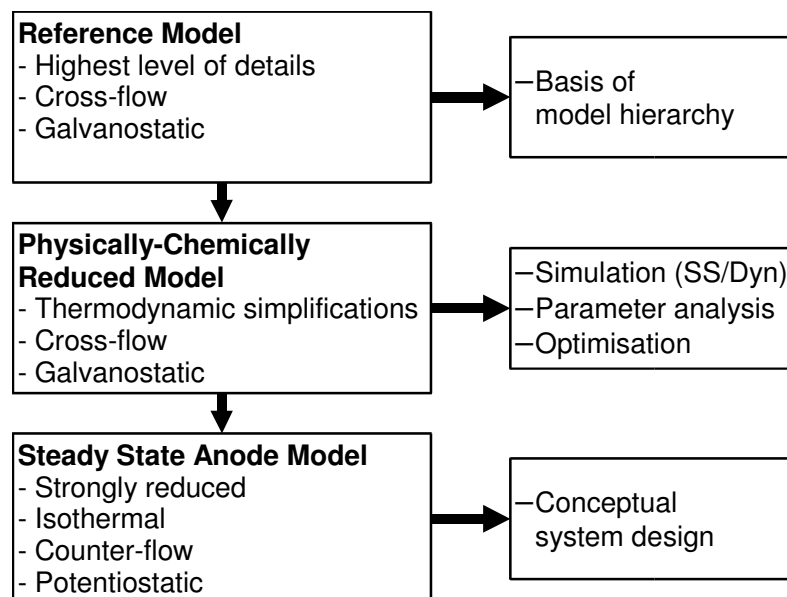


Figure 2.1: Hierarchical structure and applications of the three models presented in this work.

Within this chapter the reference model is introduced first. It describes the transient behaviour of a single cross flow MCFC. Its equations are given in full extend together with boundary and initial conditions and some physical interpretation of the major equations. An estimation of the model parameters follows.

By applying reasonable simplifications which do not change the structure or the essential characteristics of the reference model the so-called "physically-chemically reduced model" is

derived afterwards. These assumptions are discussed and the set of equations is given in short form and without extensive comments.

One further set of simplifications leads to the third model which is the steady state anode model. The assumptions made here are strongly simplifying, turning the system into a steady state model with only one spatial dimension. Because this model is very simple and contains only the major features of an MCFC, it provides useful insight into the systems principles and basic correlations.

A few more words about the modelling in general are necessary: All model equations are formulated in dimensionless parameters. Dimensionless numbers like the well-known Damköhler number or the Reynolds number describe relations of characteristic system parameters and are frequently used, for example, in fluid mechanics, aerodynamics and chemical engineering [19]. While their application does not simplify the structure of the equations by eliminating terms or non-linearities, this concept has certain advantages:

- The number of unknown parameters is reduced. Instead of determining the value of each unknown dimensional parameter one may assemble these into a dimensionless number which is unknown nevertheless, but then only one parameter has to be estimated or determined experimentally.
- The system description becomes more general. The results of a simulation with dimensionless parameters are valid not only for one specific cell, but for a whole class of systems in which the relations between all characteristic parameters (represented by the dimensionless numbers) are equal.
- The numerical solvability is increased. Contrary to dimensional parameters, dimensionless numbers often have roughly the same order of magnitude. This makes the equation system more suitable to solve for most numerical algorithms.
- Scale-up and scale-down are performed more easily.

Despite these advantages, this method also has certain drawbacks:

- For the purpose of experimental parameter validation, measurement data - which most likely possess physical units - have to be transformed into dimensionless numbers.
- Results presented in dimensionless numbers are more difficult to understand for those who are accustomed to think in dimensional parameters.

Despite these drawbacks, the mentioned advantages are dominant and thus all model equations presented in this work are completely in dimensionless form. In the appendix the reader finds some dimensional equations and the transformation into their dimensionless correspondents. A discussion of the most important dimensionless numbers together with their physical interpretation is given in Chapter 2.1.2 "Dimensionless numbers". Concerning the notation, the dimensionless parameters are expressed in Greek symbols whenever possible. Well-known numbers like the Damköhler number or the Peclet number are written in their usual notation. Only if the use of a Greek symbol could possibly cause more confusion than clarity, a latin letter is used for dimensionless quantities.

2.1 The 2D reference model

The dynamic two-dimensional reference model for a single MCFC represents the highest level of modelling detail in this work. The objective is to set up a model describing transient cell behaviour suitable for system analysis, containing a maximum number of physical and thermodynamical details disregarding the computation time necessary for solving the system. Due to its complexity and its high numerical solution effort, the model is not suitable for optimisation or control design, but may well serve as a testing device for the evaluation of control strategies based on models of lower detail level. These low level models can easily be derived from the reference model by applying further simplifications as it is shown in further sections of this work (see Chapter 2.3 "Physically-chemically reduced model" and 2.4 "Steady state anode model").

The model is introduced in three steps. In the following Chapter 2.1.1 some general assumptions and considerations are given. The most important states and parameter definitions are presented in Chapter 2.1.2. In the subsequent Chapter 2.1.3 the model equations together with specific assumptions are presented and discussed in their final form. Due to their large extent no derivations of the equations are given in these sections. An exemplary derivation of the anode gas phase equations can be found in the Appendix A.1 and A.2. We also refer to two published journal articles treating a one-dimensional version of this model ([20], [21]).

2.1.1 General considerations and assumptions

Before stepping into the assumptions used to set up the model equations one should first think of which quantities ought to be considered in the model. To fulfil its purpose the model has to accept changes in input quantities like feed gas composition, feed gas temperature and total cell current. It must deliver information about the temperatures inside the cell as well as the cell voltage, because these output quantities are of primary interest here. Nevertheless, one cannot calculate these two without knowing other states like the concentrations, flows and electric potentials inside the cell, as they are closely related to one another. Therefore, these other quantities have to be considered as well, so the model must contain equations for temperatures (ϑ), concentrations (in terms of mole fractions, X), mass flows (γ or I , respectively) and electric potentials (ϕ).

Although the stack of the HotModule is a three-dimensional block consisting of 342 cells, we assume that all cells behave alike. This assumption holds for all cells but a few at both ends of the stack. Here, heat losses cool down the cells, but this only affects a small number of them. Thus it is sufficient to model only one single cell, which is representative for most others in the stack.

Figure 2.2 shows the compartments of the cell including the catalytic combustion chamber and the reversal chamber which are connected by flows of mass and current. The figure can

be compared to Figure 1.3, in which the real geometry of these compartments in the HotModule is shown. Also the used coordinate system is indicated. The input parameters of the model describe the amount (in terms of dimensionless molar flows, I), composition (in terms of mole fractions, χ) and temperature (ϑ) of the anode and air inlet, the cathode gas recycle ratio (R_{back}) and the total cell current (I_{cell}).

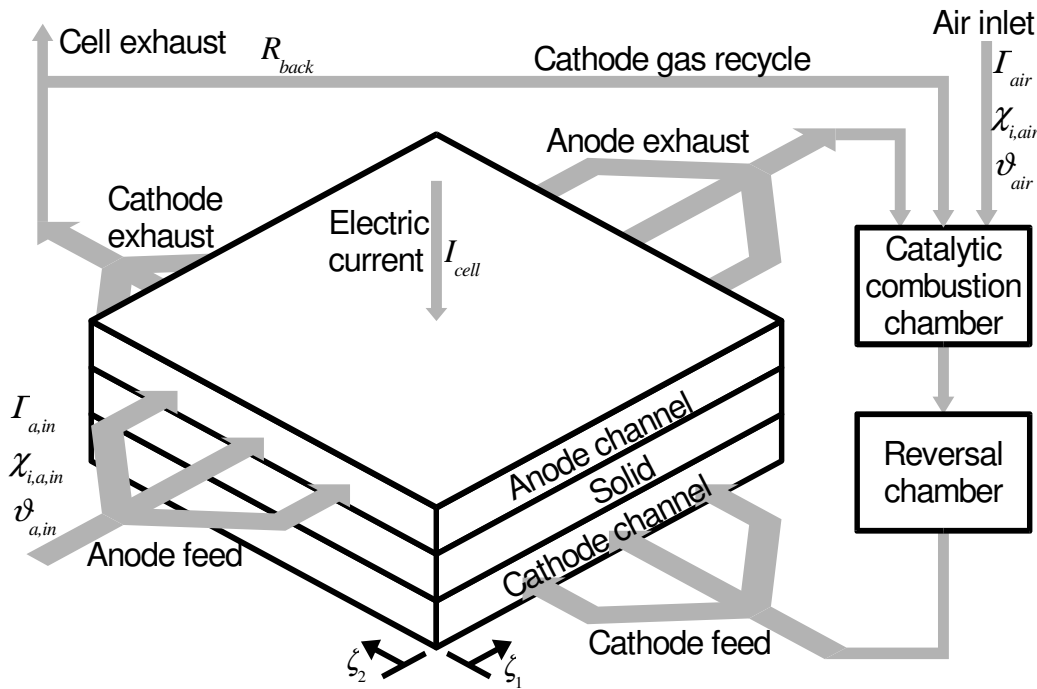


Figure 2.2: Compartments and mass flows of a cross flow cell together with the applied coordinate system.

A single fuel cell is three-dimensional in shape, although in most cases rather flat. While a number of authors in the literature (see Chapter 1.2) take on the challenge of modelling exact geometries and flow fields, this was not the way chosen here, for this would lead to unacceptable numerical effort especially for transient simulations. Consequently, assumptions are made that allow to model the system with only two geometric dimensions. Often times in an equation gradients in only one of these directions occur.

The general properties and assumptions of the model are as follows:

- There are no gradients in concentrations, velocities and temperatures perpendicular to the cell plane. For both gas phases this corresponds to a plug flow profile. It also includes that there are no concentration gradients of the reactants in the electrodes and no temperature gradients within the electrode/electrolyte compartment or the bipolar plate. This simplifies the model to a spatially two-dimensional system. Please note that two different phases like the anode gas phase and the cathode gas phase may still have different temperatures, but no temperature gradients will appear inside each of these phases.

- The cell consists of numerous parts like the two electrodes, the solid electrolyte matrix, the liquid electrolyte, the channel walls, the separator or bipolar plate and gaskets, and it contains gas in the channels and inside the porous electrodes. The temperatures of some of these components, for example several of the solid parts, are almost indistinguishable and therefore they are assumed to have the same temperature. Others show only medium heat exchange capabilities like between gas phases in the channels and the electrodes. As a result a lumped solid phase is introduced which combines the heat conductivities and heat capacities of all solid parts into one single phase. Its temperature is spatially distributed along the spatial coordinates. The temperatures of the gas inside the channels are calculated separately.
- The cell is part of a stack in which all cells behave alike. That leads to symmetry conditions at the boundaries to the neighbouring cells (insulated boundary).
- The HotModule is operated at nearly ambient pressure. As neither the simulation of pressure drop nor the dynamics of pressure changes are aims of the model, isobaric condition is assumed in the anode and cathode channels, in the combustion chamber and in the reversal chamber.
- The catalytic combustion chamber is modelled.
- The reversal chamber between combustion chamber outlet and cathode inlet is modelled.

2.1.2 Dimensionless numbers

The following model equations are written completely in dimensionless terms. To give an impression of their meanings and physical interpretations the definition of all state variables, the cell current and the most important model parameters are given in this chapter. A complete but uncommented list of dimensionless quantities can be found in the list of symbols, their values are listed in the Appendix A.6.

The definitions of the state variables are simple and easy to interpret. As the mole fraction in a dimensional equation system already is dimensionless it can be used without any changes. In order to distinguish dimensionless equations from dimensional ones, a Greek symbol is used.

$$\chi_i = x_i \quad (2.1)$$

A second measure of concentration is used in the electrode pores. The partial pressures, p_i , are related to a standard pressure, p^θ . It makes sense to use the same pressure value here which is assumed as a constant in all gas channels.

$$\varphi_i = \frac{p_i}{p^\theta} \quad (2.2)$$

The temperature, T , is made dimensionless by relating it to a standard temperature, T^θ . Out of many possible choices it has been decided to use the standard value for the definition of

thermodynamic properties (298.15 K) as the standard temperature throughout the model. Typical temperatures for the MCFC are at about 600°C to 650°C, so usually the dimensionless cell temperature has values at around 3. A dimensionless temperature difference of 0.1 corresponds to about 30 K.

$$\vartheta = \frac{T}{T^\theta} \quad (2.3)$$

Extensive molar flows, G , occur at the channels inlet and outlet and in the combustion chamber, reversal chamber and recycle. They are related to a standard value of a molar flow which is characteristic for MCFC operation, G^θ . The standard value is derived later (Chapter 2.2.1) using a well-defined standard load case. Typical values of Γ range from 0.1 for a very low gas feed to about 20 for the burner exhaust flow at load cases with high cell current.

$$\Gamma = \frac{G}{G^\theta} \quad (2.4)$$

In gas channels the intensive molar flow density, g , is used. It is related to a standard molar flow density, g^θ , resulting from the division of the standard molar flow by the respective cross sectional area. It has a similar order of magnitude as the total molar flows, Γ .

$$y_a = \frac{g_a \cdot L_2 \cdot h_a}{G^\theta} \quad (2.5)$$

$$y_c = \frac{g_c \cdot L_1 \cdot h_c}{G^\theta} \quad (2.6)$$

The electric potential, ϕ , becomes dimensionless by multiplying it by the Faraday constant, \tilde{F} , and dividing it by the gas constant, R , and the standard temperature, T^θ . This means that a dimensionless potential difference of 38.9 corresponds to 1V dimensional voltage.

$$\phi = \tilde{\phi} \cdot \frac{\tilde{F}}{RT^\theta} \quad (2.7)$$

One further dimensionless variable deserves a closer look. The dimensionless total cell current, I_{cell} , is defined as the dimensional total cell current divided by the stoichiometrically possible current under standard conditions, I^θ . That means that I_{cell} is unity at standard load case, and is less than one for lower current load cases.

$$I_{cell} = \frac{\tilde{I}_{cell}}{I^\theta} \quad (2.8)$$

The characteristic cell current, I^θ , is defined as the maximum current possible at standard feed flow, G^θ , with a standard mole fraction of methane $x_{CH_4,feed}^\theta$ under the assumption of complete reforming and oxidation conversion:

$$I^\theta = G^\theta \cdot x_{CH_4,feed}^\theta \cdot \frac{|v_{H_2,ref1} + v_{H_2,ref2}|}{|v_{CH_4,ref1}|} \cdot \frac{n_{ox} \tilde{F}}{|v_{H_2,ox1}|} \quad (2.9)$$

In the given system 4 moles of hydrogen can be produced from each mole of methane and each hydrogen molecule yields 2 electrons in the oxidation reaction defining the maximum electric current per methane feed. Thus the dimensionless cell current is:

$$I_{cell} = \frac{\tilde{I}_{cell}}{G^\theta x_{CH_4, feed}^\theta \cdot 8 \tilde{F}} \quad (2.10)$$

This definition makes the calculation of the fuel utilisation, Y_{fuel} , simple:

$$Y_{fuel} = \frac{I_{cell}}{I_{feed}} \cdot \frac{x_{CH_4, feed}^\theta}{x_{CH_4, feed}} \quad (2.11)$$

Among a number of functions and coefficients which are not discussed in detail here, but given in the list of symbols, there are some prominent and interesting dimensionless parameters in this model. Probably the most popular is the Damköhler number which always appears in connection with reactions. For the quasi-homogeneous gas phase reactions in the anode channel it reads:

$$Da_{ref} = \frac{r_{ref}^\theta \cdot L_1 L_2 h^\theta}{G^\theta} = \frac{\text{Characteristic rate of reaction ref}}{\text{Characteristic convection rate}} \quad (2.12)$$

The definition for the electrochemical (surface) reactions is:

$$Da_{ox,red} = \frac{r_{ox,red}^\theta \cdot L_1 L_2}{G^\theta} = \frac{\text{Characteristic rate of reaction ox,red}}{\text{Characteristic convection rate}} \quad (2.13)$$

In both cases a characteristic volume or surface related reaction rate under certain conditions (standard concentrations and temperature) is divided by a characteristic volume or surface related molar flow density. Volume related quantities are used for the gas phase reforming reactions, surface related quantities are applied for the electrochemical surface reactions. Thus the Damköhler number can be interpreted as a dimensionless reaction rate constant. The values of the Damköhler number are not limited. Still, if the standard conditions are chosen close enough to the realistic values the Damköhler number should lie between 1 and 100 for reactions with medium or fast rates. Due to their different structures the Damköhler numbers of the volumetric reforming reactions and the surface related electrochemical reactions are not directly comparable.

The Arrhenius number describes the temperature dependence of a reaction rate. It is defined as

$$Arr_j = \frac{E_{A,j}}{RT^\theta} = \frac{\text{Activation energy of reaction j}}{\text{Characteristic thermal energy}} \quad (2.14)$$

The mass transport between bulk gas phase in both channels and the electrode is described by some sort of dimensionless diffusion coefficient. In it a characteristic molar flux of component i is related to the standard convective flow. The characteristic molar flux is the total exchange flux of component i over the whole cell area under the assumption of a partial pressure difference between bulk phase and pore equal to standard pressure:

$$D_i = \frac{\tilde{D}_i p^\theta L_1 L_2}{\Delta h \cdot G^\theta} = \frac{\text{Characteristic diffusion flow of component } i}{\text{Characteristic convective flow}} \quad (2.15)$$

The Stanton number is a measure for the heat exchange capability at certain interfaces. Here a heat exchange coefficient for the complete exchange interface is related to the heat capacity of the standard convective flow:

$$St = \frac{k^h L_1 L_2}{G^\theta c_p^\theta} = \frac{\text{Characteristic integral heat exchange coefficient}}{\text{Characteristic convective heat capacity flow}} \quad (2.16)$$

The heat conductivity of the solid phase is described by the Peclet number. In analogy to the Stanton number it relates a characteristic measure for the conductive heat flux to the characteristic convective heat flux:

$$\frac{1}{Pe} = \frac{h_s \lambda_s}{G^\theta c_p^\theta} = \frac{\text{Characteristic conductive heat flux}}{\text{Characteristic convective heat capacity flow}} \quad (2.17)$$

Directly connected to the Peclet number is the ratio of the geometrical cell dimensions. It provides the informations necessary to calculate the dimensionless flux of conducted heat along a specific coordinate:

$$l_2 = \frac{L_2}{L_1} = \frac{\text{Cell length}}{\text{Cell width}} \quad (2.18)$$

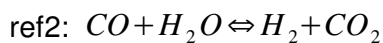
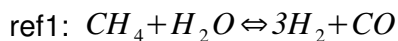
2.1.3 Model equations

In this chapter the model equations are introduced and discussed. The order in which the equations are introduced follows the gas flow through the cell starting with the anode channel, continuing with the catalytic burner, the reversal chamber, the cathode channel and finally the solid phase. As the modelling of the electric potentials offers a number of possible variations, only one single version is given here. An extensive presentation and discussion of further versions can be found in Appendix A.4. While some simple kinetics of heat and mass transfer are given along with the balance equations, the more complicated reaction kinetics for both the reforming and the electrochemical reactions are presented separately afterwards. All necessary thermodynamic relations are given in Chapter 2.1.3.9.

2.1.3.1 Anode channel

The states, fluxes and boundary conditions of the anode channel are shown in Figure 2.3. In addition to the general assumptions listed above, some further simplifications are made to describe the gas phase:

- The gas phase obeys the ideal gas law.
- The gas is assumed to flow through channels which are not crosslinked. This means the anode gas flows only along the ζ_1 coordinate without any velocity components in ζ_2 direction.
- Diffusion is negligible compared to convection.
- All reforming reactions in the anode channel are modelled as reversible, that is equilibrium limited, quasi-homogeneous gas phase reactions. The methane steam reforming (indexed "ref1") and the water-gas shift reactions (indexed "ref2") are considered:



- The heat of reaction of the gas phase reactions is fully transferred to the gas phase.
- Heat conduction is negligible compared to convective heat transport.
- Heat exchange between the gas phase and the solid phase is described by a linear approach. The heat exchange coefficient also includes a linearised form of the thermal radiation.

In the modelling of the anode gas phase, the mass transfer between electrode and gas phase is accounted for.

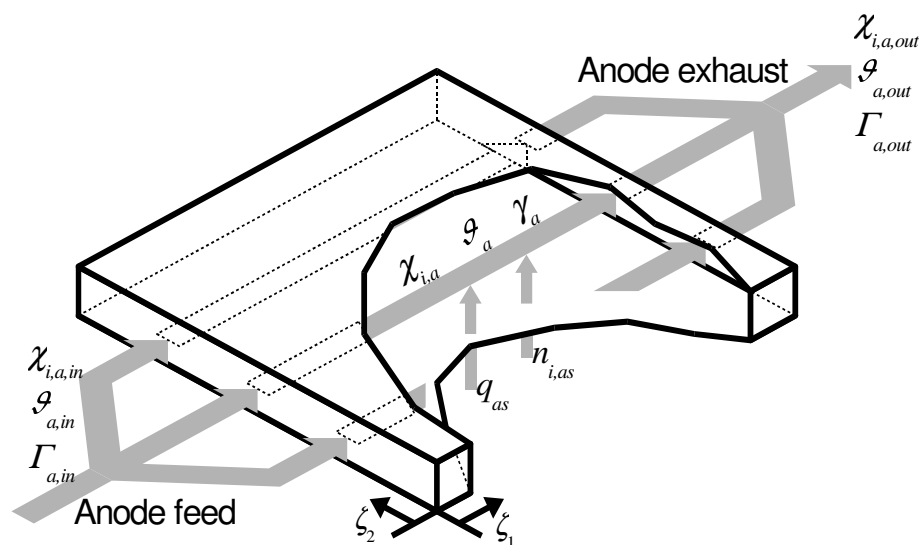


Figure 2.3: Anode channel with states, fluxes and boundary conditions.

With these assumptions one ends up with the following three equations. They are the partial mass balances, the enthalpy balance in temperature form and the total mass balance, describing the mole fractions, $X_{i,a}$, the gas temperatures, ϑ_a , and the molar flow density, γ_a . An exemplary derivation of Equation 2.19 can be found in the Appendix A.1.

$$\frac{V_a}{\vartheta_a} \frac{\partial X_{i,a}}{\partial \tau} = -\gamma_a \frac{\partial X_{i,a}}{\partial \zeta_1} + n_{i,as} - X_{i,a} \sum_l n_{l,as} + \sum_{j=ref} (v_{ij} - X_{i,a} \bar{v}_j) Da_j r_j \quad (2.19)$$

$$V_a \frac{c_{p,a}}{\vartheta_a} \frac{\partial \vartheta_a}{\partial \tau} = -\gamma_a c_{p,a} \frac{\partial \vartheta_a}{\partial \zeta_1} + \sum_i n_{i,as}^+ \cdot \int_{\vartheta_a}^{\vartheta_s} c_{p,i}(\Psi) d\Psi + \sum_{j=ref} (-\Delta_R h_j^0(\vartheta_a)) Da_j r_j + q_{as} \quad (2.20)$$

$$0 = -\frac{\partial \gamma_a \vartheta_a}{\partial \zeta_1} + \frac{1}{c_{p,a}} \left(\sum_i n_{i,as}^+ \cdot \int_{\vartheta_a}^{\vartheta_s} c_{p,i}(\Psi) d\Psi + \sum_{j=ref} (-\Delta_R h_j^0(\vartheta_a)) Da_j r_j + q_{as} \right) + \vartheta_a \sum_i n_{i,as} + \vartheta_a \sum_{j=ref} \bar{v}_j Da_j r_j \quad (2.21)$$

Here, the mass flow densities between gas phase and electrode pores are calculated from the mass balances of the electrode pores. They are distinguished according to their direction:

$$n_{i,as} \quad \text{cf. section 2.1.3.5 "Electrode pores"}$$

$$n_{i,as}^+ = \begin{cases} n_{i,as} & \text{if } n_{i,as} > 0 \\ 0 & \text{if } n_{i,as} \leq 0 \end{cases} \quad (2.22)$$

$$n_{i,as}^- = \begin{cases} 0 & \text{if } n_{i,as} > 0 \\ n_{i,as} & \text{if } n_{i,as} \leq 0 \end{cases}$$

The molar heat capacity of each component is temperature dependent and the average heat capacity is calculated depending on the temperature and gas composition.

$$c_{p,i}(\vartheta) \quad \text{cf. section 2.1.3.9 "Thermodynamics"}$$

$$c_{p,a} = \sum_i X_{i,a} c_{p,i}(\vartheta_a) \quad (2.23)$$

The heat of reforming reactions is also temperature dependent:

$$\Delta_R h_{ref}^0(\vartheta) \quad \text{cf. section 2.1.3.9 "Thermodynamics"}$$

The change of mole numbers in a reaction is described as follows:

$$\bar{v}_j = \sum_i \nu_{ij} \quad (2.24)$$

The heat exchanged between gas and solid is proportional to a heat transfer coefficient, the Stanton number, and the temperature difference between both phases:

$$q_{as} = St_{as} \cdot (\vartheta_s - \vartheta_a) \quad (2.25)$$

Chapter 2.1.3.8 discusses the reaction rates in more detail

$$r_j \quad \text{cf. section 2.1.3.8 "Reaction kinetics"}$$

Equations 2.19 and 2.20 are nonlinear hyperbolic PDEs of first order with respect to both time and the spatial coordinate ζ_l . They require one boundary and one initial condition. Equation 2.21 is a first order ODE with respect to ζ_l requiring only one boundary condition. The boundaries are defined by the inlet gas conditions, i.e. its mole fractions, temperature and molar flow, $X_{i,a,in}$, $\vartheta_{a,in}$, and $\Gamma_{a,in}$. Note that the dimensionless molar flow density at the anode channel inlet equals the dimensionless total molar feed flow (Equation 2.28).

$$X_{i,a}(\zeta_1=0, \zeta_2, \tau) = X_{i,a,in}(\tau) \quad (2.26)$$

$$\vartheta_a(\zeta_1=0, \zeta_2, \tau) = \vartheta_{a,in}(\tau) \quad (2.27)$$

$$y_a(\zeta_1=0, \zeta_2, \tau) = y_{a,in}(\tau) = \Gamma_{a,in}(\tau) \quad (2.28)$$

The initial conditions are

$$X_{i,a}(\zeta_1, \zeta_2, \tau=0) = X_{i,a,0}(\zeta_1, \zeta_2) \quad (2.29)$$

$$\vartheta_a(\zeta_1, \zeta_2, \tau=0) = \vartheta_{a,0}(\zeta_1, \zeta_2) \quad (2.30)$$

Although simple in their mathematical structure the balance equations require some explanations to understand their physical interpretation. The partial mass balances in molar form (Equation 2.19) describe the change of the mole fraction of any component i with time due to several phenomena. The first term on the right hand side describes the effect of convection of the gas through the anode channel along the ζ_l coordinate. The dimensionless molar flow density y_a does not appear inside the derivative because the total mass balance (Equation 2.21) was already inserted into this equation, eliminating y_a in the derivative. The second and third terms describe the effect of mass exchange between gas phase and electrode. The second term simply considers the direct effect of mass entering or leaving the gas phase. The third term can be interpreted to compensate mole fraction changes due to the dilution effects of overall mass transfer between the gas phase and the solid phase. In conjunction with the assumption of constant pressure an overall gas exchange flux leads to an increase or a decrease in molar gas flow density along the channel. The last term expresses the same effects for the gas phase reforming reactions. While the first part describes the source density for component i due to the reforming reactions the second one calculates the dilution / concentration effect of reactions with changes in total mole numbers. Here, Da_j can be interpreted as the dimensionless reaction rate constant, and r_j is the dimensionless reaction rate.

Equation 2.20 is the dynamic enthalpy balance in temperature form for the anode gas. Convective enthalpy transport is considered in the first term on the equation's right hand side. Components in the electrode pore have the temperature of the solid which most likely differs from the anode gas temperature. If components enter the anode from the electrode, this will influence the anode gas temperature. This is not the case for components leaving the channel into the electrode. The second term in connection with the case differentiation in

Equation 2.22 takes this into account. The heat of the reforming reactions is considered in the third term, while the last term describes the convective heat exchange between gas and solid phase.

The total molar balance (Equation 2.21) contains similar elements as the other two balance equations, but as a consequence of the constant pressure assumption this equation has no accumulation term. The first term is the spatial derivative of a product of two states, the molar flow density and the temperature. Recalling the ideal gas assumption the dimensionless temperature can be interpreted as a reciprocal molar density. Multiplying it with a molar flow density yields the gas velocity, clearly identifying this term as the convection term. The next three terms consider thermal expansion effects. Here again the same three phenomena are accounted for as in the temperature equation: temperature change connected to mass exchange with the electrode, heat of reforming reaction and convective heat transfer. The last two terms consider the increase of total molar flow due to mass exchange between gas and electrode as well as due to the reforming reactions.

While some of the variables in the equations 2.19, 2.20 and 2.21 like the Damköhler numbers are constant system parameters, most quantities are functions of state variables. Some of them are explicitly stated here (Equations 2.22, 2.23 and 2.24), yet others may be looked up in other chapters.

Before moving on to the next model compartment it is necessary to define the anode exhaust conditions at the end of the anode channel ($\zeta_1=1$). In this model only the averaged outlet conditions are required. These are calculated by integration over the whole outlet width:

$$\Gamma_{a,out} = \int_0^1 \gamma_a(\zeta_1=1, \zeta_2) d\zeta_2 \quad (2.31)$$

$$\Gamma_{a,out} \cdot X_{i,a,out} = \int_0^1 \gamma_a(\zeta_1=1, \zeta_2) \cdot X_{i,a}(\zeta_1=1, \zeta_2) d\zeta_2 \quad (2.32)$$

$$\begin{aligned} \Gamma_{a,out} \cdot \sum_i X_{i,a,out} \cdot \int_1^{\vartheta_{a,out}} c_{p,i}(\vartheta) d\vartheta \\ = \int_0^1 \gamma_a(\zeta_1=1, \zeta_2) \cdot \left(\sum_i X_{i,a}(\zeta_1=1, \zeta_2) \int_1^{\vartheta_a(\zeta_1=1)} c_{p,i}(\vartheta) d\vartheta \right) d\zeta_2 \end{aligned} \quad (2.33)$$

While the total amount and average composition of the anode exhaust gas is described explicitly, the average temperature can not be acquired that easily. It appears in Equation 2.33 only as the integration boundary on the equations left hand side and has to be adjusted so that the equation is solved, probably in an iterative way.

2.1.3.2 Catalytic combustion chamber

The specific assumptions for the catalytic combustion chamber are as follows:

- The combustion chamber has three inlets: the anode exhaust, the cathode recycle and the fresh air inlet (Figure 2.4).
- The volume of the combustion chamber is neglected. Any mass and energy accumulation capacities of the burner are accounted for in the equations of the reversal chamber.
- As the combustion chamber in the "HotModule" is surrounded by hot compartments its heat losses are negligible.
- The oxidation in the combustion chamber is total and instantaneous. No restrictions like limiting mass transfer, slow reaction kinetics or chemical equilibrium are considered.
- Due to the mixing chamber in front of the combustion chamber no spatially distributed gas composition from the anode or the cathode is considered, but averaged mole fractions and temperatures are used.

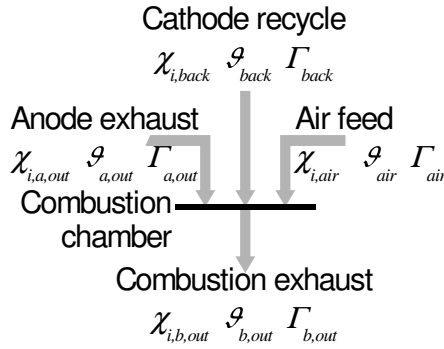


Figure 2.4: Catalytic combustion chamber with three inlet flows and one exhaust flow.

The combustion equations are the total and the partial mass balances and the enthalpy balance. They allow to calculate the amount, $\Gamma_{b,out}$, composition, $\chi_{i,b,out}$, and temperature, $\vartheta_{b,out}$, of the combustion exhaust gas. The total mass balance sums the molar flows of all inlet flows modified by the change of total mole numbers due to oxidation of combustible components:

$$\Gamma_{b,out} = \Gamma_{a,out} \cdot \left(1 + \sum_j \bar{\nu}_{Cj} X_{j,a,out}\right) + \Gamma_{back} \cdot \left(1 + \sum_j \bar{\nu}_{Cj} X_{j,back}\right) + \Gamma_{air} \cdot \left(1 + \sum_j \bar{\nu}_{Cj} X_{j,air}\right) \quad (2.34)$$

The partial mass balances are set up in a similar manner:

$$\begin{aligned} \Gamma_{b,out} \cdot \chi_{i,b,out} = & \Gamma_{a,out} \cdot \left(\chi_{i,a,out} + \sum_j \nu_{i,Cj} X_{j,a,out} \right) \\ & + \Gamma_{back} \cdot \left(\chi_{i,back} + \sum_j \nu_{i,Cj} X_{j,back} \right) \\ & + \Gamma_{air} \cdot \left(\chi_{i,air} + \sum_j \nu_{i,Cj} X_{j,air} \right) \end{aligned} \quad (2.35)$$

The enthalpy balance in temperature form demands that all enthalpy entering the system via the three inlet flows has to leave the system with the exhaust flow:

$$\begin{aligned}
& \Gamma_{b,out} \sum_i X_{i,b,out} \int_1^{\vartheta_{b,out}} c_{p,i} d\vartheta \\
& = \Gamma_{a,out} \sum_i X_{i,a,out} \left(\int_1^{\vartheta_{a,out}} c_{p,i} d\vartheta - \Delta_C h_i^0(\vartheta=1) \right) \\
& + \Gamma_{back} \sum_i X_{i,back} \left(\int_1^{\vartheta_{back}} c_{p,i} d\vartheta - \Delta_C h_i^0(\vartheta=1) \right) \\
& + \Gamma_{air} \sum_i X_{i,air} \left(\int_1^{\vartheta_{air}} c_{p,i} d\vartheta - \Delta_C h_i^0(\vartheta=1) \right)
\end{aligned} \tag{2.36}$$

Here the enthalpy of combustion is calculated at standard temperature from the enthalpies of formation weighted by the stoichiometric coefficients of the combustion reactions:

$$\Delta_C h_i^0(\vartheta=1) = \sum_j \nu_{j,Ci} \cdot \Delta_f h_j(\vartheta=1) \tag{2.37}$$

The change in total mole numbers due to a combustion reaction is calculated from

$$\bar{\nu}_{Cj} = \sum_i \nu_{i,Cj} \tag{2.38}$$

The total molar balance at the burner sums up all three inlet flows and adds the total molar change of all combustion reactions. The equation can be used to calculate the amount of the burner exhaust gas. The concentrations in the burner exhaust gas are derived from partial molar balances at the burner. According to the assumption of complete combustion, no combustible components occur in the burner exhaust. The enthalpy balance is an implicit equation for the burner exhaust temperature. This temperature only appears in the integration limit expression on the equations left hand side and must be adjusted to make the equation fit. The enthalpy of combustion of every species is defined in Equation 2.37 via the stoichiometric coefficients of the corresponding combustion reaction (see also Appendix A.6).

The three inlets are defined as follows: The conditions for the first combustion chamber inlet are identical to the averaged anode exhaust conditions (equations 2.31, 2.32 and 2.33). The conditions of the cathode gas recycle are given in the section 2.1.3.4 "Cathode channel" in equations 2.62 to 2.64. The conditions at the air inlet are given by the concentrations and the temperature of the air used and the air number. This air number, λ_{air} , defines the amount of air fed into the burner divided by the theoretically required amount for oxidising the anode feed gas. Thus the air flow is calculated as:

$$\Gamma_{air} = \Gamma_{a,in} \frac{\lambda_{air}}{X_{O_2,air}} \cdot \left(\sum_j (-\nu_{O_2,Cj} \cdot X_{j,a,in}) - X_{O_2,a,in} \right) \tag{2.39}$$

The material balance equations (2.35) may give negative results for exhaust concentrations if insufficient amounts of air are fed. This is based on the assumptions of complete combustion and the direct dependence of the burner air on the anode feed gas instead of

the anode exhaust gas. Because these results occur only at extreme conditions these equations are still applicable for usual cases. A calculation of the combustion under low oxygen feed would require the consideration of chemical equilibria in a large network of combustion reactions which would lead to an unacceptably high numerical effort – especially since this is usually not necessary and the simple equations are sufficient.

2.1.3.3 Reversal chamber

Between the combustion chamber exhaust and the cathode inlet there is a gas compartment of considerable size (Figure 1.3). There, no reactions take place but heat loss over the outer vessel wall occurs. For steady state modelling the heat loss could be incorporated into the burner equations and the volume could be neglected without loss of model precision. For a dynamic model however this compartment has its own dynamic properties which influence the interactions between anode exhaust and cathode inlet. The following assumptions are made for this compartment (Figure 2.5):

- The gas inside the compartment is highly mixed. Therefore it can be modelled as an ideal continuously stirred tank reactor (CSTR).
- Heat losses across the outer vessel wall are proportional to the difference between the gas and ambient temperature.
- The combustion exhaust is fed into the reversal chamber.

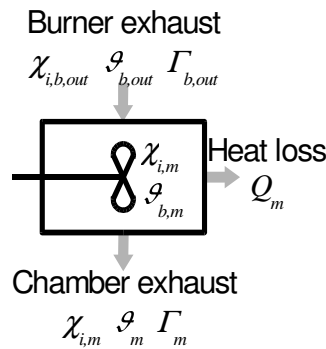


Figure 2.5: Reversal chamber with states, mass flows at inlet and outlet and heat loss.

The partial and total mass balances as well as the enthalpy balance yield the following equations:

$$\frac{V_m}{\vartheta_m} \frac{dX_{i,m}}{d\tau} = \Gamma_{b,out} (X_{i,b,out} - X_{i,m}) \quad (2.40)$$

$$\frac{V_m c_{p,m}}{\vartheta_m} \frac{d\vartheta_m}{d\tau} = \Gamma_{b,out} \sum_i X_{i,b,out} \int_{\vartheta_m}^{\vartheta_{b,out}} c_{p,i} d\vartheta - Q_m \quad (2.41)$$

$$\Gamma_m = \Gamma_{b,out} \cdot \left(1 + \frac{1}{c_{p,m} \vartheta_m} \cdot \sum_i X_{i,b,out} \int_{\vartheta_m}^{\vartheta_{b,out}} c_{p,i} d\vartheta \right) - \frac{Q_m}{c_{p,m} \vartheta_m} \quad (2.42)$$

Here the heat loss is calculated by a heat transfer coefficient, the Stanton number St_m , and the temperature difference between the reversal chamber and the surrounding air:

$$Q_m = St_m \cdot (\vartheta_m - \vartheta_u) \quad (2.43)$$

The average heat capacity is calculated as follows:

$$c_{p,m} = \sum_i X_{i,m} c_{p,i}(\vartheta_m) \quad (2.44)$$

The partial mass balances (Equation 2.40) are a simple CSTR type balance equation describing the effect of the inlet on the concentrations within the chamber. The steady state solution of this equation shows the equality of gas composition at inlet and outlet. The enthalpy balance in temperature form (Equation 2.41) looks much alike, but in addition it considers the effect of heat losses to the environment. Contrary to the preceding equation, inlet and outlet temperatures are not equal at steady state. Both equations are ODEs of first order with respect to time and each requires an initial condition:

$$X_{i,m}(\tau=0) = X_{i,m,0} \quad (2.45)$$

$$\vartheta_m(\tau=0) = \vartheta_{m,0} \quad (2.46)$$

The total mass balance (Equation 2.42) describes the amount of gas outflow as the amount of gas inlet plus the additional flow caused by gas density changes due to temperature changes. At steady state in conjunction with the enthalpy balance it simply states the equality between mass flows at inlet and outlet.

2.1.3.4 Cathode channel

The gas phase in the cathode channel is modelled under the same assumptions as the anode gas (Figure 2.6). The major differences here are that no reactions occur in the gas phase and the flow direction is perpendicular to that of the anode gas. Furthermore, a part of the cathode exhaust gas is recycled to the catalytic combustion chamber (Chapter 2.1.3.2).

Thus the equations for this phase are:

$$\frac{V_c}{\vartheta_c} \frac{\partial X_{i,c}}{\partial \tau} = -\gamma_c \frac{\partial X_{i,c}}{\partial \zeta_2} + n_{i,cs} - X_{i,c} \sum_l n_{l,cs} \quad (2.47)$$

$$V_c \frac{c_{p,c}}{\vartheta_c} \frac{\partial \vartheta_c}{\partial \tau} = -\gamma_c c_{p,c} \frac{\partial \vartheta_c}{\partial \zeta_2} + \sum_i n_{i,cs}^+ \cdot \int_{\vartheta_c}^{\vartheta_s} c_{p,i}(\Psi) d\Psi + q_{cs} \quad (2.48)$$

$$0 = -\frac{\partial \gamma_c \vartheta_c}{\partial \zeta_2} + \frac{1}{c_{p,c}} \left(\sum_i n_{i,cs}^+ \cdot \int_{\vartheta_a}^{\vartheta_s} c_{p,i}(\Psi) d\Psi + q_{cs} \right) + \vartheta_c \sum_i n_{i,cs} \quad (2.49)$$

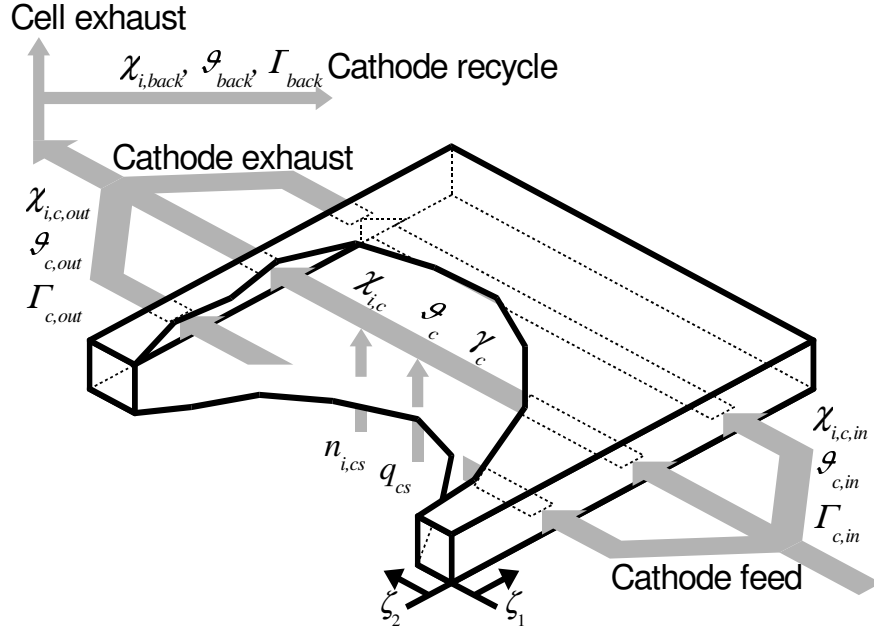


Figure 2.6: Cathode channel with states, fluxes and boundary conditions.

where

$$n_{i,cs}^+ = \begin{cases} n_{i,cs} & \text{if } n_{i,cs} > 0 \\ 0 & \text{if } n_{i,cs} \leq 0 \end{cases} \quad (2.50)$$

$$n_{i,cs}^- = \begin{cases} 0 & \text{if } n_{i,cs} > 0 \\ n_{i,cs} & \text{if } n_{i,cs} \leq 0 \end{cases}$$

$$c_{p,i}(\vartheta) \quad \text{cf. section 2.1.3.9 "Thermodynamics"}$$

$$c_{p,c} = \sum_i \chi_{i,c} c_{p,i}(\vartheta_c) \quad (2.51)$$

$$\bar{v}_j = \sum_i \nu_{ij} \quad (2.52)$$

$$q_{cs} = St_{cs} \cdot (\vartheta_s - \vartheta_c) \quad (2.53)$$

$$n_{i,cs} \quad \text{cf. section 2.1.3.5 "Electrode pores"}$$

The boundary conditions are given by the outlet conditions of the reversal chamber:

$$\chi_{i,c}(\zeta_1, \zeta_2=0, \tau) = \chi_{i,c,in}(\tau) = \chi_{i,m}(\tau) \quad (2.54)$$

$$\vartheta_c(\zeta_1, \zeta_2=0, \tau) = \vartheta_{c,in}(\tau) = \vartheta_m(\tau) \quad (2.55)$$

$$\gamma_c(\zeta_1, \zeta_2=0, \tau) = \gamma_{c,in}(\tau) = \Gamma_m(\tau) \quad (2.56)$$

Initial conditions are

$$\chi_{i,c}(\zeta_1, \zeta_2, \tau=0) = \chi_{i,c,0}(\zeta_1, \zeta_2) \quad (2.57)$$

$$\vartheta_c(\zeta_1, \zeta_2, \tau=0) = \vartheta_{c,0}(\zeta_1, \zeta_2) \quad (2.58)$$

The average exhaust values are

$$\Gamma_{c,out} = \int_0^1 \gamma_c(\zeta_1, \zeta_2=1) d\zeta_1 \quad (2.59)$$

$$\Gamma_{c,out} X_{i,c,out} = \int_0^1 \gamma_c(\zeta_1, \zeta_2=1) \cdot X_{i,c}(\zeta_1, \zeta_2=1) d\zeta_1 \quad (2.60)$$

$$\begin{aligned} \Gamma_{c,out} \sum_i X_{i,c,out} &\cdot \int_1^{\vartheta_{c,out}} c_{p,i}(\vartheta) d\vartheta \\ &= \int_0^1 \gamma_c(\zeta_1, \zeta_2=1) \cdot \left(\sum_i X_{i,c}(\zeta_1, \zeta_2=1) \int_1^{\vartheta_c(\zeta_2=1)} c_{p,i}(\vartheta) d\vartheta \right) d\zeta_1 \end{aligned} \quad (2.61)$$

A part of this cathode exhaust gas is recycled to the catalytic burner while the rest of it leaves the "HotModule" towards the media supply system which is not part of the modelling here. The compositions and temperatures of both streams are equal to the cathode exhaust conditions and the amounts of each stream are calculated according to the following equations:

$$X_{i,c,out} = X_{i,exhaust} = X_{i,back} \quad (2.62)$$

$$\vartheta_{c,out} = \vartheta_{exhaust} = \vartheta_{back} \quad (2.63)$$

$$\Gamma_{back} = R_{back} \cdot \Gamma_{c,out} \quad (2.64)$$

$$\Gamma_{exhaust} = (1 - R_{back}) \cdot \Gamma_{c,out} \quad (2.65)$$

2.1.3.5 Electrode pores

In many fuel cells the transport resistances between the gas phase and the electrochemical reaction zone inside the electrode pores are a rate limiting factor. This mass transport includes several steps, including gas film and pore diffusion, phase transition into the electrolyte melt and diffusion in the liquid electrolyte phase [22]. In addition, electrochemical reactions and mass transport happen in the same electrode region, which makes this a highly coupled system of mass and charge transport, reaction and electric field. In our model, these phenomena cannot be modelled in detail, and so a simplified model is applied according to the following assumptions:

- Instead of a spatially distributed concentration profile along the pore depth, an integral balance is used to calculate a representative partial pressure for each component inside the pore.
- Electrode pores have a certain volume which is not always negligible, especially not for dynamic effects in cells with low channel height. Thus, a certain pore volume is considered.
- The mass flux density between gas phase and solid phase, $n_{i,as}$ and $n_{i,cs}$, is described by a linear approach. The overall mass transport coefficients, $D_{i,as}$ and $D_{i,cs}$, include all transport effects that might occur between gas phase and reaction zone.
- Mass transport through the porous electrode along ζ_1 and ζ_2 is negligible.
- Contrary to all other compartments pressure is not constant inside the pores. This assumption is necessary to enable nonzero total flux densities.

- Ideal gas law is applied.
- The gas inside the electrode pores has the same temperature as the solid surrounding it. Thus no enthalpy balance is required here.
- The solid temperature changes very much slower than the partial pressures in the pores. Thus effects due to temperature dependent gas density changes are neglected.

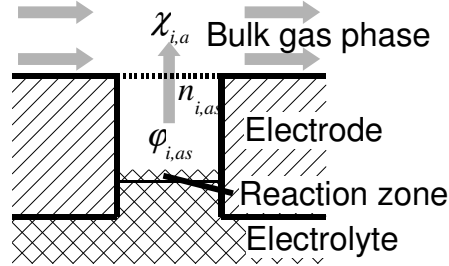


Figure 2.7: Anode pore with component partial pressures and mass exchange flux density between bulk gas phase and gas phase in pore.

According to the assumptions we come up with the following set of partial mass balance equations, describing the partial pressures, φ_i , of each component in the anode and cathode pores:

$$\frac{V_{ac}}{\vartheta_s} \frac{\partial \varphi_{i,ac}}{\partial \tau} = \sum_{j=ox} \nu_{ij} Da_j r_j - n_{i,as} \quad (2.66)$$

$$\frac{V_{cc}}{\vartheta_s} \frac{\partial \varphi_{i,cc}}{\partial \tau} = \sum_{j=red} \nu_{ij} Da_j r_j - n_{i,cs} \quad (2.67)$$

The molar flux density of each component is calculated by a mass transport coefficient and the difference in partial pressures in the electrode pore and the gas phase:

$$n_{i,as} = D_{i,as} (\varphi_{i,ac} - \chi_{i,a}) \quad (2.68)$$

$$n_{i,cs} = D_{i,cs} (\varphi_{i,cc} - \chi_{i,c}) \quad (2.69)$$

The electrochemical reaction rates are described in detail in a later chapter.

$$r_{j=ox} \quad \text{cf. section 2.1.3.8 "Reaction kinetics"}$$

$$r_{j=red} \quad \text{cf. section 2.1.3.8 "Reaction kinetics"}$$

These equations are ODEs of first order with respect to time and require initial conditions:

$$\varphi_{i,ac}(\zeta_1, \zeta_2, \tau=0) = \varphi_{i,ac,0}(\zeta_1, \zeta_2) \quad (2.70)$$

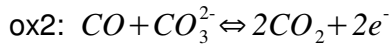
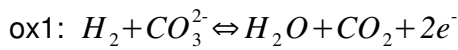
$$\varphi_{i,cc}(\zeta_1, \zeta_2, \tau=0) = \varphi_{i,cc,0}(\zeta_1, \zeta_2) \quad (2.71)$$

The equations 2.66 and 2.67 balance the effects of chemical reaction at the gas / electrolyte interface inside the pore and mass transport between pore and bulk phase. The mass transport kinetics correspond to Fick's law (equations 2.68 and 2.69). They can be substituted by any other expression like the Maxwell-Stephan equations or the dusty gas model. The use of these equations makes sure that no electrochemical reaction rate can be sustained if it consumes reactants faster than they can be transported into the pores.

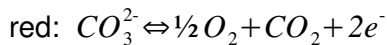
2.1.3.6 Solid phase

In the solid phase the temperature distribution in all solid parts of the fuel cell is modelled. Figure 2.8 shows the states and fluxes of this phase. As indicated, heat exchange between solid and gas phases as well as heat conduction inside the cell plane are considered. The enthalpy balance is set up under the following assumptions:

- Gas from both gas phases is brought to solid temperature at entering the electrode, influencing the solid temperature.
- Heat capacity of the gas inside the electrode pores is negligible compared to the heat capacity of the rest of the solid compartments.
- Two electrochemical reactions are considered on the anode electrode. They are the oxidation of hydrogen (indexed "ox1") and the oxidation of carbon monoxide (indexed "ox2"):



- On the cathode electrode, only the electrochemical reduction of oxygen (indexed "red") occurs:



- The electrochemical reactions induce heat in the solid phase.
- The ion transport through the electrolyte induces heat in the solid phase.
- Heat losses at the outer boundary of the solid phase are negligible.

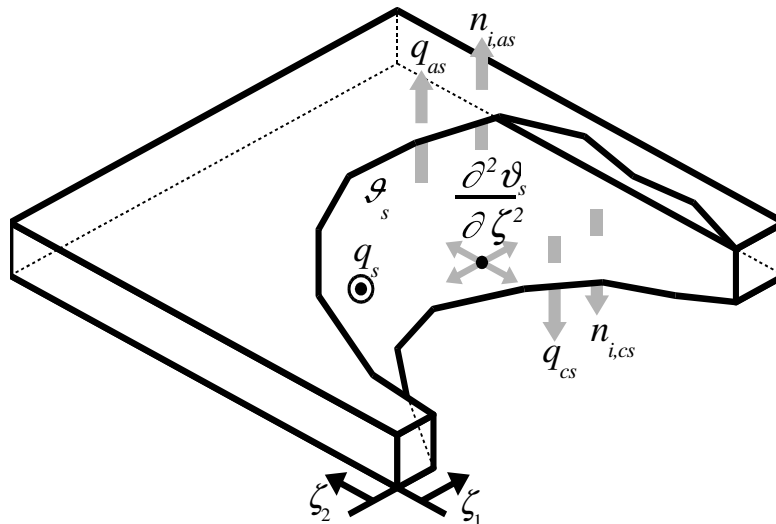


Figure 2.8: Solid phase states, mass and heat exchange flows with gas phases, heat conduction and heat source.

With these assumptions the enthalpy balance in temperature form for the solid phase describes the solid temperature, ϑ_s :

$$c_{p,s} \frac{\partial \vartheta_s}{\partial \tau} = \frac{l_2}{Pe_s} \frac{\partial^2 \vartheta_s}{\partial \zeta_1^2} + \frac{1}{Pe_s l_2} \frac{\partial^2 \vartheta_s}{\partial \zeta_2^2} + \sum_i (-n_{i,as}^-) \cdot \int_{\vartheta_s}^{\vartheta_a} c_{p,i}(\Psi) d\Psi + \sum_i (-n_{i,cs}^-) \cdot \int_{\vartheta_s}^{\vartheta_c} c_{p,i}(\Psi) d\Psi - q_{as} - q_{cs} + q_s \quad (2.72)$$

Here, the heat source inside the solid phase reads:

$$q_s = \sum_{j=ox} \left(-\Delta_R h_j^0(\vartheta_s) + n_j (\phi_a^S - \phi_a^L) \right) Da_j r_j + \sum_{j=red} \left(-\Delta_R h_j^0(\vartheta_s) + n_j (\phi_c^S - \phi_c^L) \right) Da_j r_j + (\phi_a^L - \phi_c^L) \cdot i_e \cdot \frac{1}{F} \quad (2.73)$$

The heat of electrochemical reactions is temperature dependent:

$$\Delta_R h_j^0(\vartheta) \quad \text{cf. section 2.1.3.9 "Thermodynamics"}$$

The electric potentials, the ionic current density and the electrochemical reaction rates are described in later sections:

$$\phi \quad \text{cf. section 2.1.3.7 "Potential field"}$$

$$i_e \quad \text{cf. section 2.1.3.7 "Potential field"}$$

$$r_j \quad \text{cf. section 2.1.3.8 "Reaction kinetics"}$$

Concerning temperature change, only the mass exchange flux densities of the components entering the solid are of interest here:

$$n_{i,as}^- = \begin{cases} 0 & \text{if } n_{i,as} > 0 \\ n_{i,as} & \text{if } n_{i,as} \leq 0 \end{cases} \quad (2.74)$$

$$n_{i,cs}^- = \begin{cases} 0 & \text{if } n_{i,cs} > 0 \\ n_{i,cs} & \text{if } n_{i,cs} \leq 0 \end{cases} \quad (2.75)$$

$$n_{i,as}, n_{i,cs} \quad \text{cf. section 2.1.3.5 "Electrode pores"}$$

The heat capacities of the gas components are

$$c_{p,i}(\vartheta) \quad \text{cf. section 2.1.3.9 "Thermodynamics"}$$

Heat exchange densities between solid and gas phases are proportional to a heat transfer coefficient, the Stanton number, and the corresponding temperature difference:

$$q_{as} = St_{as} \cdot (\vartheta_s - \vartheta_a) \quad (2.76)$$

$$q_{cs} = St_{cs} \cdot (\vartheta_s - \vartheta_c) \quad (2.77)$$

The temperature equation for the solid phase (Equation 2.72) is a parabolic PDE of first order with respect to time and second order with respect to both spatial coordinates. Thus, a

new type of PDE is introduced into the equation system, i.e. a parabolic PDE. It requires boundary conditions given by the insulation assumption and an initial condition:

$$\left. \frac{\partial \vartheta_s}{\partial \zeta} \right|_{\delta \zeta} = 0 \quad (2.78)$$

$$\vartheta_s(\zeta_1, \zeta_2, \tau=0) = \vartheta_{s,0}(\zeta_1, \zeta_2) \quad (2.79)$$

The first two terms on the right hand side of the enthalpy balance describe the heat conduction along both coordinates. The next two terms consider the temperature effect caused by components flowing into the porous electrodes and being heated up or cooled down to solid temperature. The fifth and sixth term stand for the convective heat exchange between both gas phases and the solid phase. The last term contains all heat induced into the solid by reactions and ion conduction and is given in detail in Equation 2.73. There the reaction heat of all electrochemical reactions is calculated as the standard reaction enthalpy at reaction temperature diminished by the electric energy generated by the reaction. The losses by ion conduction are the product of the ionic current density and the voltage drop across the electrolyte. The solid phase enthalpy balance together with the enthalpy balances of both gas phases, the combustion chamber and the reversal chamber are consistent, that means the overall energy conservation law is fulfilled.

2.1.3.7 Electric potential field

The modelling of the electric potential field is essential to the complete model. Some authors in the literature only vaguely describe their assumptions in this topic, and the approach chosen here has not occurred in the literature as yet. Several sets of equations can be used here, they differ only in with respect to steady state assumptions of several variables. Appendix A.4 gives a detailed derivation of this model together with its different versions. The equations used in the reference model are set up according to the following assumptions (Figure 2.9):

- The electrodes combined with the current collectors are perfect electric conductors. This is equivalent to the assumption of spatially constant electric potentials at each electrode. The electric potential at the anode electrode is arbitrarily set to zero.
- The charged double layers at both electrodes are modelled as flat planes.
- Due to the extremely thin electrolyte layer, carbonate ions are assumed to be transported through the electrolyte only in a direction orthogonal to the cell plane. No ion flux is possible along the ζ_1 and ζ_2 coordinates.
- The charge balances at the double layers are considered transient.

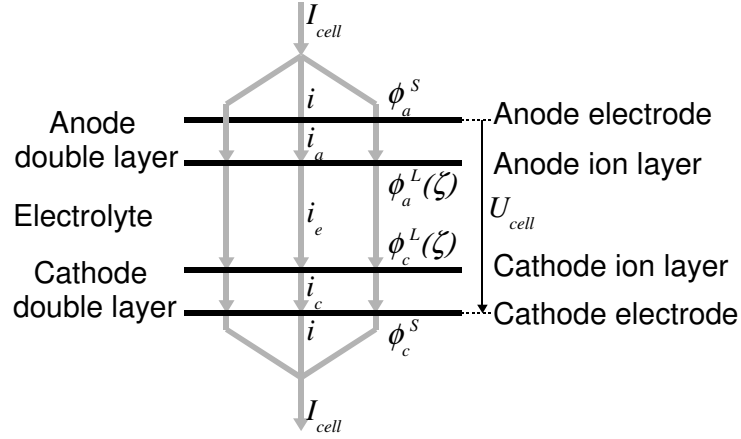


Figure 2.9: States and charge fluxes of the electric potential field model.

The electric potential at the anode electrode is arbitrarily set to zero:

$$\phi_a^S = 0 \quad (2.80)$$

The spatially distributed potentials at in the electrode near the anode and cathode double layer change depending on the current density from the electrode, i , and the current density produced by the electrochemical reaction, i_a and i_c , respectively:

$$\frac{\partial \phi_a^L}{\partial t} = -\frac{1}{c_a} \cdot (i - i_a) \quad (2.81)$$

$$\frac{\partial \phi_c^L}{\partial t} = -\frac{1}{c_a} \cdot (i - i_a) - \frac{1}{c_e} \cdot (i - i_e) \quad (2.82)$$

The cathode electrode potential depends on the differences of the overall currents produced by the electrochemical reactions respectively the overall current through the electrolyte from the given total cell current:

$$\frac{d\phi_c^S}{dt} = \frac{I_a - I_{cell}}{c_a} + \frac{I_e - I_{cell}}{c_e} + \frac{I_c - I_{cell}}{c_c} \quad (2.83)$$

where the total currents are calculated from

$$I_a = \int_A i_a d\zeta \quad ; \quad I_e = \int_A i_e d\zeta \quad ; \quad I_c = \int_A i_c d\zeta \quad (2.84)$$

The total cell current is distributed across the electrodes as follows:

$$i = \left(\frac{1}{c_a} + \frac{1}{c_e} + \frac{1}{c_c} \right)^{-1} \cdot \left(\frac{i_a}{c_a} + \frac{i_e}{c_e} + \frac{i_c}{c_c} - \frac{I_a}{c_a} - \frac{I_e}{c_e} - \frac{I_c}{c_c} \right) + I_{cell} \quad (2.85)$$

The density of current production by the reactions are calculated from a dimensionless Faraday law:

$$i_a(\phi_a^L) = \sum_{j=ox} n_j F D a_j r_j(\phi_a^L) \quad (2.86)$$

$$i_c(\phi_c^L, \phi_c^S) = - \sum_{j=red} n_j F D a_j r_j(\phi_c^L, \phi_c^S) \quad (2.87)$$

The ionic current through the electrolyte is assumed to be linearly depending on the corresponding potential difference, the factor, κ_e , is the dimensionless ion conductivity of the electrolyte layer:

$$i_e(\phi_a^L, \phi_c^L) = \kappa_e \cdot (\phi_a^L - \phi_c^L) \quad (2.88)$$

The cell voltage is defined as the difference between the anode and the cathode electric potential and is usually positive:

$$U_{cell} = \phi_c^S - \phi_a^S \quad (2.89)$$

Only initial conditions for several electric potentials are required:

$$\phi_a^L(\zeta_1, \zeta_2, \tau=0) = \phi_{a,0}^L(\zeta_1, \zeta_2) \quad (2.90)$$

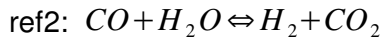
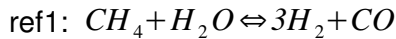
$$\phi_c^L(\zeta_1, \zeta_2, \tau=0) = \phi_{c,0}^L(\zeta_1, \zeta_2) \quad (2.91)$$

$$\phi_c^S(\tau=0) = \phi_{c,0}^S \quad (2.92)$$

For the numerical solution of the model the potential field equations prove to be a critical point. The set of ordinary differential and algebraic equations (DAE) used here has a differential index of 1, so it can be solved by most numerical integrators. Some variants of the potential field model, expressed in slightly different ways, possess a differential index of 2.

2.1.3.8 Reaction kinetics

In this model two different kinds of reactions occur: the chemical reactions of the methane reforming process in the anode channel and the electrochemical reactions inside the electrode pores. The first are modelled according to a power law and Arrhenius law. Two reactions are implemented in the model. These are the methane steam reforming reaction (indexed "ref1") and the water-gas shift reaction (indexed "ref2"):



The kinetics of these reactions are described as follows:

$$r_{ref1} = \exp\left(Arr_{ref1} \cdot \left(\frac{1}{\vartheta_{ref1}^0} - \frac{1}{\vartheta_a} \right) \right) \cdot \left(X_{CH_4,a} X_{H_2O,a} - \frac{1}{K_{ref1}(\vartheta_a)} X_{CO,a} X_{H_2,a}^3 \right) \quad (2.93)$$

$$r_{ref2} = \exp\left(Arr_{ref2} \cdot \left(\frac{1}{\vartheta_{ref2}^0} - \frac{1}{\vartheta_a} \right) \right) \cdot \left(X_{CO,a} X_{H_2O,a} - \frac{1}{K_{ref2}(\vartheta_a)} X_{CO_2,a} X_{H_2,a} \right) \quad (2.94)$$

where the equilibrium constant is calculated according to

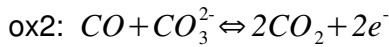
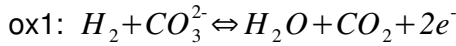
$$K_{j=ref}(\vartheta_a) = \exp\left(-\frac{\Delta_R g_j^0(\vartheta_a)}{\vartheta_a} \right) \quad (2.95)$$

with the Gibbs enthalpy of reaction

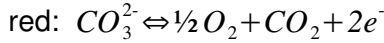
$$\Delta_R g_j^0(\vartheta_a) \quad \text{cf. section 2.1.3.9 "Thermodynamics"}$$

The first exponential term describes the temperature dependence of the reaction in the form of an Arrhenius law. The Arrhenius number is the dimensionless activation energy of the respective reaction. The second term considers the concentration dependence of the reaction rate. Any number of further gas phase reactions or different reaction kinetics can be inserted into the model. A short discussion of reaction kinetics from literature can be found in section 2.2.2.

The second type of reactions are the electrochemical reactions. In this model the anode oxidation reactions of hydrogen (indexed "ox1") and that of carbon monoxide (indexed "ox2") are considered:



At the cathode only the reduction of oxygen (indexed "red") is considered to be important. In the MCFC it usually runs in backward direction according to the following reaction scheme:



The reaction rate for the electrochemical reactions are set up under the following assumptions:

- Reversible Butler-Volmer kinetics [23] in combination with an Arrhenius law are applied.
- As the reaction takes place inside the electrode pores, the partial pressures in the pores are relevant for the reaction kinetics.
- Mass transport limitations are already considered in the pore model, so no additional limitations are needed in the reaction kinetics.
- Carbonate ion concentration in the electrolyte is assumed to be constant.

Thus, the oxidation rates are described by

$$r_{ox1} = \exp\left(Arr_{ox1} \cdot \left(\frac{1}{\vartheta_{ox1}^0} - \frac{1}{\vartheta_s} \right) \right) \cdot \left\{ \begin{aligned} & \varphi_{H_2,ac} \cdot \exp\left(\alpha_{ox1,+} \cdot n_{ox1} \frac{(\phi_a^S - \phi_a^L) - \Delta\phi_{ox1,0}(\vartheta_s)}{\vartheta_s} \right) \\ & - \varphi_{H_2O,ac} \varphi_{CO_2,ac} \cdot \exp\left(-(1 - \alpha_{ox1,+}) \cdot n_{ox1} \frac{(\phi_a^S - \phi_a^L) - \Delta\phi_{ox1,0}(\vartheta_s)}{\vartheta_s} \right) \end{aligned} \right\} \quad (2.96)$$

$$r_{ox2} = \exp\left(Arr_{ox2} \cdot \left(\frac{1}{\vartheta_{ox2}^0} - \frac{1}{\vartheta_s} \right) \right) \cdot \left\{ \begin{aligned} & \varphi_{CO,ac} \cdot \exp\left(\alpha_{ox2,+} \cdot n_{ox2} \frac{(\phi_a^S - \phi_a^L) - \Delta\phi_{ox2,0}(\vartheta_s)}{\vartheta_s} \right) \\ & - (\varphi_{CO_2,ac})^2 \cdot \exp\left(-(1 - \alpha_{ox2,+}) \cdot n_{ox2} \frac{(\phi_a^S - \phi_a^L) - \Delta\phi_{ox2,0}(\vartheta_s)}{\vartheta_s} \right) \end{aligned} \right\} \quad (2.97)$$

where the standard open circuit voltage is only depending on temperature

$$\Delta \phi_{j,0}(\vartheta_s) = \frac{\Delta_R g_j^0(\vartheta_s)}{n_j} \quad (2.98)$$

$$\Delta_R g_j^0(\vartheta_s) \quad \text{cf. section 2.1.3.9 "Thermodynamics"}$$

Commonly the cathode reaction is found to be the limiting reaction in MCFC (for example [24]) and therefore deserves special attention. Various scientific groups had been working for four decades on the oxygen reduction mechanism in carbonate melts [25]. There are five reaction mechanisms primarily under discussion, of which two seem to correlate well with experimental results [26, 27]. Bednarz [28] has conducted kinetic experiments with cathode electrodes from the HotModule and proposes still another mechanism which is very similar to the common superoxide reaction mechanism. Thus the reaction rate expression derived from the superoxide mechanism is applied in the present work. In the appendix the reader may find a complete list of all five reaction mechanisms an article by Prins-Jansen et al. [26] together with a derivation of the overall reaction rate expressions. The general form for this expression is given in the following Equation 2.99 together with the corresponding coefficients for each reaction mechanism in Table 2.1.

The reader may notice that the kinetics used in this work are not quite identical to those in the article by Prins-Jansen. The difference is that Prins-Jansen uses a temperature and concentration dependent equilibrium voltage to define the overpotential. In our case only a temperature dependent equilibrium potential is applied (Equation 2.98). When considering this fact it turns out that both formulations are equivalent.

$$r_{\text{red}} = \exp\left(Arr_{\text{red}} \cdot \left(\frac{1}{\vartheta_{\text{red}}^0} - \frac{1}{\vartheta_s} \right) \right) \cdot \left\{ \begin{aligned} & (\varphi_{CO_2,cc})^{a1} \cdot \exp\left(\alpha_{\text{red},+} \frac{(\phi_c^S - \phi_c^L) - \Delta \phi_{\text{red},0}(\vartheta_s)}{\vartheta_s} \right) \\ & - (\varphi_{O_2,cc})^{a2} (\varphi_{CO_2,cc})^{a3} \cdot \exp\left(-\alpha_{\text{red},-} \frac{(\phi_c^S - \phi_c^L) - \Delta \phi_{\text{red},0}(\vartheta_s)}{\vartheta_s} \right) \end{aligned} \right\} \quad (2.99)$$

Table 2.1: Coefficients for the reaction rate for various mechanisms as described by Prins-Jansen et al. [26].

Mechanism	<i>a1</i>	<i>a2</i>	<i>a3</i>	$\alpha_{\text{red},+}$	$\alpha_{\text{red},-}$
Peroxide	-2	0.50	-1.0	1.5	0.5
Superoxide	-2	0.75	-0.5	2.5	0.5
Peroxycarbonate	-1	0.50	0.0	1.5	0.5
Oxygen I	-2	1.00	0.0	3.5	0.5
Oxygen II	-1	0.50	0.0	1.5	0.5

The expressions for the electrochemical reaction rates and the electric cell potentials used in this model deviate from those expressions often found in the literature. The concept often used there is that of an open loop voltage at inlet conditions being diminished by a series of overpotentials describing the voltage losses due to anode and cathode reactions, ion conduction or concentration deviations. Besides the fact that this is not possible if the anode inlet contains no hydrogen, this concept is not required. Instead of this, explicit potential differences at the anode and cathode double layers are used and related to the equilibrium voltage under hypothetical standard conditions where all dimensionless partial pressures $\varphi_i=1$. Nevertheless it is still possible to recalculate for example the concentration overpotential or activation overpotential should their contribution to the overall cell voltage be of interest.

2.1.3.9 Thermodynamics

Thermodynamic relations are used to calculate temperature dependent heat capacities, reaction enthalpies and free (Gibbs) enthalpies of reactions. Also the definition of a carbonisation criterion, the electric cell power and the electric cell efficiency is given here.

Heat capacities

The heat capacity of any component i is calculated from a polynomial with four coefficients:

$$c_{p,i}(\vartheta) = A_{i,1} + A_{i,2} \cdot \vartheta + \frac{A_{i,3}}{\vartheta^2} + A_{i,4} \cdot \vartheta^2 \quad (2.100)$$

Enthalpies and Gibbs enthalpies of reactions

The enthalpy and entropy of any reaction j at any temperature is the sum of the enthalpy or entropy of formation weighted with the stoichiometric factor of the reaction under consideration:

$$\Delta_R h_j^0(\vartheta) = \sum_i \nu_{ij} h_{fi}(\vartheta) \quad (2.101)$$

$$\Delta_R s_j^0(\vartheta) = \sum_i \nu_{ij} s_{fi}(\vartheta) \quad (2.102)$$

The temperature dependencies of these properties is described as a formation value at standard temperature plus an integral term

$$h_{fi}(\vartheta) = h_{fi}(1) + \int_1^\vartheta c_{p,i}(\Psi) d\Psi \quad (2.103)$$

$$s_{fi}(\vartheta) = s_{fi}(1) + \int_1^\vartheta \frac{c_{p,i}(\Psi)}{\Psi} d\Psi \quad (2.104)$$

From Equations 2.103 and 2.104 follows the temperature dependence of the reaction enthalpy and entropy, respectively:

$$\begin{aligned} \Delta_R h_j^0(\vartheta) = & \Delta_R h_j^0(1) + \sum_i \nu_{ij} A_{i,1} \cdot (\vartheta - 1) + \frac{1}{2} \sum_i \nu_{ij} A_{i,2} \cdot (\vartheta^2 - 1) \\ & - \sum_i \nu_{ij} A_{i,3} \cdot \left(\frac{1}{\vartheta} - 1\right) + \frac{1}{3} \sum_i \nu_{ij} A_{i,4} \cdot (\vartheta^3 - 1) \end{aligned} \quad (2.105)$$

$$\begin{aligned} \Delta_R s_j^0(\vartheta) = & \Delta_R s_j^0(1) + \sum_i \nu_{ij} A_{i,1} \cdot \ln \vartheta + \sum_i \nu_{ij} A_{i,2} \cdot (\vartheta - 1) \\ & - \frac{1}{2} \sum_i \nu_{ij} A_{i,3} \cdot \left(\frac{1}{\vartheta^2} - 1\right) + \frac{1}{2} \sum_i \nu_{ij} A_{i,4} \cdot (\vartheta^2 - 1) \end{aligned} \quad (2.106)$$

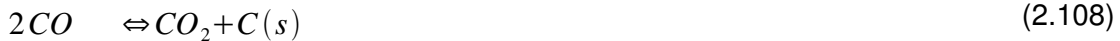
The free enthalpy of reaction (Gibbs enthalpy) is then given by

$$\Delta_R g_j^0(\vartheta) = \Delta_R h_j^0(\vartheta) - \vartheta \cdot \Delta_R s_j^0(\vartheta) \quad (2.107)$$

Thermodynamic carbonisation criterion

For high temperature fuel cells, carbonisation is a serious issue especially within the anode channel. Solid carbon may be formed and deposited on the anode electrode catalyst, blocking its active sites and thereby quickly degenerating the catalyst.

Several carbonisation reactions are known to occur in the gas mixtures present here:



All of these reactions are two-phase reversible reactions. Their Gibbs enthalpy of reaction is an indicator as to whether these reaction happen:

$$\Delta_R g_{carbon}(\vartheta_a, X_{i,a}) = \Delta_R g_{carbon}^0(\vartheta_a) + \vartheta_a \cdot \ln \prod_i X_{i,a}^{\nu_{i,carbon}} \quad (2.111)$$

If this Gibbs enthalpy is positive, the carbonisation reaction happens in the backward direction, or, if no carbon is available as an educt, it does not happen at all. If the Gibbs enthalpy of one of the three reactions is negative it forms carbon, but the other reactions consume it again. Only if the Gibbs enthalpies of all three carbonisation reactions are negative at a certain coordinate under anode conditions, carbonisation occurs. Note that this carbonisation criterion only plays a role in the optimisations in Chapter 5.

Electric cell power and electric efficiency

The electric cell power output is defined as the product of the cell voltage and the total cell current divided by the dimensionless equivalent of the dimensionless Faradaic constant:

$$P_{cell} = \frac{U_{cell} \cdot I_{cell}}{F} \quad (2.112)$$

The constant, F , occurs here because two different values are used for the standard power: one standard electric power and a standard energy flux. This is explained in Chapter 2.2.1, where the standards are defined.

To calculate the total electric system efficiency, additional electric power losses are accounted for. Considerable losses are caused by the blowers driving the gases through the cell system, in the case of the HotModule they are mounted on top of the catalytic burner. The electric system efficiency then relates the produced electric power diminished by the power losses divided by the combustion enthalpy flux of the inlet stream:

$$\eta_{el,system} = \frac{P_{cell} - P_{losses}}{H_{a,in}} \quad (2.113)$$

with

$$H_{a,in} = \Gamma_{a,in} \cdot \sum_i \chi_{i,a,in} \cdot (-\Delta_c h_i^0(1)) \quad (2.114)$$

$$\Delta_c h_j^0(1) = \sum_i \nu_{i,Cj} \cdot h_{f,i}(1) \quad (2.115)$$

As the cathode flow is by far the largest mass flow in the system, the power consumption of the blowers is assumed to depend on the cathode inlet flow:

$$P_{losses} = P_{blower} = f_{blower} \cdot \Gamma_{m,out} \quad (2.116)$$

Further losses like those at the electric converters can be taken into account.

2.2 Model parameters

To solve the model equations given above, concrete values have to be assigned to the model parameters. For some of the parameters these values may be calculated precisely from thermodynamic data. For others, knowledge of the cell geometry and material data is required. Nevertheless there are a few parameters whose values can only be estimated using values from literature or first experimental results from the HotModule. Regardless how the parameter values are acquired, their validity has to be proven by experiments, which is not part of this work.

In this section after the definition of the dimensional standard parameters the values of the more interesting dimensionless model parameters are introduced. These are kinetic parameters and accumulation capacities. Simple parameters with obvious values like the stoichiometric coefficients and thermodynamic properties are omitted here. A comprehensive list of all parameters together with their values can be found in the Appendix A.6.

2.2.1 Definition of standard values

The used standard temperature and standard pressure are equal to the thermodynamic standard conditions, at which the standard properties of all substances are defined. The fuel cell is assumed to be operated at this pressure.

$$T^\theta = 298.15 \text{ K} \quad (2.117)$$

$$p^\theta = 10^5 \text{ Pa} \quad (2.118)$$

The gas constant is used as the standard heat capacity:

$$c_p^\theta = R = 8.314 \frac{J}{mol \cdot K} \quad (2.119)$$

The molar concentration of an ideal gas under standard temperature and pressure is used as standard concentration:

$$c_i^\theta = \frac{p^\theta}{RT^\theta} = \frac{10^5}{8.314 \cdot 298.15} \frac{N \cdot mol \cdot K}{m^2 \cdot J \cdot K} = 40.34 \frac{mol}{m^3} \quad (2.120)$$

The standard electric potential, ϕ^θ , is defined with the standard temperature:

$$\frac{1}{\phi^\theta} = \frac{\tilde{F}}{RT^\theta} = \frac{96485}{8.314 \cdot 298.15} \frac{C \cdot mol \cdot K}{mol \cdot J \cdot K} = 38.9 \frac{1}{V} \quad (2.121)$$

The definition of the standard molar flow is slightly more complex as it requires the definition of standard cell operating conditions. These are derived in the following. At standard conditions, let the cell have an electric power and an electric efficiency according to

$$P_{el,stack}^\theta = 250 \text{ kW} \quad (2.122)$$

$$\eta_{el}^\theta = 0.5 \quad (2.123)$$

Furthermore, let the standard steam to carbon ratio of the feed gas be

$$S/C^\theta = 2.5 \quad (2.124)$$

and subsequently the standard mole fraction of methane in the feed gas be

$$x_{CH_4,feed}^\theta = \frac{1}{1 + S/C^\theta} = \frac{1}{3.5} \quad (2.125)$$

Together with the combustion enthalpy of methane at standard temperature

$$\Delta_c \tilde{h}_{CH_4}^\theta(T^\theta) = -802361 \frac{J}{mol} \quad (2.126)$$

this yields the amount of feed gas required for the whole cell stack

$$G_{feed,stack}^\theta = \frac{P_{el,stack}^\theta}{\eta_{el}^\theta \cdot x_{CH_4,feed}^\theta \cdot (-\Delta_c \tilde{h}_{CH_4}^\theta(T^\theta))} = 2.181 \frac{mol}{s} \quad (2.127)$$

With a total of $n_{cell} = 342$ cells in the stack this gives the standard molar flow

$$G^\theta = \frac{G_{feed,stack}^\theta}{n_{cell}} = 6.377 \frac{mmol}{s} \quad (2.128)$$

With this the standard total cell current is

$$I^\theta = G^\theta \cdot x_{CH_4,feed}^\theta \cdot 8 \tilde{F} = 1406.4 \text{ A} \quad (2.129)$$

There are two different standard powers available. The standard electric power is defined as the product of standard cell voltage and standard cell current:

$$P_{el}^\theta = U^\theta \cdot I^\theta = \frac{RT^\theta}{\tilde{F}} \cdot G^\theta \cdot x_{CH_4,feed}^\theta \cdot 8 \tilde{F} = G^\theta \cdot RT^\theta \cdot x_{CH_4,feed}^\theta \cdot 8 \quad (2.130)$$

The thermal energy flux is defined as the product of molar flow and standard sensitive heat:

$$P_{th}^{\theta} = G^{\theta} \cdot RT^{\theta} \quad (2.131)$$

To convert from one standard power to another, as is the case in equation 2.112, a constant factor is used. This factor also appears in equation 2.86, where it occupies the same place as does the dimensional Faraday constant. It is therefore denoted F . It can also be interpreted as a stoichiometric factor, relating the possible electric current to the standard feed flow.

$$F = \frac{P_{th}^{\theta}}{P_{el}^{\theta}} = \frac{3.5}{8} \quad (2.132)$$

The standard time is defined as the residence time of a standard molar flow through a standard volume at standard density. The total anode channel volume is used as the standard volume:

$$t^{\theta} = \frac{V^{\theta} c_t^{\theta}}{G^{\theta}} = \frac{L_1 L_2 h_a \cdot c_t^{\theta}}{G^{\theta}} = \frac{1.2 \text{ m} \cdot 0.8 \text{ m} \cdot 2 \cdot 10^{-3} \text{ m} \cdot 40.34 \text{ mol m}^{-3}}{6.377 \cdot 10^{-3} \text{ mol m}^{-3}} = 12.15 \text{ s} \quad (2.133)$$

The above given values are the standard values used to calculate the model parameters. They are not essential for the model itself, but are used only for the parameter estimation and for any retransformation of the dimensionless results into dimensional values.

2.2.2 Parameter values

Two groups of parameters deserve special attention in a process model. The first ones are kinetic parameters for chemical reactions and for the transport of heat and mass. As a second group, capacities for mass, heat and charge accumulation are of interest for dynamic models.

The parameters describing the reaction kinetics are of outstanding importance in a chemical system. In the dimensionless model applied here, these are covered by the Damköhler numbers representing the reaction rate constant or exchange current density and the Arrhenius numbers describing the reactions' activation energy. First the Arrhenius numbers of the reactions considered are evaluated, afterwards the corresponding Damköhler numbers are discussed.

Although numerous publications can be found treating the electrochemical reaction kinetics in MCFC, only few authors have performed temperature dependent experiments. Yuh and Selman [25] present empirical temperature dependent expressions for the anodic and cathodic electric resistances, Z_{anode} and $Z_{cathode}$, in MCFC:

$$Z_{anode} \sim \exp\left(\frac{6435 \text{ K}}{T}\right) \quad (2.134)$$

$$Z_{cathode} \sim \exp\left(\frac{9298 \text{ K}}{T}\right) \quad (2.135)$$

From these one can approximate activation energies of the electrochemical reactions at anode and cathode, respectively:

$$i \sim \frac{1}{Z_{anode}} \sim \exp\left(-\frac{6435 K}{T}\right) \sim \exp\left(-\frac{E_A}{RT^\theta}\right) \quad (2.136)$$

$$\Rightarrow E_{A,ox} = 6435 K \cdot R = 53.5 \frac{kJ}{mol}$$

and

$$E_{A,red} = 77.3 \frac{kJ}{mol} \quad (2.137)$$

Due to the lack of more detailed information the activation energies of both electrochemical reactions at the anode are assumed to have the same value. In dimensionless form this yields:

$$Arr_{ox1} = Arr_{ox2} = 21.6 \quad (2.138)$$

$$Arr_{red} = 31.2 \quad (2.139)$$

The Damköhler numbers for the electrochemical reactions are the dimensionless exchange current densities. Values for these are given in various articles. Those experiments were conducted using electrodes and electrolytes of diverse materials, porosities and active inner surfaces under varying gas compositions and electrolyte hold up in the electrode pores. The results give a rough idea of the order of magnitude of the exchange current density but to receive reliable values for the HotModule system, kinetic experiments with an original cell would be necessary. As these data are not available, the Damköhler numbers have to be adjusted to experimental data from the HotModule. To minimise the influence of mass transport resistances, a load case with medium electric current is chosen and the Damköhler numbers are fitted so that the simulated cell voltage is approximately equal to the measured value. Here the fact is incorporated that the anodic exchange current density is approximately ten times higher than the cathodic one (for example Christensen and Livbjerg [24]). As there is no data available on the carbon monoxide oxidation, its Damköhler number is assumed to be equal to that of the hydrogen oxidation. Nevertheless, due to the usually low concentration of carbon monoxide its oxidation rate is low compared to that of the hydrogen oxidation. According to these considerations, the Damköhler numbers of the electrochemical reactions are set to the following values:

$$Da_{ox1} = Da_{ox2} = 5 \quad (2.140)$$

$$Da_{red} = 0.3 \quad (2.141)$$

The methane reforming reactions are described with various Langmuir-Hinshelwood type kinetics in the scientific literature. Hou and Hughes [29] as well as Xu and Froment [30] present a thorough investigation of methane steam reforming mechanism on commercial nickel catalysts and give a complete set of reaction kinetics with dependence on partial pressures and temperature. Although the kinetics used by both groups are similar in

structure, the experimental validation yields different parameters, the reason for this being different catalysts. Thus the parameters like activation energies, adsorption coefficients and reaction orders strongly depend on the specific catalyst used. Therefore they have to be considered unknown and must be determined experimentally. The HotModule is not suitable for such detailed kinetic experiments and therefore those kinetics can not be used here. That is why simple kinetics are being used with a smaller number of unknown parameters. However, the activation energies from the paper of Xu and Froment [30] may give a good estimation for the Arrhenius numbers in this model. They are

$$Arr_{ref1} = \frac{E_{a,ref1}}{RT^\theta} = \frac{209.2 \text{ kJ mol}^{-1}}{8.314 \text{ J mol}^{-1} \text{ K}^{-1} 298.15 \text{ K}} = 84.4 \quad (2.142)$$

$$Arr_{ref2} = \frac{E_{a,ref2}}{RT^\theta} = \frac{15.4 \text{ kJ mol}^{-1}}{8.314 \text{ J mol}^{-1} \text{ K}^{-1} 298.15 \text{ K}} = 6.21 \quad (2.143)$$

As is known from literature ([29] and others), the steam reforming reactions in MCFC are very fast. Especially the water-gas shift reaction ("ref2") is often assumed to be in chemical equilibrium ([8], [7]). The Damköhler numbers for these two reactions are adjusted according to this knowledge. Thus the Damköhler number of the first reaction is set a little lower than the Damköhler number of the second reaction:

$$Da_{ref1} = 25 \quad (2.144)$$

$$Da_{ref2} = 100 \quad (2.145)$$

At small or medium current densities the mass transport resistance in the electrode pores plays only a minor role. It becomes important as the current density approaches the limiting current density corresponding to the maximum possible mass transport rate. Because there is no data available about the limit current density for the HotModule electrodes, the mass transport coefficients can not be determined from literature values. But also here a rough adjustment to experimental data is possible. As already stated, the mass transport should have no or only little influence on the cell voltage at low to medium current densities. Assuming equal transport coefficients for all components their value should be chosen so that in the simulation only a small voltage loss occurs compared to a system with infinite mass transport coefficients. Thus the values of the mass transport coefficients between anode and cathode gas phases and their electrodes are set to

$$D_{i,as} = D_{i,cs} = 100 \quad (2.146)$$

Another mass transport coefficient is the ion conductivity in the electrolyte. Here an ohmic conductivity for carbonate ions in eutectic carbonate salt melt through the complete electrolyte layer from the cathode to the anode reaction zone is required. Wilemski [31] gives a temperature dependent ohmic resistance for the electrolyte. For typical MCFC temperatures the value of the dimensionless ion conductivity is at about 0.35. In the model a slightly better conductivity is assumed:

$$\kappa_e = 1.0 \quad (2.147)$$

The Stanton numbers describing the heat exchange coefficients between different phases are of primary interest with respect to heat management. Approximations for these are available for a variety of different channel shapes and a broad range of gas velocities. These relations describe the heat exchange coefficient at smooth or slightly rough surfaces without convective flux coming from or going into that surface. For fuel cells this is not the case as we have very porous electrode surfaces and mass exchange between electrodes and gas phases. Thus using these relations would come with additional numerical effort but with no certainty of a better approximation. Therefore, constant exchange coefficients are used. Their values are chosen so that the temperatures measured at the HotModule and the simulated temperatures are roughly equal. Due to the differences in typical gas velocities in the anode and cathode channel, the Stanton numbers have different values:

$$St_{as} = 80 \quad (2.148)$$

$$St_{cs} = 120 \quad (2.149)$$

For the Stanton number of the reversal chamber which lies at the outer vessel wall of the HotModule the following considerations give a rough estimate. It is assumed that the complete HotModule stack has heat losses of about 10 kW. This leads to a heat loss of approximately 29 W per cell corresponding to a dimensionless heat flux of $Q_m=2$. According to Equation 2.41 with a temperature difference of 650°C (dimensionless $\vartheta_m \approx 3$) minus the ambient temperature of 20°C ($\vartheta_u \approx 1$) this results in a Stanton number for the reversal chamber of

$$St_m = \frac{Q_m}{\vartheta_m - \vartheta_u} = \frac{2}{3-1} = 1 \quad (2.150)$$

The Peclet number is relevant for the heat conduction in the solid phase. It contains the heat conduction properties of all solid parts in the cell. These are not only the electrodes and the electrolyte but also the channel walls made of steel and the separator plates. Assuming an overall height of the heat conducting solid components of 1.1 mm per cell and a heat conductivity of 20 Wm⁻¹K⁻¹ (roughly half the value for steel) leads to a dimensionless heat conduction resistance of

$$Pe_s = \frac{G^\theta c_p^\theta}{\lambda_s h_s} = \frac{6.377 \cdot 10^{-3} \text{ mol s}^{-1} \cdot 8.314 \text{ J mol}^{-1} \text{ K}^{-1}}{20 \text{ W m}^{-1} \text{ K}^{-1} \cdot 1.1 \cdot 10^{-3} \text{ m}} \approx 2.5 \quad (2.151)$$

Besides the kinetic parameters the mass, charge and energy accumulation capacities of the system are of importance in a dynamic model. They determine the characteristic time constants of the system. Mass can be accumulated in the electrode pores. The capacity is described by the pore volume related to the standard volume which is the anode gas channel volume. Thus the dimensionless pore capacity can be interpreted as the ratio of the height of an abstract pore volume and the anode channel height. The electrode thickness is

assumed to be about 0.5 mm for both electrodes and the gas volume fraction is estimated to be 3/8 for the anode and 0.3 for the cathode electrode. Then with an anode channel height of 2 mm the pore capacities are

$$V_{ac} = \frac{0.5 \text{ mm} \cdot 0.375}{2 \text{ mm}} = 0.09 \quad (2.152)$$

$$V_{cc} = \frac{0.5 \text{ mm} \cdot 0.3}{2 \text{ mm}} = 0.075 \quad (2.153)$$

The heat capacity of the solid phase causes by far the largest time constant in the system. It therefore may be estimated only roughly. Using the assumption already mentioned for the solid height together with an approximate density and heat capacity of steel one comes up with

$$c_s = \frac{1.1 \cdot 10^{-3} \text{ m} \cdot 8 \cdot 10^6 \text{ g m}^{-3} \cdot 0.75 \text{ J g}^{-1} \text{ K}^{-1}}{2 \cdot 10^{-3} \text{ m} \cdot 40.34 \text{ mol m}^{-3} \cdot 8.314 \text{ J mol}^{-1} \text{ K}^{-1}} \approx 10000 \quad (2.154)$$

For the charge accumulation the double layer capacities at the anode and cathode reaction zones are of interest. Authors ([28], [32], [26]) give values for this parameter ranging from 1.4 .. 55 · 10⁻³ Fm⁻². In dimensionless terms this roughly corresponds to

$$c_a = c_c = 1 \cdot 10^{-8} \quad (2.155)$$

Thermodynamic properties of substances like heat capacity and enthalpy of formation are taken from the NIST Chemistry WebBook [33].

2.2.3 Time constants in MCFC

The different physical and chemical phenomena in an MCFC like convective mass and heat transport in the gaseous phase, temperature change of the solid phase and charge transport processes at the electrode double layers are governed by time constants with different orders of magnitude. These time constants are represented by the according capacities of mass, heat and charge.

The dimensionless parameters (see Chapter 2.2.2) indicate that there are three different categories of time constants present in this model. The double layer capacities, c_a and c_c , indicate that the charging of the double layers happens extremely fast, usually within milliseconds or even microseconds. The mole fractions and temperature within the gas phases change within a few seconds, corresponding to their residence time in the corresponding compartment. The dimensionless volumes, V_a , V_c and V_m , are the determining capacities here. The temperature change of the solid phase is by far the slowest process in the cell, which is indicated by the large solid phase heat capacity, $c_{p,s}$. It usually takes 2 to 4 hours for the HotModule to reach its new steady state stack temperature after a load change. The time constants of the system are illustrated in figure 2.10.

The fact that the time constants have distinctive order of magnitudes allows to easily derive new models. Depending on the time scale of interest for a specific question, quasi steady

state assumptions for fast processes lead to new model formulations. Also, the assumption of a spatially distributed, but steady state solid temperature for a short period of time can be useful to reduce models. Nevertheless, the models derived in the next two chapters follow a different approach. Physical and thermodynamical simplifications lead to reduced and more efficient models.

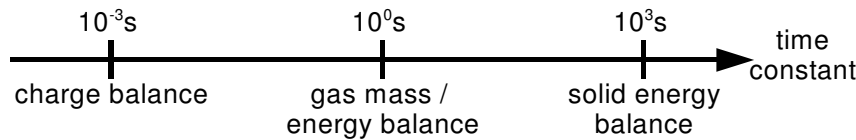


Figure 2.10: Characteristic time constants of different phenomena in MCFC.

2.3 Physically-chemically reduced model

In order to perform model based optimisations it is necessary to solve the equations system several hundred times with reasonable computational effort. This is not possible with the reference model, so a reduced model requiring considerably less numerical effort must be derived. This could be done by applying mathematical reduction methods to the reference model (Mangold et al. [34]), but within this work a different way is chosen. Simplifications based on physical and chemical assumptions are applied to the reference model. This procedure does not change the structure of the main model equations but reduces the complexity of the thermodynamical correlations. The aim is to decrease the numerical effort while losing only little of the model precision. In this section the assumptions and equations of the physically-chemically reduced model (or short: reduced model) are presented.

2.3.1 Assumptions

The simplifications made in the derivation of this model are mainly in the field of thermodynamics. It turns out that the calculation of temperature dependent heats of reaction and equilibrium constants as well as the temperature and concentration dependent heat capacities consume a lot of computation time. Although these correlations are rather simple in their structure, they often make model equations implicit and thereby harder to solve. This is especially easy to see in the enthalpy balance of the burner. On the other hand certain temperature dependencies may not be neglected. An example of this are the equilibrium constants of the reforming reactions which change considerably over the temperature range of the MCFC and may not be approximated by constant values.

Further simplifications can be made for the mass exchange flux densities between electrodes and gas channels. If quasi steady state of the mass balance in the electrode pores is assumed the differential equation turns into an algebraic expression. Furthermore, as the electrochemical reactions usually run in one direction only, the direction of the exchange flux is known for each component. The mass transport resistance can not be neglected, as it is dominant at high cell current.

The simplifications applied to the reference model to derive the reduced model are listed below.

- All chemical components have the same heat capacity which is independent of temperature. The value represents weighted average of the heat capacities of all components at typical MCFC operating temperatures. Consequently, the heat capacity of the mixture is constant and the integral of the heat capacity over temperature is simplified. These simplifications are not applied to the heat capacity of the solid phase.
- All reaction enthalpies are approximated by constant values.
- The equilibrium constants of the reforming reactions change considerably over the range of typical MCFC operating temperatures from 550°C – 650°C. They can be approximated by an expression similar to the thermodynamically correct one but with constant reaction enthalpies and reaction entropies (Table 2.2, Equations 36).
- The standard potential differences also show a temperature dependence that may not be neglected but which can be approximated using constant reaction enthalpies and entropies (Table 2.2, Equations 37).
- The electrode pore mass balances are assumed to be in steady state (Table 2.2, Equations 21). Nevertheless the mass transport resistance is still considered (Table 2.2, Equations 22).
- With the direct coupling of the electrochemical reactions and the mass exchange fluxes the direction of each components` exchange flux density is determined. Thus the case differentiation appearing in many model equations (Equations 2.22 and 2.50, for example) is eliminated. Only for very small total cell current can it happen that some electrochemical reaction locally runs in backwards direction. In this case this only causes very small mass transport densities, whose contribution to the enthalpy exchange between gas phases and solid is assumed to be negligible.

2.3.2 Model equations

The reduced model is the result of the above mentioned approximations and assumptions applied to the reference model. The model equations are given in uncommented form in Table 2.2 on the following pages. For a discussion of the equations we refer to Chapter 2.1.

Table 2.2: Equations of the physically-chemically reduced model

Anode		
Partial mass balance	$\frac{V_a}{\vartheta_a} \frac{\partial X_{i,a}}{\partial \tau} = -\gamma_a \frac{\partial X_{i,a}}{\partial \zeta_1} + \sum_{j=\text{ox}} (v_{ij} - X_{i,a} \nabla_j) Da_j r_j + \sum_{j=\text{ref}} (v_{ij} - X_{i,a} \nabla_j) Da_j r_j$	(1)
Enthalpy balance	$\frac{V_a}{\vartheta_a} \frac{\partial \vartheta_a}{\partial \tau} = -\gamma_a \frac{\partial \vartheta_a}{\partial \zeta_1} + \sum_{j=\text{ox}} \nabla_j^+ Da_j r_j (\vartheta_s - \vartheta_a) + \sum_{j=\text{ref}} \frac{(-\Delta_R h_j^0)}{c_p} Da_j r_j + \frac{q_{as}}{c_p}$	(2)
Total mass balance	$0 = -\frac{\partial \gamma_a \vartheta_a}{\partial \zeta_1} + \sum_{j=\text{ox}} \nabla_j^+ Da_j r_j (\vartheta_s - \vartheta_a) + \sum_{j=\text{ref}} \frac{(-\Delta_R h_j^0)}{c_p} Da_j r_j + \frac{q_{as}}{c_p} + \vartheta_a \sum_{j=\text{ref}} \nabla_j Da_j r_j$	(3)
Average outlet conditions	$\Gamma_{a,\text{out}} = \int_0^1 \gamma_a (\zeta_1=1, \zeta_2) d\zeta_2 \quad ; \quad X_{i,a,\text{out}} = \frac{1}{\Gamma_{a,\text{out}}} \int_0^1 \gamma_a (\zeta_1=1, \zeta_2) X_{i,a} (\zeta_1=1, \zeta_2) d\zeta_2 \quad ; \quad \vartheta_{a,\text{out}} = \frac{1}{\Gamma_{a,\text{out}}} \int_0^1 \gamma_a (\zeta_1=1, \zeta_2) \vartheta_a (\zeta_1=1, \zeta_2) d\zeta_2$	(4)
Stoichiometric coefficients	$\nabla_j^+ = \sum_i v_{ij} \quad \text{for all } i: v_{ij} > 0$	(5)
Heat exchange density	$q_{as} = St_{as} (\vartheta_s - \vartheta_a)$	(6)
Burner		
Total mass balance	$\Gamma_{b,\text{out}} = \Gamma_{a,\text{out}} \left(1 + \sum_j \nabla_{Cj} X_{j,\text{back}} \right) + \Gamma_{\text{back}} \left(1 + \sum_j \nabla_{Cj} X_{j,\text{back}} \right) + \Gamma_{\text{air}} \left(1 + \sum_j \nabla_{Cj} X_{j,\text{air}} \right)$	(7)
Partial mass balance	$\Gamma_{b,\text{out}} X_{i,b,\text{out}} = \Gamma_{a,\text{out}} \left(X_{i,a,\text{out}} + \sum_j v_{i,Cj} X_{j,a,\text{out}} \right) + \Gamma_{\text{back}} \left(X_{i,\text{back}} + \sum_j v_{i,Cj} X_{j,\text{back}} \right) + \Gamma_{\text{air}} \left(X_{i,\text{air}} + \sum_j v_{i,Cj} X_{j,\text{air}} \right)$	(8)
Enthalpy balance	$\Gamma_{b,\text{out}} c_p (\vartheta_{b,\text{out}} - 1) = \Gamma_{a,\text{out}} \left(\sum_i X_{i,a,\text{out}} (-\Delta_c h_i^0(1)) + c_p (\vartheta_{a,\text{out}} - 1) \right) + \Gamma_{\text{back}} \left(\sum_i X_{i,\text{back}} (-\Delta_c h_i^0(1)) + c_p (\vartheta_{\text{back}} - 1) \right) + \Gamma_{\text{air}} \left(\sum_i X_{i,\text{air}} (-\Delta_c h_i^0(1)) + c_p (\vartheta_{\text{air}} - 1) \right)$	(9)
Reversal chamber		
Partial mass balance	$\frac{V_m}{\vartheta_m} \frac{dX_{i,m}}{d\tau} = \Gamma_{b,\text{out}} (X_{i,b,\text{out}} - X_{i,m})$	(10)
Enthalpy balance	$\frac{V_m}{\vartheta_m} \frac{d\vartheta_m}{d\tau} = \Gamma_{b,\text{out}} (\vartheta_{b,\text{out}} - \vartheta_m) - \frac{Q_m}{c_p \vartheta_m}$	(11)
Total mass balance	$\Gamma_m = \Gamma_{b,\text{out}} \frac{\vartheta_{b,\text{out}}}{\vartheta_m} - \frac{Q_m}{c_p \vartheta_m}$	(12)
Heat loss	$Q_m = St_m (\vartheta_m - \vartheta_a)$	(13)
Cathode channel		
Partial mass balance	$\frac{V_c}{\vartheta_c} \frac{\partial X_{i,c}}{\partial \tau} = -\gamma_c \frac{\partial X_{i,c}}{\partial \zeta_2} + \sum_{j=\text{red}} (v_{ij} - X_{i,c} \nabla_j) Da_j r_j$	(14)
Enthalpy balance	$\frac{V_c}{\vartheta_c} \frac{\partial \vartheta_c}{\partial \tau} = -\gamma_c \frac{\partial \vartheta_c}{\partial \zeta_2} + \sum_{j=\text{red}} \nabla_j Da_j r_j (\vartheta_s - \vartheta_c) + \frac{q_{cs}}{c_p}$	(15)
Total mass balance	$0 = -\frac{\partial \gamma_c \vartheta_c}{\partial \zeta_2} + \vartheta_c \sum_{j=\text{red}} \nabla_j Da_j r_j + \sum_{j=\text{red}} \nabla_j Da_j r_j (\vartheta_s - \vartheta_c) + \frac{q_{cs}}{c_p}$	(16)
Average outlet conditions	$\Gamma_{c,\text{out}} = \int_0^1 \gamma_c (\zeta_2=1, \zeta_1) d\zeta_1 \quad ; \quad X_{i,c,\text{out}} = \frac{1}{\Gamma_{c,\text{out}}} \int_0^1 \gamma_c (\zeta_2=1, \zeta_1) X_{i,c} (\zeta_2=1, \zeta_1) d\zeta_1 \quad ; \quad \vartheta_{c,\text{out}} = \frac{1}{\Gamma_{c,\text{out}}} \int_0^1 \gamma_c (\zeta_2=1, \zeta_1) \vartheta_c (\zeta_2=1, \zeta_1) d\zeta_1$	(17)
Stoichiometric coefficients	$\nabla_j^- = \sum_i v_{ij} \quad \text{for all } i: v_{ij} < 0$	(18)
Heat exchange density	$q_{cs} = St_{cs} (\vartheta_s - \vartheta_c)$	(19)
Cathode gas recycle	$X_{i,\text{back}} = X_{i,c,\text{out}} \quad ; \quad \vartheta_{\text{back}} = \vartheta_{c,\text{out}} \quad ; \quad \Gamma_{\text{back}} = R \frac{\Gamma_{c,\text{out}}}{\Gamma_{a,\text{out}}}$	(20)

Table 2.2 (continued): Equations of the physically-chemically reduced model

Electrode pores			(21)
Steady state mass balance	$\sum_{j=ox} v_{ij} Da_j r_j = n_{i,as}$; $\sum_{j=red} v_{ij} Da_j r_j = n_{i,cs}$		(21)
Partial pressures from transport kinetics	$\varphi_{i,as} = X_{i,a} + \frac{n_{i,as}}{D_{i,as}}$; $\varphi_{i,cs} = X_{i,c} + \frac{n_{i,cs}}{D_{i,cs}}$		(22)
Solid phase			
Enthalpy balance	$c_{ps} \frac{\partial \varphi_s}{\partial \tau} = \frac{I_a}{Pe_s} \frac{\partial^2 \varphi_s}{\partial \zeta^2} + \frac{1}{Pe_s} \frac{\partial^2 \varphi_s}{\partial \zeta^2} - c_p \sum_{j=ox} \nabla_j Da_j r_j (\varphi_a - \varphi_s) - c_p \sum_{j=red} \nabla_j Da_j r_j (\varphi_c - \varphi_s) - q_{as} - q_{cs} + q_{solid}$		(23)
Heat source density	$q_s = \sum_{j=ox} (-\Delta_R h_j^0(\varphi_s) + n_j(\phi_a^S - \phi_a^L)) Da_j r_j + \sum_{j=red} (-\Delta_R h_j^0(\varphi_s) + n_j(\phi_c^S - \phi_c^L)) Da_j r_j + (\phi_a^L - \phi_c^L) \cdot i_e \frac{1}{F}$		(24)
Stoichiometric coefficients	$\nabla_j^* = \sum_i v_{ij}$ for all $i: v_{ij} < 0$; $\nabla_j^* = \sum_i v_{ij}$ for all $i: v_{ij} > 0$		(25)
Potential field			
Electric potentials	$\phi_a^S = 0$; $\frac{\partial \phi_a^L}{\partial \tau} = -\frac{1}{c_a} (i - i_a)$; $\frac{\partial \phi_c^L}{\partial \tau} = -\frac{1}{c_c} (i - i_c)$; $\frac{\partial \phi_c^S}{\partial \tau} = \frac{I_a - I_{cell}}{c_a} + \frac{I_c - I_{cell}}{c_c}$; $U_{cell} = \phi_c^S - \phi_a^S$		(26)
Total currents	$I_a = \int_A i_a d\zeta$; $I_e = \int_A i_e d\zeta$; $I_c = \int_A i_c d\zeta$		(27)
Current density	$i_a(\phi_a^L) = \sum_{j=ox} n_j F Da_j r_j(\phi_a^L) ; i_c(\phi_c^L, \phi_c^S) = -\sum_{j=red} n_j F Da_j r_j(\phi_c^L, \phi_c^S) ; i_e(\phi_a^L, \phi_c^L) = \kappa_c \cdot (\phi_a^L - \phi_c^L) ; i = \left(\frac{1}{c_a} + \frac{1}{c_c} + \frac{1}{c_e} \right) \cdot \left(\frac{i_a}{c_a} + \frac{i_c}{c_c} + \frac{i_e}{c_e} \right) \cdot \left(\frac{I_a}{c_a} + \frac{I_c}{c_c} + \frac{I_e}{c_e} \right) + I_{cell}$		(28)
Reaction Kinetics			
Methane steam reforming	$r_{ref1} = \exp \left(A_{rr} \text{ref1} \cdot \left(\frac{1}{\varphi_s^0} - \frac{1}{\varphi_s} \right) \right) \cdot \left(X_{CH_4,a} X_{H_2O,a} - \frac{1}{K_{ref1}(\varphi_s)} X_{CO,a} X_{H_2,a}^3 \right)$		(29)
Water-gas shift reaction	$r_{ref2} = \exp \left(A_{rr} \text{ref2} \cdot \left(\frac{1}{\varphi_s^0} - \frac{1}{\varphi_s} \right) \right) \cdot \left(X_{CO,a} X_{H_2O,a} - \frac{1}{K_{ref2}(\varphi_s)} X_{CO_2,a} X_{H_2,a} \right)$		(30)
Hydrogen oxidation	$r_{ox1} = \exp \left(A_{rr} \text{ox1} \cdot \left(\frac{1}{\varphi_s^0} - \frac{1}{\varphi_s} \right) \right) \cdot \left(\varphi_{H_2,ac} \exp \left(\alpha_{ox1,+} n_{ox1} \right) \left(\frac{\phi_a^S - \phi_a^L}{\varphi_s} - \Delta \phi_{ox1,0}(\varphi_s) \right) - \varphi_{H_2O,ac} \varphi_{CO_2,ac} \exp \left(-(1 - \alpha_{ox1,+}) n_{ox1} \left(\frac{\phi_a^S - \phi_a^L}{\varphi_s} - \Delta \phi_{ox1,0}(\varphi_s) \right) \right) \right)$		(31)
Carbon monoxide oxidation	$r_{ox2} = \exp \left(A_{rr} \text{ox2} \cdot \left(\frac{1}{\varphi_s^0} - \frac{1}{\varphi_s} \right) \right) \cdot \left(\varphi_{CO,ac} \exp \left(\alpha_{ox2,+} n_{ox2} \right) \left(\frac{\phi_a^S - \phi_a^L}{\varphi_s} - \Delta \phi_{ox2,0}(\varphi_s) \right) - (\varphi_{CO_2,ac})^2 \exp \left(-(1 - \alpha_{ox2,+}) n_{ox2} \left(\frac{\phi_a^S - \phi_a^L}{\varphi_s} - \Delta \phi_{ox2,0}(\varphi_s) \right) \right) \right)$		(32)
Oxygen reduction	$r_{red} = \exp \left(A_{rr} \text{red} \cdot \left(\frac{1}{\varphi_{red}^0} - \frac{1}{\varphi_s} \right) \right) \cdot \left(\varphi_{CO_2,ac} \right)^{-2} \exp \left(2.5 \left(\frac{\phi_c^S - \phi_c^L}{\varphi_s} - \Delta \phi_{red,0}(\varphi_s) \right) \right) - (\varphi_{O_2,ac})^{0.75} (\varphi_{CO_2,ac})^{-0.5} \exp \left(-0.5 \left(\frac{\phi_c^S - \phi_c^L}{\varphi_s} - \Delta \phi_{red,0}(\varphi_s) \right) \right)$		(33)
Thermodynamics			
Heat capacity	$c_p(\varphi) = \text{const} = 4.5$		(34)
Enthalpies of reaction	$\Delta_R h_{ref1}^0 = +90.5$; $\Delta_R h_{ref2}^0 = -14.5$; $\Delta_R h_{ox1}^0 = -14.5$; $\Delta_R h_{ox2}^0 = 56.0$; $\Delta_R h_{red}^0 = 156.0$		(35)
Equilibrium constants	$K_{ref1}(\varphi) = \exp \left(30.19 - \frac{90.41}{\varphi} \right)$; $K_{ref2}(\varphi) = \exp \left(-3.97 + \frac{14.57}{\varphi} \right)$		(36)
Open circuit voltages	$\Delta \phi_{ox1,0}(\varphi) = 28.26 - 19.84 \cdot \varphi$; $\Delta \phi_{ox2,0}(\varphi) = 20.98 - 17.86 \cdot \varphi$; $\Delta \phi_{red,0}(\varphi) = 70.00 - 23.06 \cdot \varphi$		(37)

2.4 Steady state anode model

The two models introduced in the previous chapters are spatially distributed transient models with a high level of detail. They simulate a MCFC single cell with good precision and are the basis for the development of control strategies and system optimisation. On the other hand due to the many competing dependencies in these models they do not give much insight into the basic correlations of fuel cells with direct internal reforming.

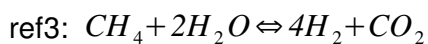
For this purpose a significantly simpler model is required focussing on the anode, containing a small number of state variables and considering only the most important dependencies. The following model is derived from the reduced model (see Chapter 2.3). There exists one basic version of it together with two extensions. The basic version is the most simple model and works well for the analysis of reforming strategies. The extensions consider the anode gas recycle and anode gas enthalpy balance.

In the following the simplifying assumptions and the equations for the simplified anode model are presented in detail. The extensions are then introduced in short form.

2.4.1 Assumptions

The following assumptions are applied to the reduced model:

- The system is in steady state, thus all derivatives with respect to time are zero. Consequently, all terms describing effects based on the thermal gas expansion add up to zero.
- An infinite cathode reflux ratio leads to spatially constant cathode conditions. The composition and amount of cathode gas are identical to the product of a complete oxidation of the anode feed gas with the air feed. With this all anode channels are operated under the same conditions, so the spatial ζ_2 coordinate can be eliminated.
- The temperatures of the anode and cathode gas as well as the temperature of the solid is fixed to one arbitrary, but representative value.
- One single reforming reaction is considered (indexed "ref3") which is the sum of the steam reforming reaction of methane and the water-gas shift reaction.



- Because no carbon monoxide is produced by the reforming reaction under this assumption, its oxidation reaction can be omitted. Thus, only the oxidation of hydrogen is considered.
- The anode gas composition is described in terms of dimensionless yields. This reduces the number of state variables.
- The mass transport resistances between gas phases and electrode pores are neglected, so the gas composition inside the pores is identical to that in the gas phase.

- The catalytic combustion chamber and the reversal chamber are no longer required in this model, as the cathode gas composition is calculated from a complete oxidation of the feed gas.
- The cell is operated in potentiostatic mode instead of galvanostatic mode. This means that the cell voltage no longer is an output quantity, but an input variable. On the other hand, the total cell current turns into an output quantity.
- The cell length can be set to any arbitrary positive value.
- The electrolyte has infinite ion conductivity.

The equation system following from these assumptions is given in the next section.

2.4.2 Model equations

The model equations of the anode model are introduced in a similar order as in the other modelling sections. First the anode mass and enthalpy balances are given. In this model the mass balances are written in terms of yield numbers, so the equations from the reduced model have to be transformed first. After the anode channel the cathode gas conditions are considered. Afterwards the electrochemical reaction kinetics are discussed.

Anode mass balances

The mole fraction of a certain component in the anode, $\chi_{i,a}$, can be described as the molar flow density of that specific component, $\gamma_{i,a}$, divided by the total molar flow density through the channel, γ_a . Both flows can be calculated as an initial amount of flow, $\Gamma_{i,feed}$ and Γ_{feed} , respectively, modified by the influence of the reforming and oxidation reactions, that is the extensive extents of reaction, $\tilde{\xi}_j$. The extensive variables in this expression are made intensive by division with the total feed flow, Γ_{feed} , and normalised by the maximum reaction extent possible from a stoichiometrical point of view, $\xi_{j,max}$. The result describes the mole fractions in the anode gas phase in dependence of the reaction extent numbers, ξ_j :

$$\chi_{i,a} = \frac{\gamma_{i,a}}{\gamma_a} = \frac{\Gamma_{i,feed} + \sum_{j=ox1,ref3} \nu_{i,j} \tilde{\xi}_j}{\Gamma_{feed} + \sum_{j=ox1,ref3} \bar{\nu}_j \tilde{\xi}_j} = \frac{\chi_{i,feed} + \sum_{j=ox1,ref3} \nu_{i,j} \xi_j \xi_{j,max}}{1 + \sum_{j=ox1,ref3} \bar{\nu}_j \xi_j \xi_{j,max}} \quad (2.156)$$

where the feed composition and the reaction extent numbers are defined as

$$\chi_{i,feed} = \frac{\gamma_{i,feed}}{\gamma_{feed}} = \frac{\Gamma_{i,feed}}{\Gamma_{feed}} \quad (2.157)$$

$$\xi_j = \frac{\tilde{\xi}_j}{\xi_{j,max}} \cdot \frac{1}{\Gamma_{feed}} \quad (2.158)$$

The maximum possible yield of the reforming reaction is equal to the mole fraction of methane in the feed gas, which is described by the steam to carbon ratio in the feed gas, S/C:

$$\xi_{ref,max} = x_{CH_4,feed} = \frac{1}{1+S/C} \quad (2.159)$$

From each mole of methane, four moles of hydrogen can be generated, so the maximum possible yield of the hydrogen oxidation reaction reads

$$\xi_{ox,max} = 4 \cdot x_{CH_4,feed} = \frac{4}{1+S/C} \quad (2.160)$$

In the denominator the extensive expression for the total molar flux is already used. It can be modified in a similar way to give the anode molar flow as a function of the extents of reaction:

$$\gamma_a = \Gamma_{feed} + \sum_j \bar{v}_j \tilde{\xi}_j = \Gamma_{feed} \cdot \left(1 + \sum_j \bar{v}_j \xi_j \xi_{j,max} \right) \quad (2.161)$$

The partial mass balance of the anode phase (Equation 2.1) is subjected to the assumptions mentioned above, resulting in:

$$\gamma_a \frac{dX_{i,a}}{d\zeta_1} = \sum_{j=ref,ox} (v_{ij} - X_{i,a} \bar{v}_j) Da_j r_j \quad (2.162)$$

After inserting equations 2.156 and 2.161, some manipulations and a comparison of coefficients one receives an ordinary differential equation describing the extents of reaction along the channel length:

$$\frac{d\xi_j}{d\zeta_1} = \frac{Da_j r_j}{\Gamma_{feed}} \cdot \frac{1}{\xi_{j,max}} \quad (2.163)$$

The equation is an ordinary differential equation of first order with respect to ζ_1 and requires one boundary condition for each reaction. These are given by the extents of the reforming and oxidation reaction at the anode inlet:

$$\xi_j(\zeta_1=0) = \xi_{j,in} \quad (2.164)$$

The reforming reaction kinetics for the overall reforming reaction reads

$$r_{ref3} = \exp\left(Arr_{ref3} \cdot \left(\frac{1}{\vartheta_{ref3}^0} - \frac{1}{\vartheta} \right) \right) \cdot \left(X_{CH_4,a} X_{H_2O,a}^2 - \frac{1}{K_{ref3}(\vartheta_a)} X_{CO_2,a} X_{H_2,a}^4 \right) \quad (2.165)$$

Cathode conditions

Due to the infinite reflux ratio in the cathode channel the concentrations and the temperature in the channel are constant and equal to the exhaust conditions. The composition of the exhaust gas can be calculated by looking at the cell as a black box in which the anode feed gas is oxidised with the burner air. Hence we have

$$\Gamma_{air} = \Gamma_{feed} \frac{\lambda_{air}}{X_{O_2,air}} \cdot 2 \cdot X_{CH_4,feed} \quad (2.166)$$

$$\Gamma_c = \Gamma_{feed} + \Gamma_{air} \quad (2.167)$$

$$\chi_{CH_4,c} = \chi_{CO,c} = \chi_{H_2,c} = 0 \quad (2.168)$$

$$\chi_{H_2O,c} = \frac{\Gamma_{feed}}{\Gamma_c} \cdot (2\chi_{CH_4,feed} + \chi_{H_2O,feed}) \quad (2.169)$$

$$\chi_{CO_2,c} = \frac{\Gamma_{feed}}{\Gamma_c} \cdot \chi_{CH_4,feed} \quad (2.170)$$

$$\chi_{O_2,c} = \frac{\Gamma_{air}}{\Gamma_c} \cdot \chi_{O_2,air} - \frac{\Gamma_{feed}}{\Gamma_c} \cdot 2\chi_{CH_4,feed} \quad (2.171)$$

$$\chi_{N_2,c} = \frac{\Gamma_{air}}{\Gamma_c} \cdot \chi_{N_2,air} \quad (2.172)$$

Current density

Because the cell in this model is driven potentiostatically it is possible to determine the local current density without calculating the current density distribution over the complete cell length. From the steady state charge balances (Table 2.2, Equations 26) it follows that the anodic and cathodic current density are equal:

$$i := i_a = i_c \quad (2.173)$$

$$i_a = n_{ox} F Da_{ox} \exp\left(Arr_{oxl} \cdot \left(\frac{1}{\vartheta_{oxl}^0} - \frac{1}{\vartheta} \right) \right) \cdot \left\{ \chi_{H_2,a} \exp\left(\alpha_{oxl,+} n_{oxl} \frac{(\phi_a^S - \phi_a^L) - \Delta\phi_{ox,0}(\vartheta)}{\vartheta} \right) - \chi_{H_2O,a} \chi_{CO_2,a} \exp\left(-(1 - \alpha_{oxl,+}) n_{oxl} \frac{(\phi_a^S - \phi_a^L) - \Delta\phi_{ox,0}(\vartheta)}{\vartheta} \right) \right\} \quad (2.174)$$

$$i_c = n_{red} F Da_{red} \exp\left(Arr_{red} \cdot \left(\frac{1}{\vartheta_{red}^0} - \frac{1}{\vartheta} \right) \right) \cdot \left\{ \chi_{O_2,c}^{a2} \chi_{CO_2,c}^{a3} \exp\left(-\alpha_{red,-} \frac{(\phi_c^S - \phi_c^L) - \Delta\phi_{red,0}(\vartheta)}{\vartheta} \right) - \chi_{CO_2,c}^{al} \exp\left(\alpha_{red,+} \frac{(\phi_c^S - \phi_c^L) - \Delta\phi_{red,0}(\vartheta)}{\vartheta} \right) \right\} \quad (2.175)$$

Neglecting voltage losses in the electrolyte leads to the same electric potential in the electrolyte at the anode and cathode electrodes.

$$\phi^L := \phi_a^L = \phi_c^L \quad (2.176)$$

In addition, the electric potential in the anode electrode is still arbitrarily set to zero, and the potential at the cathode electrode corresponds to the given cell voltage:

$$\phi_a^S = 0 \quad (2.177)$$

$$\phi_c^S = U_{cell} \quad (2.178)$$

After short manipulation, two equations follow which contain two unknown variables: the electric potential in the electrolyte, ϕ^L , and the current density, i . The current density can be determined from these iteratively.

$$i = n_{ox} F D a_{ox} \cdot \exp\left(Arr_{oxl} \cdot \left(\frac{1}{\vartheta_{oxl}^0} - \frac{1}{\vartheta} \right) \right) \cdot \left\{ \chi_{H_2,a} \exp\left(\alpha_{oxl,+} n_{oxl} \frac{-\phi^L - \Delta\phi_{ox,0}(\vartheta)}{\vartheta} \right) - \chi_{H_2O,a} \chi_{CO_2,a} \exp\left(-(1 - \alpha_{oxl,+}) n_{oxl} \frac{-\phi^L - \Delta\phi_{ox,0}(\vartheta)}{\vartheta} \right) \right\} \quad (2.179)$$

$$i = n_{red} F D a_{red} \cdot \exp\left(Arr_{red} \cdot \left(\frac{1}{\vartheta_{red}^0} - \frac{1}{\vartheta} \right) \right) \cdot \left\{ \chi_{O_2,c}^{a2} \chi_{CO_2,c}^{a3} \exp\left(-\alpha_{red,-} \frac{U_{cell} - \phi^L - \Delta\phi_{red,0}(\vartheta)}{\vartheta} \right) - \chi_{CO_2,c}^{a1} \exp\left(\alpha_{red,+} \frac{U_{cell} - \phi^L - \Delta\phi_{red,0}(\vartheta)}{\vartheta} \right) \right\} \quad (2.180)$$

The oxidation reaction rate can be calculated afterwards from Faraday's law:

$$r_{oxl} = \frac{i}{n_{oxl} F D a_{oxl}} \quad (2.181)$$

Thermodynamics

Because the reforming reaction considered in the anode model is the sum of the two reforming reactions from the reduced model, its free enthalpy of reaction equals the sum of the free enthalpies of both reforming reactions. Thus, the equilibrium constant can be calculated as:

$$K_{ref}(\vartheta) = \exp\left(26.22 - \frac{75.83}{\vartheta} \right) \quad (2.182)$$

The standard electric potentials of the electrochemical reactions are calculated in the same way as in the reduced model:

$$\Delta\phi_{ox,0}(\vartheta) = 28.26 - 19.84 \cdot \vartheta \quad (2.183)$$

$$\Delta\phi_{red,0}(\vartheta) = 78.00 - 23.06 \cdot \vartheta \quad (2.184)$$

2.4.3 Steady state anode model extensions

Extension I: Anode gas recycle

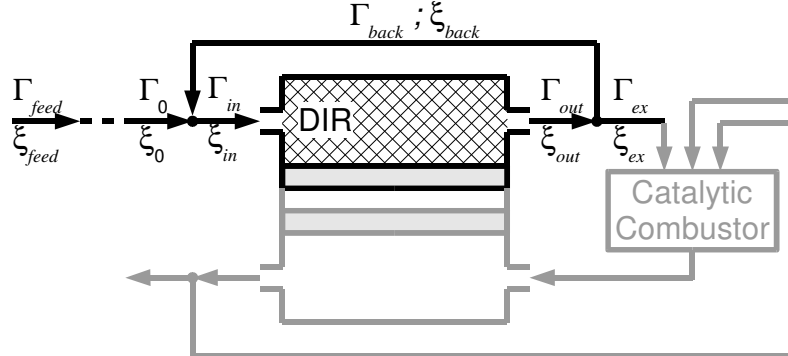


Figure 2.11: Flow scheme with anode recycle

If a gas recycle at the anode side is to be considered, the reduced model has to be changed slightly. Figure 2.11 shows an anode recycle together with the assigned variables. The total mass balance at the mixing point reads

$$\Gamma_{in} = \Gamma_0 + \Gamma_{back} \quad (2.185)$$

The partial mass balance at this point is

$$\Gamma_{in} \chi_{i,in} = \Gamma_0 \chi_{i,0} + \Gamma_{back} \chi_{i,back} \quad (2.186)$$

The recycle ratio is the ratio of the reflux flow corrected by the total molar change due to the reaction and the molar feed flow. This definition is chosen so that the recycle flow rate is independent of the unknown flow rate at the anode outlet:

$$R_a = \frac{\Gamma_{back}}{\left(1 + \sum_{j=ref,ox} \bar{v}_j \cdot \xi_{j,back} \xi_{j,max}\right) \cdot \Gamma_{feed}} \quad (2.187)$$

The mole fractions in the anode outlet, the reflux and the exhaust are identical:

$$\chi_{i,back} = \chi_{i,ex} = \chi_{i,out} \quad (2.188)$$

and thus also

$$\xi_{j,back} = \xi_{j,ex} = \xi_{j,out} \quad (2.189)$$

After some manipulation the following system equations follow:

The states in front of the anode channel are

$$\Gamma_0 = \Gamma_{feed} \cdot \left(1 + \sum_{j=ref,ox} \bar{v}_j \cdot \xi_{j,0} \xi_{j,max}\right) \quad (2.190)$$

$$\Gamma_{back} = \Gamma_{feed} \cdot R_a \cdot \left(1 + \sum_{j=ref,ox} \bar{v}_j \cdot \xi_{j,out} \xi_{j,max}\right) \quad (2.191)$$

$$\Gamma_{in} = \Gamma_0 + \Gamma_{back} = \Gamma_{feed} \cdot (1 + R_a) \cdot \left(1 + \sum_{j=ref,ox} \bar{v}_j \cdot \xi_{j,in} \xi_{j,max}\right) \quad (2.192)$$

$$\xi_{j,in} = \xi_j(\zeta_1=0) = \frac{\xi_{j,0} + R_a \cdot \xi_{j,out}}{1 + R_a} \quad (2.193)$$

Inside the anode channel the extents of reaction are described by

$$\frac{d\xi_j}{d\zeta_1} = \frac{Da_j r_j}{\Gamma_{feed} \cdot (1+R_a)} \cdot \frac{1}{\xi_{j,max}} \quad (2.194)$$

$$y_a = \Gamma_{feed} \cdot (1+R_a) \cdot \left(1 + \sum_{j=ref,ox} \bar{v}_j \cdot \xi_j \xi_{j,max}\right) \quad (2.195)$$

The states at the anode outlet are calculated from

$$\xi_{j,out} = \xi_j(\zeta_1 = \zeta_{end}) \quad (2.196)$$

$$\Gamma_{ex} = \Gamma_{feed} \cdot \left(1 + \sum_{j=ref,ox} \bar{v}_j \cdot \xi_{j,out} \xi_{j,max}\right) \quad (2.197)$$

While most of these equations describe the molar flows outside the cell and are not of interest for the calculations inside the channel, the mixing rule in Equation 2.193 and the ordinary differential equations for the extents of reaction (Equation 2.194) are important. They replace the corresponding equations 2.163 and 2.164 in the previous model without anode recycle. All other equations remain unchanged.

Extension II: Anode enthalpy balance

The anode enthalpy balance (Table 2.2, Equation 2) subjected to the assumption of the steady state anode model yields:

$$y_a c_p \frac{\partial \vartheta_a}{\partial \zeta_1} = \left(\bar{v}_{ox}^+ Da_{ox} r_{ox} + St_{as}\right) \cdot (\vartheta_s - \vartheta_a) + \left(-\Delta_R h_{ref}^0\right) Da_{ref} r_{ref} \quad (2.198)$$

This enthalpy balance may be used to get an impression of the anode gas temperature profile. However, the model still contains the assumption of a constant solid temperature. This model extension is used to compare its results with those from a modified reduced model in Chapter 4.2.

2.5 Concluding remarks on MCFC modelling

The MCFC reference model introduced in this chapter simulates a transient single cross flow cell. It is based on the description of physical and chemical phenomena and consists of balances of mass, enthalpy and charges together with a number of kinetic expressions and thermodynamic relations. Direct internal reforming in the anode channel, a catalytic burner and a cathode gas recycle are implemented. The level of detail is high, ranging from mass transport resistances in the electrode pores over transient charge balances at the electrode double layers to complete thermodynamic equilibrium calculations in the reaction kinetics.

The model is formulated completely in dimensionless form in order to make the simulation results more general. Numbers like the Damköhler or the Stanton number characterise the properties not only of one specific cell, but the simulation results describe the behaviour of a whole group of cells with the same dimensionless numbers. The parameters are either calculated from well known relations or estimated so that the simulated values are within reasonable range.

The reference model is the basis of a hierarchy of further models, which can be derived from it for various purposes. The physically reduced model is one example for that. Among other changes, it neglects or simplifies certain temperature dependencies where they are of minor importance. The numerical treatment of this reduced model is far easier and faster, so it is widely used within this work.

A far simpler model is the steady state anode model, which is derived from the reduced model under strongly simplifying assumptions. Two extensions are introduced for this model, one describing an anode recycle and the other featuring a simplified anode enthalpy balance. These models are applied in Chapter 3 to study the principles of the interplay of reforming and oxidation in the anode channel.

Everything should be made as simple as possible, but not simpler.

Albert Einstein

3 Conceptual system design based on the steady state anode model

In fuel cells with direct internal reforming (DIR-FC) the electrochemical and the reforming reactions are coupled via mass and energy exchange. Neglecting minor physical phenomena the spatially distributed steady state anode model focusses on the description of these two features at steady state. Its results are not of quantitatively exact nature but they show the interrelations in a qualitative and simple way. The conversion diagram of the reforming and the oxidation reaction is closely related to the anode model. Large amounts of information can be put into this diagram and many basic interrelations can be read from it.

In this chapter the conversion diagram is introduced first. Then the steady state anode model is used to gain some insight into different reforming concepts for fuel cells. In the last two sections anode flow schemes are analysed. Here the application of an anode cascade and anode gas recycle are treated.

3.1 The conversion diagram

For the steady state anode model the two states of interest are the spatially distributed extents of reaction of the reforming and the electrochemical oxidation, respectively. These are plotted against each other in a phase diagram denoted as "conversion diagram" (Figure 3.1). At $\xi_{ref}=0$ no reforming has occurred so far in the anode gas, while $\xi_{ref}=1$ implies a completely reformed gas mixture regardless of any equilibrium limitation. $\xi_{ox}=0$ describes an anode gas composition from which no hydrogen has been oxidised. A gas at $\xi_{ox}=1$ is fully oxidised and contains no more combustible species. Note that the extent of the oxidation reaction can be interpreted as the degree of fuel utilisation.

The mole fractions in the anode gas are described by the extents of the reactions according to Equation 2.163, so each point in the diagram corresponds to an anode gas composition. As the mole fractions cannot be negative, certain restrictions define the stoichiometrically attainable region (Figure 3.1):

$$X_{CH_4} \geq 0 \quad \Leftrightarrow \quad \xi_{ref} \leq \frac{1}{1+S/C} \cdot \frac{1}{\xi_{ref,max}} = 1 \quad (3.1)$$

$$X_{H_2O} \geq 0 \quad \Leftrightarrow \quad \xi_{ox} \geq -\frac{S/C}{1+S/C} \cdot \frac{1}{\xi_{ox,max}} + \xi_{ref} \cdot \frac{\xi_{ref,max}}{\xi_{ox,max}} = -0.625 + \frac{1}{4} \xi_{ref} \quad (3.2)$$

$$x_{H_2} \geq 0 \Leftrightarrow \xi_{ox} \leq 4 \xi_{ref,max} \cdot \frac{\xi_{ref,max}}{\xi_{ox,max}} = \xi_{ref} \quad (3.3)$$

$$x_{CO_2} \geq 0 \Leftrightarrow \xi_{ox} \geq -\xi_{ref} \cdot \frac{\xi_{ref,max}}{\xi_{ox,max}} = -\frac{1}{4} \xi_{ref} \quad (3.4)$$

According to Equation 3.4, a negative extent of the oxidation reaction is possible. If the reforming reaction has produced some carbon dioxide and the cell voltage is very high, the oxidation reaction runs in backward direction. This can be interpreted as the electrolysis of carbon dioxide with water producing hydrogen and carbonate ions. Although this is not usual in fuel cells, it may happen in cells operated at very low current density, i.e. high cell voltage. When integrating the ODE system of the anode model along the spatial ζ_l coordinate the extents of reaction change with ζ_l . The reforming reaction leads to a progression of the trajectory to the right in the diagram, while the oxidation moves the state point vertically. With given temperature and cell voltage the electrochemical reaction rates can be calculated from equations 2.179 and 2.180 at every point in the diagram. The reaction rates at any point may be interpreted as the components of a vector. The Damköhler numbers are weighting factors applied to both vector components and transform it into the tangent of the trajectory through that point. In case of a cell without DIR the Damköhler number of the reforming reaction is zero and thus the tangent only points vertically. A pure reforming reactor can be simulated by setting the electrochemical Damköhler numbers to zero.

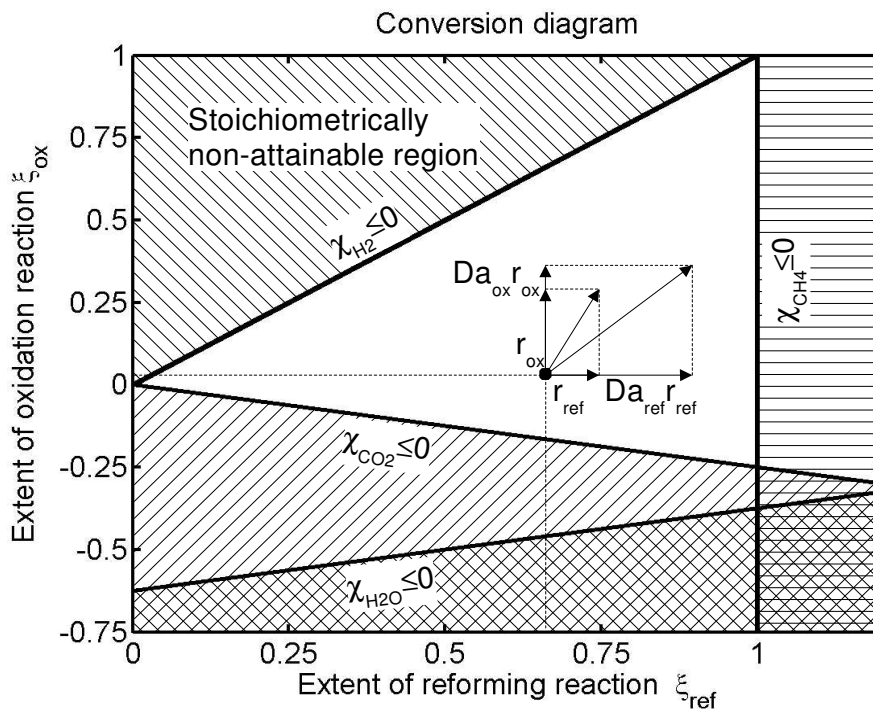


Figure 3.1: Axes, stoichiometric limits and reaction vectors in the conversion diagram.

Both reactions considered here are equilibrium limited. Inserting the definition of the mole fractions into the equilibrium condition of each reaction one receives an algebraic equation

depending on both reaction extents. Using one of the extents as a continuation parameter it is possible to evaluate the other reaction extent at equilibrium condition. In Figure 3.2 the equilibrium curves are shown for a dimensionless temperature of $\vartheta=3$ and a dimensionless cell voltage of $U_{cell}=35$. From a system theoretic point of view the equilibrium curves are nullclines, because on them one gradient represented by the corresponding reaction rate becomes zero. This is illustrated by the exemplary reaction rate vectors displayed in Figure 3.2. On the electrochemical equilibrium line the reaction vectors point in horizontal direction and vice versa on the reforming equilibrium line.

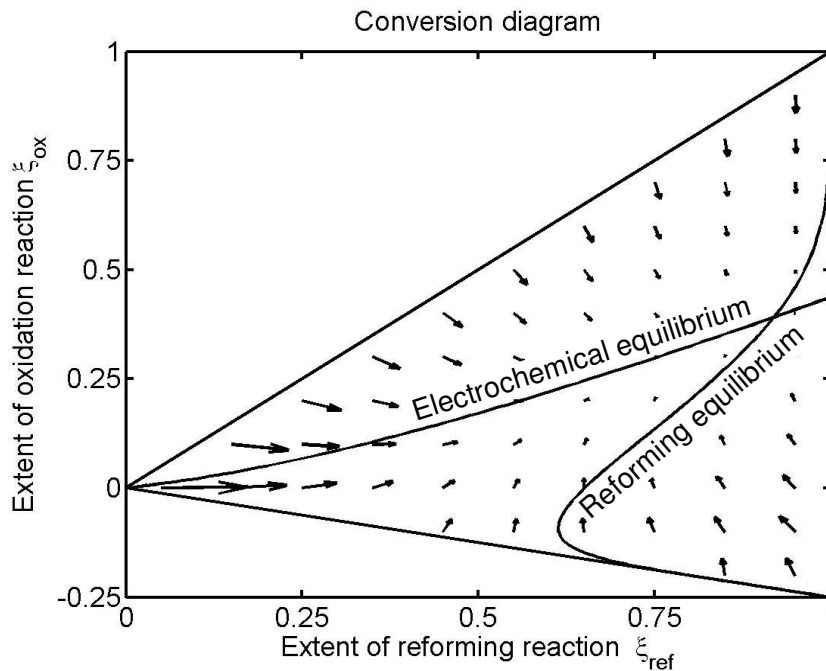


Figure 3.2: Conversion diagram; Equilibrium lines and corresponding field of reaction rate vectors for temperature $\vartheta=3$ and cell voltage of $U_{cell}=35$.

The reforming equilibrium curves depend on temperature and the electrochemical equilibrium line depends on temperature and cell voltage. Figure 3.3 shows some exemplary reforming equilibrium lines for various temperatures and several electrochemical equilibrium lines at constant temperature, $\vartheta=3$, for three different cell voltages. The reforming equilibrium curve always starts in the right bottom corner and ends in the upper right corner of the diagram. Its electrochemical counterpart runs from the coordinate origin to a point on the right axis. Thus, both curves always have one intersection point.

A curve describing a spatially distributed cell according to the anode model starts at the point defined by the reaction extents at the anode inlet. It then follows the reaction vectors weighted by the Damköhler numbers and tends towards the intersection point of both reaction equilibria. Only at infinite channel length that point is theoretically reached. An example is given in Figure 3.4, where a completely unreformed gas enters the anode channel and is being reformed and oxidised at temperature $\vartheta=3$ (approx. 600 °C) and cell

voltage $U_{cell}=35$ (approx. 0.9 V). Additionally, a second curve is plotted for a completely reformed gas entering the anode under the same conditions. While the oxidation takes place the reforming reaction goes backwards at first. For infinite channel length it ends at the same point as the unreformed gas does. The intersection point of both nullclines is the attractor of the system. Like the nullclines its location depends on temperature and cell voltage.

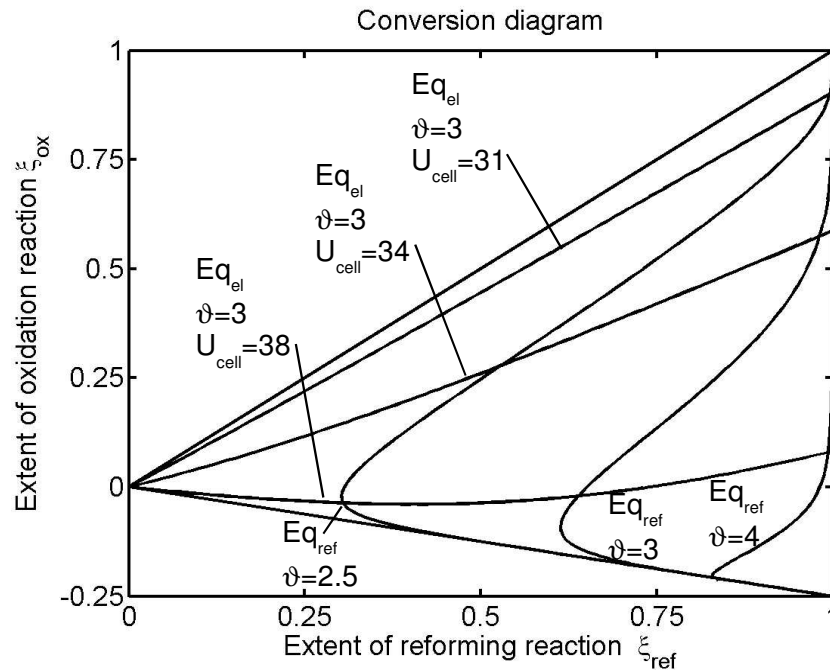


Figure 3.3: Temperature and voltage depending equilibrium lines for reforming and electrochemical equilibrium.

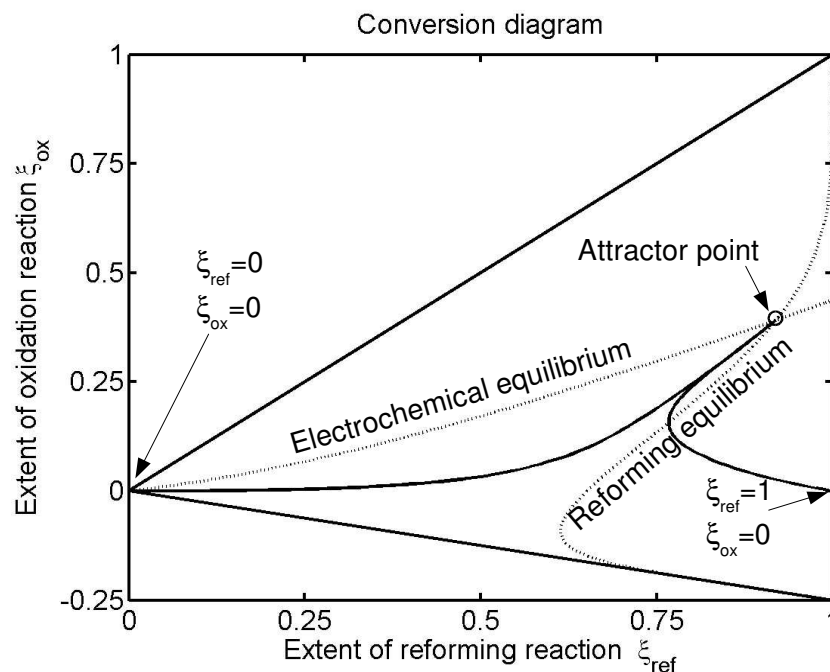


Figure 3.4: Conversion diagram for isothermal model with temperature $\vartheta=3$ ($\approx 600^\circ\text{C}$) and cell voltage $U_{cell}=35$ (≈ 0.9 V). Two exemplary trajectories for two different inlet conditions.

3.2 Comparison of reforming strategies

Independent of the concrete technical implementation there are three types of reforming concepts known for fuel cells which are shown in Figure 3.5. The first is a separate reactor – the so-called external reformer (ER) – which is fed with unreformed fuel and converts it to a certain extent which is limited by the reaction equilibrium. This concept requires energy input to the endothermic reforming process. Energy can be delivered in various ways, for example by the oxidation of a part of the feed gas, by using the heat of an exothermic process, or by the feed gas itself, in case it is fed hot into the reactor. This makes the design of the reformer rather flexible, as some operating parameters like temperature and pressure can be chosen independently from the following fuel cell. On the other hand this is an additional reactor making the whole fuel cell system larger. An ER can be simulated using the anode model by setting the electrochemical Damköhler numbers to zero and choosing ϑ_{cell} as the ER temperature.

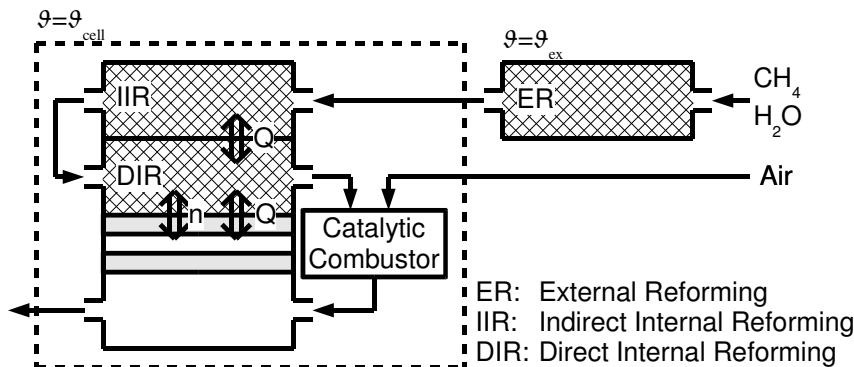


Figure 3.5: Different reforming concepts for MCFC.

The second type of reforming is integrated into the cell stack, but not inside the cells. The indirect internal reforming (IIR) is performed in separate channels which are located between the cells and contain reforming catalyst. The heat required for the reforming process is taken from the cell in which the exothermic electrochemical reactions happen, thus this concept features energetic integration but not mass integration. The heating of the endothermic reforming by the heat generated by the electrochemical reactions is the major advantage of the IIR concept. To a limited extent the IIR can also be used for local cooling of hot spots in the cell. For the steady state anode model the IIR can be interpreted as an external reforming at fuel cell temperature. It is also equilibrium limited.

Performing the reforming reaction inside the anode channel itself is called the direct internal reforming concept (DIR). It is a highly integrated concept with energy and mass exchange between reforming and electrochemical reactions. The reforming process is not only heated in a direct way by the exothermic electrochemical reactions, but also the equilibrium limitation can be pushed further towards the products by immediate electrochemical consumption of the reforming products. Further possibilities arise concerning the heat

management inside the stack. The reforming reaction can be used for local cooling and the avoidance of hot spots in the stack.

A fuel cell system can be designed with any combination of the three reforming concepts mentioned. If the cell has no DIR, then only ER or IIR can be chosen. Figure 3.6 shows these configurations using the conversion diagram for IIR at cell temperature ($\vartheta=3$) and for one low and one high temperature ER ($\vartheta=2.5$ and $\vartheta=4$). The electrochemical yield inside the MCFC can not be higher than the reforming yield obtained from the reformer. Thus the electrochemical conversions are satisfactorily high only if a high temperature ER is used. Admittedly, high temperature ER always requires external heating by oxidation of a part of the fuel gas or by electric heating. This usually leads to a dramatic decrease of the overall electric system efficiency.

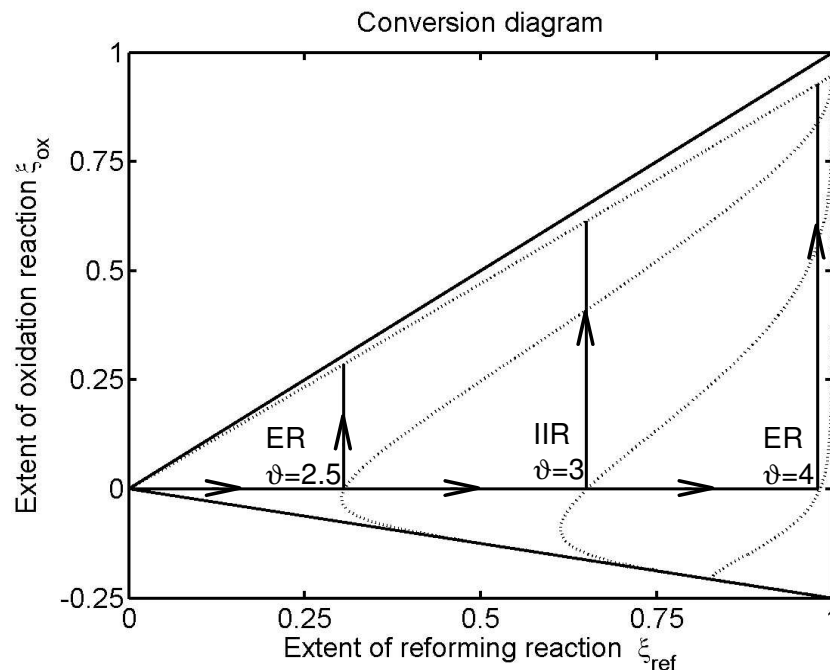


Figure 3.6: Conversion diagram for a MCFC without DIR with IIR or ER at high or low temperature. The electrochemical yield is limited by the equilibrium reforming conversion. $U_{cell}=33.0$; $\vartheta_{cell}=3$; infinite channel length.

Higher degrees of electrochemical conversion can be achieved if DIR is employed. In Figure 3.7 the same external reformers are used as before but now their products are fed into a DIR-MCFC. Additionally the trajectory for a pure DIR system is plotted. All four trajectories end at the intersection point of the reforming and electrochemical equilibrium at high extent of the electrochemical reaction. Thus it becomes clear that high degrees of fuel utilisation can be realised when DIR is applied.

For a DIR cell the use of a high temperature ER is not useful, because the reforming reaction runs backwards when the hot reformer product is fed into the colder fuel cell. The low temperature ER and the IIR have one advantage. Upon entering the anode channel the

gas contains hydrogen and the electrochemical reaction can start at once. This is not the case with DIR only, thus the inlet part of the electrode is not used for oxidation. On the other hand using ER or IIR causes higher investment costs compared to a system with DIR only. Concluding the analysis one can state that DIR offers high degrees of fuel utilisation and a very compact cell system design. From this point of view a system featuring only DIR is the most preferable reforming configuration. Nevertheless, there are certain arguments to employ IIR or ER, for example the hydrogen content at the anode inlet or the problem of catalyst poisoning, which could possibly be detected in an ER before entering and damaging the fuel cell stack itself.

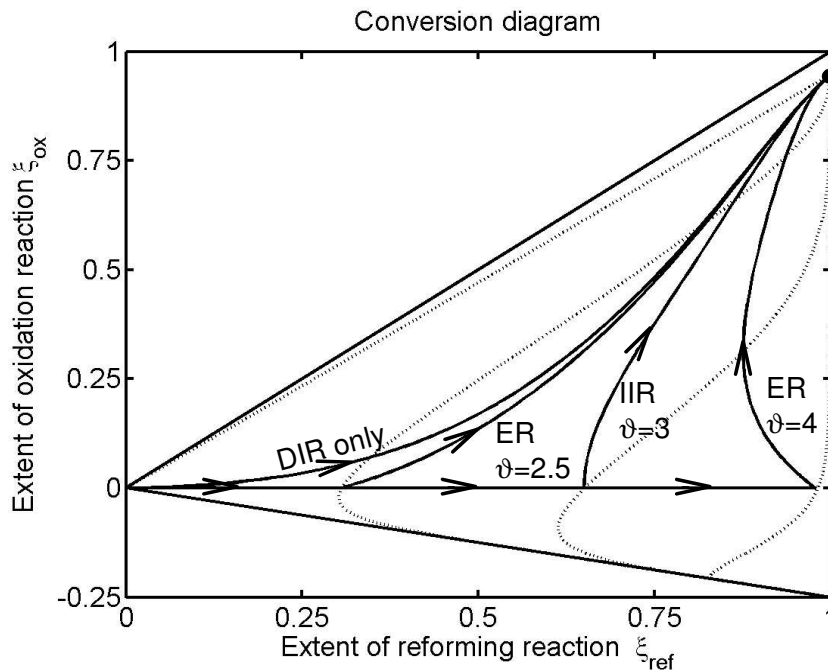


Figure 3.7: Conversion diagram for an MCFC with DIR only and for a MCFC with DIR and IIR or ER at high or low temperature. All trajectories end in the equilibrium point at high electrochemical conversion. $U_{cell}=33.0$; $\vartheta_{cell}=3$; infinite channel length.

3.3 Anode cascades

In the literature several authors discuss appropriate flow schemes for high temperature fuel cells. One proposal appearing fairly often (e.g. Fellows et al. [35, 36]) is to connect several fuel cells to a fuel cell cascade (cf. Figure 3.8). The advantage is that each fuel cell can be operated at an individual cell voltage and thereby the overall electrical power output can be improved beyond the power output of one single cell. The steady state anode model together with the conversion diagram can be used to compare the single cell against a cascade configuration and allows for a rough design of the system.

Considering the electric configuration of the system, two options seem possible, one being a parallel electric configuration using separate electric converters for each cell in the cascade

to transform their individual voltage to a common value (Figure 3.9a). The other is an electric series connection of all cells (Figure 3.9b). While the first option offers more degrees of freedom for an optimal system design, the second requires less hardware components in the electric part of the system.

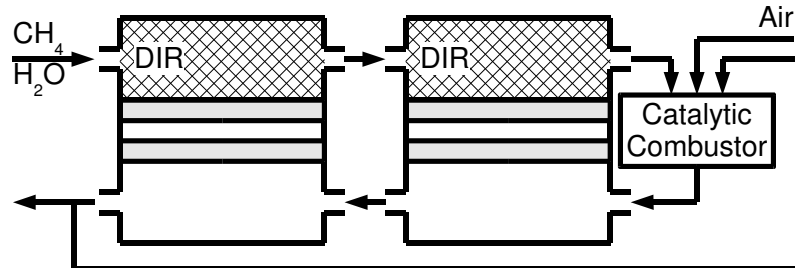


Figure 3.8 : Flow scheme of a fuel cell cascade.

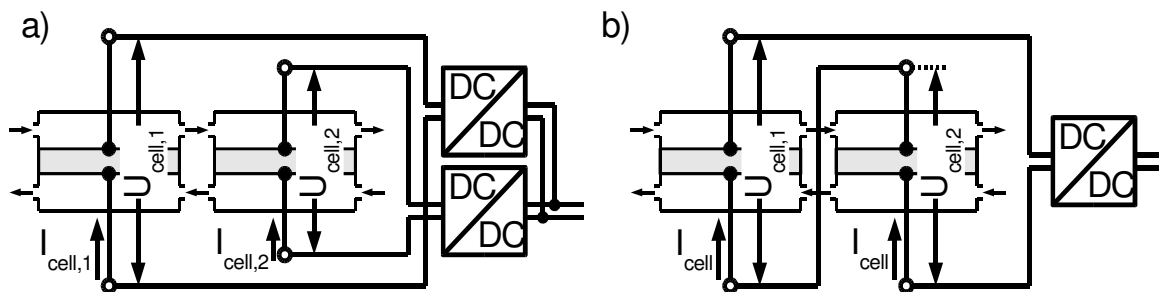


Figure 3.9: Different possibilities of electric connections with fuel cell cascades.

- Parallel connection with separate electric converters;
- Series connection with single electric converter.

In the following the electric power output of the two cascade configurations mentioned is compared with the power output of a single cell. With respect to comparability, all systems under discussion are to have the same total geometric size. Thus with an anode channel length of 1 for the single cell the sum of the lengths of all cascade cells in each configuration must also be equal to 1. Additionally, the feed conditions and the temperature for all simulations are identical. The cell voltages and the individual length of each cascade cell is subject to an optimisation aiming at the maximisation of the overall electric power output:

$$P_{el}(U_{cell,k}, \Delta \zeta_k) = \sum_{k=1}^N U_{cell,k} \cdot \Delta \xi_{ox,k} \rightarrow \max! \quad (3.5)$$

In order to avoid damage to the electrodes, the cell voltage may not fall short of a certain minimum value. This adds a constraint to the optimisation:

$$U_{cell,k} \geq U_{cell,min} \quad (3.6)$$

The optimisation results for a single cell and for a two cell cascade with parallel electric configuration (Figure 3.9a) are listed in Table 3.1. With the results of this optimisation the trajectories for the systems under discussion are calculated and plotted in Figure 3.10. The electric power of each cell is equal to the product of the cell voltage and the cell current represented by the extent of oxidation reaction (cf. Equation 2.112). The cell voltage is

plotted on the left side of the horizontal axis and thus the electric power in a cell equals the area of the rectangle on the left side of the diagram. With this the electric power output of both systems can be illustrated graphically.

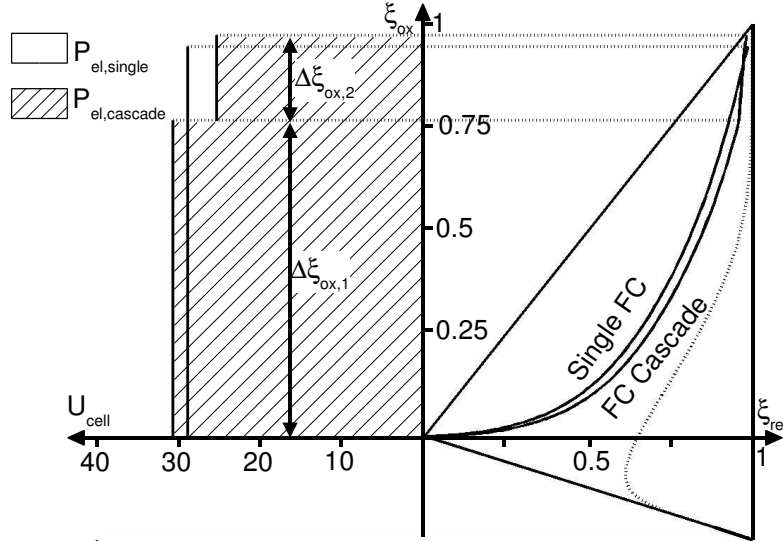


Figure 3.10: Comparison of a single fuel cell with a two cell cascade with parallel electric configuration. Conversion trajectories and total electric power for optimised cell voltages and anode length. $Da_{ref}=25$; $Da_{ox}=25$; $Da_{ref}=0.3$; $\vartheta=3$. For further details see Table 3.1.

While the single cell shows a maximum possible electric power output of $P_{el,single}=62.4$, the two cell cascade delivers $P_{el,cascade}=65.27$, which is an increase of electric power output by 4.6%. The reason for this is that a part of the current is produced at a higher voltage and that more current is produced. It can be shown that increasing the number of fuel cells in the cascade while keeping the total anode length constant further increases the total electric power output of the cascade.

Table 3.1: Optimisation results for single cell and two cell cascade. Compare for Figure 3.10.

	Length, ζ	Voltage, U_{cell}	Ext. of ox. reaction, $\Delta\xi$	El. power output, P_{el}
Single cell	1.000	28.83	0.947	62.4
Two cell cascade				
1. cell	0.674	30.81	0.683	48.10
2. cell	0.326	27.00	0.278	17.17
Total	1.000	---	0.961	65.27

The cascades discussed so far have a parallel electric configuration. This allows to load each cell in the cascade with an individual voltage and current. The disadvantage is that this requires additional electric converters to transform the voltage of each segment to a common value (Figure 3.9a). The alternative is to configure the cascade cells in an electric series. Thus each cascade cell still has its individual voltage, but all are loaded with an identical current. This adds another constraint to the objective function (Equation 3.5):

$$\Delta \xi_{ox,1} = \Delta \xi_{ox,2} \quad (3.7)$$

The results of this optimisation for a two cell cascade are shown in Figure 3.11 and Table 3.2. The power output $P_{el,cascade}=64.7$ is only slightly lower than that of the two cell cascade with parallel electric configuration. Compared to the single cell case this is a power increase of 3.7%.

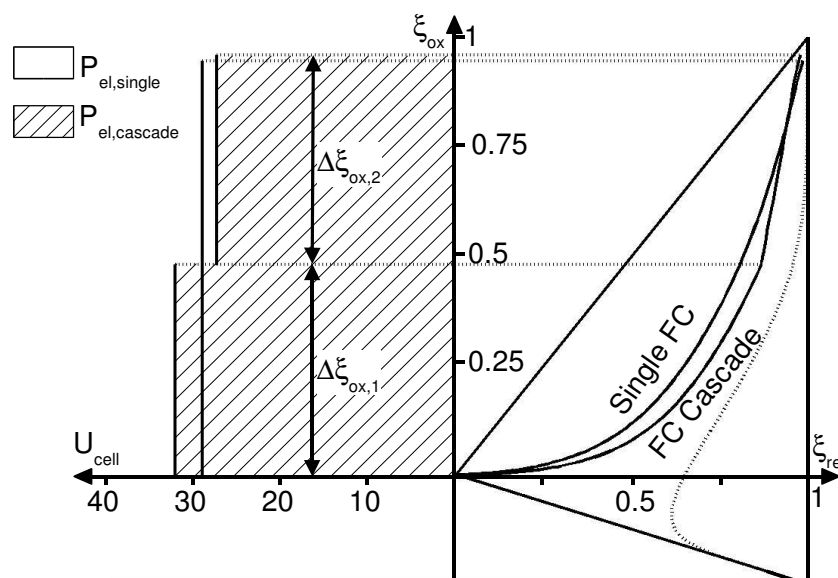


Figure 3.11: Comparison of a single fuel cell with a two cell cascade for electric series connection. Trajectories and total electric power for optimised cell voltages and anode length. $Da_{ref}=25$; $Da_{ox}=25$; $Da_{ref}=0.3$; $\vartheta=3$. The extent of the oxidation reaction is identical in both cascade cells. For further details see Table 3.2.

Table 3.2: Optimisation results for single cell and two cell series cascade. Compare for Figure 3.11.

	Length, ζ	Voltage, U_{cell}	Ext. of ox. reaction, $\Delta \xi$	El. power output, P_{el}
Single	1.000	28.83	0.947	62.40
Two cell cascade				
1. cell	0.508	31.84	0.480	34.93
2. cell	0.492	27.20	0.480	29.84
Total	1.000	---	0.960	64.7

With these theoretical results in mind one can proceed to economical considerations. A fuel cell cascade can be realised by dividing a conventional cell stack into several parts which are electrically isolated from one another. Thus the stack may keep its original shape and size. One should also take into account the fact that a segmentation into more than two or three cells does not significantly improve electric power output. Regarding the additional hardware effort for a segmentation, a cascade design can be economically useful only for large fuel cells. Although a parallel electric configuration offers higher electric output it also demands additional electric converters which increases the production costs of this version. The serial electric configuration offers nearly as high output while causing less additional investment costs. The drawback of this cell configuration is that it offers less degrees of freedom for selecting the operating conditions.

The results presented here are generic and state that cascading a fuel cell might be advantageous. They do not analyse the question of the technical feasibility and the economic profitability of this idea. For that, further analysis is necessary including the simulation of the temperature field, finding suitable operating conditions for a broad range of electric loads and a thorough economical investigation on the preferable configuration. Some of these tasks can be performed using models from this work, but their detailed treatment is not a subject here.

3.4 Anode gas recycle

Another aspect in MCFC flow schemes mentioned in the fuel cell literature (e.g. Fellow et al. [35, 36]) is the application of an anode gas recycle. This feature has two advantages. First it solves one of the problems with pure DIR systems. In these systems no hydrogen is available for the oxidation reaction at the anode inlet. This can be amended by recycling a part of the anode exhaust gas which contains hydrogen. The second advantage is that the anode gas temperature is homogenised over the channel length. Especially the sharp temperature drop due to the fast endothermic reforming reaction at the anode inlet is diminished. The first effect can be simulated by the steady state anode model.

When comparing a cell without reflux with an optimal cell voltage (maximum cell power) to an identical cell with an anode gas recycle and also an optimised cell voltage, the cell without the anode gas recycle will always yield a higher electric output.

The reason for this can be seen in Figure 3.12. Here the case with a recycle ratio of $R=0.3$ is shown together with the case without anode recycle, both at optimal cell voltage. The trajectory for $R=0$ runs at a comparably large distance from the electrochemical equilibrium line resulting in high oxidation reaction rates and consequently in high electric power output. In contrast to this the trajectory for the recycle system lies closer to the main diagonal of the conversion diagram. This means that either the cell voltage has to be decreased in order to achieve oxidation rates comparable to those in the cell without recycle, or the cell voltage is

kept high and the oxidation rate is decreased. In any case, the local electric power production is lower if the trajectory is situated closer to the main diagonal.

This consideration holds for any combination of cell voltage and recycle ratio. The reason for this is that the trajectory of any pure DIR-system is bent to the left. When an anode recycle is applied the inlet point can only be situated inside this bend and therefore be closer to the main diagonal, in the region of electrochemical equilibrium lines with lower voltages, where the local power output of the cell is comparably small. Also the increased gas velocity slows down the increase of oxidation along the channel length. Thus, the electric power output is always smaller for the system with an anode gas recycle.

The anode steady state model predicts a decrease in electric power output from a stoichiometric and equilibrium point of view when an anode recycle is applied. Nevertheless, it may still be favourable if the temperature distribution is considered. The steady state anode model can not serve as a system design tool here, even with its anode enthalpy extension, because it does not consider the solid temperature distribution. Nevertheless, its conversion diagram is very useful to illustrate the effect of anode recycling on the cell performance.

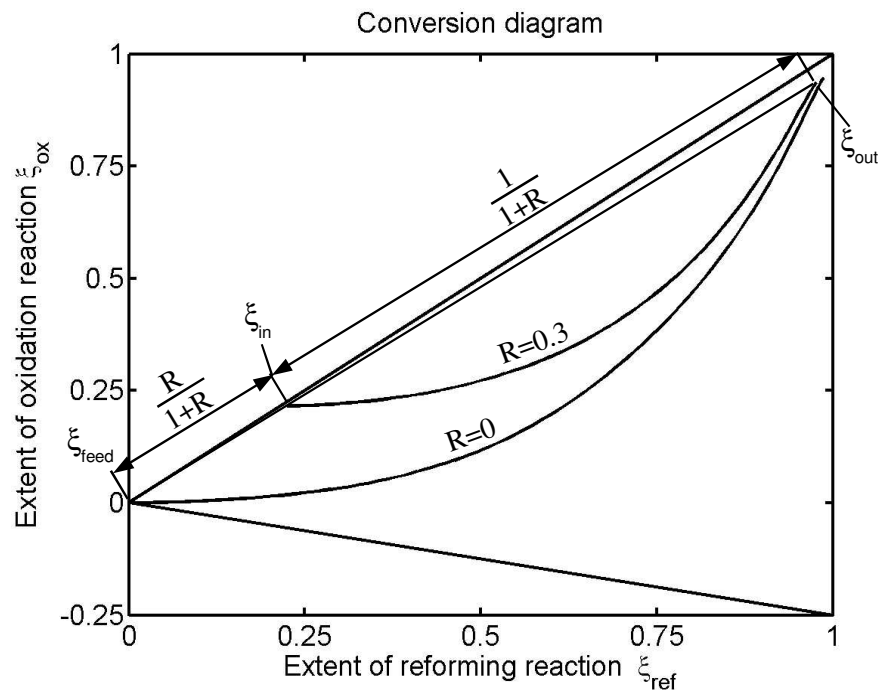


Figure 3.12: Conversion diagram for a system with anode recycle ($R=0.3$, $P_{el}=60.6$) and without anode recycle ($R=0$, $P_{el}=64.4$). The lever rule for the calculation of the inlet condition is indicated. $Da_{ref}=25$; $Da_{ox}=25$; $Da_{ref}=0.3$; $\theta=3$; $U_{cell}=33.0$.

3.5 Concluding remarks on fundamental system design

The steady state anode model considers the substantial interplay of reforming and oxidation reaction in a single counter flow cell at steady state without considering the enthalpy balance.

Within this chapter its usefulness is demonstrated by applying it to analyse different aspects of anode fuel flow configurations. By comparison of various reforming configurations including external, indirect internal and direct internal reforming (ER, IIR and DIR) the DIR turns out to be the best possibility to reach high degrees of fuel utilisation.

A second analysis focusses on the application of an anode cascade. Though more complex to design and more costly to build than a single cell system, it offers higher electric power output which for large systems should compensate for the higher investment costs. Although this result requires further analysis considering also the temperature profiles in the stack it is a useful hint as to when and how to debate an anode cascade configuration with two or three cell stacks.

Finally the possibility of an anode gas recycle is evaluated. It turns out that this is not of advantage with respect to purely stoichiometric arguments. Further analysis might reveal that temperature effects outbalance the substantial disadvantages.

Besides the system design results the conversion diagram which is used to display the results of the steady state anode model is proven to be a suitable tool for the illustration of the stoichiometric interplay between reforming and oxidation in the anode channel.

I don't know what I may seem to the world,
but as to myself, I seem to have been only a boy
playing on the sea-shore and diverting myself
in now and then finding a smoother pebble
or a prettier shell than ordinary, whilst
the great ocean of truth lay all undiscovered
before me.

Sir Isaac Newton

4 Simulation results of the reduced model

This chapter discusses the numerical solution of the spatially two-dimensional simplified MCFC model (see Chapter 2.3) and its results. In the first section the model implementation is explained shortly. Afterwards, steady state simulation results at one chosen operating point are presented and their physical validity is demonstrated. Then the chapter continues with some transient results from the simulation of a load step. Finally, the sensitivity of the simulation results with respect to some major system parameters is analysed.

4.1 Numerical solution of the reduced model

To solve the physically-chemically reduced model introduced in Chapter 2.3 the PDEs (partial differential equations) are first transformed into a system of algebraic and ordinary differential equations (DAE) by finite volume discretisation with respect to the local coordinates. The resulting equations are then implemented using ProMoT (Process Modelling Tool, version 0.7.0, [37]) and solved in the simulation environment DIVA (version 3.9, [38]).

ProMoT is a tool for hierarchical modeling based on the state-fluxes-principle [39]. Contrary to other implementations [40] the hierarchical principle is not applied here to its full depth, but is only used to divide the complete model into several blocks (Figure 4.1). The anode and the cathode block contain the mass and enthalpy balances for the gas phases in both channel layers. The solid temperature balance, the pore mass balances and the electric potential equations are implemented in the solid block. Information about temperatures, gas phase mole fractions and mass flux densities are exchanged between these blocks via so-called terminals within the blocks. The burner and mixer blocks connect the anode outlet to the cathode inlet. The input block contains all input variables including total cell current, anode inlet conditions, air inlet conditions and cathode reflux ratio. The exhaust block serves only as a termination block for the cathode exhaust terminal.

The structure is organised so that inserting additional blocks is quite simple. For example a direct internal reforming block can be added easily. Also further recycles can be accounted for with only minor changes to the model structure.

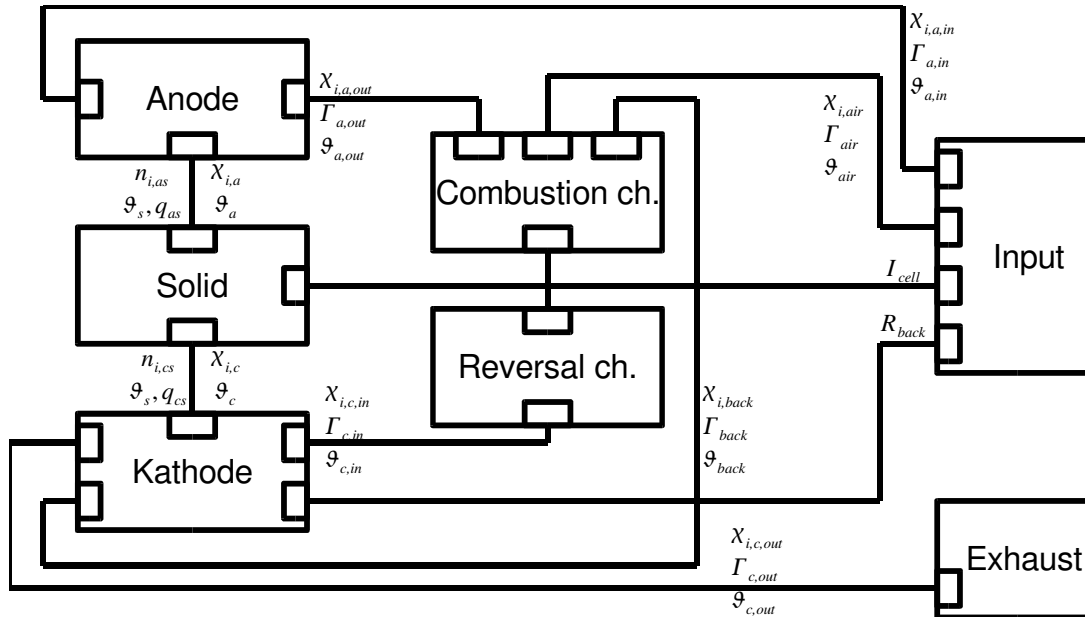


Figure 4.1: Block representation of the reduced model as implemented in ProMoT.

4.2 Steady state results

The steady state presented here is the simulation result of a standard load case of the 2D cell. The operating conditions of this "base case" are similar to typical conditions of the HotModule at high load. The input parameters are collected in Table 4.1, all other system parameters are shown in the Appendix A.6.

Table 4.1: Input quantities at base case. For convenience some dimensional quantities are calculated for the HotModule system.

	Dim.-less	Dimensional (HotModule)
Feed gas		
Steam/carbon ratio S/C	2.5	
Pre-reforming	0	
Molar flow rate $\Gamma_{a,in}$	1.0	0.569 Nm ³ /h per cell
Temperature $\vartheta_{a,in}$	3.0	621.3°C
Burner air number λ_{air}	2.2	
Cathode recycle ratio R_{back}	0.5	
Total cell current I_{cell}	0.7	984.5 A * 125 mA/cm ²
corresponding to fuel utilisation	70.0 %	

All plots are oriented in the same way as indicated in Figure 4.2. The results are obtained using a 12x12 spatial discretisation.

Figure 4.2 to 4.5 show the important states within the anode gas phase. The mole fraction of methane is plotted in Figure 4.2. The high reaction rate of the steam reforming reaction determines the profile near the inlet: Methane is consumed and its mole fraction is decreased quickly. In the rear section of the channel, as the gas approaches equilibrium

composition, the methane concentration is governed by the anode gas temperature and the hydrogen consumption of the oxidation reaction. The mole fraction of methane at the anode outlet is at a few percent.

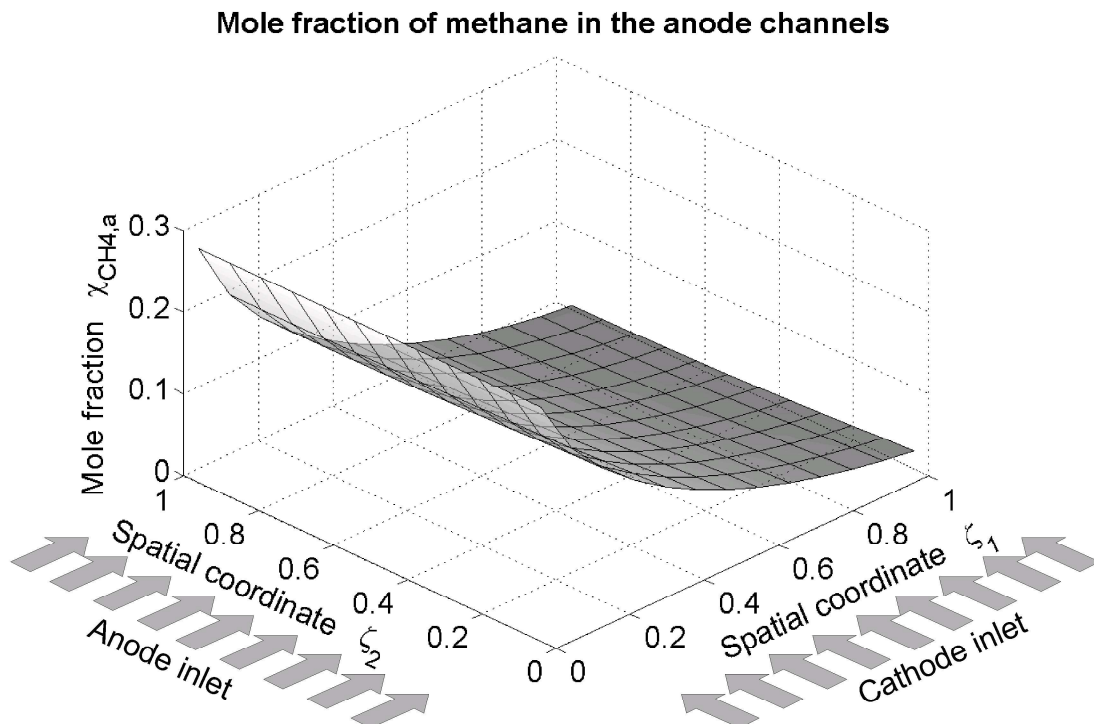


Figure 4.2: Steady state mole fraction of methane in the anode channels at base case conditions (see Table 4.1). For further parameter values see Appendix A.6.

The consumption of methane comes with a production of hydrogen, as can be seen from Figure 4.3. With no hydrogen in the inlet gas, it is quickly produced by the reforming reactions in the channel. Simultaneously, hydrogen is consumed by the anodic oxidation reaction, so when the reforming reaction slows down in the middle and rear part of the channel, the hydrogen concentration is decreased again. Thus it has a maximum value within the first half of the anode channel. Here the hydrogen oxidation reaction is promoted best. Obviously the hydrogen profiles are not identical for every anode channel. One reason for this is the spatially distributed current density. On the other hand, the different temperature profiles in each channel give rise to different reforming equilibrium constants, which influence the hydrogen concentration.

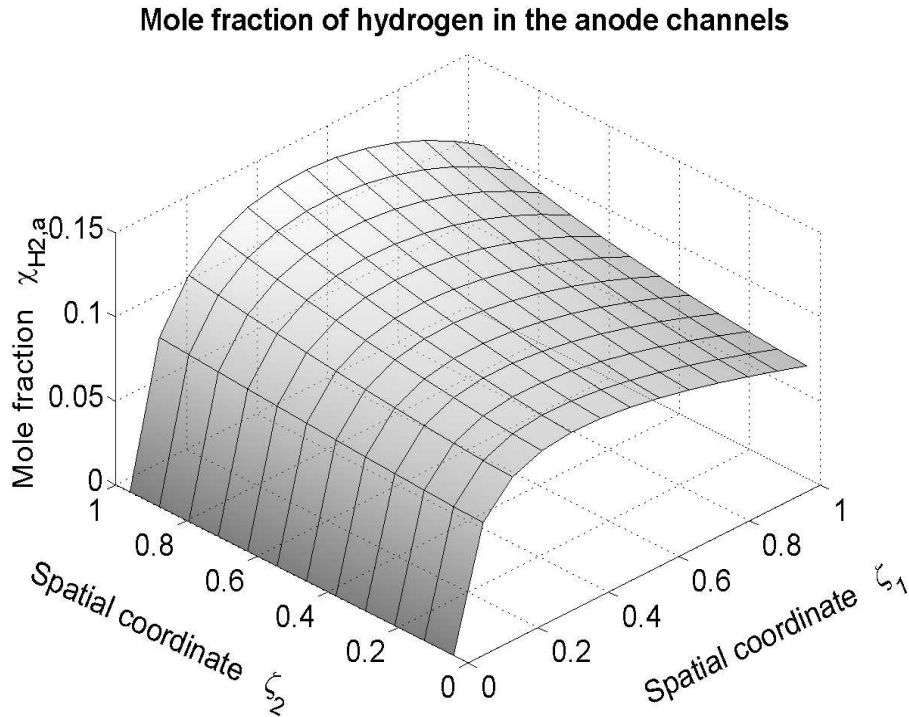


Figure 4.3: Steady state mole fraction of hydrogen in the anode channels at base case conditions (see Table 4.1). For further parameter values see Appendix A.6.

Due to the very fast endothermic reforming reaction at the anode inlet, the anode gas temperature drops down considerably. Figure 4.4 shows a temperature drop of approximately 0.25 corresponding to about 75°C. The decreased temperature moves the equilibrium constant of the steam reforming reaction towards the educts, so that the reaction rate is slowed down not only due to the Arrhenius effect, but also because the equilibrium is shifted towards the actual gas composition. In the middle and rear parts of the channel the gas is heated up again by hot oxidation products emerging from the electrode and due to heat exchange with the hot solid parts. The minimum of the anode gas temperature close to the anode inlet is expected to have a strong impact on the solid temperature distribution.

Since all reactions within the anode channel lead to a change in total mole number, the molar flow density is steadily increasing along the anode channel. Figure 4.5 shows that the molar flow at the anode outlet is more than 2.5 times higher than at the inlet. Although some concentrations and the gas temperature are rather inhomogeneous at the anode outlet, the molar flow density is relatively constant over ζ_2 . The inhomogeneity of the anode gas outlet may give rise to problems like hot and cold spots in the following catalytic combustion chamber, a fact that is not considered in this model.

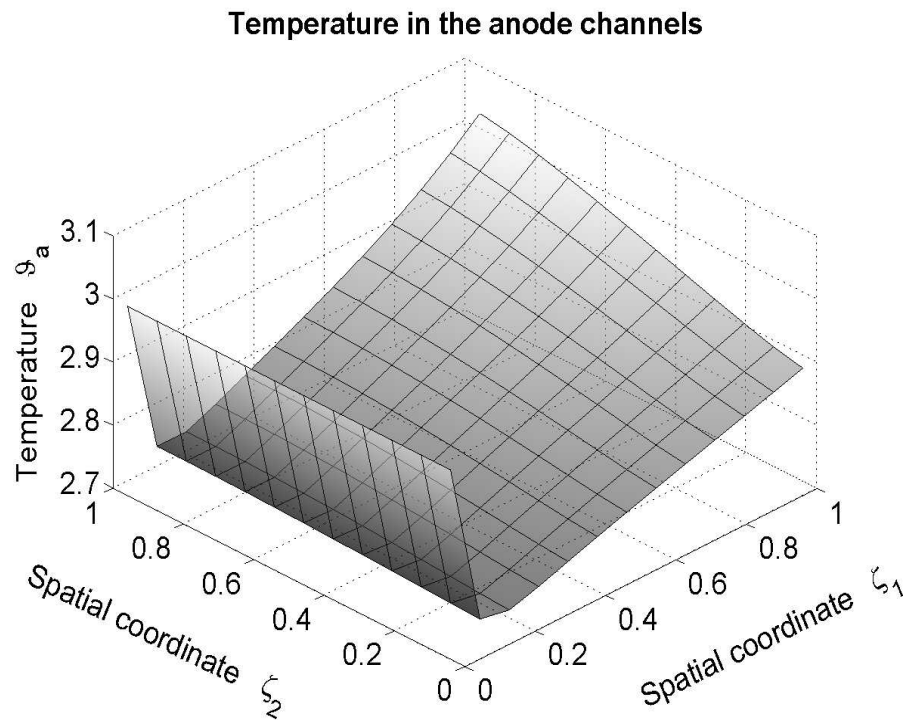


Figure 4.4: Steady state gas temperature in the anode channels at base case conditions (see Table 4.1). For further parameter values see Appendix A.6.

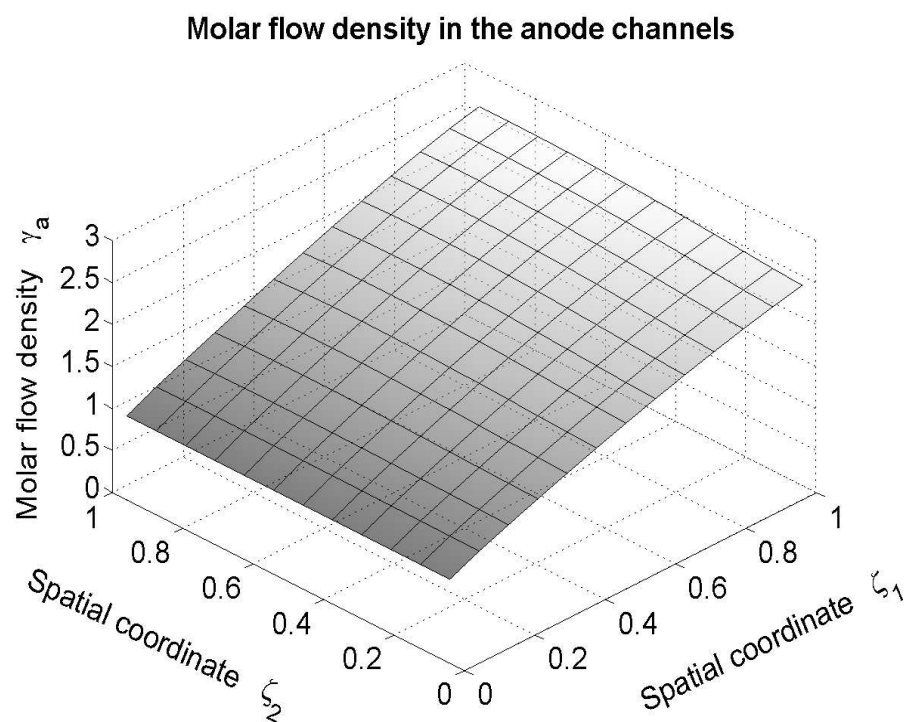


Figure 4.5: Steady state molar flow density through the anode channels at base case conditions (see Table 4.1). For further parameter values see Appendix A.6.

The important states in the cathode gas phase are plotted in figures 4.6 to 4.9. The first two plots show the mole fractions of carbon dioxide and oxygen. Both enter the cathode with relatively high concentrations and are then consumed by the electrochemical reduction reaction, so that their mole fractions are reduced along the cathode channels. Note that the oxygen consumption is only half that of the carbon dioxide consumption due to stoichiometry, so that the oxygen profile is flatter. It can be concluded that oxygen promotes the reduction reaction almost homogeneously over the whole cell area. Due to the negative reaction order of the reduction reaction with respect to carbon dioxide, this species may give rise to a higher current density near the cathode outlet.

Mole fraction of carbon dioxide in the cathode channels

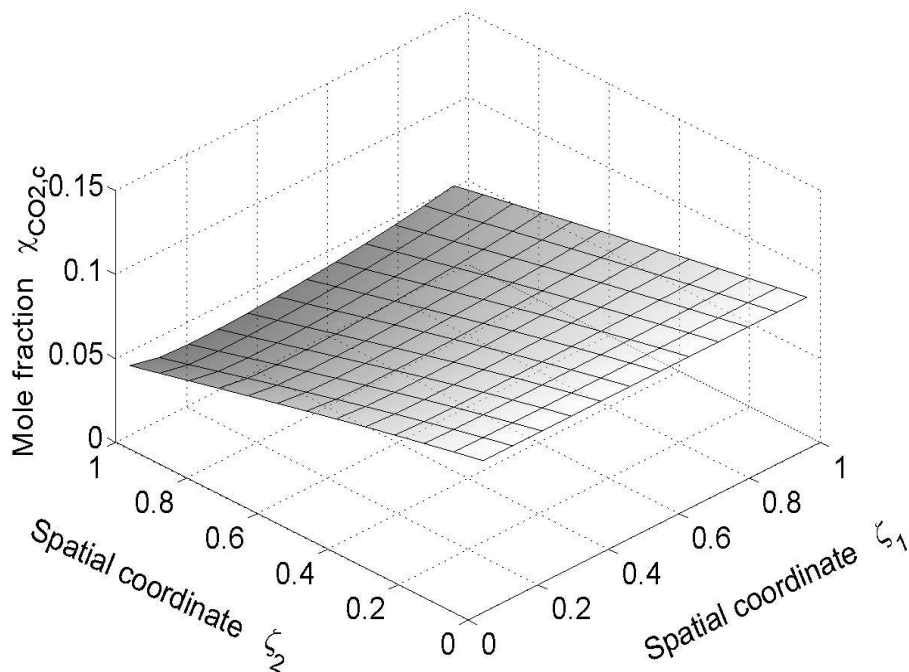


Figure 4.6: Steady state mole fraction of carbon dioxide in the cathode channels at base case conditions (see Table 4.1). For further parameter values see Appendix A.6.

Figure 4.8 shows the temperature profile of the cathode gas. At entering the cell, the gas from the burner is colder than the solid compartments. This is due to the large amounts of cold air that are required for the complete combustion in the catalytic burner. Flowing along the cathode channels, the temperature is increased by the heat transfer from the solid cell parts. The comparison of the cathode temperature with the solid temperature in Figure 4.12 shows that the cathode gas acts as a cooling agent in this load case.

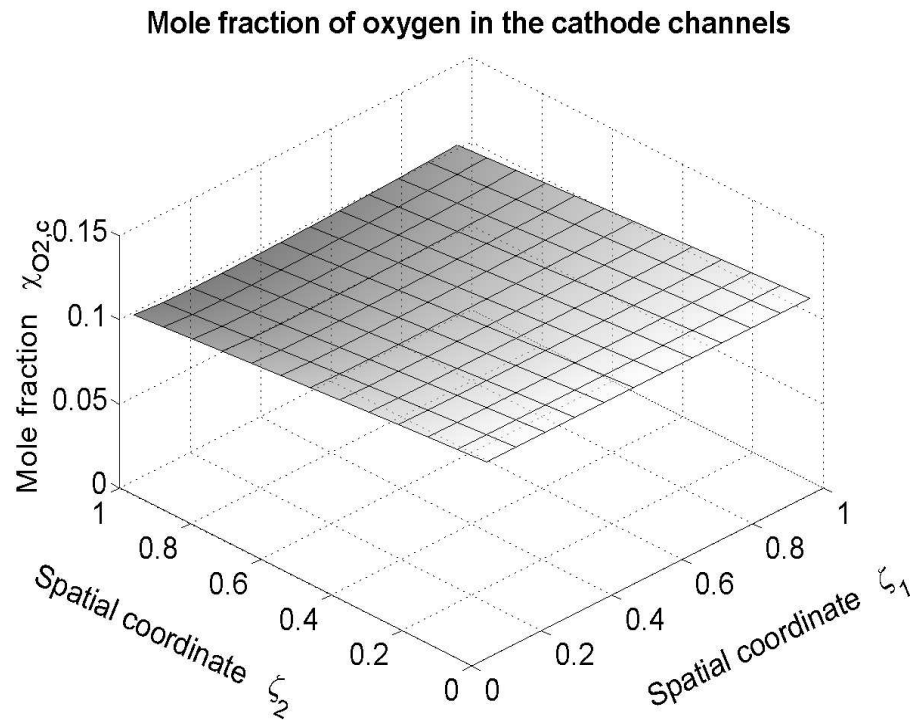


Figure 4.7: Steady state mole fraction of oxygen in the cathode channels at base case conditions (see Table 4.1). For further parameter values see Appendix A.6.

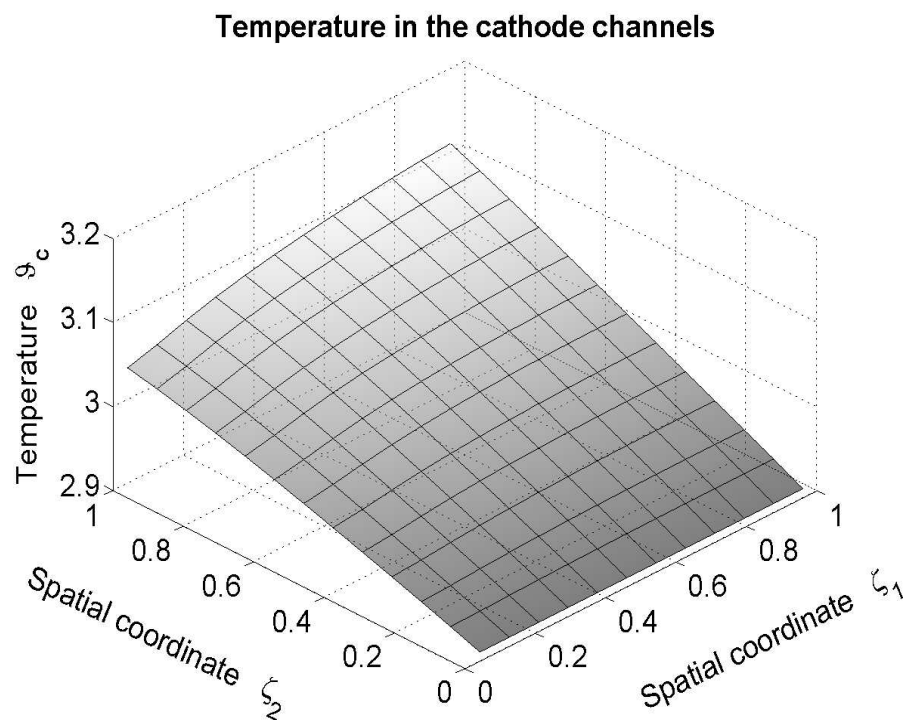


Figure 4.8: Steady state gas temperature in the cathode channels at base case conditions (see Table 4.1). For further parameter values see Appendix A.6.

The molar flow density in the cathode channels can be seen in Figure 4.9. With values of about 15 this is much larger than on the anode side, where values between 1 and 2 are typical. This is due to the large amount of air, mostly inert nitrogen, which are fed into the combustion chamber and because of the cathode recycle, which doubles the molar flow density in the cathode channels. This high flow rate requires relatively high pressure differences and therefore it is the main reason for the high power consumption of the recycle blowers of this system.

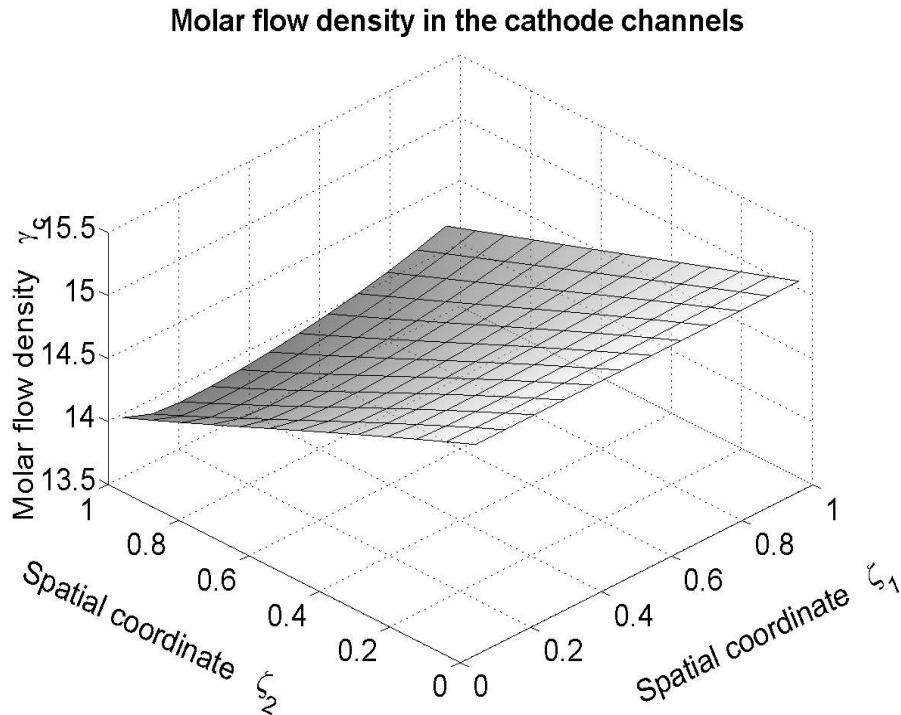


Figure 4.9: Steady state molar flow density through the cathode channels at base case conditions (see Table 4.1). For further parameter values see Appendix A.6.

Within the solid phase, the most interesting states are the temperature and the current density. Furthermore, the cell voltage is of major importance. The temperature within the solid parts of the cell is plotted in Figure 4.11. Heat is produced over the whole cell area mainly by electrochemical and ohmic losses. The heat is then transported along the spatial coordinates by two mechanisms: Heat conduction within the solid parts and convection by the anode and cathode gas. Here, the convective transport is dominant and thus the heat is transported towards the outlet/outlet corner of the anode and cathode channels. This is where the maximum temperature in the solid phase occurs. The minimum and maximum temperatures are listed in Table 4.2 together with some additional simulation results.

The current density distribution is plotted in Figure 4.12. Its maximum is located near the middle anode channel closely by its inlet. Here the hydrogen concentration is highest, so that the oxidation reaction is promoted best. The additional effects of solid temperature and carbon dioxide concentration in the cathode channel seem to be of lower importance. They

cause the maximum to be situated in the middle channel. The range of current density is from $I_{cell}=0.57$ to 0.78 .

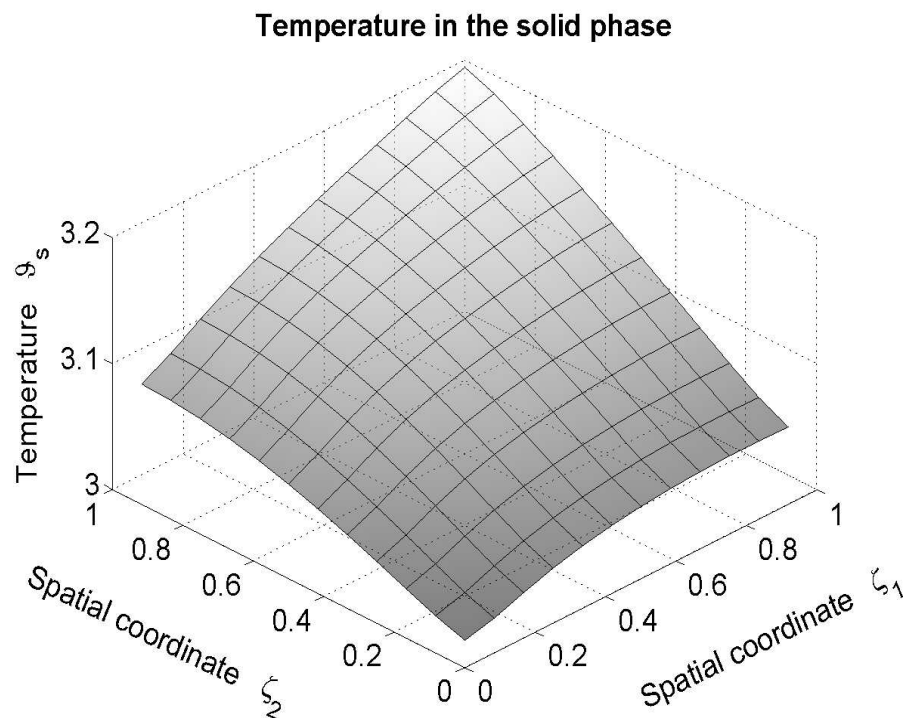


Figure 4.10: Steady state solid temperature at base case conditions (see Table 4.1). For further parameter values see Appendix A.6.

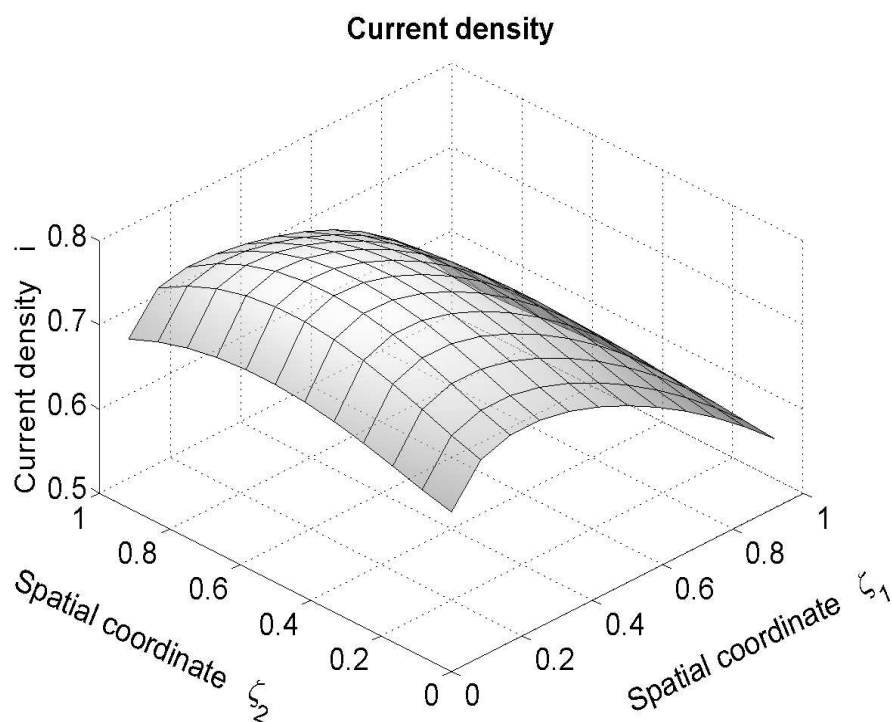


Figure 4.11: Steady state current density distribution at base case conditions (see Table 4.1). For further parameter values see Appendix A.6.

Table 4.2: Steady state simulation results at base case conditions (Table 4.1). Dimensional quantities are calculated for the single cells of the HotModule.

	Dim.-less	Dimensional (HotModule)
Cell voltage	29.80	0.766 V
Cell power	47.68	0.754 kW per cell
Blower power	1.52	0.072 kW per cell
Electric efficiency	49.89 %	49.89 %
Minimum solid temperature	3.01	624 °C
Maximum solid temperature	3.21	684 °C
Maximum temp. difference	0.20	60 °C

Isothermal 2D model

To separate the influence of solid temperature and mole fractions in the gas phase on the current density, a modified 2D model is applied. Here, the solid phase is modeled isothermally, substituting its enthalpy balance (Table 2.2, Equation 23) by the algebraic equation

$$\vartheta_s(\zeta, \tau) = 3.0 \quad (4.1)$$

With this, the steady profiles of the states of both gas phases look qualitatively similar to those presented in figures 4.2 to 4.9. The current density for the isothermal model version is shown in Figure 4.12.

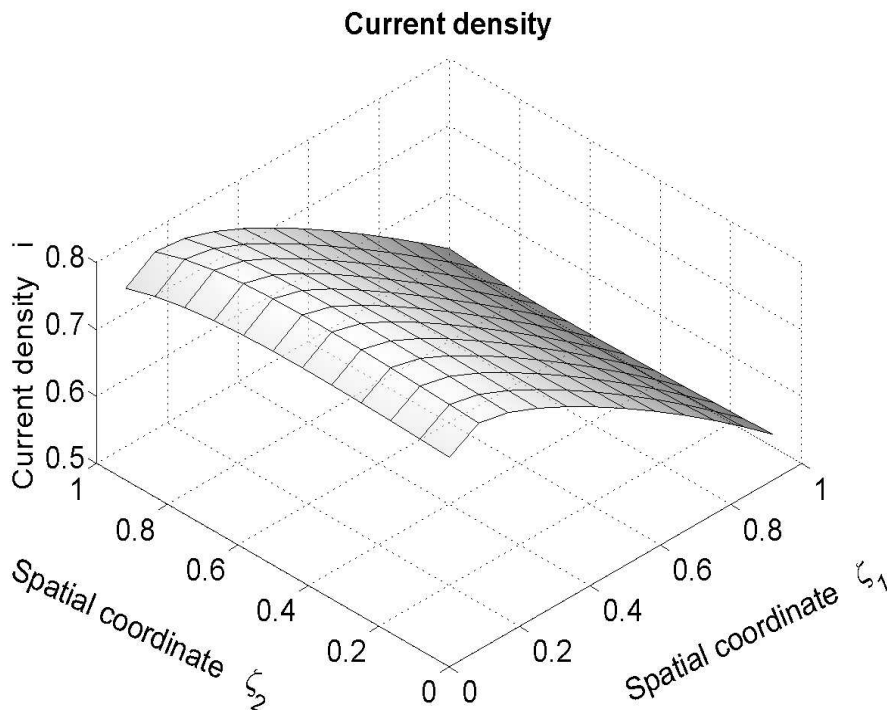


Figure 4.12: Steady state current density distribution at base case conditions from the 2D model with isothermal solid phase (see Table 4.1). For further parameter values see Appendix A.6.

Without the influence of the solid temperature, the current density distribution is obviously determined by the distribution of hydrogen in the anode channel. The concentrations of oxygen and carbon dioxide on the cathode side either have a minor effect, or their effects compensate each other. By comparing the current density distributions of the isothermal and the non-isothermal model, one can conclude that the solid temperature distribution has a significant quantitative influence on the current density distribution, but it does not dominate its shape qualitatively.

Another very important diagram for the characterisation of fuel cells is the current-voltage curve (U-I-curve). With non-isothermal models like the one used here, several different U-I curves are computable:

- I_{cell} is varied and all other input quantities, especially fuel and air flow, are adopted to the electric load in order to fulfill some temperature restrictions or some optimisation criterion. The result of this calculation depends on too many parameters to allow for a simple interpretation and requires very high computational effort. Nevertheless, as this curve shows the various possible operating points of the cell, it is quite interesting.
- I_{cell} is varied and all other input quantities, especially fuel and air flow rate, are kept constant. The enthalpy balances are fully taken into account. While this curve is easy to compute, it leads to unrealistic results, especially regarding temperature, for unrealistic load conditions.
- I_{cell} is varied while all other input quantities, especially fuel and air flow, are kept constant. The solid temperature is set to a constant value, while enthalpy balances in anode and cathode gas channel are fully taken into account. This corresponds to an experimental measurement of the U-I curve in an oven where the cell temperature is controlled.

The last type of U-I curve is most suitable to be compared to experimental data and is thus presented here. Again, the same modified 2D model as before is applied with an isothermal solid phase: $\vartheta_s=3.0$. All input parameters correspond to the base case (i.e. unreformed anode gas at inlet, $\lambda_{air}=2.5$) and the total cell current is varied from $I_{cell}=0$ to a value close to the limit current. Figure 4.13 shows an open-circuit voltage of $U_{cell,i=0}=37.7$ and an almost linear decrease of the curve afterwards. The kinetically controlled nonlinear part of the curve is not very pronounced. The total cell current is limited by the reforming reaction to $I_{cell}\approx 0.77$.

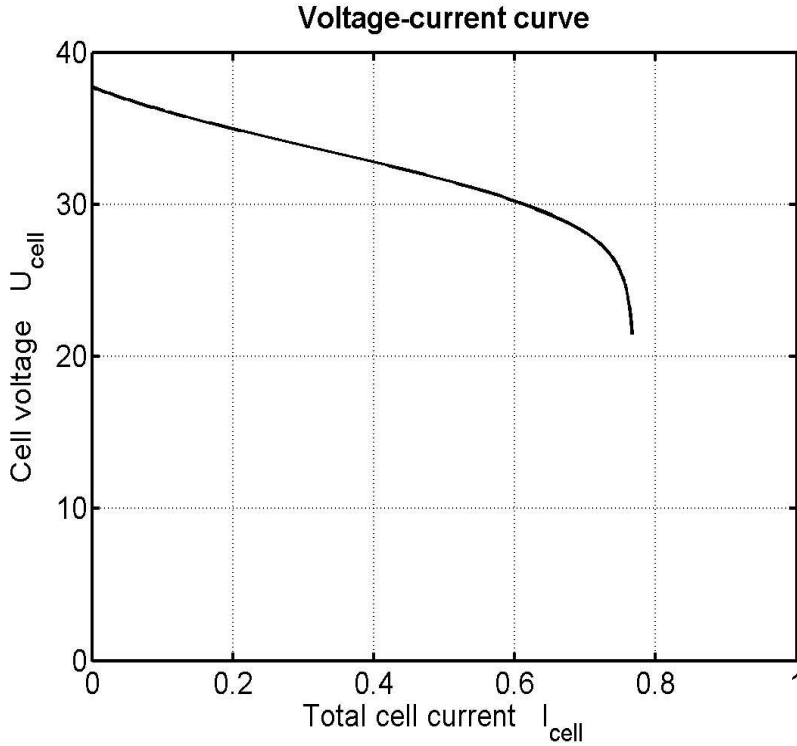


Figure 4.13: Current-voltage curve at base case conditions (see Table 4.1) from the 2D model with isothermal solid phase. The solid temperature is arbitrarily set to $\vartheta_s(\tau, \zeta)=3.0$. For further parameter values see Appendix A.6.

This steady state result can be used to validate the steady state anode model. To do this it is necessary to transform the anode mole fractions obtained from the 2D simulation into reaction extents. First, the states in all anode channels are averaged by:

$$\bar{y}_a(\zeta_1) = \int_0^1 y_a(\zeta_1, \zeta_2) d\zeta_2 \quad (4.2)$$

$$\bar{\chi}_{i,a}(\zeta_1) = \frac{\int_0^1 y_a(\zeta_1, \zeta_2) \cdot \chi_{i,a}(\zeta_1, \zeta_2) d\zeta_2}{\bar{y}_a(\zeta_1)} \quad (4.3)$$

$$\bar{\vartheta}_a(\zeta_1) = \frac{\int_0^1 y_a(\zeta_1, \zeta_2) \cdot \vartheta_a(\zeta_1, \zeta_2) d\zeta_2}{\bar{y}_a(\zeta_1)} \quad (4.4)$$

To compute the extents of reaction for the reforming and oxidation reactions, the averaged molar flows of each component are required:

$$\bar{y}_{i,a} = \bar{y}_a \cdot \bar{\chi}_{i,a} = \int_0^1 y_a(\zeta_1, \zeta_2) \cdot \chi_{i,a}(\zeta_1, \zeta_2) d\zeta_2 \quad (4.5)$$

Now, in principle, the extents of reactions could be computed from the molar flows using the interrelation between the mole fractions and the extents of reactions in Equation 2.156. Unfortunately, the matrix of stoichiometric coefficients for the reforming and oxidation reactions used in the reduced model are of rank 3: the water-gas shift reaction plus the

hydrogen oxidation are equivalent to the carbon monoxide oxidation, they are linearly dependent. The rank of the stoichiometric matrix is lower than the number of unknown extents of reactions, which is 4, one for each reaction. Thus not all of them can be calculated from the gas composition. Nevertheless, it is possible to calculate the extents of the overall reforming and overall oxidation reaction, which are defined according to

$$\xi_{ref} \cdot \xi_{ref,max} = \xi_{ref1} \cdot \xi_{ref1,max} + 0 \cdot \xi_{ref2} \cdot \xi_{ref2,max} \quad (4.6)$$

$$\xi_{ox} \cdot \xi_{ox,max} = \xi_{ox1} \cdot \xi_{ox1,max} + \xi_{ox2} \cdot \xi_{ox2,max} \quad (4.7)$$

The second reforming reaction, the water-gas shift reaction, does not increase the overall reforming yield, as it simply transforms one oxidation educt (carbon monoxide) into another one (hydrogen). If the oxidation reaction of carbon monoxide were not considered here, Equation 4.6 would be different. If carbon monoxide oxidation occurs, the extent of hydrogen oxidation can no longer reach unity, but the combination of both in Equation 4.7 is still unity for complete oxidation.

Now, starting from equations 2.156 and 2.161 with the definition of the total extent of the reforming and oxidation reactions from equations 4.6 and 4.7 one receives after some manipulation

$$\xi_{ref} \cdot \xi_{ref,max} = X_{CH_4,feed} - \frac{\bar{Y}_{CH_4,a}}{Y_{feed}} \quad (4.8)$$

$$\xi_{ox} \cdot \xi_{ox,max} = \frac{\bar{Y}_{CO,a} + \bar{Y}_{CO_2,a} + \bar{Y}_{CH_4,a}}{Y_{feed}} - X_{CH_4,feed} \quad (4.9)$$

The extents of reaction are normalised by

$$\xi_{ref,max} = \xi_{ref1,max} = \xi_{ref2,max} = \xi_{ox2,max} = \frac{1}{1+S/C} \quad (4.10)$$

$$\xi_{ox,max} = \xi_{ox1,max} = \frac{4}{1+S/C} \quad (4.11)$$

With Equations 4.8 and 4.9 it is possible to calculate the extents of the overall reforming and oxidation reaction from the averaged simulation results of the 2D model. These are plotted in a conversion diagram adopted from Chapter 3 in Figure 4.14. For one, the anode exhaust conditions are plotted here under varying total cell current. Three exemplary trajectories at certain cell currents are added. All results from the 2D model are plotted as solid lines.

These data are compared with results obtained from the steady state anode model with its anode enthalpy extension in Figure 4.14. In both models, the same inlet conditions, the same voltage and identical parameter sets are used. The full lines are the recalculated trajectories from the averaged results of the 2D model. The trajectories plotted in dashed lines come from the steady state anode model.

The figure shows very good agreement between the steady state results of the simplified 2D model and the extended steady state anode model. It confirms the validity of the steady state anode model and the results obtained from it in Chapter 3. It also indicates that the

spatial discretisation of the 2D model (a 12x12 volume grid is used here) yields a good approximation compared to the much finer discretisation of the steady state anode model. The simulated anode gas temperatures for both cases are plotted in Figure 4.15 for $U_{cell} = 32.75$ corresponding to $I_{cell} = 0.4$ in the 2D model. While the temperatures are quite identical in the middle and the exhaust part of the anode channel, they are somewhat different in the anode inlet region due to the curvature there. This could be amended by a refinement of the spatial discretisation, if computation time would allow that. On the other hand it turns out that further refinement of the mesh leads to a significant increase of computation times, so it was not done here.

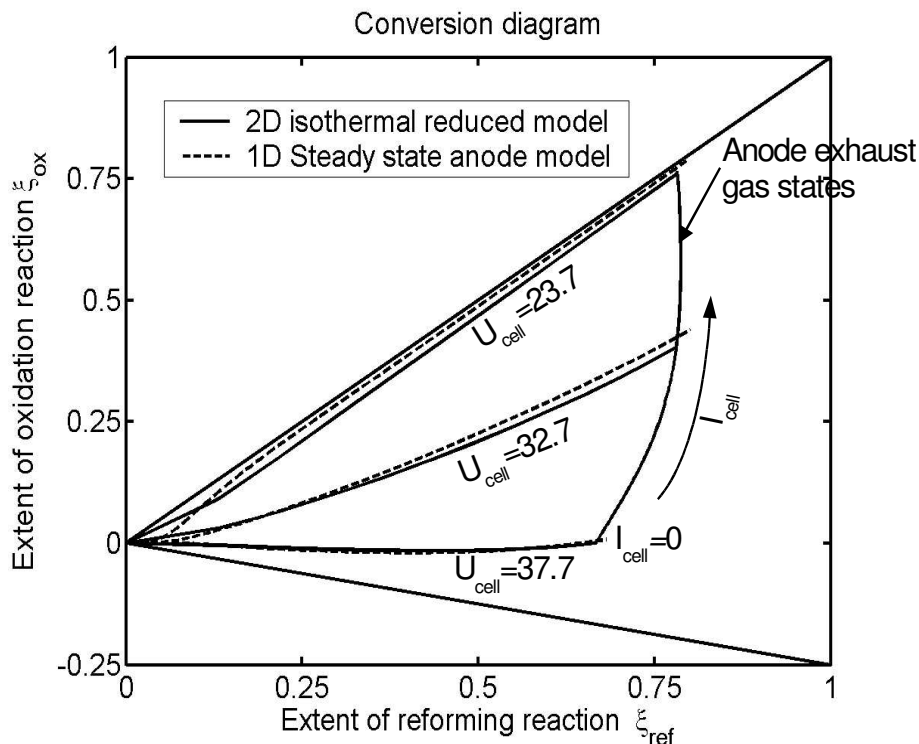


Figure 4.14: Comparison of the results obtained from the 2D model with isothermal solid phase at steady state and the results from the steady state anode model using the conversion diagram (cf. Chapter 3). Three trajectories are calculated for both models under identical inlet conditions and cell voltages.

With this, the demonstration of the steady state simulation results of the physically simplified 2D model is complete. The calculated spatial distributions of various states is shown to be physically reasonable. A current voltage curve is presented for the 2D model with isothermal solid phase which is in good agreement with the results obtained from an extended steady state anode model. The spatial discretisation applied in the numerical solution of the 2D model could be optimised in the anode inlet region, but overall it is a reasonable compromise between computation time and numerical precision.

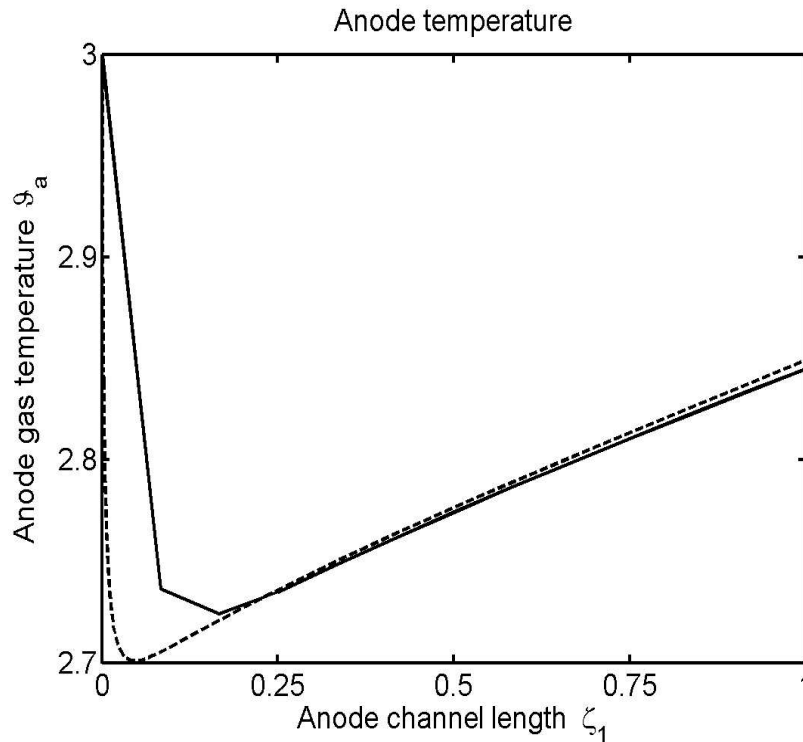


Figure 4.15: Comparison of the steady state anode gas temperature simulated by the isothermal 2D model and the simplified steady state anode model. Both profiles are at $U_{cell} = 32.75$, corresponding to $I_{cell} = 0.4$ in the 2D model.

4.3 Transient cell behaviour at load change

The physically reduced model is a dynamic one, so simulations of the transient behaviour can be performed with it. As an example, the results of a load change simulation are shown, starting from steady state under base case conditions (see Table 4.1). All input quantities are kept constant, except the total cell current is increased from $I_{cell}=0.7$ to $I_{cell}=0.85$ following a step function at the dimensionless time $\tau_{step}=0.1$. The equations are then integrated until $\tau_{end}=0.4$. For a system like the HotModule, the integration time corresponds to the first 3.6 seconds after the load change (cf. Equation 2.133), so the short-time behaviour can be observed.

The stepwise increase in current density means an increased demand for oxidation educts, i.e. hydrogen and carbon monoxide. This leads to a decrease in the mole fractions of both species, as can be seen in Figures 4.16 and 4.17. The steam reforming reaction can do little to sustain the mole fractions of the oxidation educts, because the methane concentration is already quite low at the initial condition. Figure 4.18 shows an almost constant methane concentration profile which shows that the steam reforming reaction is not promoted shortly after the load change. The carbon dioxide concentration is raised due to the increased oxidation rates (Figure 4.19).

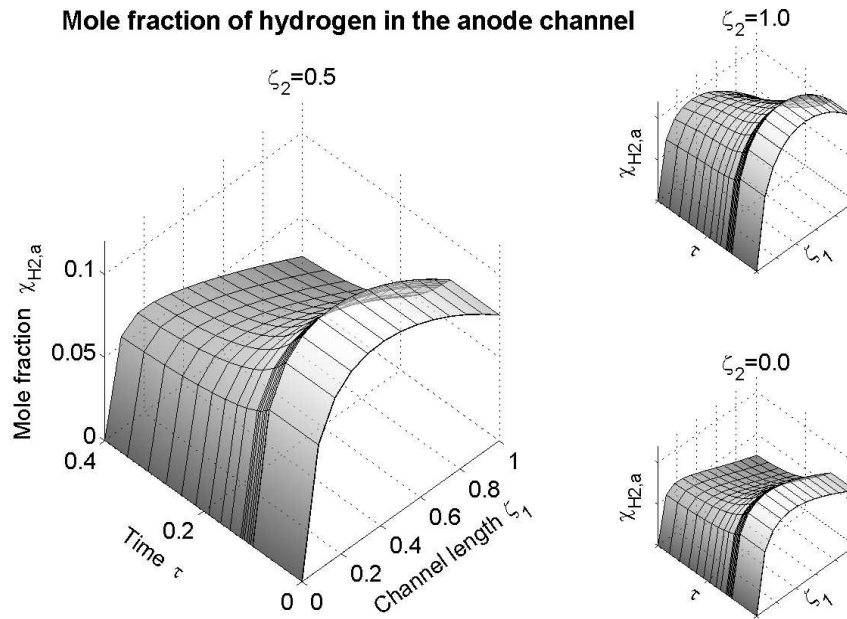


Figure 4.16: Mole fraction of hydrogen in different anode channels during a stepwise load change from $I_{cell} = 0.7$ to $I_{cell} = 0.85$. Concentration profiles within three representative channels are shown.

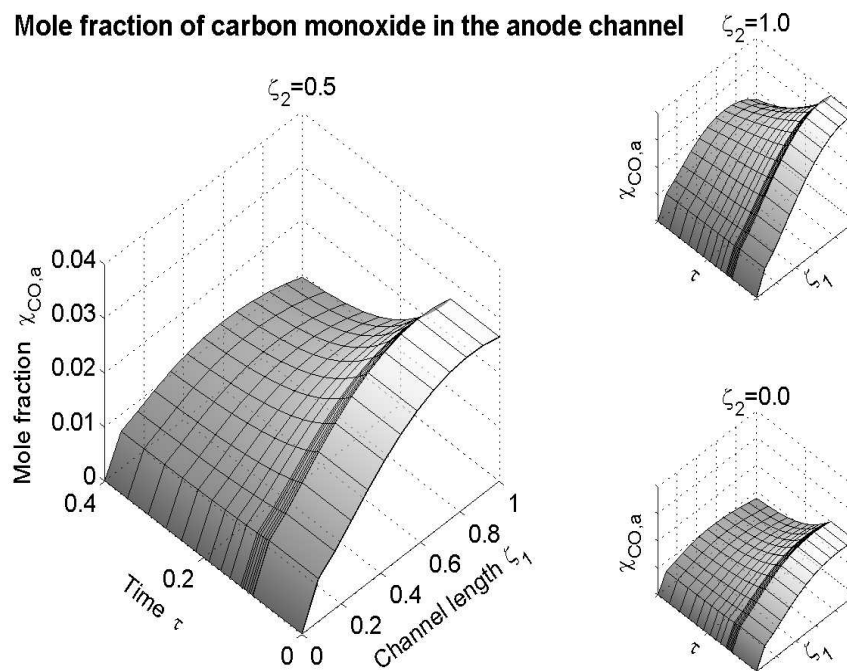


Figure 4.17: Mole fraction of carbon monoxide in different anode channels during a stepwise load change from $I_{cell} = 0.7$ to $I_{cell} = 0.85$. Concentration profiles within three representative channels are shown.

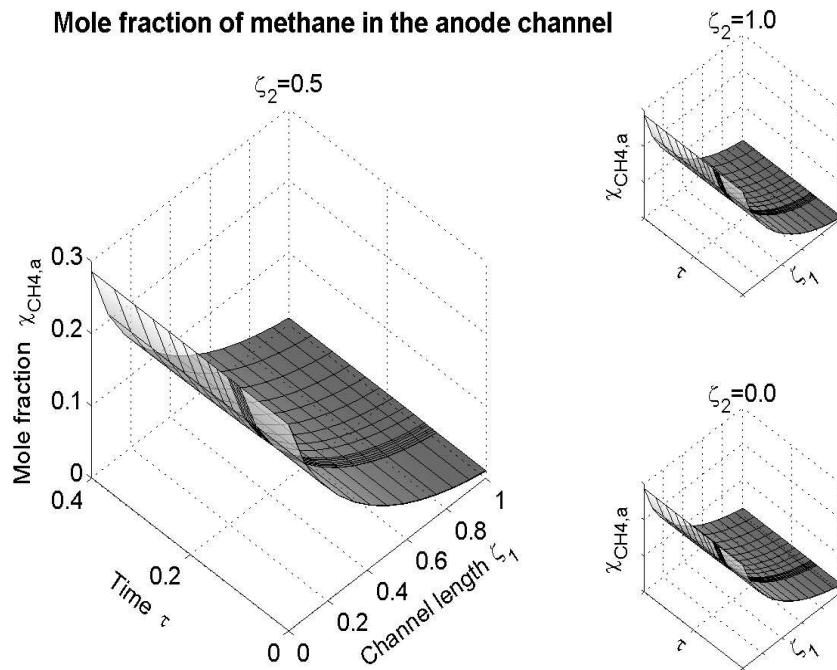


Figure 4.18: Mole fraction of methane in different anode channels during a stepwise load change from $I_{\text{cell}}=0.7$ to $I_{\text{cell}}=0.85$. Concentration profiles within three representative channels are shown.

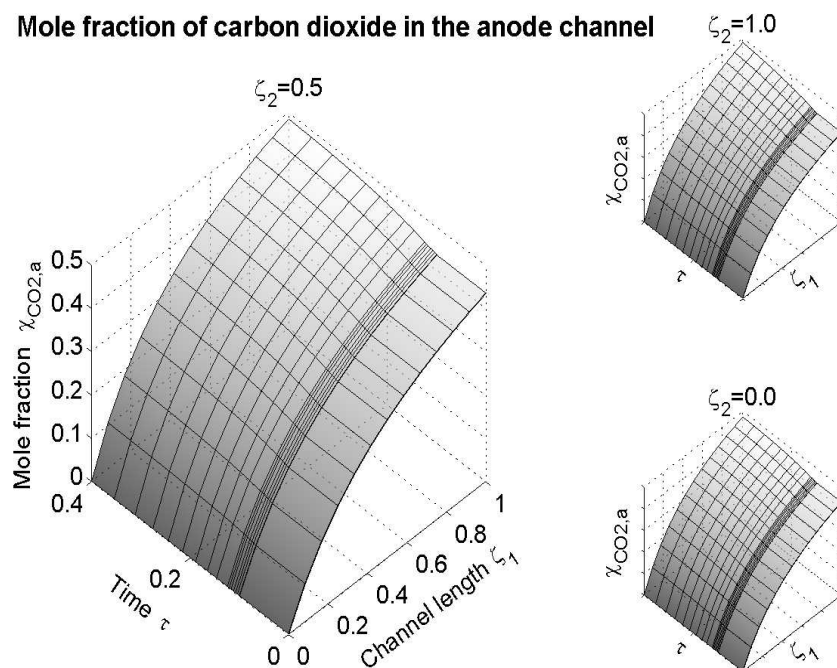


Figure 4.19: Mole fraction of carbon dioxide in different anode channels during a stepwise load change from $I_{\text{cell}}=0.7$ to $I_{\text{cell}}=0.85$. Concentration profiles within three representative channels are shown.

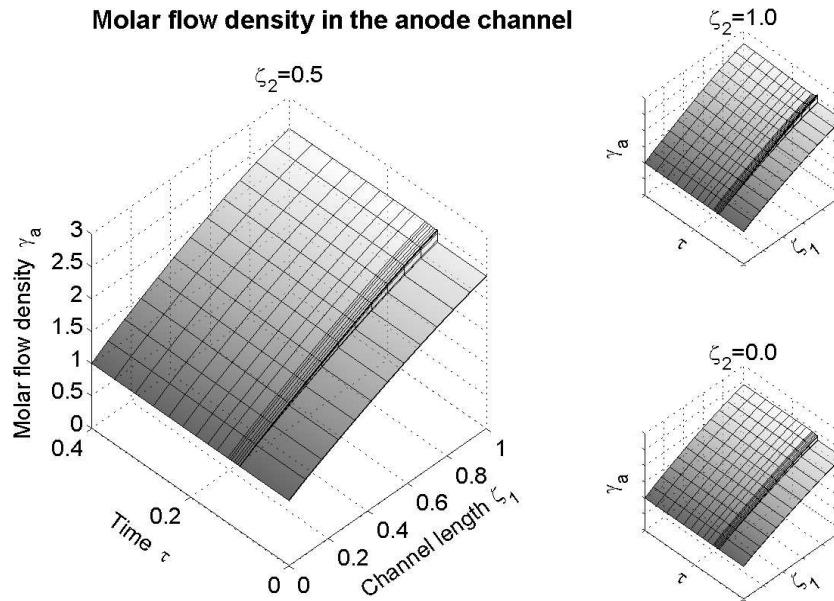


Figure 4.20: Molar flow rate in different anode channels during a stepwise load change from $I_{cell}=0.7$ to $I_{cell}=0.85$. Flow rate profiles within three representative channels are shown.

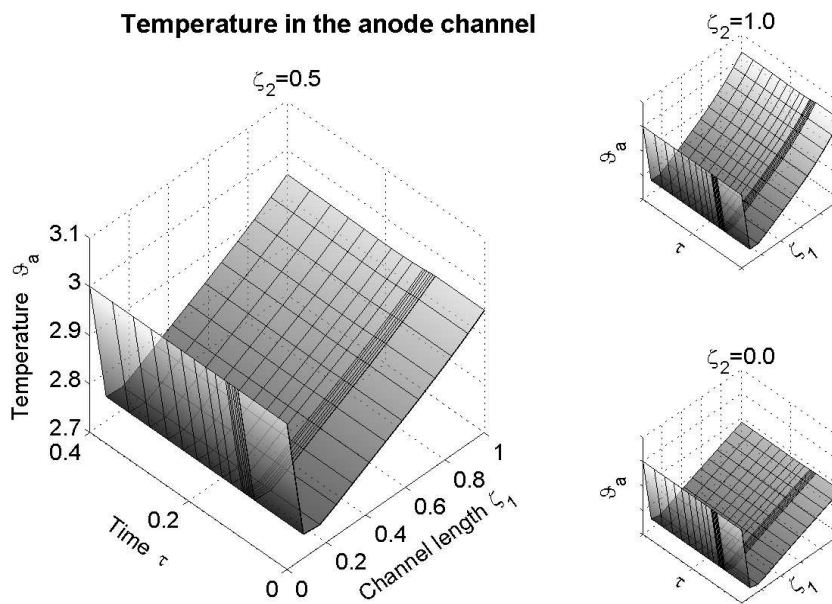


Figure 4.21: Gas temperature in different anode channels during a stepwise load change from $I_{cell}=0.7$ to $I_{cell}=0.85$. Temperature profiles within three representative channels are shown.

Because both oxidation reactions come with a net mole number increase of gas phase species, the anode molar flow rate is increased instantaneously, as can be seen in Figure 4.20.

The anode gas temperature profile (Figure 4.21) is determined on the one hand by the endothermic steam reforming reaction, and on the other hand by the heat exchange between the solid and the gas phase. With the almost constant steam reforming rate, only heat exchange phenomena remain as for reasons to changes in the anode temperature. The increased mass flow out of the anode electrode promotes the heat exchange, while the decreased residence time diminishes it. Both effects together lead to an almost constant anode gas temperature profile.

On the cathode side, the increased current density leads to an increased consumption rate of oxygen and carbon dioxide, as can be seen in Figures 4.22 and 4.23. The result is a decrease of the mole fractions of both components along the whole channel. The increased anode exhaust flow rate (cf. Figure 4.20) supplies the burner with a larger amount of carbon which, in the form of carbon dioxide, is fed into the cathode channel. This effect raises the carbon dioxide concentration in the cathode inlet and overcompensates for the increased consumption rate there. Thus the concentration rises at one end of the channel, while it decreases at the other end, which from a system theoretic point of view is an interesting behaviour. Note that the cathode reflux adds cathode exhaust gas to the inlet and therefore reduces this effect. After some time, the mole fraction of carbon dioxide starts to increase again. This happens when the anode exhaust gas, now oxidised at a higher degree by the increased oxidation rate, reaches the cathode inlet.

The oxygen concentration of the cathode feed is diminished at first. The anode exhaust gas, which is fed into the burner, has a higher flow rate, but its degree of oxidation is still low. Thus the oxygen demand in the burner is high and this causes the low oxygen content in the cathode feed (Figure 4.23). Without the compensation due to the cathode recycle this effect can be expected to be even stronger. At the new steady state the oxygen concentration at the cathode inlet is higher than before.

Note that the cathode outlet concentrations of all species at steady state are independent of the cell current. This is because the anode feed is always completely oxidised within the fuel cell, either electrochemically or in the catalytic burner, and the product stream always has the same composition at steady state.

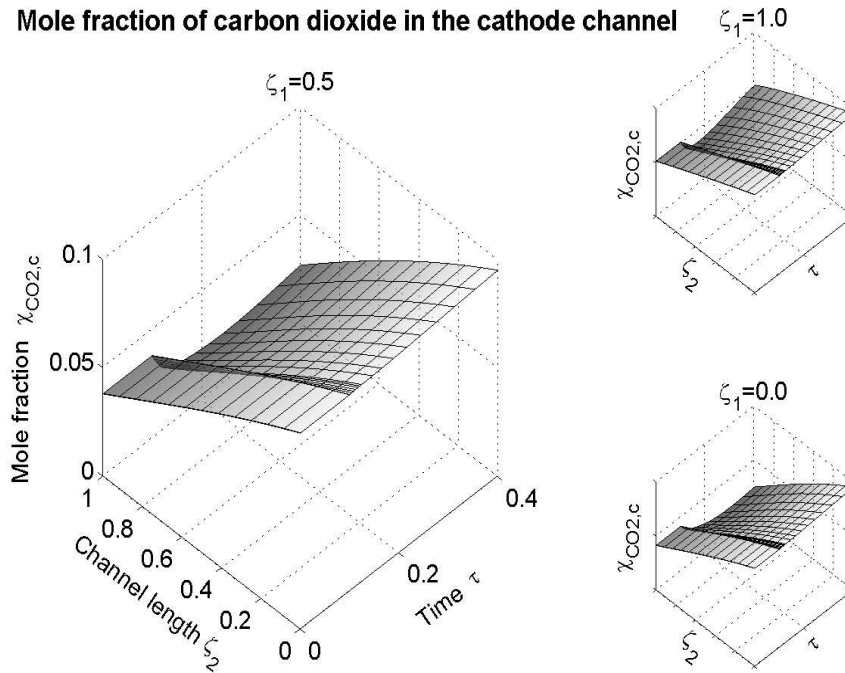


Figure 4.22: Mole fraction of carbon dioxide in different cathode channels during a stepwise load change from $I_{cell}=0.7$ to $I_{cell}=0.85$. Concentration profiles within three representative channels are shown.

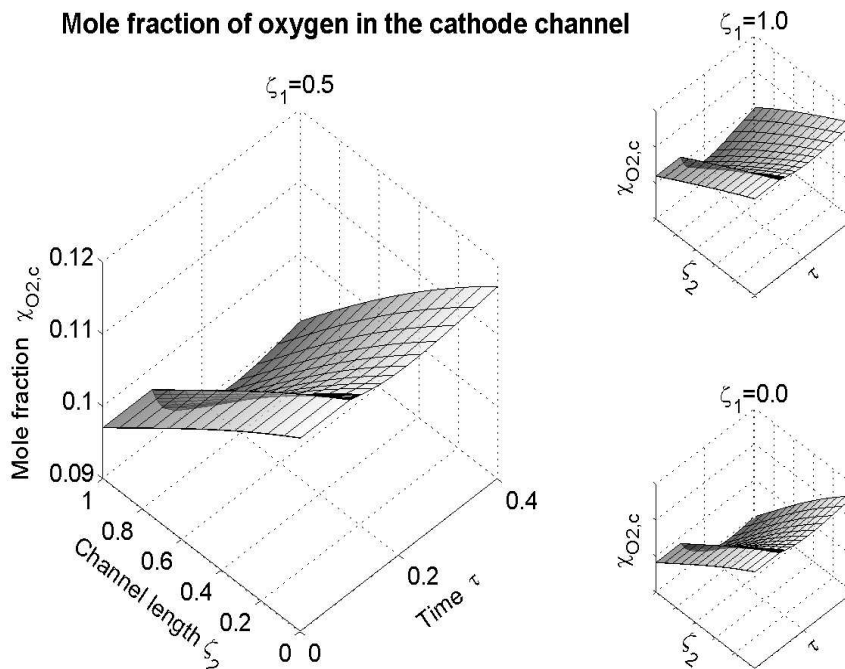


Figure 4.23: Mole fraction of oxygen in different cathode channels during a stepwise load change from $I_{cell}=0.7$ to $I_{cell}=0.85$. Concentration profiles within three representative channels are shown.

With the higher feed flow from the anode exhaust and with constant air flow, the burner exhaust temperature is increased at first, leading to an increased cathode gas temperature at the inlet. Shortly after that, the burner feed gas is oxidised to a higher degree by the anode electrochemical oxidation reactions, so less oxidation occurs within the catalytic burner. Thus, the burner exhaust temperature is decreased and the cathode gas temperature follows (Figure 4.24).

Another interesting state is the current density distribution. It increases instantaneously at the load change and afterwards follows the mole fractions in the gas phases according to the electrochemical reaction kinetics (Figure 4.25).

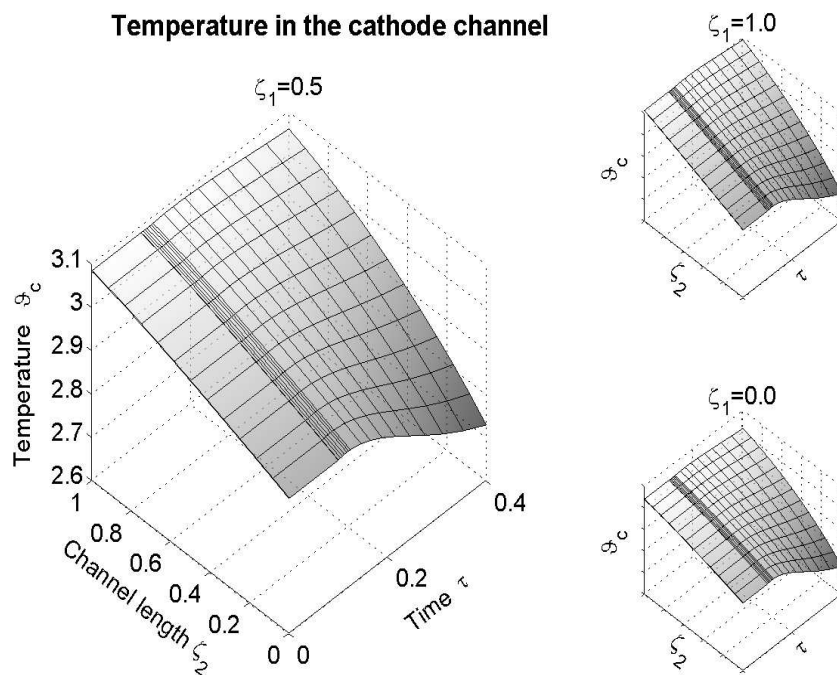


Figure 4.24: Gas temperature in different cathode channels during a stepwise load change from $I_{cell}=0.7$ to $I_{cell}=0.85$. Temperature profiles within three representative channels are shown.

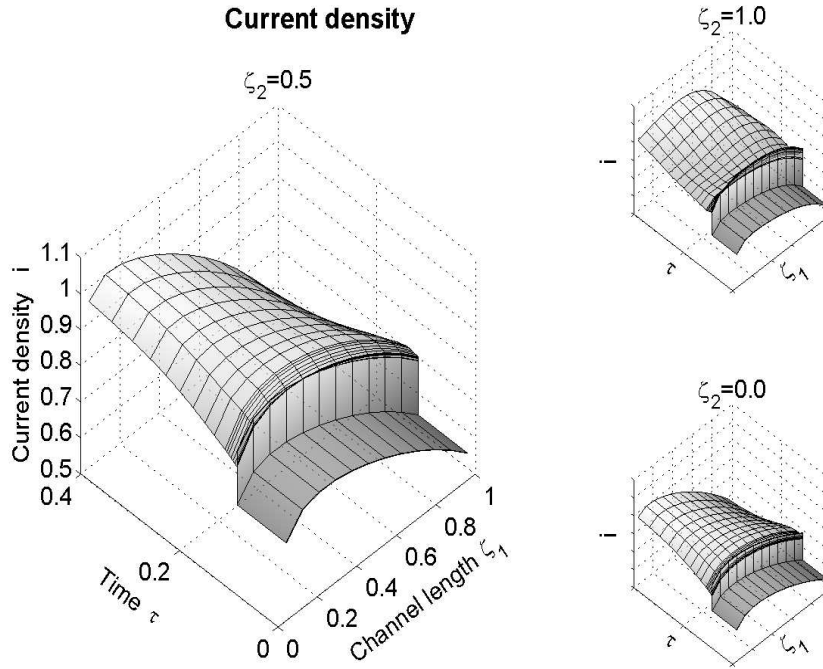


Figure 4.25: Current density during a stepwise load change from $I_{cell}=0.7$ to $I_{cell}=0.85$. Current density profiles along three representative anode channels are shown.

Finally, the cell voltage behaviour shall be discussed. Figure 4.26 shows an instantaneous drop of the cell voltage at the time of load change. Because dynamic charge balances at the electrochemical double layers at anode and cathode are implemented in the simulation, this does not really happen instantaneously, but the charge densities change extremely fast and so does the cell voltage. Afterwards the cell voltage decreases further according to the transient behaviour of the mole fractions in both gas phases. Speaking in terms of activation and concentration overpotentials, one can interpret the instantaneous drop as the additional activation overpotential required to accelerate the electrochemical reaction rates to the new level plus the additional voltage losses the ionic flux across the electrolyte layer causes. The additional losses at the electrolyte layer can be estimated following Equation 2.88:

$$\eta_{e,0.85} - \eta_{e,0.7} = (0.85 - 0.7) / \kappa_e = 0.15 \quad (4.12)$$

The further voltage loss until can be interpreted as concentration overpotential, because it is mainly caused by concentration changes.

The simulated time corresponds to a few seconds in a HotModule system. After a time period of about $\tau=2$ (corresponding to 24.3 seconds in the HotModule), the states governed by a medium time constant have reached a quasi-steady state. After that, the very large time constant of the solid temperature dominates the system behaviour, and all other states follow the changes in the temperature profile. At about $\tau=500$, the solid temperature reaches

its new steady state and, with it, all other states. This can be seen in the cell voltage behaviour in Figure 4.27 and in the solid temperature in Figure 4.28.

Thus, the cell voltage shows behaviour according to all three time constants in the system (cf. Figure 2.10): very fast voltage drop upon load change due to the small double layer charge capacity, fast voltage decrease due to concentration change and slow change due to temperature dynamics.

This is only a small excerpt from the numerous transient results provided by the simplified 2D model. With respect to limited space this section is restricted to the results given above. They demonstrate the capabilities of the model and its implementation in ProMoT / DIVA with regards to dynamic simulations and the physical meaningfulness of the obtained numerical solution.

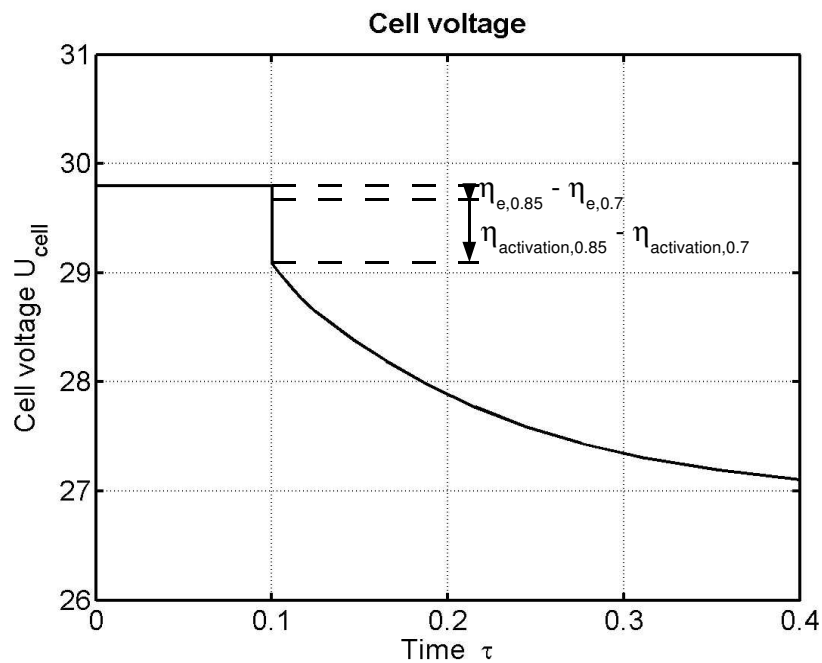


Figure 4.26: Cell voltage during load change from $I_{cell}=0.7$ to $I_{cell}=0.85$. The potential differences, η , can be interpreted as overpotentials.

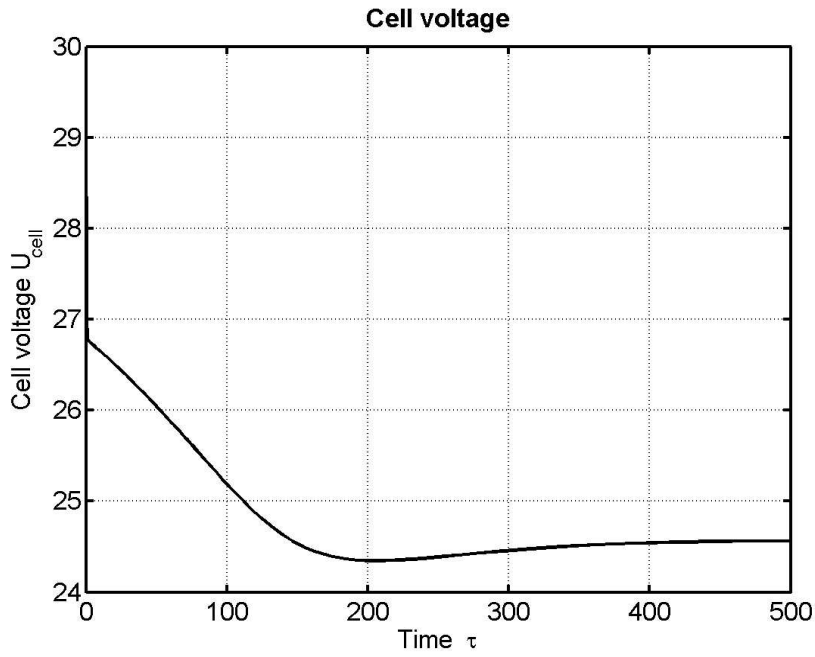


Figure 4.27: Long time behaviour of cell voltage during load change from $I_{cell}=0.7$ to $I_{cell}=0.85$.

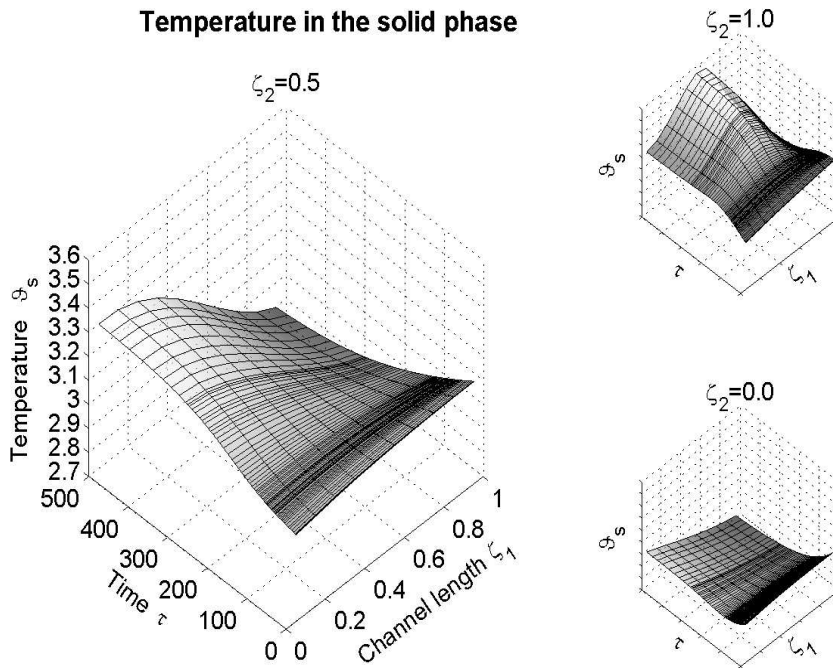


Figure 4.28: Long time behaviour of solid temperature during load change from $I_{cell}=0.7$ to $I_{cell}=0.85$.

4.4 Parameter analysis

The 2D model contains a large number of system parameters. Some are well known and others can be estimated at least to the correct order of magnitude. There are also a few parameters that can not be determined a priori. Therefore, an experimental parameter validation is necessary. A parameter sensitivity analysis can be very helpful to simplify this validation and to perform it efficiently. The investigation of parametric sensitivities may reveal system parameters whose exact value is of minor importance and it gives hints as to which experiments should be carried out to determine certain parameters.

A complete sensitivity analysis would have to be performed under variation of all input parameters and all uncertain system parameters within their physically reasonable range. This would surely produce an enormous amount of data which could hardly be interpreted adequately. Therefore, the parameter analysis presented here is restricted to a few steady state examples, which are of special interest.

This is carried out in two ways. First, the influence of some system parameters on the current-voltage curve is investigated. Therefore, the reduced model with isothermal solid phase is applied. Second, the differential parameter sensitivities of several states are evaluated at base case conditions using the complete reduced model.

The restriction to the analysis of parameter sensitivity on the steady state results means that time constants are not discussed here. This is acceptable, because their number is small and they can be determined fairly easily if the other parameters are known from steady state measurements beforehand. Thus an analysis of these parameters is of minor importance.

4.4.1 Parametric sensitivity of the current-voltage curve

The current-voltage curve is influenced by several kinetic parameters. These are the Damköhler numbers of the reforming and the electrochemical reactions, but also the kinetic parameters of charge and mass transport. An a priori estimation of these parameters is not reliable, because they depend on too many parameters which are vaguely known like the pore size distribution, electrolyte holdup, effective catalyst surface and others. To determine their importance, sets of current-voltage curves are plotted for various parameter values.

The parameters under investigation are

- the Damköhler number of the methane steam reforming reaction, Da_{ref1} ;
- the Damköhler number of the hydrogen oxidation reaction, Da_{ox1} ;
- the Damköhler number of the carbon monoxide oxidation reaction, Da_{ox2} ;
- the Damköhler number of the oxygen reduction reaction, Da_{red} ;
- the ion conductivity of the electrolyte, κ_e ;
- and the mass exchange coefficients between bulk gas phases and the electrochemical reaction zones inside the electrode pores, $D_{i,as}$ and $D_{i,cs}$.

According to Figure 4.29, the Damköhler number of the methane steam reforming reaction is of high importance for the current-voltage curve. Increasing the Damköhler number not only increases the cell voltage, but also pushes the limit current density to significantly higher values. This proves that the reforming reaction is the limiting factor for the cell current in this configuration. Its ability to provide the anodic oxidation reactions with educts determines the maximum total cell current. The system steady state strongly depends on this Damköhler number, consequently its value must be determined with high accuracy. Considering to the unavoidable effect of catalyst degradation this means that the current-voltage curve of the DIR-MCFC undergoes significant changes during its life cycle.

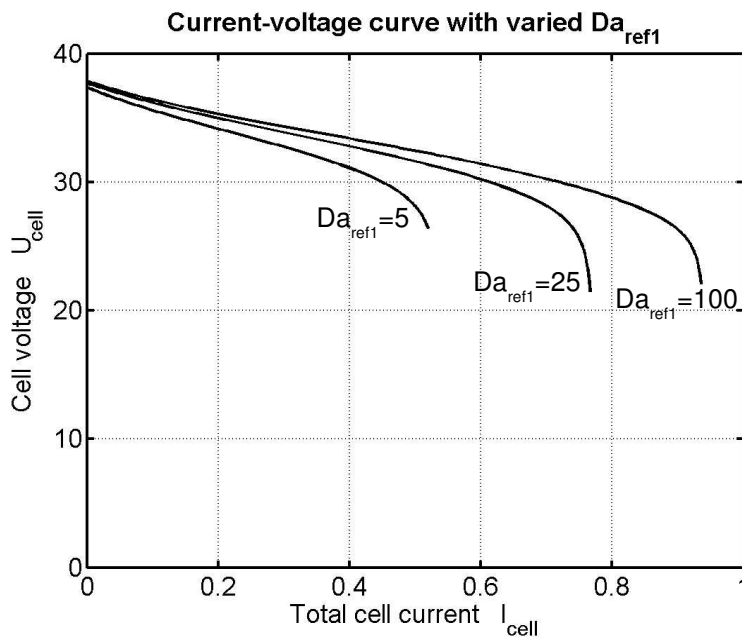


Figure 4.29: Current-voltage curve from the 2D model with isothermal solid phase for various Damköhler numbers of the methane steam reforming Da_{ref1} . The default value under base case conditions is $Da_{ref1}=25.0$.

The high importance of the dimensionless reaction rate constant of the hydrogen oxidation, Da_{ox1} , is clearly seen in Figure 4.30. In addition to the current-voltage curve at base case with $Da_{ox1}=5.0$ two curves with lower and two curves with higher Da_{ox1} are plotted. As expected, the higher the Damköhler number gets, the higher the cell voltage becomes. Above $Da_{ox1}\approx 30.0$ the reaction seems to be very close to chemical equilibrium, so any further increase of Da_{ox1} does not influence the simulation result. For Damköhler numbers below the default value, the curves turn to significantly lower voltages. Da_{ox1} has no influence on the limiting cell current. These findings confirm that Da_{ox1} is an important parameter and that, with the chosen default value, the system is operated outside the electrochemical equilibrium.

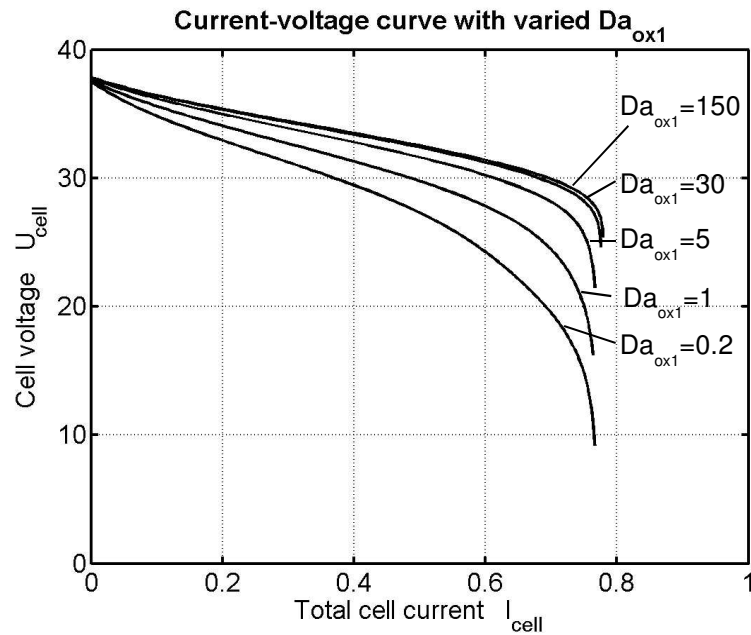


Figure 4.30: Current-voltage curve from the 2D model with isothermal solid phase for various Damköhler numbers of the hydrogen oxidation Da_{ox1} . The default value under base case conditions is $Da_{ox1}=5.0$.

Figure 4.31 shows the influence of the carbon monoxide oxidation reaction on the current-voltage curve. The default value used under base case conditions is $Da_{ox2}=5.0$. Almost identical over a large range of cell current values, the curves for other values of Da_{ox2} deviate significantly only in the vicinity of the limiting total cell current. In general, the hydrogen oxidation is faster than that of carbon monoxide. Even for the highest Damköhler value the hydrogen oxidation produces twice as much electric current as the carbon monoxide, so the hydrogen oxidation is the dominating source for electric current. In addition, the standard potential difference of the carbon monoxide oxidation reaction is almost identical to that of the hydrogen oxidation at the given cell temperature. This means that an increase of Da_{ox2} does not significantly influence the cell voltage. The only effect of the carbon monoxide oxidation reaction can be seen in the limiting current. Here, an increase of Da_{ox2} causes a decrease in the limiting current. This may be due to the fact that the almost instantaneous consumption of carbon monoxide suppresses the water-gas shift reaction, so that the hydrogen concentration is decreased and the hydrogen oxidation reaction is slowed down considerably.

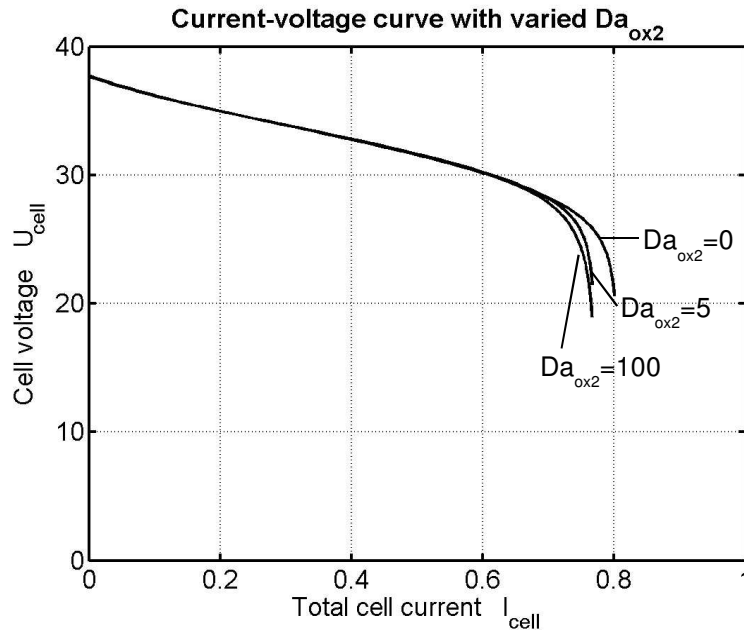


Figure 4.31: Current-voltage curve from the 2D model with isothermal solid phase for various Damköhler numbers of the carbon monoxide oxidation Da_{ox2} .

The default value under base case conditions is $Da_{ox2}=5.0$.

The reduction reaction is fairly close to equilibrium, as can be concluded from Figure 4.32. As with Da_{ox1} , the current-voltage curve is very sensitive to Da_{red} for values below $Da_{red}=0.3$. Higher values do not show significant influence on the voltage, while a lower value leads to a decreased cell voltage over the whole range of cell currents.

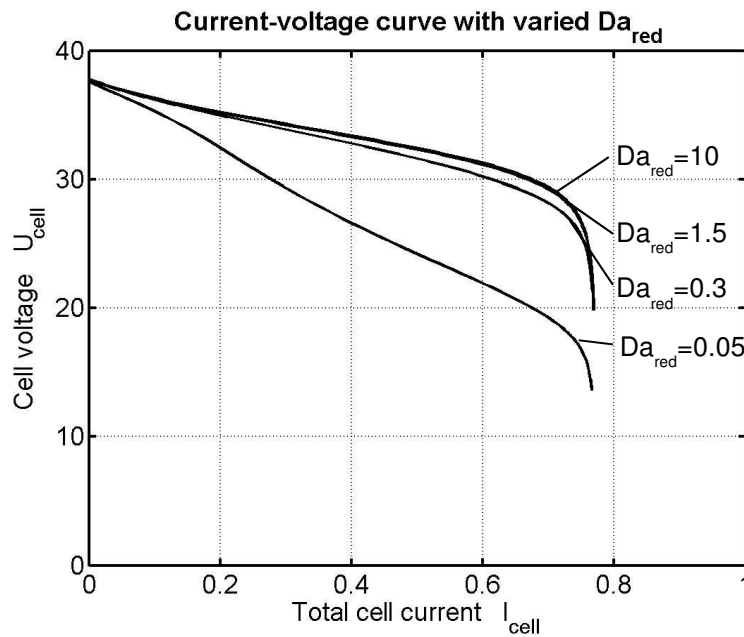


Figure 4.32: Current-voltage curve from the 2D model with isothermal solid phase for various Damköhler numbers of the oxygen reduction Da_{red} . The default value under base case conditions is $Da_{red}=0.3$.

From the analysis of these three figures the Damköhler numbers of hydrogen oxidation and oxygen reduction are found to be of major importance, while the Damköhler number of carbon monoxide oxidation is not. Generally, the oxidation reactions in MCFC are said to be inherently faster than the reduction reaction ([24]), thus for simplification, the hydrogen oxidation reaction can be assumed to be close to electrochemical equilibrium, i.e. $Da_{ox2} \geq 5.0$. Figure 4.33 shows the dependence of the current-voltage curve on the ion conductivity of the electrolyte. The ion conduction resistance causes significant voltage losses for $\kappa_e < 1.0$. With the default value of $\kappa_e = 1.0$, these losses play a minor role.

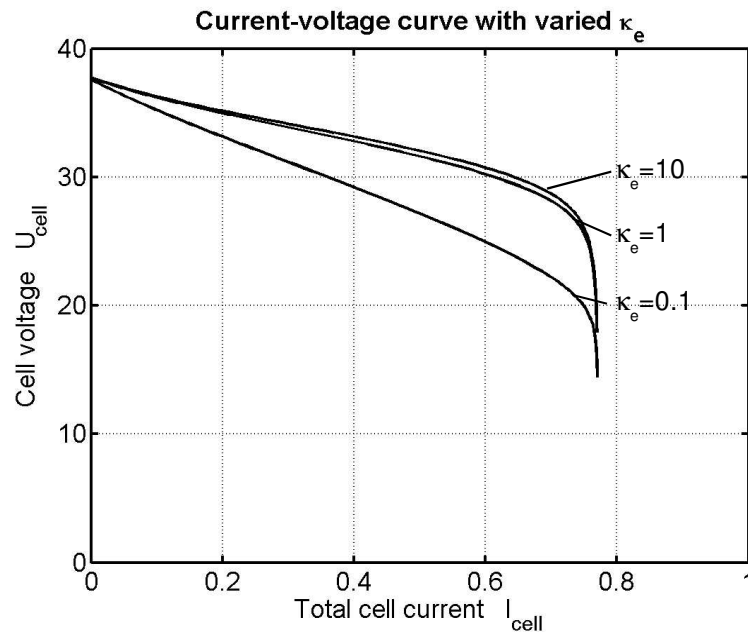


Figure 4.33: Current-voltage curve from the 2D model with isothermal solid phase for various ion conductivities κ_e . The default value under base case conditions is $\kappa_e = 1.0$.

The dependence of the current-voltage curve on the mass transport coefficient at the electrode pores is shown in Figure 4.34. For values higher than the default value of $D_{i,as} = 100.0$ the curve does not change significantly. That means that with this value, the voltage loss due to mass transport are fairly low and $D_{i,as}$ is of minor importance to the cell voltage. For $D_{i,as} < 30.0$ the mass transport into the electrode pores becomes the limiting factor for the electric cell current.

The dependence of the current-voltage curve on the mass transport coefficient at the electrode pores is shown in Figure 4.34. For values higher than the default value of $D_{i,as} = 100.0$ the curve does not change significantly. That means that with this value, the voltage loss due to mass transport are fairly low and $D_{i,as}$ is of minor importance to the cell voltage. For $D_{i,as} < 30.0$ the mass transport into the electrode pores becomes the limiting factor for the electric cell current.

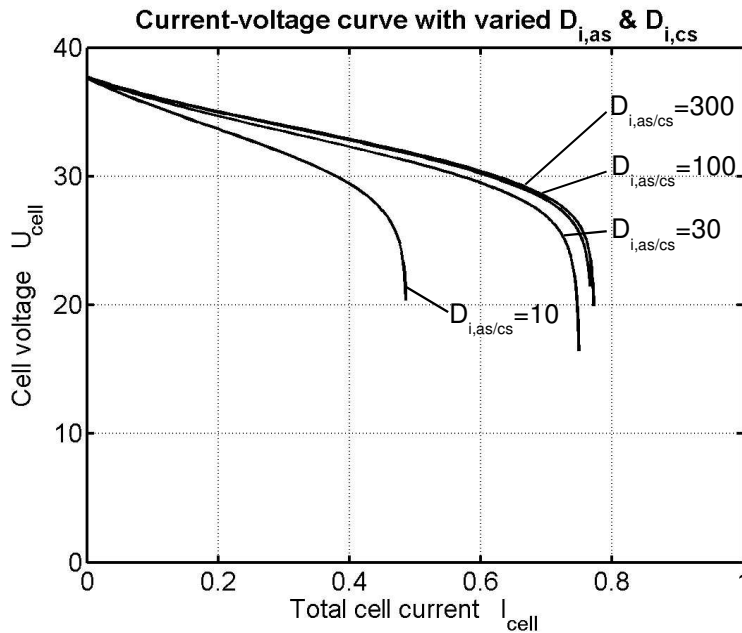


Figure 4.34: Current-voltage curve from the 2D model with isothermal solid phase for various mass transport coefficients $D_{i,as}$. The default value under base case conditions is $D_{i,as} = D_{i,cs} = 100.0$.

The analysis of these six exemplary system parameters shows that five of them have a strong impact on the current-voltage curve. Only the Damköhler number of the carbon monoxide oxidation does not seem to play an important role here. With respect to experimental validation, at least for the first approximation this parameter can be set to zero. The default values of most other parameters are in the region of medium sensitivity on the current-voltage curve. The influence of the five parameters on the current-voltage curve is very similar in shape, which makes it hard to discriminate their influence based on a single measured current-voltage curve. This does not mean that they cannot be determined from steady state experiments, but that current-voltage measurements with varying inlet concentrations are necessary.

4.4.2 Parametric sensitivity under base case conditions

The sensitivity analysis at of a system at steady state reveals the impact of certain system parameters on the states. Here, a sensitivity analysis of the complete physically reduced model (including the solid enthalpy balance) is used to find out which unknown parameters can be determined by the measurable states.

Among the numerous simulated states of the model only a few are accessible by measurements. In case of the HotModule, these are:

- the anode outlet concentrations and temperature,
- the cathode inlet concentrations and temperature,
- the cathode outlet concentrations and temperature,
- the solid temperature profile,
- the cell voltage.

At steady state, the gas compositions at the cathode inlet and outlet are determined by simple combustion calculations and are therefore independent of any kinetic system parameters. Thus, the list of states considered in this sensitivity analysis is:

$$x = (X_{i,a,out}, \vartheta_{a,out}, \vartheta_{c,in}, \vartheta_{c,out}, U_{cell}, \vartheta_s(\zeta_1, \zeta_2)) \quad (4.13)$$

The parameters, whose impact on the measurable values is calculated are kinetic parameters which are to be determined by experiments:

$$p = (Da_{ref1}, Da_{ref2}, Da_{ox1}, Da_{ox2}, Da_{red}, St_{as}, St_{cs}, Pe_s, \kappa_e) \quad (4.14)$$

Table 4.3 lists the sensitivities of the measured states. The sensitivities are calculated under base case conditions at steady state, thus they are the partial derivative of the measured states at steady state with respect to the parameters considered, normalised by the actual value of the parameter and state. Thus the values are directly comparable to one another:

$$S_{j,k} = \left(\frac{\partial x_{ss,j}}{\partial p_k} \right) \cdot \left(\frac{p_k}{x_{ss,j}} \right) \quad (4.15)$$

Plots of the solid temperature sensitivity suggest that the sensitivities are highest in the four corners of the two dimensional cell. Therefore only these values are given here. Note that under base case conditions the highest solid temperature occurs at $\zeta_1 = \zeta_2 = 1$ and the lowest temperature occurs at $\zeta_1 = \zeta_2 = 0$, cf. Figure 4.10.

Comparison of the sensitivities confirms some of the results from the parameter variation in the preceding section 4.4.1. The impact of Da_{ref2} and Da_{ox2} on the steady state is rather small, also the heat conductivity of the solid phase is of secondary importance for most measurable states. The experimental validation of their values is probably not possible with the integral measurement data available from the HotModule. Other parameters like Da_{ref} , Da_{ox1} and Da_{red} as well as both Stanton numbers, St_{as} and St_{cs} , are of high importance. In the experimental validation process, their values should be determined with great care.

Unfortunately, most of these parameters influence the same group of measurable states, so it might prove difficult to differentiate between them.

Table 4.3: Parameter sensitivities of measurable states at base case. Significant values are highlighted.

	Da_{ref1}	Da_{ref2}	Da_{ox1}	Da_{ox2}	Da_{red}	κ_e	St_{as}	St_{cs}	Pe_s
$\chi_{CH_4,a,out}$	-8.9e-1	-2.2e-2	2.3e-1	1.6e-1	5.5e-1	3.5e-1	-2.2e+0	9.6e-1	8.3e-3
$\chi_{H_2O,a,out}$	-3.7e-2	-5.3e-4	1.1e-2	3.7e-3	1.7e-2	1.1e-2	-7.6e-2	3.3e-2	4.1e-4
$\chi_{H_2,a,out}$	3.1e-1	5.6e-3	-8.8e-2	-3.9e-2	-1.6e-1	-1.1e-1	6.9e-1	-3.0e-1	-3.3e-3
$\chi_{CO,a,out}$	2.9e-1	1.3e-2	-5.5e-2	-9.9e-2	-2.7e-1	-1.6e-1	9.4e-1	-4.3e-1	-1.6e-3
$\chi_{CO_2,a,out}$	-1.7e-2	-8.4e-4	3.2e-3	6.2e-3	1.7e-2	1.0e-2	-5.8e-2	2.6e-2	9.2e-5
$\vartheta_{a,out}$	-5.4e-3	3.8e-4	-9.2e-3	-5.1e-3	-2.3e-2	-1.2e-2	6.6e-2	-2.8e-2	1.4e-4
$\vartheta_{c,in}$	4.3e-3	2.4e-4	-8.9e-3	-3.3e-3	-1.8e-2	-9.8e-3	2.7e-2	-1.2e-2	2.1e-5
$\vartheta_{c,out}$	-1.0e-2	-2.1e-4	-1.0e-2	-9.5e-4	-1.5e-2	-7.9e-3	-2.1e-2	8.4e-3	1.8e-4
U_{cell}	2.3e-2	7.9e-4	2.2e-2	5.5e-4	3.0e-2	1.5e-2	5.6e-2	-2.0e-2	-4.1e-4
$\vartheta_s(0,0)$	-1.0e-2	-7.5e-4	-5.6e-4	7.8e-4	5.7e-4	-8.3e-3	-3.3e-2	-2.6e-2	-1.9e-3
$\vartheta_s(0,1)$	-2.1e-2	-1.4e-3	4.3e-3	3.7e-3	-1.2e-2	-3.7e-3	-8.1e-2	2.9e-3	-9.9e-4
$\vartheta_s(1,0)$	3.1e-3	3.0e-4	-1.5e-2	-3.3e-3	-2.4e-2	-1.3e-2	2.6e-2	-4.7e-2	-2.4e-3
$\vartheta_s(1,1)$	-9.2e-3	6.5e-5	-1.9e-2	-1.7e-3	-2.6e-2	-1.1e-2	-4.3e-3	-1.5e-2	2.0e-3
$\Delta \vartheta_s$	2.5e-3	1.3e-2	-3.0e-1	-4.0e-2	-4.3e-1	-5.5e-2	4.3e-1	1.6e-1	6.2e-2

Another interesting observation is the fact that some measurable states are nearly insensitive to the unknown system parameters. While the cathode inlet and outlet concentrations are not mentioned in Table 4.3, because their sensitivity is zero, also several anode outlet concentrations show only small sensitivity, which is probably too low with respect to measurement errors. Therefore, these states can be measured, but they are of little use in the validation.

4.5 Concluding remarks on simulation results

Within this chapter, simulation results from a spatially discretised simplified 2D model are presented. A base case configuration is defined containing a set of system and operating parameters typical for the HotModule. The steady state profiles for selected concentrations, temperatures, flow densities and current densities are physically reasonable and when the dimensionless results are transformed back to dimensional ones, their values are in the same range as measurement data from the HotModule. Using a modified reduced model with isothermal solid phase, a current-voltage curve for base case configuration is predicted. With this, the comparability of the steady state results of the physically reduced model with those obtained from the steady state anode model is demonstrated. As an example for a

transient scenario, a load change simulation is presented. The results can be interpreted physically, which confirms the principal validity of the model.

Finally, the effects of unknown model parameters are analysed. With the isothermal model version, current-voltage curves are calculated for various parameters values, identifying their importance for the overall cell voltage. A parameter sensitivity analysis under base case configuration reveals the dependencies of measured states on unknown parameters, which gives further information for experimental validation.

Wohin auch der Wind weht,
Welchen Weg auch die Welt geht
Ist ganz und gar gut so für mich!

Unbekannter Taoist

5 Optimisation based on the reduced model

In this chapter the reduced model (cf. Chapter 2.3 "Physically-chemically reduced model") is applied for two different steady state optimisations. First, the input parameters of a single cross flow cell at given cell current are optimised to yield an optimal electric efficiency while fulfilling several temperature restrictions and avoiding carbonisation in the anode channel. The optimisation is performed at different cell currents, so that several points of a current-voltage curve with optimal operating conditions are evaluated.

The second application concerns the optimisation of the fuel cell design with respect to the reforming catalyst distribution. This design parameter predominantly determines the location of the endothermic reforming reaction and can therefore be expediently changed to homogenise the solid temperature profile. Because the reforming catalyst distribution cannot be changed during the system life time, this optimisation is performed only for one typical load case, which is the base case already considered in Chapter 4.2 ("Steady state results"). The resulting configuration is then evaluated with some other load cases to investigate its usefulness over a range of operating conditions.

5.1 Optimisation of input parameters

To ensure a safe and efficient operation of the cell, the optimisation of all available operating parameters according to a reasonable objective function is desirable. When the cell is operated at constant load over a long period of time, the overall electric efficiency is a suitable criterion for the quality of the operating conditions. Under different conditions, for example during dynamic load changes, other aspects like fast and safe transition may become important, but those are not considered here.

5.1.1 Objective function and constraints

The electric efficiency which is being used as the objective function of the optimisation relates the total electric cell power diminished by the system's parasitic power consumption to the combustion enthalpy input of the fuel gas. The optimisation has to fulfill several constraints concerning the solid temperature and the possibility of carbonisation. The temperature must not exceed a minimum and a maximum temperature, also the maximum temperature difference within the solid phase is limited. Additionally, no carbon deposition in

the anode channel is allowed to occur, and the cell voltage may not fall short of a specific value to avoid electrochemical destruction of the anode catalyst. The following input quantities serve as optimisation variables: amount of fuel gas, steam to carbon ratio in the fuel gas, air number and cathode gas recycle ratio. Another input quantity, the total cell current, is fixed within each optimisation. Also the temperatures of feed gas and air are assumed to be constant. Thus, we have the objective function

$$\eta_{el}(\Gamma_{a,in}, S/C, \lambda_{air}, R_{back}) = \frac{P_{el,system}}{H_{a,in}} = \frac{P_{cell} - P_{blower}}{\Gamma_{a,in} \cdot \sum_i X_{i,a,in} \cdot (-\Delta_C h_i^0)} \rightarrow max! \quad (5.1)$$

subject to

$$\min(\vartheta_s(\zeta)) \geq \vartheta_{s,min} \quad (5.2)$$

$$\max(\vartheta_s(\zeta)) \leq \vartheta_{s,max} \quad (5.3)$$

$$\max(\vartheta_s(\zeta)) - \min(\vartheta_s(\zeta)) \leq \Delta \vartheta_{s,max} \quad (5.4)$$

$$U_{cell} \geq U_{cell,min} \quad (5.5)$$

$$\exists j: \Delta_R g_{Cj}(\vartheta_a(\zeta_1, \zeta_2), X_{i,a}(\zeta_1, \zeta_2)) \geq 0 \quad \text{at every } (\zeta_1, \zeta_2) \in [0..1; 0..1] \quad (5.6)$$

and additionally the steady state fuel cell balances as equality constraints. Equations 5.2 and 5.3 demand that the solid temperature does not exceed a minimum and a maximum temperature at any point in the cell. In Equation 5.4 the difference between the highest and the lowest temperature is limited, and Equation 5.5 demands that the cell voltage stays above a certain level. According to Equation 5.6, at least one carbonisation reaction at every location of the cell must have a positive free enthalpy of reaction in order to avoid carbon deposition. For details on carbonisation see Chapter 2.1.3.9 ("Thermodynamics").

This formulation does not account for the enthalpy of the water in the feed gas. Like the constant inlet temperatures, this is a significant simplification. To include the energetic effort for the water in the feed gas, the modelling of the gas pre-treatment would be necessary. Without pre-reforming and with methane as the only combustible species in the gas at anode inlet, the relevant enthalpy flow at anode inlet is equal to

$$H_{a,in} = \Gamma_{a,in} \cdot \frac{1}{1+S/C} \cdot (-\Delta_C h_{CH_4}^0(1)) \quad (5.7)$$

The introduced steam to carbon ratio, S/C , allows to describe the anode inlet composition in dependence on only one parameter, which simplifies the optimisation task.

5.1.2 Optimisation results

The steady state optimisation of the input parameters is performed for eight different values of the total cell current, using the sequential quadratic programming (SQP) algorithm E04UCF from the NAG library [41], which is implemented in the software package DIVA. The computation times for one single optimisation with an 8x8 discretisation grid on a standard

1 GHz personal computer is between 1 hour for medium load cases and 6 hours for low and high cell current cases. Table 5.1 shows the input quantities at the optimum points together with additional information like temperature, cell voltage and fuel utilisation (cf. Equation 2.11) of the respective load case.

The optimisation results are mainly determined by the temperature constraints (equations 5.2 - 5.4). For low cell currents the solid temperature is at the lower end of the admissible range. Because the addition of cool air poses a considerable cooling effect, a low air number is necessary in order to reach the minimum temperature. Although this leads to a low oxygen concentration in the cathode channel, this configuration yields an optimal value for the electric efficiency.

Table 5.1: Results of the steady state optimisation of input parameters.

I_{cell}	0.3	0.4	0.5	0.6	0.7	0.8	0.9	1.0
R_{back}	0.5	0.5	0.5	0.5	0.5	0.5	0.5	0.5
Γ_{feed}	0.57	0.49	0.59	0.67	0.98	1.14	1.35	1.49
S/C	3.95	2.16	2.02	1.85	2.50	2.51	2.46	2.14
λ_{air}	1.87	1.96	1.99	2.04	2.17	2.45	2.63	2.97
Y_{fuel}	0.742	0.737	0.728	0.723	0.717	0.703	0.658	0.602
\mathcal{G}_{min}	2.90	2.90	2.97	3.00	3.00	3.00	3.00	3.00
\mathcal{G}_{max}	3.10	3.10	3.17	3.20	3.20	3.20	3.20	3.20
U_{cell}	32.0	31.6	31.1	30.5	29.6	28.6	27.9	27.1
$P_{el,system}$	21.4	28.1	34.6	40.7	45.8	50.5	55.0	58.9
η_{el}	57.1 %	56.0 %	54.5 %	53.0 %	50.7 %	47.9 %	43.4 %	38.3 %

At $I_{cell}=0.5$, the solid temperature is in the middle of the admissible temperature range, and all load cases above that have a temperature distribution at the upper end of the range. The high current load configurations are also mainly governed by the temperature constraints. As a tendency, high cell currents lead to more inhomogeneously distributed current densities, which again come with larger temperature gradients. On the other hand, a low degree of fuel utilisation means that in all cell areas there are sufficient amounts of educts available for the reaction, which favours a homogenous temperature distribution. Thus, as the cell current is increased, the fuel utilisation must be lowered in order to fulfill the maximum allowable temperature difference constraint. This again leads to a higher amount of heat released in the catalytic burner, which is compensated by an increase of air flow into the burner. The low fuel utilisation together with the high air number lead to a significant decrease of the electric efficiency at high cell currents.

Due to the small impact of the steam to carbon ratio on the electric efficiency, its value does not follow a clear tendency. Applying different objective functions, which also consider the effort necessary to evaporate the steam in the feed flow, should yield more interpretable results with respect to the steam to carbon ratio, but requires additional modelling of the pre-

treatment of the feed gas. The cathode gas recycle ratio is always at its maximum value (i.e. $R_{back}=0.5$). Obviously, the benefit for the temperature field is higher than the parasitic losses caused by the additional gas flow through the blowers.

The following two Figures 5.1 and 5.2 show the obtained cell voltage, fuel utilisation and the value of the objective function, that is the electric efficiency, for the eight optimised load cases. An extrapolation of the voltage curve in Figure 5.1 to higher currents shows that for $I_{cell}=1.1$ a cell voltage lower than $U_{cell,min}=27.0$ is expected, so in order to fulfill this inequality constraint, the system efficiency is expected to decrease even steeper. Load cases from $I_{cell}=0.0$ to $I_{cell}=0.2$ are not optimised, because they are considered unattractive for system operation. They occur only during start-up and shut-down phase, but it is unattractive to continuously operate the system at such low power output.

The diagrams show that, although the cell voltage remains at a nearly constant level the electric efficiency rapidly decreases at high cell currents due to the lower degree of fuel utilisation, i.e. increased amount of feed gas. Except for the steam to carbon ratio, which is not plotted in the figures but can be seen from Table 5.1, all parameters show continuous increase or decrease across the range of cell current. This suggests that all solutions are global optima or at least in a local optimum close to it. If a local optimum far from the global one exists, one would expect at least one or more solutions deviating significantly from its neighbouring points.

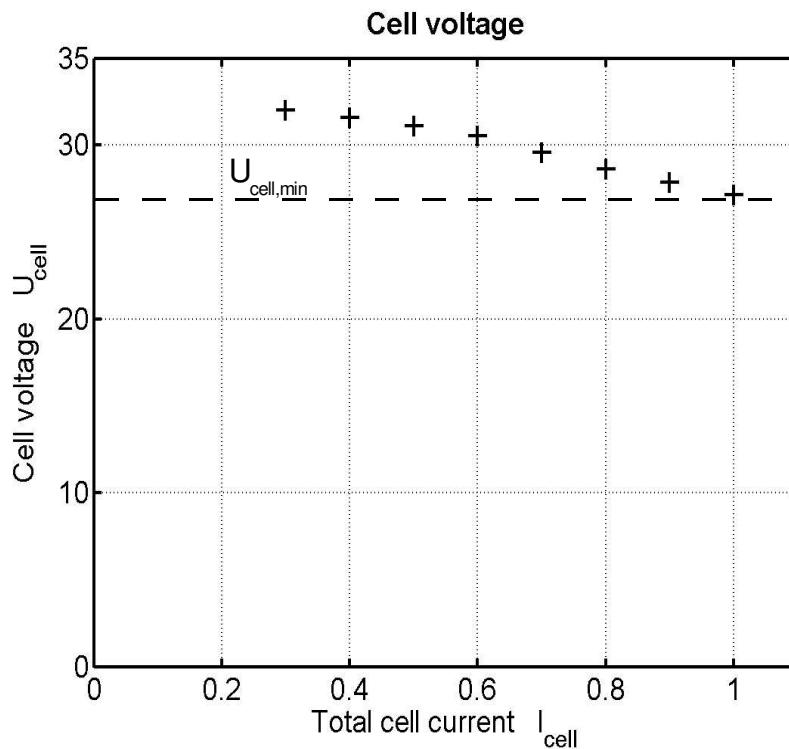


Figure 5.1: Cell voltage at optimal operating points at different cell currents obtained from the 2D model.

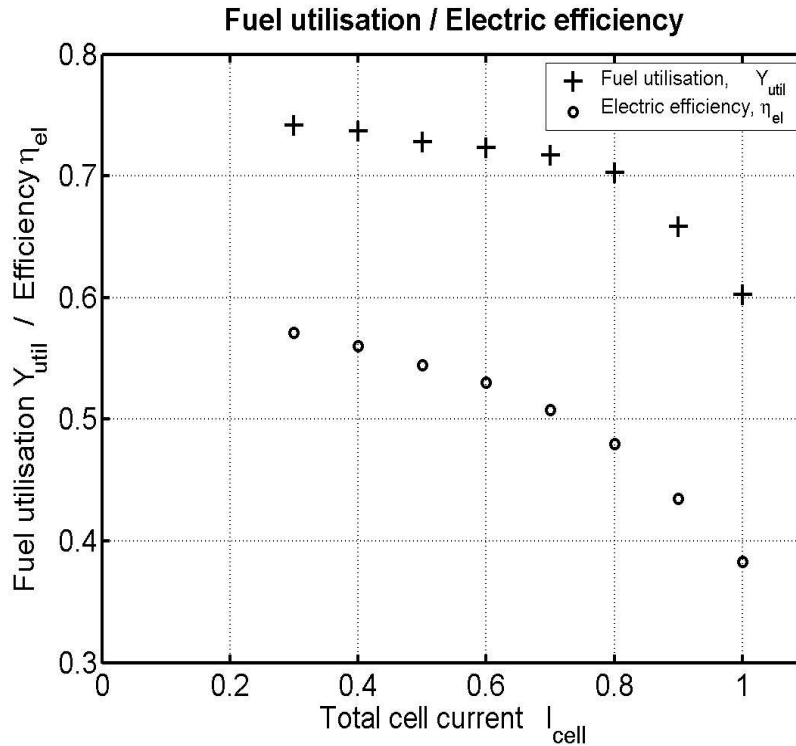


Figure 5.2: Fuel utilisation and electric efficiency at optimal operating points at different cell currents obtained from the 2D model.

5.2 Optimisation of reforming catalyst distribution

The temperature distribution in MCFC is of critical significance for the system's performance and life time. It is governed by strongly interrelated phenomena like the endothermic reforming and the exothermic electrochemical reactions, conductive and convective heat transport and heat exchange between phases. These interrelations are characterised by a number of system parameters, most of which can be influenced deliberately: Heat exchange parameters can be increased by means of increased surface area and heat conductivities can be increased by the choice of material or the thickness of some compartments. However, the most promising possibility seems to be the sophisticated distribution of the reforming reaction as a heat sink so that temperature peaks are decreased and cold spots are avoided. This leads to the necessity to spatially distribute the reforming catalyst inside the anode channels.

Contrary to the preceding optimisation this one does not only manipulate input quantities to achieve an optimal performance, but system parameters are also included in the optimisation. Because system parameters are equal for all load cases, the optimisation is performed only once under base case conditions. Its usefulness is then evaluated at other load cases.

To achieve a catalyst distribution optimal for the whole range of cell currents, the optimisation would have to consider all possible load cases simultaneously and find a result that suits all these cases. This is not the intention of this chapter, instead it demonstrates the

usefulness of the reduced model for system optimisation and evaluate the potential of reforming catalyst distribution.

5.2.1 Objective function and constraints

In this optimisation the formerly constant reforming Da_{ref} , which can be interpreted as the reforming catalyst density inside the anode channel, is now a function of the spatial coordinates ζ_1, ζ_2 . To keep the number of optimisation parameters low, the cell is divided into four equal rectangular segments each with constant Damköhler numbers. This stepwise Damköhler function corresponds best to what can be realised in a technical fuel cell stack. From a practical point of view, a continuous distribution of catalyst density cannot be realised with reasonable effort. Therefore, catalyst stepping is frequently applied in industry. Thus, the application of a stepwise distribution of the Damköhler number in this optimisation is justified.

Strictly speaking, with four segments across the cell area, there are eight reforming Damköhler numbers, because the model considers two reforming reactions (see Chapter 2.1.3.8). As both reactions occur at the same catalyst, a change of the catalyst density affects both Damköhler numbers in the same way. Thus, a Damköhler factor, F_{Da} , is introduced for each segment, with which the standard reforming Damköhler numbers are multiplied. With this, the ratio between Da_{ref1} and Da_{ref2} is equal in each segment. Because the catalyst density in the anode channel is limited, F_{Da} is limited to a maximum value of 3.0. The objective function is identical to the one used in the preceding chapter, but it depends on additional optimisation variables:

$$\eta_{el}(\Gamma_{a,in}, S/C, \lambda_{air}, R_{back}, F_{Da,1}, F_{Da,2}, F_{Da,3}, F_{Da,4}) = \frac{P_{el,system}}{H_{a,in}} \quad (5.8)$$

subject to

$$\min(\vartheta_s(\zeta)) \geq \vartheta_{s,min} \quad (5.9)$$

$$\max(\vartheta_s(\zeta)) \leq \vartheta_{s,max} \quad (5.10)$$

$$\max(\vartheta_s(\zeta)) - \min(\vartheta_s(\zeta)) \leq \Delta \vartheta_{s,max} \quad (5.11)$$

$$U_{cell} \geq U_{cell,min} \quad (5.12)$$

$$\exists j: \Delta_R g_{C_j}(\vartheta_a(\zeta), \chi_{i,a}(\zeta)) \geq 0 \quad \text{at each } \zeta = (\zeta_1, \zeta_2) = [0..1; 0..1] \quad (5.13)$$

and with the fuel cell balances in steady state as equality constraints.

5.2.2 Optimisation results

The reforming catalyst distribution is optimised at base case cell current, that is at $I_{cell}=0.7$. Like the preceding optimisations of the operating conditions alone, this extended optimisation needs a few hours computational time. Table 5.2 lists all relevant optimisation results and compares them with the results of the optimisation where only the input

parameters were optimised at the same cell current. It turns out that with a reforming catalyst distribution in four segments, the cell's electric efficiency can be increased by 1.7%. The catalyst distribution is shown in Figure 5.3, where the four optimal Damköhler factors are shown in their corresponding segments. In the anode channels on the right hand side ($\zeta_2=0..0.5$) a medium reforming catalyst density at the anode inlet ($F_{Da,1}=1.11$) provides a sufficient concentration of hydrogen for the oxidation reaction (Figure 5.4). This causes a moderate drop in anode gas temperature (Figure 5.5) and a moderate cooling effect at the coldest spot in the cell (Figure 5.6). Afterwards the relatively depleted gas enters the third segment, where a maximum amount of reforming catalyst ($F_{Da,3}=3.00$) pushes the slow reforming reaction rate to a maximum. Because temperature in this segment is not critical, the reforming rate is maximised in order to maximally promote the electrochemical reactions. The anode channels on the left hand side ($\zeta_2=0.5..1.0$) face a completely different situation. Here the reforming rate is significantly decreased ($F_{Da,2}=0.42$), yielding lower hydrogen concentrations than in the other channels. This is done even though temperature in this segment is not critical. The reason for this is that the cooling effect caused by the reforming reaction must be saved for the fourth segment, in which the maximum temperature occurs. The gas enters the fourth segment at a low extent of reforming reaction. Thus it is possible to use this cooling effect to decrease the anode gas temperature here and thereby induce an extra cooling at the hot spot of the cell ($F_{Da,4}=1.78$). If the gas entering the fourth segment was already reformed to a high degree, this cooling effect would be reduced.

Nevertheless, the catalyst density in this segment is not at maximum level. Setting $F_{Da,4}=3.0$ leads to a higher hydrogen concentration in the fourth segment, promoting the electrochemical reactions there. With increased current production in this segment, the current density in all other segments is lowered, as the total cell current is fixed. Thus, the current density in the first segment is decreased and with this the important heat source in this cell area is diminished. As a consequence, the temperature there drops and the maximum allowed temperature difference is exceeded.

The resulting current density distribution can be seen in Figure 5.7. As a tendency, it is more homogeneously distributed than for example at base case in Chapter 4 (Figure 4.11). This means that the electrodes are used better, i.e. there are no zones of very low reaction rates.

Table 5.2: Results of the optimisation of reforming catalyst and input parameters at $I_{cell}=0.7$ in comparison to the non-optimised reforming catalyst configuration.

Optimised parameters	Input conditions (Chapter 5.1)	Input conditions + Damköhler factors (This chapter)
R_{back}	0.5	0.5
Γ_{feed}	0.49	0.685
S/C	2.16	1.508
λ_{air}	1.96	2.086
$F_{Da,1}$	1.0	1.109
$F_{Da,2}$	1.0	0.425
$F_{Da,3}$	1.0	3.000
$F_{Da,4}$	1.0	1.777
Y_{fuel}	0.737	0.732
\mathcal{S}_{min}	2.90	3.00
\mathcal{S}_{max}	3.10	3.20
U_{cell}	31.6	29.82
$P_{el,system}$	45.8	46.4
η_{el}	50.7 %	52.42 %

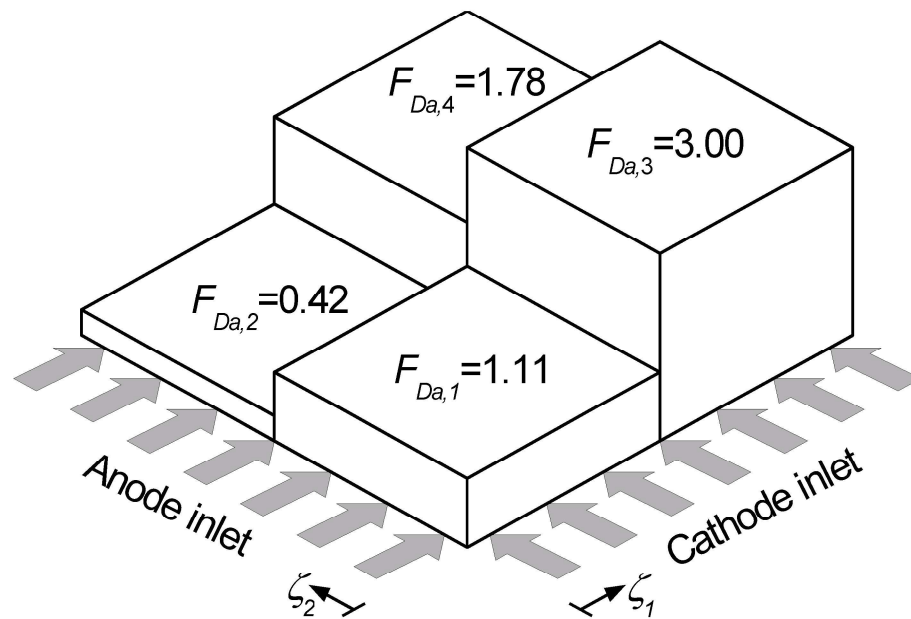


Figure 5.3: Optimal reforming Damköhler factors in the anode channel at $I_{cell}=0.7$. The original Damköhler numbers are $Da_{ref1}=25.0$ and $Da_{ref2}=100.0$.

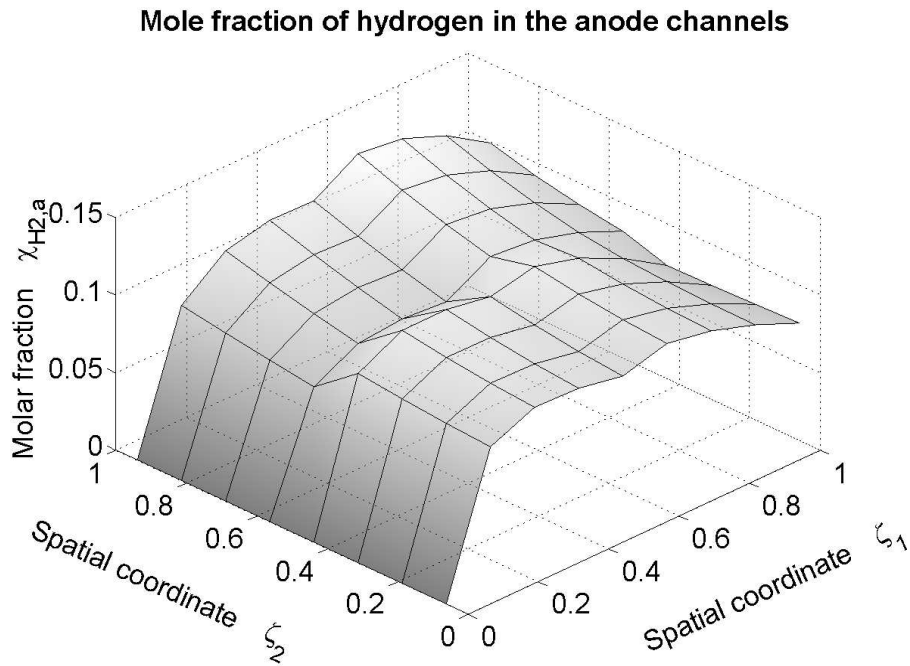


Figure 5.4: Steady state mole fraction of hydrogen in the anode channel at optimised reforming catalyst distribution and optimal operating conditions at $I_{cell}=0.7$.

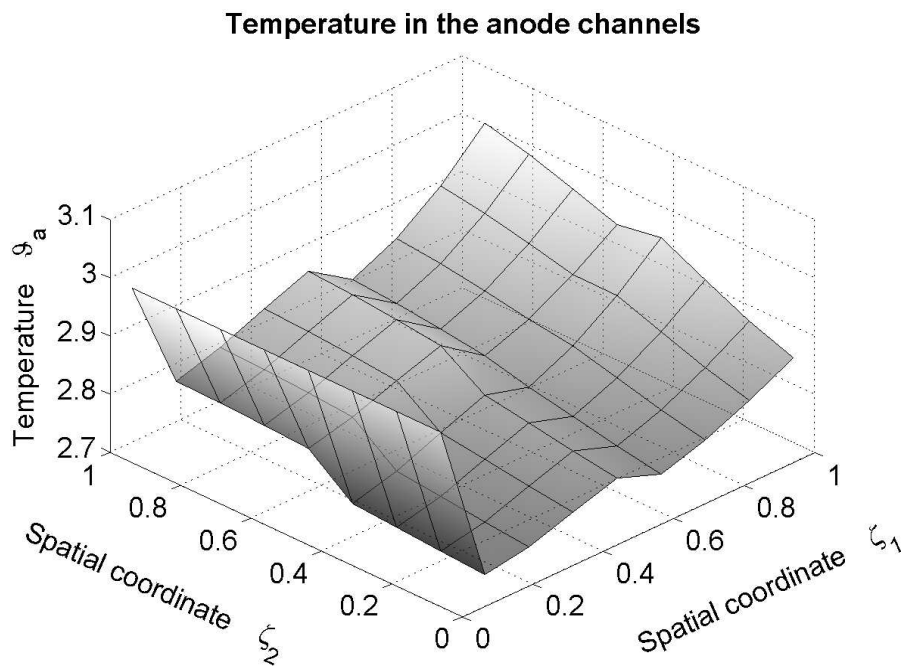


Figure 5.5: Steady state anode gas temperature at optimised reforming catalyst distribution and optimal operating conditions at $I_{cell}=0.7$.

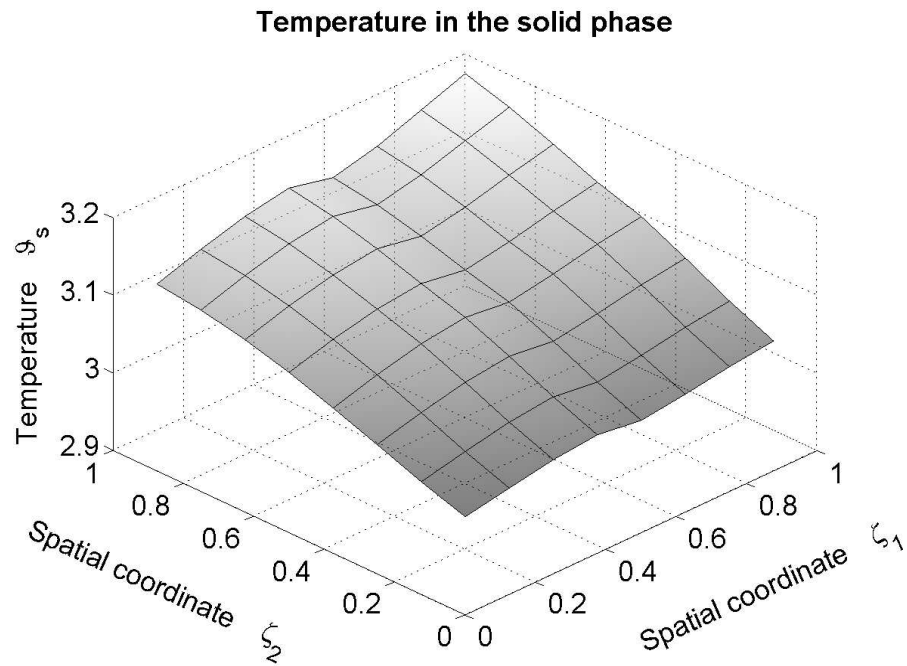


Figure 5.6: Steady state solid temperature at optimised reforming catalyst distribution and optimal operating conditions at $I_{cell}=0.7$.

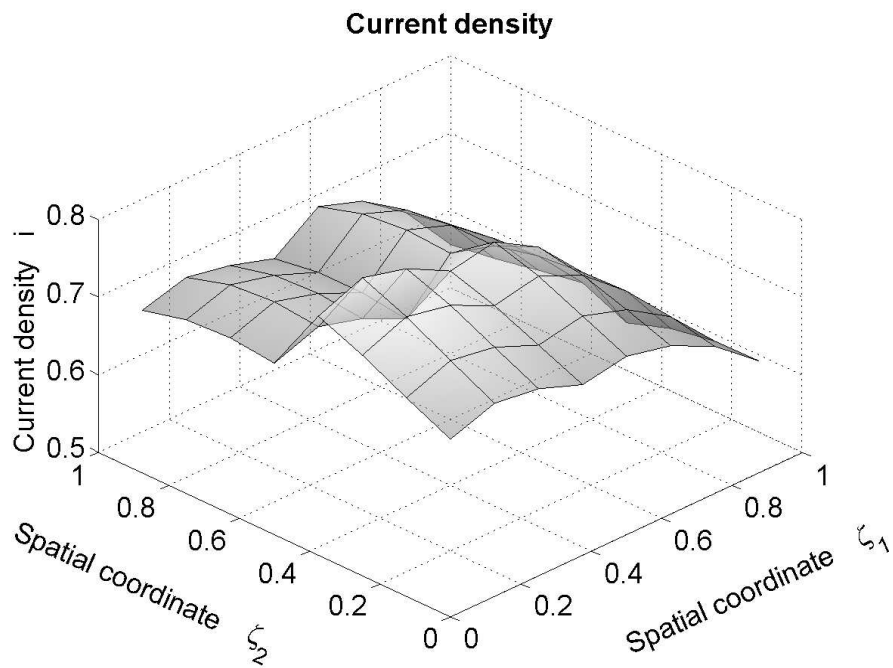


Figure 5.7: Steady state current density distribution at optimised reforming catalyst distribution and optimal operating conditions at $I_{cell}=0.7$.

5.2.3 Effect of catalyst distribution on other load cases

In the preceding section, the optimum spatial distribution for the reforming catalyst in the anode channel at one certain cell current ($I_{cell}=0.7$) is calculated. Because the MCFC is operated under various loads, the feasibility of this catalyst distribution must be evaluated at other cell currents as well. Therefore, the same optimisations are performed as in Chapter 5.1, where input parameters were optimised for different given cell currents. The only difference here is that the catalyst distribution from Chapter 5.2.2 is applied in all cases.

The results of these calculations are summarised in Table 5.3. For comparison, the electric efficiencies, η_{el} , of the system with homogeneous reforming catalyst distribution are also given here. In general, the operating conditions are similar to those obtained from Chapter 5.1: low cell currents have low air number and low temperatures, high cell currents show high air number and high temperatures. The reasons for this trend are already discussed in the preceding section. The important result is that the electric efficiency of the medium and high current cases is significantly increased by the application of the catalyst distribution. Only at very low currents, the electric efficiency is slightly decreased. That is because the situation in the low current case is significantly different from those at medium or high currents. As the cell is seldom operated in that low current region, one can state that the catalyst distribution increases the cell performance over the complete range of technically relevant cell currents up to more than three percent.

Table 5.3: Results of the steady state optimisation of input parameters at inhomogeneous catalyst distribution from Chapter 5.2.2. For comparison, the electric efficiencies of the same load cases without optimised catalyst density distribution (Chapter 5.1) are given.

I_{cell}	0.3	0.4	0.5	0.6	0.7	0.8	0.9	1.0
R_{back}	0.5	0.5	0.5	0.5	0.5	0.5	0.5	0.5
Γ_{feed}	0.53	0.48	0.55	0.66	0.69	0.80	1.28	1.38
S/C	3.52	2.16	1.84	1.94	1.51	1.51	2.48	2.17
λ_{air}	1.88	1.93	1.99	1.99	2.08	2.25	2.49	2.79
Y_{fuel}	0.736	0.746	0.744	0.736	0.732	0.719	0.702	0.655
\mathcal{S}_{min}	2.90	2.90	2.93	3.00	3.00	3.00	3.00	3.005
\mathcal{S}_{max}	3.10	3.10	3.13	3.20	3.20	3.20	3.20	3.200
U_{cell}	32.1	31.6	31.0	30.5	29.8	29.0	27.7	27.0
$P_{el,system}$	21.5	28.1	34.4	40.7	46.4	51.3	54.9	59.0
η_{el}	56.9 %	56.7 %	55.3 %	54.0 %	52.4 %	49.8 %	46.3 %	41.8 %
$\eta_{el} (5.1)$	57.1 %	56.0 %	54.5 %	53.0 %	50.7 %	47.9 %	43.4 %	38.3 %

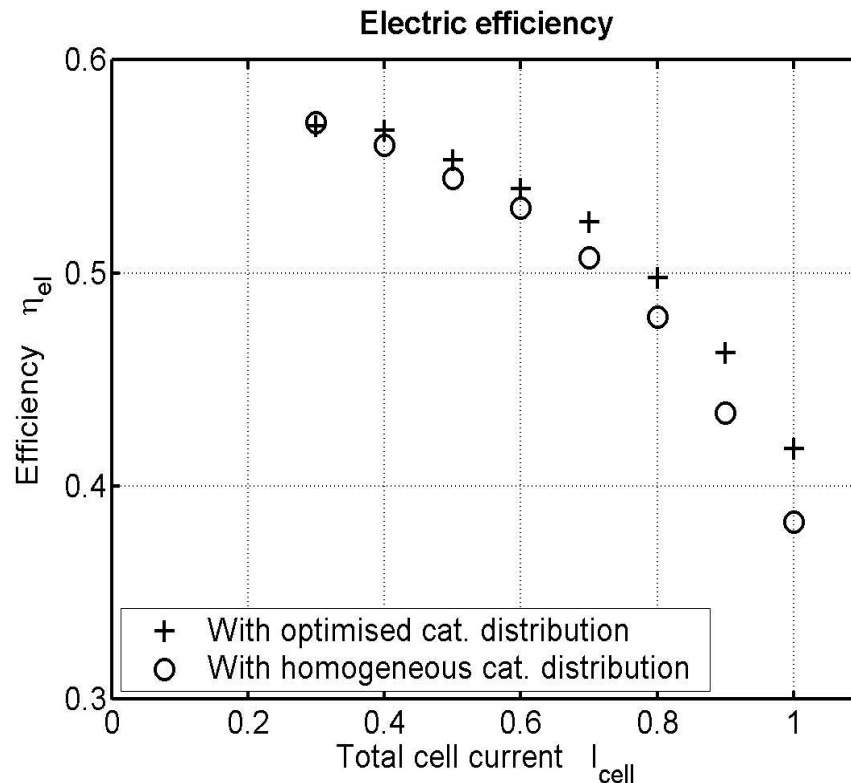


Figure 5.8: Electric efficiencies under different loads. Comparison of MFCs with homogeneous and distributed reforming catalyst. Inhomogeneous catalyst density optimised at $I_{cell}=0.7$ (Chapter 5.2.2).

5.3 Concluding remarks on optimisation

This chapter demonstrates the usefulness of the physically simplified two-dimensional model for optimisation purposes. Two optimisations are performed, both using a simple objective function with four (respectively eight) optimisation parameters and several inequality and equality constraints. The optimisation of operating conditions at various cell currents not only yields optimal input quantities at various cell currents, it also ensures that the resulting system states comply with the constraints concerning cell temperature, cell voltage and the thermodynamic possibility of carbon formation. The second optimisation also includes the reforming catalyst distribution inside the anode channel, which helps to homogenise the temperature field and thereby makes increased power output possible. This optimisation is performed at one load case, and its usefulness at all other load cases is evaluated.

Both types of optimisation take between one and 6 hours computation time, which is quite acceptable for offline optimisation. Their results are physically interpretable and lead to a significant increase of the cell performance, while the temperature restrictions are fulfilled. The optimal spatial distribution of the reforming catalyst inside the anode channel helps to homogenise the temperature profile. This allows to manipulate the input conditions in such a way that the electric efficiency is increased at all cell currents by up to 3.5%.

The Road goes ever on and on
Down from the door where it began.
Now far ahead the Road has gone,
And I must follow, if I can,
Pursuing it with eager feet,
Until it joins some larger way
Where many paths and errands meet.
And whither then? I cannot say.

John Ronald Reuel Tolkien

6 Conclusions and outlook

The main focus of this work is to establish a hierarchy of models for a single cross flow Molten Carbonate Fuel Cell (MCFC). These models will be applied in system design, optimisation and optimal control of MCFCs systems. A detailed reference model in dimensionless formulation is introduced as the top hierarchy element. This model considers a number of physical and chemical phenomena and is based on balances of mass and enthalpy. It includes a catalytic combustion chamber between the anode exhaust and the cathode inlet. The model not only allows to simulate the cell voltage at any given operating condition, but it also describes the spatially two-dimensional profiles of mole fractions and temperatures in the anode and cathode gas phases and the temperature profile in the solid parts of the cell. The reference model mainly serves as a basis for the derivation of reduced models for various applications. Two models are presented which are derived from the reference model: A physically reduced model and a steady state anode model.

The spatially one-dimensional, isothermal steady state anode model focusses on the conceptual issues of the integration of the reforming and the oxidation process within MCFCs. Together with its accompanying conversion diagram the model is a useful tool for MCFC system design, because it allows to quickly compare different system configurations against each other by graphical and quantitative means. Additionally, the conversion diagram offers intuitive insight into the interplay of the reforming and the oxidation process in MCFC. Three applications are demonstrated in this work: a comparison of reforming concepts, the arrangement of fuel cells in cascades and the application of anode gas recycle. Essentially, this model teaches that the fundamentals even of highly complex systems like the MCFC can be formulated in a very compact and plausible manner.

The applications of the physically reduced model are different. This dynamic, spatially two-dimensional model allows to simulate steady state and transient behaviour of the cell. Besides qualitative insight into the system behaviour it also provides quantitative information on the system's performance. Especially the cell temperature is of high interest for the cell's performance and its life time, it must be kept within an admissible temperature range. It is a

result of the heat sources and sinks (the electrochemical and the reforming reactions, respectively), the heat exchange between the solid and both gas phases and the convective and conductive heat transport in the gas phases and the solid. In dynamic scenarios like the stepwise load change demonstrated in this work, it shows that the MCFC is governed by time constants of three different orders of magnitude. Very fast processes like the charging of the electrode double layers happen within the milli-second range. Mass and energy balances in the gas phases have time constants in the range of a few seconds, and the slowest processes are temperature changes of the solid cell compartments, which typically take several hours.

Based on the physically reduced model, an optimisation of the input variables provides optimal operating conditions at various electric loads. These conditions grant the highest possible electric efficiency while the safety of the system with respect to temperature is ensured. From the steady state simulations, the cooling effect of the endothermic reforming process is known. The objective of another optimisation is to purposefully use this effect. Therefore, the reforming catalyst is spatially distributed in such a way that the temperature field is homogenised. This again allows to adjust the input parameters to significantly increase the electric efficiency.

Currently, the model parameters are validated experimentally, so that transferability to the HotModule MCFC is ensured. Once the model is validated, the optimisation results can be verified with the HotModule. Other works are concerned with the derivation of further models in the model hierarchy by mathematical reduction methods. They are supposed to serve as a basis for the design of state observers and optimal control strategies.

Appendix

A.1 Derivation of the anode channel balance equations in dimensional form

Within this section, the derivations of a few chosen model equations are given. All variables in the following equations are in dimensional form, although sometimes identical symbols are used for their dimensionless counterparts. For easier reading there is no marking of dimensional variables.

Especially the gas phase balances deserve special interest, because their derivation is not always obvious. Afterwards, the solid phase enthalpy balance is derived.

Anode gas phase balance equations

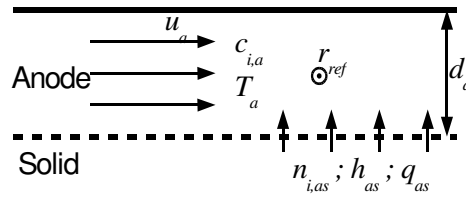


Figure A.1: Scheme for the balances at the anode gas channel.

Figure A.1 shows the states inside the anode channel and the fluxes influencing these states. The gas is described by the molar flow density, mole fractions and temperature. The fluxes are the mass flux density between gas phase and electrode pores and the enthalpy flux related to it, the heat exchange rate between anode and solid phase and the reaction rates in the gas phase.

The partial mass balance for the anode channel under model assumptions reads in dimensional form:

$$\frac{\partial c_{i,a}}{\partial t} = -\frac{\partial}{\partial z_1} (u_a \cdot c_{i,a}) + \frac{n_{i,as}}{d_a} + \sum_{j=ref} \nu_{i,j} r_j \quad (\text{A.1})$$

With

$$c_{t,a} = \sum_i c_{i,a} \quad (\text{A.2})$$

the total mass balance follows:

$$\frac{\partial c_{t,a}}{\partial t} = -\frac{\partial}{\partial z_1} (u_a \cdot c_{t,a}) + \sum_l \frac{n_{l,as}}{d_a} + \sum_{j=ref} \bar{\nu}_j r_j \quad (\text{A.3})$$

where

$$\bar{\nu}_j = \sum_i \nu_{i,j} \quad (\text{A.4})$$

The enthalpy balance reads

$$\frac{\partial}{\partial t} (c_{t,a} \bar{h}_a) = -\frac{\partial}{\partial z_1} (u_a c_{t,a} \bar{h}_a) + \frac{h_{as}^+}{d_a} + \frac{h_{as}^-}{d_a} + \frac{q_{as}}{d_a} \quad (\text{A.5})$$

Here \bar{h}_a is the average volume related enthalpy of the anode gas, h_{as}^+ and h_{as}^- are surface related enthalpy flux densities at the anode gas / electrode pores interface and d_a is the height of the anode channel. These enthalpies and the enthalpy fluxes are defined according to:

$$c_{t,a} \cdot \bar{h}_a = \sum_i c_{i,a} \cdot h_{f,i}(T_a) \quad (\text{A.6})$$

$$h_{as}^+ = \sum_i n_{i,as}^+ \cdot h_{f,i}(T_s) \quad (\text{A.7})$$

$$h_{as}^- = \sum_i n_{i,as}^- \cdot h_{f,i}(T_a) \quad (\text{A.8})$$

$$h_{f,i}(T) = h_{f,i}(T^\theta) + \int_{T^\theta}^T c_{p,i}(\Psi) d\Psi \quad (\text{A.9})$$

where

$$n_{i,as}^+ = \begin{cases} n_{i,as} & \text{if } n_{i,as} > 0 \\ 0 & \text{if } n_{i,as} \leq 0 \end{cases} \quad (\text{A.10})$$

$$n_{i,as}^- = \begin{cases} 0 & \text{if } n_{i,as} > 0 \\ n_{i,as} & \text{if } n_{i,as} \leq 0 \end{cases} \quad (\text{A.11})$$

A description in terms of mole fractions is desired. The definition of mole fractions is:

$$x_{i,a} = \frac{c_{i,a}}{c_{t,a}} \quad (\text{A.12})$$

Thus its derivative by time reads:

$$\frac{\partial x_{i,a}}{\partial t} = \frac{\partial}{\partial t} \left(\frac{c_{i,a}}{c_{t,a}} \right) = \dots = \frac{1}{c_{t,a}} \cdot \frac{\partial c_{i,a}}{\partial t} - \frac{x_{i,a}}{c_{t,a}} \cdot \frac{\partial c_{t,a}}{\partial t} \quad (\text{A.13})$$

Inserting the partial and the total mass balance (equations A.1 and A.3) yields the partial differential equation for the mole fractions in the anode channel:

$$c_{t,a} \frac{\partial x_{i,a}}{\partial t} = -g_a \cdot \frac{\partial x_{i,a}}{\partial z_1} + \frac{n_{i,as}}{d_a} - x_{i,a} \cdot \sum_l \frac{n_{l,as}}{d_a} + \sum_{j=ref} (v_{i,j} - x_{i,a} \bar{v}_j) r_j \quad (\text{A.14})$$

The volumetric gas velocity, u_a , has been replaced here by the molar flow density, g_a , according to

$$g_a = u_a \cdot c_{t,a} \quad (\text{A.15})$$

The energy balance is formulated in the enthalpy form. It is desirable to transform it into a form from which the temperature can be calculated explicitly. Therefore, the time derivative in balance Equation A.5 is manipulated using the definition of the average enthalpy, A.6:

$$\frac{\partial}{\partial t} (c_{t,a} \bar{h}_a) = \frac{\partial}{\partial t} \left(\sum_i c_{i,a} h_{f,i}(T_a) \right) = \sum_i c_{i,a} \frac{\partial h_{f,i}(T_a)}{\partial t} + \sum_i \frac{\partial c_{i,a}}{\partial t} h_{f,i}(T_a) \quad (\text{A.16})$$

The derivative of the enthalpy of formation with respect to time is reformulated by

$$\frac{\partial h_{fi}(T_a)}{\partial t} = \frac{\partial h_{fi}(T)}{\partial T} \bigg|_{T_a} \cdot \frac{\partial T_a}{\partial t} = c_{p,i}(T_a) \cdot \frac{\partial T_a}{\partial t} \quad (\text{A.17})$$

The spatial derivative in Equation A.5 is manipulated likewise:

$$\begin{aligned} \frac{\partial}{\partial z_1} (u_a c_{t,a} \bar{h}_a) &= \frac{\partial}{\partial z_1} \left(u_a \sum_i c_{i,a} h_{fi}(T_a) \right) \\ &= u_a \sum_i c_{i,a} \frac{\partial h_{fi}(T_a)}{\partial z_1} + \sum_i \frac{\partial}{\partial z_1} (u_a c_{i,a}) \cdot h_{fi}(T_a) \end{aligned} \quad (\text{A.18})$$

Both equations, A.16 and A.18, are inserted into the enthalpy balance. The partial mass balance A.1 is then subtracted from it, eliminating several derivative terms. After some manipulation, the result is the enthalpy balance in temperature form:

$$c_{t,a} \bar{c}_{p,a} \frac{\partial T_a}{\partial t} = -g_a \bar{c}_{p,a} \frac{\partial T_a}{\partial z_1} + \sum_i \frac{n_{i,as}^+}{d_a} \int_{T_s}^{T_a} c_{p,i}(\Psi) d\Psi + \sum_{j=ref} (-\Delta_R h_j(T_a)) r_j + \frac{q_{as}}{d_a} \quad (\text{A.19})$$

where the enthalpy of reaction is calculated according to

$$(-\Delta_R h_j(T_a)) = -\sum_i \nu_{ij} \cdot h_{fi}(T_a) \quad (\text{A.20})$$

According to the ideal gas law, the total concentration in the total mass balance must adhere to

$$c_{t,a} = \frac{p}{RT_a} \quad (\text{A.21})$$

With R as a constant and the assumption of constant pressure in the channel, the derivative with respect to time is

$$\frac{\partial c_{t,a}}{\partial t} = \frac{p}{R} \frac{\partial T_a^{-1}}{\partial t} = -\frac{p}{RT_a^2} \cdot \frac{\partial T_a}{\partial t} = -\frac{c_{t,a}}{T_a} \cdot \frac{\partial T_a}{\partial t} \quad (\text{A.22})$$

The total mass balance A.3 and the enthalpy balance in temperature form are inserted here. After some manipulation the result is an ordinary differential equation for the calculation of the molar flow density in the anode channel:

$$\begin{aligned} 0 = -\frac{\partial}{\partial z_1} (T_a g_a) + \frac{1}{\bar{c}_{p,a}} &\left(\sum_i \frac{n_{i,as}^+}{d_a} \int_{T_s}^{T_a} c_{p,i}(\Psi) d\Psi + \sum_{j=ref} (-\Delta_R h_j(T_a)) r_j + \frac{q_{as}}{d_a} \right) \\ &+ T_a \left(\sum_i \frac{n_{i,as}}{d_a} + \sum_{j=ref} \bar{\nu}_j r_j \right) \end{aligned} \quad (\text{A.23})$$

Thus the three balance equations A.14, A.19 and A.23 for the anode channel are derived in dimensional form. The derivation of the corresponding cathode equations is similar and is not given here in detail.

Solid phase enthalpy balance

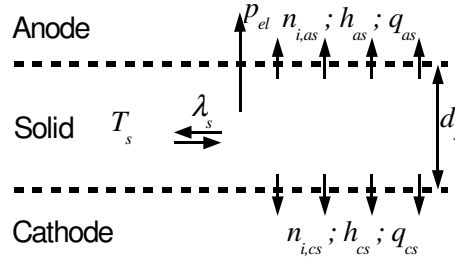


Figure A.2: Scheme for the enthalpy balance in the solid phase.

The enthalpy balance of the solid phase considers heat conduction in the cell plane, enthalpy fluxes between both gas phases and the solid phase, heat exchange between gas and solid phases and the flow of electric energy out of the solid phase (Figure A.2):

$$d_s \frac{\partial h_s}{\partial t} = d_s \frac{\partial}{\partial z_1} \left(\lambda_s \cdot \frac{\partial T_s}{\partial z_1} \right) + d_s \frac{\partial}{\partial z_2} \left(\lambda_s \cdot \frac{\partial T_s}{\partial z_2} \right) - h_{as}^+ - h_{as}^- - h_{cs}^+ - h_{cs}^- - q_{as} - q_{cs} - p_{el} \quad (\text{A.24})$$

The solid phase enthalpy can be split into two parts: the enthalpy stored in the immobile cell parts like channel walls, electrode material and the electrolyte on the one hand and the enthalpy of the gaseous components in the electrode pores on the other hand.

$$h_s = h_{s,1} + h_{s,2} \quad (\text{A.25})$$

The enthalpy of the immobilised parts reads:

$$h_{s,1} = h_s^0(T^0) + \int_{T^0}^{T_s} c_s \rho_s d\Psi \quad (\text{A.26})$$

With constant density and heat capacity its derivative with respect to time reads:

$$\frac{\partial h_{s,1}}{\partial t} = c_s \rho_s \frac{\partial T_s}{\partial t} \quad (\text{A.27})$$

The other part is the sum of the enthalpy of all chemical species stored in the electrode pores:

$$d_s h_{s,2} = \sum_i c_{i,ac} d_{ac} h_{f,i}(T_s) + \sum_i c_{i,cc} d_{cc} h_{f,i}(T_s) \quad (\text{A.28})$$

Its time derivative reads:

$$\begin{aligned} d_s \frac{\partial h_{s,2}}{\partial t} = & \left(d_{ac} \sum_i c_{i,ac} c_{p,i}(T_s) + d_{cc} \sum_i c_{i,cc} c_{p,i}(T_s) \right) \frac{\partial T_s}{\partial t} \\ & + d_{ac} \sum_i \frac{\partial c_{i,ac}}{\partial t} h_{f,i}(T_s) + d_{cc} \sum_i \frac{\partial c_{i,cc}}{\partial t} h_{f,i}(T_s) \end{aligned} \quad (\text{A.29})$$

The partial mass balances in the electrode pores describe the required concentration changes:

$$d_{ac} \frac{\partial c_{i,ac}}{\partial t} = -n_{i,as} + \sum_{j=ox} \nu_{ij} r_j \quad (\text{A.30})$$

$$d_{cc} \frac{\partial c_{i,cc}}{\partial t} = -n_{i,cs} + \sum_{j=red} \nu_{ij} r_j \quad (\text{A.31})$$

With this, the left hand side of the enthalpy balance (Equation A.24) reads:

$$\begin{aligned} d_s \frac{\partial h_s}{\partial t} = & \left(d_{ac} \sum_i c_{i,ac} c_{p,i}(T_s) + d_{cc} \sum_i c_{i,cc} c_{p,i}(T_s) + d_s c_s \rho_s \right) \cdot \frac{\partial T_s}{\partial t} \\ & + \sum_i (-n_{i,as}) h_{f,i}(T_s) + \sum_{j=ox} (-\Delta_R h_j(T_s)) \cdot r_j \\ & + \sum_i (-n_{i,cs}) h_{f,i}(T_s) + \sum_{j=red} (-\Delta_R h_j(T_s)) \cdot r_j \end{aligned} \quad (\text{A.32})$$

The heat capacity is assembled of three different terms, one for the immobile parts of the cell and two terms for the chemical components in the electrode pores. A rough estimate of their order of magnitude shows that the capacity of the gas components is negligible compared to the capacity of the immobile parts:

$$d_{ac} \sum_i c_{i,ac} c_{p,i}(T_s) \approx d_{cc} \sum_i c_{i,cc} c_{p,i}(T_s) \ll d_s c_s \rho_s \quad (\text{A.33})$$

On the right hand side of the enthalpy equation (A.24), the enthalpy flux densities are described by equations A.7 and A.8, while the electric power taken out of the system is:

$$p_{el} = i \cdot U_{cell} = i \cdot (\phi_c^S - \phi_a^S) \quad (\text{A.34})$$

Inserting all this into Equation A.24 and assuming a constant heat conductivity, several terms are eliminated and after some manipulation one receives:

$$\begin{aligned} d_s c_s \rho_s \frac{\partial T_s}{\partial t} = & d_s \lambda_s \frac{\partial^2 T_s}{\partial z_1^2} + d_s \lambda_s \frac{\partial^2 T_s}{\partial z_2^2} + \sum_i (-n_{i,as}^-) \int_{T_s}^{T_a} c_{p,i}(\psi) d\psi \\ & + \sum_i (-n_{i,cs}^-) \int_{T_s}^{T_c} c_{p,i}(\psi) d\psi - q_{as} - q_{cs} + q_s \end{aligned} \quad (\text{A.35})$$

where

$$q_s = \sum_{j=ox} (-\Delta_R h_j(T_s)) \cdot r_j + \sum_{j=red} (-\Delta_R h_j(T_s)) \cdot r_j - i \cdot (\phi_c^S - \phi_a^S) \quad (\text{A.36})$$

This equation describes the change of solid temperature, T_s , due to heat conduction, due to gas components entering the electrode pores at a different temperature than solid temperature, due to heat exchange with both gas phases and due to heat released by the electrochemical reactions. Here, the reaction heat term considers the full heat of each electrochemical reaction and diminishes this sum by the electric power delivered by the system. With Faraday's law (Equations 2.86 and 2.87) and if the electric potentials are at steady state (Equations 2.81, 2.82 and 2.83), the heat source term from Equation A.36 can be rewritten as:

$$\begin{aligned} q_s = & \sum_{j=ox} \left(-\Delta_R h_j(T_s) + n_j F (\phi_a^S - \phi_a^L) \right) \cdot r_j \\ & + \sum_{j=red} \left(-\Delta_R h_j(T_s) + n_j F (\phi_c^S - \phi_c^L) \right) \cdot r_j \\ & - i \cdot (\phi_c^L - \phi_a^L) \end{aligned} \quad (\text{A.37})$$

In this form, the heat source is interpreted as the heat of each electrochemical reaction diminished by its individual contribution to the electric cell power plus the heat released due

to ion transport. Strictly, this version may only be applied under the assumption of steady state charge balances. Due to the fact that the time constants of the charge balances are very much smaller than those of the solid phase enthalpy balance (by roughly 6 to 9 orders of magnitude), this second version does not show any detectable deviation from a calculation using the version in Equation A.36.

A.2 Transformation of model equations into dimensionless form

In this section the transformation of the dimensional equations into dimensionless form is demonstrated. The mass and energy balances of the anode channel and the energy balance of the solid phase, which are derived in dimensional form in Appendix A.1, are used as examples to show the procedure. In each case, the model equation is multiplied with certain term composed of standard values. Afterwards, suitable groups of variables are connected to dimensionless parameters. Please note that in this section some variables have similar symbols in their dimensional and dimensionless form. In this case, the dimensional variable is always marked with a tilde. In addition, all dimensionless equations are marked and no equation contains dimensionless and dimensional variables at the same time.

The partial mass balance of the anode channel reads (cf. Equation A.14):

$$c_{i,a} \frac{\partial x_{i,a}}{\partial t} = -g_a \cdot \frac{\partial x_{i,a}}{\partial z_1} + \frac{\tilde{n}_{i,as}}{d_a} - x_{i,a} \cdot \sum_l \frac{\tilde{n}_{l,as}}{d_a} + \sum_{j=ref} (v_{ij} - x_{i,a} \bar{v}_j) \tilde{r}_j \quad (\text{A.38})$$

The time, t , is made dimensionless by division with the standard time, t^θ , which is defined in Equation 2.133:

$$t^\theta = \frac{V^\theta \cdot c_t^\theta}{G^\theta} \quad (\text{A.39})$$

The total concentration, $c_{i,a}$, is made dimensionless by the standard total concentration according to the ideal gas law (Equation 2.120):

$$c_t^\theta = \frac{p^\theta}{RT^\theta} \quad (\text{A.40})$$

Thus, the complete equation is multiplied with the term

$$\frac{t^\theta}{c_t^\theta} = \frac{V^\theta}{G^\theta} \quad (\text{A.41})$$

After regrouping follows

$$\begin{aligned} \frac{c_{i,a}}{c_t^\theta} \cdot \frac{\partial x_{i,a}}{\partial t/t^\theta} = & \frac{g_a L_2 d_a}{G^\theta} \left(\frac{V^\theta}{L_1 L_2 d_a} \right) \frac{\partial x_{i,a}}{\partial z_1/L_1} + \frac{\tilde{n}_{i,as} L_1 L_2}{G^\theta} \left(\frac{V^\theta}{L_1 L_2 d_a} \right) \\ & - x_{i,a} \cdot \sum_l \frac{\tilde{n}_{l,as} L_1 L_2}{G^\theta} \left(\frac{V^\theta}{L_1 L_2 d_a} \right) + \sum_{j=ref} (v_{ij} - x_{i,a} \bar{v}_j) \frac{r_j^\theta L_1 L_2 d_a}{G^\theta} \left(\frac{V^\theta}{L_1 L_2 d_a} \right) \frac{\tilde{r}_j}{r_j^\theta} \end{aligned} \quad (\text{A.42})$$

In this equation, all variables are grouped into dimensionless groups with specific physical interpretations. They are replaced by dimensionless parameters and variables, which are

listed in Symbol Table 1. The ratio of the standard volume, V^θ , and the anode volume (marked with dotted lines) appears in every term on the right hand side. It is multiplied to the left hand side of the equation. The ratio of total concentrations reads according to the ideal gas law:

$$\frac{c_{i,a}}{c_i^\theta} = \frac{p}{RT_a} \cdot \frac{RT^\theta}{p} = \frac{T^\theta}{T_a} \quad (\text{A.43})$$

This leads to the following dimensionless partial mass balance for the anode gas phase (Equation 2.19):

$$\frac{V_a}{\vartheta_a} \frac{\partial X_{i,a}}{\partial \tau} = -\gamma_a \frac{\partial X_{i,a}}{\partial \zeta_1} + n_{i,as} - X_{i,a} \sum_l n_{l,as} + \sum_{j=ref} (v_{ij} - X_{i,a} \bar{v}_j) Da_j r_j \quad (\text{dim.-less}) \quad (\text{A.44})$$

The dimensional enthalpy balance in temperature form for the anode gas phase reads (Equation A.19):

$$c_{i,a} \tilde{c}_{p,a} \frac{\partial T_a}{\partial t} = -g_a \tilde{c}_{p,a} \frac{\partial T_a}{\partial z_1} + \sum_i \frac{\tilde{n}_{i,as}^+}{d_a} \int_{T_a}^{T_s} c_{p,i}(\psi) d\psi + \sum_{j=ref} (-\Delta_R \tilde{h}_j(T_a)) \tilde{r}_j + \frac{\tilde{q}_{as}}{d_a} \quad (\text{A.45})$$

This equation is multiplied with

$$\frac{t^\theta}{c_i^\theta c_p^\theta T^\theta} = \frac{V^\theta}{G^\theta c_p^\theta T^\theta} \quad (\text{A.46})$$

After regrouping, the result reads:

$$\begin{aligned} \frac{c_{i,a}}{c_i^\theta} \frac{\tilde{c}_{p,a}}{c_p^\theta} \frac{\partial T_a / T^\theta}{\partial t / t^\theta} &= -\frac{g_a L_2 d_a}{G^\theta} \frac{\tilde{c}_{p,a}}{c_p^\theta} \frac{\partial T_a / T^\theta}{\partial z_1 / L_1} \frac{V^\theta}{L_1 L_2 d_a} \\ &+ \sum_i \frac{\tilde{n}_{i,as}^+ L_1 L_2}{G^\theta} \frac{V^\theta}{L_1 L_2 d_a} \int_{T_a / T^\theta}^{T_s / T^\theta} \frac{c_{p,i}}{c_p^\theta}(\psi / T^\theta) d\psi / T^\theta \\ &+ \sum_{j=ref} \frac{-\Delta_R \tilde{h}_j(T_a) r_j L_1 L_2 d_a}{c_p^\theta T^\theta} \frac{V^\theta}{G^\theta} \frac{\tilde{r}_j}{L_1 L_2 d_a r_j} + \frac{\tilde{q}_{as} L_1 L_2}{G^\theta c_p^\theta T^\theta} \frac{V^\theta}{L_1 L_2 d_a} \end{aligned} \quad (\text{A.47})$$

Replacing the parameter groups with dimensionless variables leads to the dimensionless form (Equation 2.20):

$$\begin{aligned} V_a \frac{c_{p,a}}{\vartheta_a} \frac{\partial \vartheta_a}{\partial \tau} &= -\gamma_a c_{p,a} \frac{\partial \vartheta_a}{\partial \zeta_1} + \sum_i n_{i,as}^+ \int_{\vartheta_a}^{\vartheta_s} c_{p,i}(\Psi) d\Psi \\ &+ \sum_{j=ref} (-\Delta_R h_j^0(\vartheta_a)) Da_j r_j + q_{as} \end{aligned} \quad (\text{dim.-less}) \quad (\text{A.48})$$

The dimensional heat flux density, \tilde{q}_{as} , is defined via a heat exchange coefficient. Inserting it into the corresponding dimensionless parameter group in Equation A.47 yields:

$$\frac{\tilde{q}_{as} L_1 L_2}{G^\theta c_p^\theta T^\theta} = \frac{k_{as} L_1 L_2}{G^\theta c_p^\theta} \frac{T_s - T_a}{T^\theta} \quad (\text{A.49})$$

The Stanton number is defined according to this equation (cf. Symbol Table 1).

The transformation of the total mass balance of the anode phase is not shown here, because it essentially contains the same terms as the partial mass balance and the enthalpy balance, and therefore this transformation offers nothing new.

The solid phase enthalpy balance is transformed into dimensionless form in a similar way. For easier reading, only the accumulation term, the two heat conduction terms and one general heat source term of the solid enthalpy balance (Equation A.35) is discussed here. All other terms are treated like many others in the anode equations. The simplified solid enthalpy balance reads:

$$d_s c_s \rho_s \frac{\partial T_s}{\partial t} = d_s \lambda_s \frac{\partial^2 T_s}{\partial z_1^2} + d_s \lambda_s \frac{\partial^2 T_s}{\partial z_2^2} + \tilde{q} \quad (\text{A.50})$$

The equation is multiplied with the term

$$\frac{t^\theta \cdot L_1 L_2}{T^\theta V^\theta c_t^\theta c_p^\theta} = \frac{L_1 L_2}{T^\theta G^\theta c_p^\theta} \quad (\text{A.51})$$

The result reads:

$$\frac{L_1 L_2 d_s c_s \rho_s}{V^\theta c_p^\theta c_t^\theta} \cdot \frac{\partial T_s / T^\theta}{\partial t / t^\theta} = \frac{d_s \lambda_s}{G^\theta c_p^\theta} \cdot \frac{L_2}{L_1} \cdot \frac{\partial^2 T_s / T^\theta}{\partial (z_1 / L_1)^2} + \frac{d_s \lambda_s}{G^\theta c_p^\theta} \cdot \frac{L_1}{L_2} \cdot \frac{\partial^2 T_s / T^\theta}{\partial (z_2 / L_2)^2} + \frac{\tilde{q} L_1 L_2}{G^\theta c_p^\theta T^\theta} \quad (\text{A.52})$$

From this, the dimensionless enthalpy balance of the solid phase follows (cf. Equation 2.72):

$$c_{p,s} \frac{\partial \vartheta_s}{\partial \tau} = \frac{l_2}{Pe_s} \frac{\partial^2 \vartheta_s}{\partial \zeta_1^2} + \frac{1}{l_2 Pe_s} \frac{\partial^2 \vartheta_s}{\partial \zeta_2^2} + q \quad (\text{dim.-less}) \quad (\text{A.53})$$

With this, the method of the transformation into dimensionless form is demonstrated. All other equations are transformed accordingly.

A.3 Spatial discretisation of the model equations

For the numerical integration of the partial differential equations, a spatial discretisation of the dimensionless equations is required prior to implementation in software code. Here the finite volume method (FVM) is used. Although it is applied to all spatially distributed states and variables, only the resulting discretised equations for the gas phase and solid phase balances are presented here.

Anode phase balances

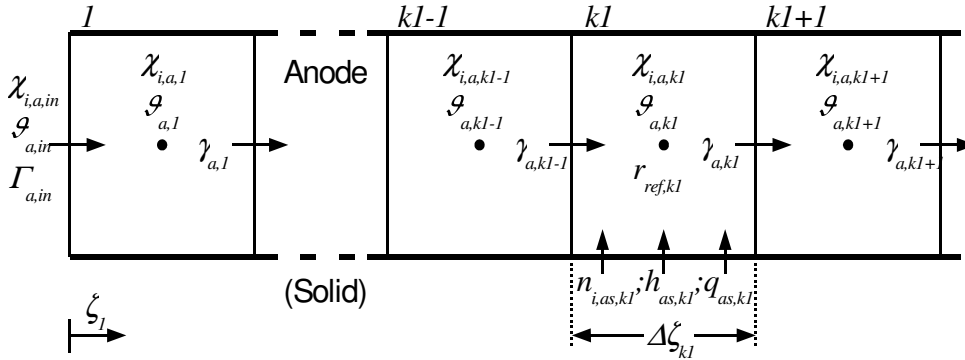


Figure A.3: Discretisation scheme for the equations in the anode gas phase.

The dimensionless anode phase equations are introduced in Chapter 2.1.3.1. The flow direction in the anode channels is assumed to be positive at all times, so a backward difference scheme (see Figure A.3) is applied. kl denotes the volume index along ζ_1 . For easier reading, the volume index along ζ_2 , $k2$, is omitted. Thus the partial mass balance in discretised form reads:

$$\begin{aligned} \frac{V_a}{\vartheta_{a,1}} \frac{d\chi_{i,a,1}}{d\tau} &= \gamma_{a,in} \frac{\chi_{i,a,in} - \chi_{i,a,1}}{\Delta\zeta_{1,1}} \\ &\quad + n_{i,as,1} - \chi_{i,a,1} \sum_l n_{l,as,1} + \sum_{j=ref} (\nu_{ij} - \chi_{i,a,1} \bar{\nu}_j) Da_j r_{j,1} \\ \frac{V_a}{\vartheta_{a,kl}} \frac{d\chi_{i,a,kl}}{d\tau} &= \gamma_{a,kl-1} \frac{\chi_{i,a,kl-1} - \chi_{i,a,kl}}{\Delta\zeta_{1,kl}} \\ &\quad + n_{i,as,kl} - \chi_{i,a,kl} \sum_l n_{l,as,kl} + \sum_{j=ref} (\nu_{ij} - \chi_{i,a,kl} \bar{\nu}_j) Da_j r_{j,kl} \end{aligned} \quad (\text{A.54})$$

The same discretisation scheme is applied to the total mass balance. This yields

$$\begin{aligned} \gamma_{a,1} \vartheta_{a,1} &= \Gamma_{a,in} \vartheta_{a,in} + \Delta\zeta_{1,1} \vartheta_{a,1} \cdot \left(\sum_i n_{i,as,1} + \sum_{j=ref} \bar{\nu}_j Da_j r_{j,1} \right) \\ &\quad + \frac{\Delta\zeta_{1,1}}{c_{p,a,1}} \left(\sum_i n_{i,as,1}^+ \int_{\vartheta_{a,1}}^{\vartheta_{a,1}} c_{p,i}(\psi) d\psi + \sum_{j=ref} (-\Delta_R h_j^0(\vartheta_{a,1})) Da_j r_{j,1} + q_{as,1} \right) \\ \gamma_{a,k} \vartheta_{a,kl} &= \gamma_{a,kl-1} \vartheta_{a,kl-1} + \Delta\zeta_{1,kl} \vartheta_{a,kl} \cdot \left(\sum_i n_{i,as,kl} + \sum_{j=ref} \bar{\nu}_j Da_j r_{j,kl} \right) \\ &\quad + \frac{\Delta\zeta_{1,kl}}{c_{p,a,kl}} \left(\sum_i n_{i,as,kl}^+ \int_{\vartheta_{a,kl}}^{\vartheta_{a,kl}} c_{p,i}(\psi) d\psi + \sum_{j=ref} (-\Delta_R h_j^0(\vartheta_{a,kl})) Da_j r_{j,kl} + q_{as,kl} \right) \end{aligned} \quad (\text{A.55})$$

with

$$kl = 2 \dots n_{z1} \quad (\text{A.56})$$

and $\Delta\zeta_{1,kl}$ as the length in ζ_1 -direction of the kl -th discretisation volume.

For the enthalpy balance the discretised equations are

$$\begin{aligned} \frac{V_a c_{p,a,l}}{\vartheta_{a,l}} \frac{d\vartheta_{a,l}}{d\tau} &= \gamma_{a,in} c_{p,a,in} \frac{\vartheta_{a,in} - \vartheta_{a,l}}{\Delta\zeta_{1,1}} + \sum_i n_{i,as,l}^+ \int_{\vartheta_{a,l}}^{\vartheta_{s,l}} c_{p,i}(\psi) d\psi \\ &\quad + \sum_{j=ref} (-\Delta_r h_j^0(\vartheta_{a,l})) Da_j r_{j,l} \quad (\text{A.57}) \\ \frac{V_a c_{p,a,kl}}{\vartheta_{a,kl}} \frac{d\vartheta_{a,kl}}{d\tau} &= \gamma_{a,kl-1} c_{p,a,kl-1} \frac{\vartheta_{a,kl-1} - \vartheta_{a,kl}}{\Delta\zeta_{1,kl}} + \sum_i n_{i,as,kl}^+ \int_{\vartheta_{a,kl}}^{\vartheta_{s,kl}} c_{p,i}(\psi) d\psi \\ &\quad + \sum_{j=ref} (-\Delta_r h_j^0(\vartheta_{a,kl})) Da_j r_{j,kl} \end{aligned}$$

57)

Comparing the discretised equations with those known from a cascade of spatially concentrated reactors (CSTR cascade), the reader will find them almost identical. Only in the enthalpy balance there is a small simplification concerning the temperature dependence of the heat capacities, which can be neglected for sufficiently small temperature and concentration differences between neighbouring volumes.

It should be mentioned here that the way to derive the enthalpy balances by FVM is not quite obvious. With the convective term as a mixed derivative term, the profile assumptions have to be chosen very carefully, or otherwise the different heat capacities of the volume inlet and inside the volume do not appear in the resulting equation. This difficulty can be avoided if the continuous enthalpy balance is formulated in terms of enthalpies together with thermodynamic algebraic equations for the relation of enthalpy with temperature. This balance equation can be discretised more easily. Inserting the thermodynamic equations into the discretised equation yields the discretised enthalpy balance in temperature form as it is given above. The cathode gas phase equations are discretised in a similar manner along the ζ_1 -coordinate.

Solid phase enthalpy balance

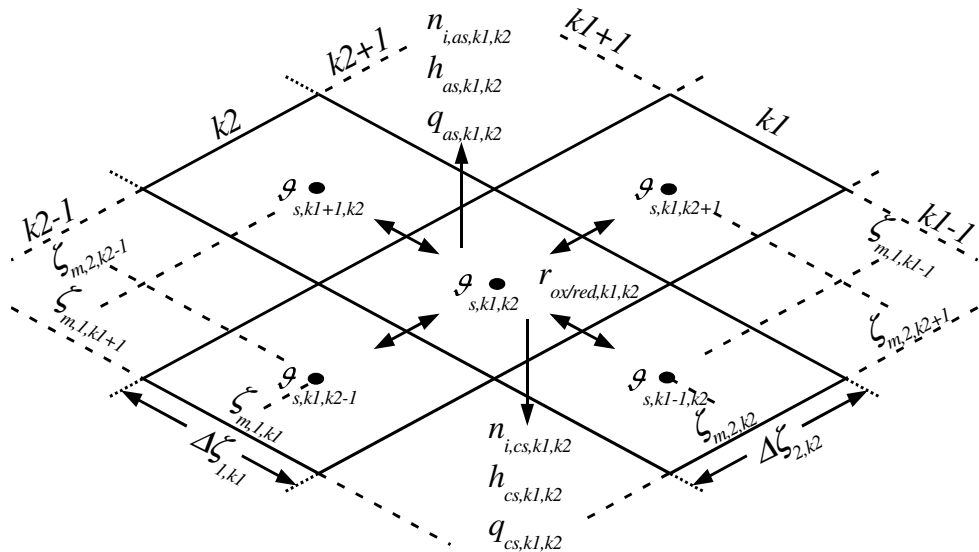


Figure A.4: Discretisation scheme for the enthalpy balance in the solid phase.

For the solid phase, the same grid of finite volumes is applied as for the gas phase discretisation. Due to the unsigned heat conduction term, a central difference scheme is applied (Figure A.4):

$$\begin{aligned}
c_{p,s} \frac{\partial \vartheta_{s,k1,k2}}{\partial \tau} = & \frac{l_2}{Pe_s} \left\{ \frac{\vartheta_{s,k1+1,k2} - \vartheta_{s,k1,k2}}{\zeta_{m,1,k1+1,k2} - \zeta_{m,1,k1,k2}} - \frac{\vartheta_{s,k1,k2} - \vartheta_{s,k1-1,k2}}{\zeta_{m,1,k1,k2} - \zeta_{m,1,k1-1,k2}} \right\} \frac{1}{\Delta \zeta_{1,k1,k2}} \\
+ & \frac{1}{Pe_s l_2} \left\{ \frac{\vartheta_{s,k1,k2+1} - \vartheta_{s,k1,k2}}{\zeta_{m,2,k1,k2+1} - \zeta_{m,2,k1,k2}} - \frac{\vartheta_{s,k1,k2} - \vartheta_{s,k1,k2-1}}{\zeta_{m,2,k1,k2} - \zeta_{m,2,k1,k2-1}} \right\} \frac{1}{\Delta \zeta_{2,k1,k2}} \\
+ & \sum_i (-n_{i,as,k1,k2}^-) \cdot \int_{\vartheta_{s,k1,k2}}^{\vartheta_{a,k1,k2}} c_{p,i}(\Psi) d\Psi + \sum_i (-n_{i,cs,k1,k2}^-) \cdot \int_{\vartheta_{s,k1,k2}}^{\vartheta_{c,k1,k2}} c_{p,i}(\Psi) d\Psi \\
- & q_{as,k1,k2} - q_{cs,k1,k2} + q_{s,k1,k2}
\end{aligned} \tag{A.58}$$

This ODE has to be adopted in each boundary volume element with regard to the insulation condition. This means that in these boundary volumes one or two of the temperature differences become zero. The resulting equations are not given here in detail.

A.4 Potential field models

In the fuel cell literature, the electric potential field is seldom modelled based on the description of physical phenomena. In this section, an attempt is made to establish this very vital part of a fuel cell model from the very basics. When modelling the electric field, it turns out that many variations of the potential field equations are possible. Each of them comes with its individual advantages and drawbacks, especially with respect to its numerical properties.

The common scheme of all model versions is given in Figure A.5. Here the two electrodes together with their charged double layers are shown. The electrodes are electrically connected to an external consumer. The gas channels are omitted here for clarity, they are above and below the electrodes, respectively. All models are based on a common set of simplifying assumptions:

- All charge layers are plane.
- The wires between the fuel cells electrodes and the external consumer are ideal current conductors with an infinite conductivity.
- Both electrodes are assumed to be ideal current conductors.
- The external consumer has a finite electric conductivity.
- The ion conductivity in the electrolyte is finite in the direction orthogonal to the cell plane. Due to the very small thickness of the electrolyte, its ion conductivity in cell plane direction is negligible.

The consequences of these assumptions are:

- There is no electric field along the external wires. Any current is transported through them without a gradient in electric potential.

- The infinite conductivity of the electrodes leads to spatially homogeneous electric potentials at the charged layers in both electrodes. Nevertheless, the charge density may be inhomogeneous.
- The neglected ion transport through the electrolyte in cell plane direction allows for a inhomogeneous distribution of charges and electric potential at both charge layers in the electrolyte.

Figure A.5 illustrates the charge densities and the electric potentials in such a system of flat charge layers according to the assumptions.

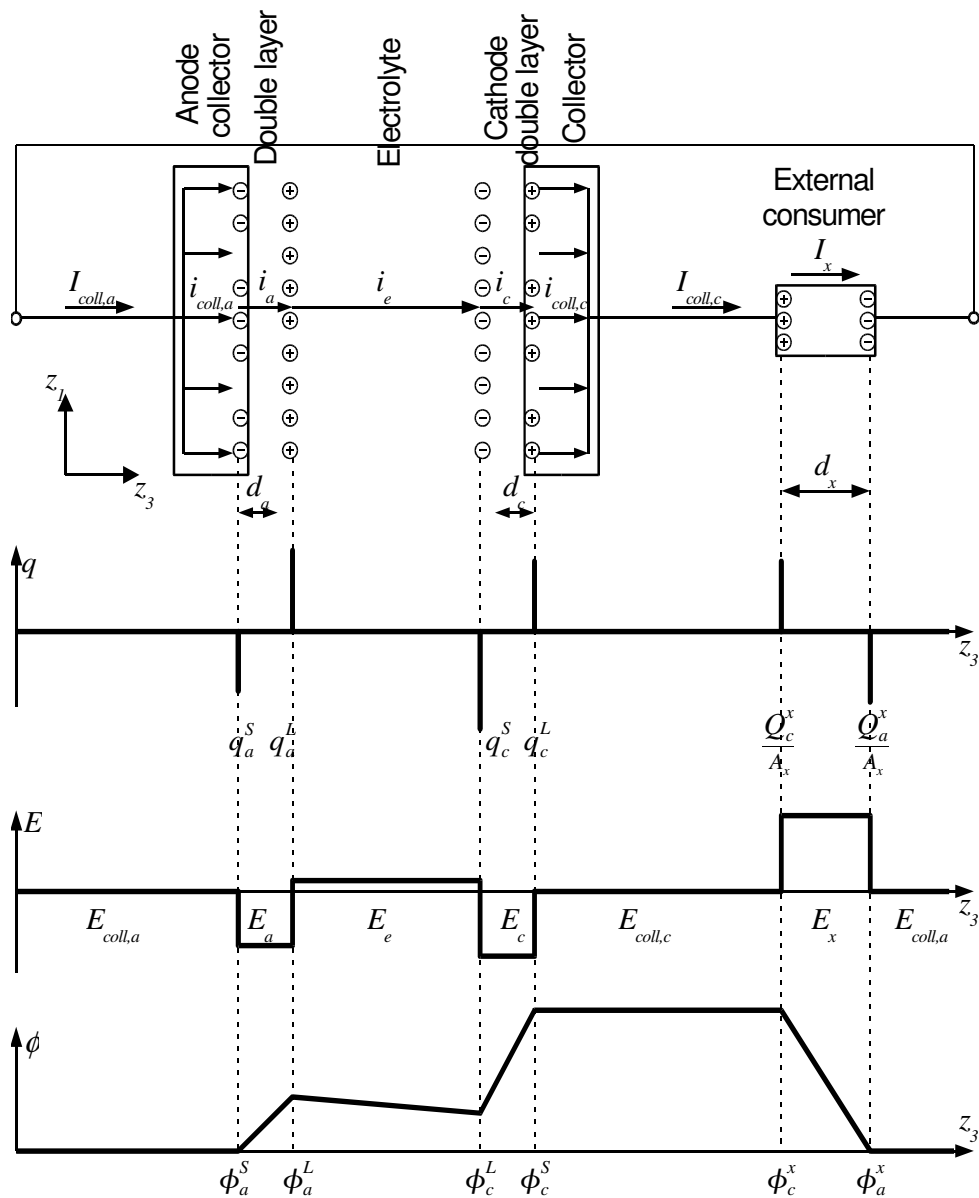


Figure A.5: Charge densities, electric field and electric potential in a fuel cell and an ohmic consumer.

The electric potential field is described by the Poisson equation, which in tensor notation reads:

$$\frac{\partial^2 \phi}{\partial \zeta_k^2} = -\frac{\rho}{\epsilon_0 \epsilon_r} \quad (\text{A.59})$$

Introducing the electric field, this equation can be split into

$$\frac{\partial \phi}{\partial \zeta_k} = -E_k \quad (\text{A.60})$$

$$\frac{\partial E_k}{\partial \zeta_k} = \frac{\rho}{\epsilon_0 \epsilon_r} \quad (\text{A.61})$$

Applying Equation A.61 in discretised form to the problem at hand (Figure A.5) one receives expressions for the electric fields:

$$\begin{aligned} E_{coll,a} &= 0 & E_a &= E_{coll,a} + \frac{q_a^S}{\epsilon_0} = \frac{q_a^S}{\epsilon_0} & E_e &= E_a + \frac{q_a^L}{\epsilon_0} = \frac{q_a^S + q_a^L}{\epsilon_0} \\ E_c &= E_e + \frac{q_c^L}{\epsilon_0} = \frac{q_a^S + q_a^L + q_c^L}{\epsilon_0} & E_{coll,c} &= E_c + \frac{q_c^S}{\epsilon_0} = \frac{q_a^S + q_a^L + q_c^L + q_c^S}{\epsilon_0} = 0 \\ E_x &= E_{coll,c} + \frac{Q_c^x}{A_x} = \frac{Q_c^x}{A_x} & E_{coll,a} &= E_x + \frac{Q_a^x}{A_x} = \frac{Q_c^x + Q_a^x}{A_x} = 0 \end{aligned} \quad (\text{A.62})$$

Here the dielectric coefficients of all substances are set to one. These material properties contribute to the electric capacities, c_a , c_e and c_c , which are unknown anyway.

From the condition that the electric fields in both collectors is zero, two conditions of electric neutrality follow:

$$q_a^S + q_a^L + q_c^L + q_c^S = 0 \quad (\text{A.63})$$

$$Q_a^x + Q_c^x = 0 \quad (\text{A.64})$$

Equation A.60 in discretised form describes the electric potential in terms of the electric field. Inserting Equation A.62 yields the following set of equations describing the electric potentials depending on the charge densities:

$$\phi_a^L(z_1) = \phi_a^S - E_a \cdot d_a = \phi_a^S - q_a^S \cdot \frac{1}{c_a} \quad (\text{A.65})$$

$$\phi_c^L(z_1) = \phi_a^L(z_1) - E_e \cdot d_e = \phi_a^L(z_1) - q_a^L \cdot \frac{1}{c_e} = \phi_a^S(z_1) - q_a^S \cdot \left(\frac{1}{c_a} + \frac{1}{c_e} \right) - q_a^L \cdot \frac{1}{c_e} \quad (\text{A.66})$$

$$\begin{aligned} \phi_c^S &= \phi_c^L(z_1) - E_c \cdot d_c = \phi_c^L(z_1) - q_c^L \cdot \frac{1}{c_c} \\ &= \phi_a^S - q_a^S \cdot \left(\frac{1}{c_a} + \frac{1}{c_e} + \frac{1}{c_c} \right) - q_a^L \cdot \left(\frac{1}{c_e} + \frac{1}{c_c} \right) - q_c^L \cdot \frac{1}{c_c} \end{aligned} \quad (\text{A.67})$$

$$\phi_c^x = \phi_c^S \quad (\text{A.68})$$

$$\phi_a^x = \phi_c^x - E_x \cdot d_x = \phi_c^x - Q_c^x \cdot \frac{1}{C_x} \quad (\text{A.69})$$

$$\phi_a^S = \phi_a^x \quad (\text{A.70})$$

The charge densities are subject to changes and are balanced as follows:

$$\frac{\partial q_a^S}{\partial t} = i_{coll,a} - i_a \quad (\text{A.71})$$

$$\frac{\partial q_a^L}{\partial t} = i_a - i_e \quad (\text{A.72})$$

$$\frac{\partial q_c^L}{\partial t} = i_e - i_c \quad (\text{A.73})$$

$$\frac{\partial q_c^S}{\partial t} = i_c - i_{coll,c} \quad (\text{A.74})$$

$$I_{coll,c} = \int_A i_{coll,c} dz_1 \quad (\text{A.75})$$

$$\frac{\partial Q_c^x}{\partial t} = I_{coll,c} - I_x \quad (\text{A.76})$$

$$\frac{\partial Q_a^x}{\partial t} = I_x - I_{coll,a} \quad (\text{A.77})$$

$$I_{coll,a} = \int_A i_{coll,a} dz_1 \quad (\text{A.78})$$

From the conditions of electric neutrality (Equations A.63 and A.64) follow

$$i_{coll,a} = i_{coll,c} \equiv i \quad (\text{A.79})$$

$$I_{coll,a} = I_{coll,c} \equiv I \quad (\text{A.80})$$

With these elements several potential field models are set up. They differ with respect to quasi steady state assumptions. The first is a fully dynamic model, the second neglects the charge dynamics of the external consumer and the third version is a complete steady state model. In potential fields, not the absolute value of the potential is important, but only differences are of interest. Thus one value may be fixed arbitrarily. This is done by setting the anode electrode potential to zero.

Fully dynamic version

The fully dynamic equation set considers all charge layers transient, including the charges in the electric consumer. Although it seems strange to balance charges at an electric load, especially as for systems more complex than an ohmic resistance this also becomes quite difficult, it helps to solve the complete equation system. The charge capacity of the load is assumed as a constant of the same size as the capacities of the anode and cathode double layers.

$$\phi_a^S = \phi_a^x = 0 \quad (\text{A.81})$$

$$\frac{\partial \phi_a^L(z_1)}{\partial t} = -\frac{1}{c_a} \cdot (i - i_a) \quad (\text{A.82})$$

$$\frac{\partial \phi_c^L(z_1)}{\partial t} = -\frac{1}{c_a} \cdot (i - i_a) - \frac{1}{c_e} \cdot (i - i_e) \quad (\text{A.83})$$

$$\frac{d\phi_c^S}{dt} = -\frac{1}{c_a} \cdot (i - i_a) - \frac{1}{c_e} \cdot (i - i_e) - \frac{1}{c_c} \cdot (i - i_c) = \frac{d\phi_c^x}{dt} \quad (\text{A.84})$$

$$\frac{d\phi_a^x}{dt} = -\frac{1}{c_a} \cdot (i - i_a) - \frac{1}{c_e} \cdot (i - i_e) - \frac{1}{c_c} \cdot (i - i_c) - \frac{1}{C_x} \cdot (I - I_x) = \frac{d\phi_a^S}{dt} = 0 \quad (\text{A.85})$$

where

$$I = \int_A i dz_1 \quad (\text{A.86})$$

Inserting Equation A.85 into the Equation A.84 simplifies the system a bit. The cell voltage is described by

$$\frac{d\phi_c^S}{dt} = \frac{1}{C_x} \cdot (I - I_x) \quad (\text{A.87})$$

The electric current through the external consumer is equal to the total cell current demanded:

$$I_x = I_{cell} \quad (\text{A.88})$$

Partially dynamic version

In this version, the charge balances in the external consumer are assumed to be in steady state. Thus follows:

$$\phi_a^S = 0 \quad (\text{A.89})$$

$$\frac{\partial \phi_a^L(z_1)}{\partial t} = -\frac{1}{c_a} \cdot (i - i_a) \quad (\text{A.90})$$

$$\frac{\partial \phi_c^L(z_1)}{\partial t} = -\frac{1}{c_a} \cdot (i - i_a) - \frac{1}{c_e} \cdot (i - i_e) \quad (\text{A.91})$$

$$\frac{d\phi_c^S}{dt} = -\frac{1}{c_a} \cdot (i - i_a) - \frac{1}{c_e} \cdot (i - i_e) - \frac{1}{c_c} \cdot (i - i_c) \quad (\text{A.92})$$

where

$$I = \int_A i dz_1 \quad (\text{A.93})$$

From the steady state charge balance at the external load follows:

$$I = I_{cell} = I_x \quad (\text{A.94})$$

The equation set only contains the collector current density i in an implicit way. An explicit equation can be achieved by manipulating Equation A.92 to

$$i = \left(\frac{1}{c_a} + \frac{1}{c_e} + \frac{1}{c_c} \right)^{-1} \cdot \left(\frac{i_a}{c_a} + \frac{i_e}{c_e} + \frac{i_c}{c_c} - \frac{d\phi_c^S}{dt} \right) \quad (\text{A.95})$$

Inserting this expression into the integral in Equation A.93 yields after some further manipulation:

$$\frac{d\phi_c^S}{dt} = \frac{I_a - I}{Ac_a} + \frac{I_e - I}{Ac_e} + \frac{I_c - I}{Ac_c} \quad (\text{A.96})$$

where

$$I_a = \int_A i_a dz_1 \quad ; \quad I_e = \int_A i_e dz_1 \quad ; \quad I_c = \int_A i_c dz_1 \quad (\text{A.97})$$

Equations A.95 and A.96 yield an explicit equation for the current density:

$$i = \left(\frac{1}{c_a} + \frac{1}{c_e} + \frac{1}{c_c} \right)^{-1} \cdot \left(\frac{i_a}{c_a} + \frac{i_e}{c_e} + \frac{i_c}{c_c} - \frac{I_a}{Ac_a} - \frac{I_e}{Ac_e} - \frac{I_c}{Ac_c} \right) + \frac{I}{A} \quad (\text{A.98})$$

Thus with equations A.89 to A.91 and A.96 to A.98 a fully explicit equation system of differential index 1 is available. It can be solved by any usual integration algorithm and is used throughout the simulations in this work. Due to very small double layer capacitances, the time constants of these equations are very small compared to the other time constants in the model. Therefore numerical solvers with good capabilities to solve stiff systems are needed.

Fully steady state version

Setting all charge balances to steady state yields a small set of algebraic equations:

$$i = i_a(\phi_a^L) = i_e(\phi_a^L, \phi_c^L) = i_c(\phi_c^L, \phi_c^S) \quad (\text{A.99})$$

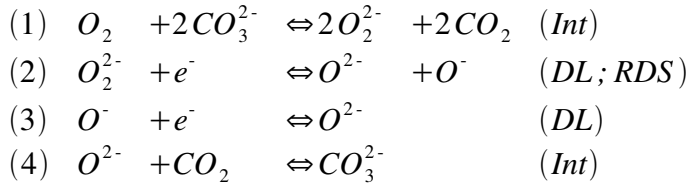
$$I_{cell} = \int_A i dz_1 \quad (\text{A.100})$$

Here, the unknown electric potentials occur implicitly in the current density expressions. Due to the size and nonlinearity of a discretised equation system, a powerful algebraic solver and quite good starting values are necessary to solve this model. Therefore its usefulness is rather limited.

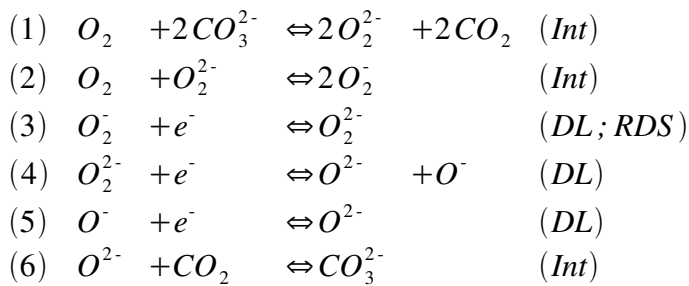
A.5 Kinetics of the reduction reaction

According to Prins-Jansen [26], there are five reaction mechanisms for the reduction reaction in MFCs. Some of these reaction mechanisms can be found in numerous articles about reaction kinetics ([24, 25]). These are:

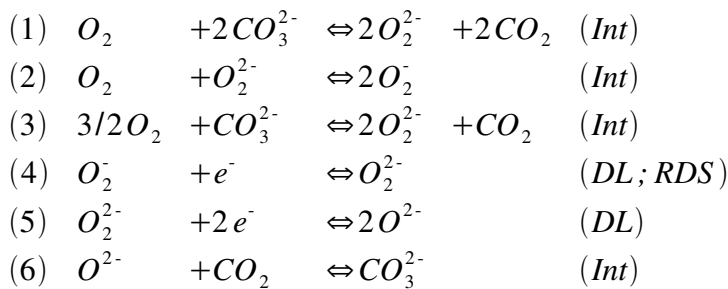
The peroxide mechanism



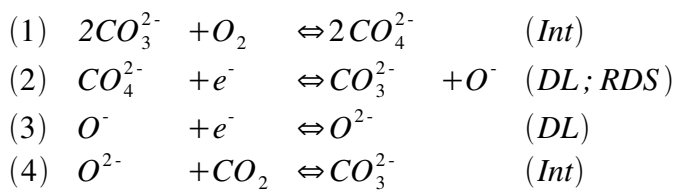
The superoxide mechanism (used in this work)



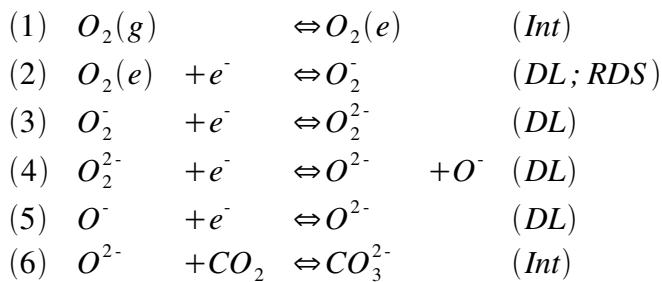
Variation of superoxide mechanism proposed by Bednarz [28]



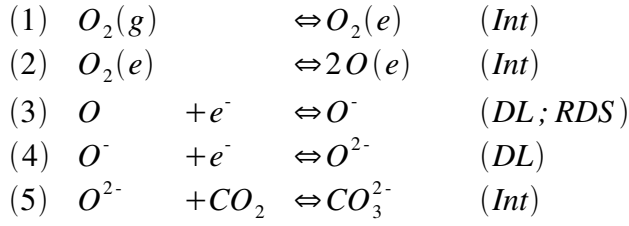
The peroxy carbonate mechanism



The oxygen mechanism I



The oxygen mechanism II



Here "Int" states that the reaction occurs near the gas / electrolyte interface while reaction steps marked with "DL" happen at the double layer. "RDS" denotes the rate determining step.

With only one rate determining step in each reaction mechanism, it is possible to derive one single rate expression for each mechanism by assuming equilibrium for all other reaction steps. As an example, this derivation is shown here for the peroxide mechanism. First, a reaction rate expression is required for each reaction step. These are assumed to be elementary reactions, so simple kinetics according to the power law apply here:

$$r_1 = k_1(T) \cdot \left(a_{O_2} \cdot (a_{CO_3^{2-}})^2 - (a_{O_2^{2-}})^2 \cdot (a_{CO_2})^2 \cdot \frac{1}{K_1(T)} \right) \quad (A.101)$$

$$\begin{aligned}
r_2 = k_2(T) \cdot & \left(\left(\frac{a_{O_2^{2-}}}{a_{O_2^{2-},ref}} \right) \cdot \exp\left(-0.5 \frac{F}{RT} (\Delta\phi - \Delta\phi_{0,2}(T))\right) \right. \\
& \left. - \left(\frac{a_{O^{2-}}}{a_{O^{2-},ref}} \right) \cdot \left(\frac{a_{O^-}}{a_{O^-,ref}} \right) \cdot \exp\left(0.5 \frac{F}{RT} (\Delta\phi - \Delta\phi_{0,2}(T))\right) \right) \quad (RDS) \quad (A.102)
\end{aligned}$$

$$\begin{aligned}
r_3 = k_3(T) \cdot & \left(\left(\frac{a_{O^-}}{a_{O^-,ref}} \right) \cdot \exp\left(-0.5 \frac{F}{RT} (\Delta\phi - \Delta\phi_{0,3}(T))\right) \right. \\
& \left. - \left(\frac{a_{O^{2-}}}{a_{O^{2-},ref}} \right) \cdot \exp\left(0.5 \frac{F}{RT} (\Delta\phi - \Delta\phi_{0,3}(T))\right) \right) \quad (A.103)
\end{aligned}$$

$$r_4 = k_4(T) \cdot \left(a_{O^{2-}} \cdot a_{CO_2} - a_{CO_3^{2-}} \cdot \frac{1}{K_4(T)} \right) \quad (A.104)$$

The activities within the reaction rate expressions are mostly unknown so far. Only the activity of the carbonate ion CO_3^{2-} is assumed to have a constant value. This assumption is justified, because the influence of consumption and production of carbonate ions does not significantly change the concentration of these.

Reaction steps 1, 3 and 4 being in equilibrium means that the forward and backward reaction rates are equal. This gives the opportunity to eliminate several unknown activities. From reaction 1 follows:

$$a_{O_2^{2-}} = K_1(T)^{1/2} \left(a_{O_2} \right)^{1/2} \frac{a_{CO_3^{2-}}}{a_{CO_2}} \quad (A.105)$$

For the reference activities it holds

$$a_{O_2^{2-},ref} = K_1(T)^{1/2} (a_{O_2,ref})^{1/2} \frac{a_{CO_3^{2-}}}{a_{CO_2,ref}} \quad (A.106)$$

From reaction 4 one gets

$$a_{O^{2-}} = \frac{a_{CO_3^{2-}}}{a_{CO_2}} \frac{1}{K_4(T)} \quad (A.107)$$

and

$$a_{O^{2-},ref} = \frac{a_{CO_3^{2-}}}{a_{CO_2,ref}} \frac{1}{K_4(T)} \quad (A.108)$$

The equilibrium condition of reaction 3 yields

$$\left(\frac{a_{O^-}}{a_{O^-,ref}} \right) = \left(\frac{a_{O^{2-}}}{a_{O^{2-},ref}} \right) \cdot \exp\left(\frac{F}{RT} (\Delta\phi - \Delta\phi_{0,3}(T)) \right) \quad (A.109)$$

Inserting these expressions into the rate expression of the rate determining step 2 results in

$$\begin{aligned} r_2 = k_2(T) \cdot & \left\{ \left(\frac{a_{O_2}}{a_{O_2,ref}} \right)^{1/2} \left(\frac{a_{CO_2}}{a_{CO_2,ref}} \right)^{-1} \cdot \exp\left(-0.5 \frac{F}{RT} (\Delta\phi - \Delta\phi_{0,2}(T)) \right) \right. \\ & \left. - \left(\frac{a_{CO_2}}{a_{CO_2,ref}} \right)^{-2} \cdot \exp\left(\frac{F}{RT} (\Delta\phi - \Delta\phi_{0,3}(T)) + 0.5 \frac{F}{RT} (\Delta\phi - \Delta\phi_{0,2}(T)) \right) \right\} \\ = k_2(T) \cdot \exp\left(0.5 \frac{F}{RT} \Delta\phi_{0,2}(T) \right) \cdot & \left\{ \left(\frac{a_{O_2}}{a_{O_2,ref}} \right)^{1/2} \left(\frac{a_{CO_2}}{a_{CO_2,ref}} \right)^{-1} \cdot \exp\left(-0.5 \frac{F}{RT} \Delta\phi \right) \right. \\ & \left. - \left(\frac{a_{CO_2}}{a_{CO_2,ref}} \right)^{-2} \cdot \exp\left(1.5 \frac{F}{RT} \Delta\phi - \frac{F}{RT} (\Delta\phi_{0,3}(T) + \Delta\phi_{0,2}(T)) \right) \right\} \end{aligned} \quad (A.110)$$

The activities of the dissolved gas components oxygen and carbon dioxide are related to their partial gas pressures via

$$a_i = H_i \cdot \frac{p_i}{p^\theta} \quad ; \quad i = \{O_2, CO_2\} \quad (A.111)$$

The activities in the reference case are correlated to the reference partial gas pressures:

$$a_{i,ref} = H_i \cdot \frac{p_{i,ref}}{p^\theta} = H_i \cdot \frac{p^\theta}{p^\theta} = H_i \quad ; \quad i = \{O_2, CO_2\} \quad (A.112)$$

Thus the activities in the reaction rate expression can be substituted by ratios of partial pressures:

$$\left(\frac{a_i}{a_{i,ref}} \right) = \left(\frac{p_i}{p^\theta} \right) \quad ; \quad i = \{O_2, CO_2\} \quad (A.113)$$

The equilibrium potential differences in Equation A.110 are defined as

$$\Delta\phi_{0,2} = \frac{1}{F} (\mu_{O_2^{2-},ref} - \mu_{O^{2-},ref} - \mu_{O^-,ref}) \quad (A.114)$$

$$\Delta \phi_{0,3} = \frac{1}{F} (\mu_{O^{\cdot-},ref} - \mu_{O_2^{\cdot-},ref}) \quad (A.115)$$

In addition, in the reference equilibrium case for all non-electrochemical reactions the sum of the chemical potential weighted by the stoichiometric factors is zero. For reaction 1 this gives

$$-\mu_{O_2,ref} - 2 \cdot \mu_{CO_3^{2-},ref} + 2 \cdot \mu_{O_2^{\cdot-},ref} + 2 \cdot \mu_{CO_2,ref} = 0 \quad (A.116)$$

From reaction 4 follows:

$$-\mu_{O_2^{\cdot-},ref} - \mu_{CO_2,ref} + \mu_{CO_3^{2-},ref} = 0 \quad (A.117)$$

The reference case is chosen so that the gas / liquid equilibrium yields:

$$\mu_{i,ref} = \mu_{i,ref}^{gas} = \mu_i^\theta + RT \ln \frac{P_{i,ref}}{p^\theta} = \mu_i^\theta \quad (A.118)$$

With this the expression containing the equilibrium potential differences can be modified:

$$\frac{F}{RT} (\Delta \phi_{0,3}(T) + \Delta \phi_{0,2}(T)) = \frac{1}{RT} \left(\frac{1}{2} \mu_{O_2}^\theta + \mu_{CO_2}^\theta - \mu_{CO_3^{2-}}^\theta \right) = \frac{2F}{RT} \Delta \phi_0 \quad (A.119)$$

Here

$$\Delta \phi_0 = \frac{1}{2F} \left(\frac{1}{2} \mu_{O_2}^\theta + \mu_{CO_2}^\theta - \mu_{CO_3^{2-}}^\theta \right) \quad (A.120)$$

is the standard equilibrium potential of the overall reduction reaction based on the chemical potential of the gases and the carbonate ion. After short manipulation one receives the overall reaction rate expression

$$r_2 = \tilde{k}_2(T) \cdot \left\{ \left(\frac{P_{O_2}}{p^\theta} \right)^{1/2} \left(\frac{P_{CO_2}}{p^\theta} \right)^{-1} \cdot \exp \left(-0.5 \frac{F}{RT} (\Delta \phi - \Delta \phi_0) \right) - \left(\frac{P_{CO_2}}{p^\theta} \right)^{-2} \cdot \exp \left(1.5 \frac{F}{RT} (\Delta \phi - \Delta \phi_0) \right) \right\} \quad (A.121)$$

with

$$\begin{aligned} \tilde{k}_2(T) &= k_2^0 \cdot \exp \left(-\frac{E_{A,2}}{RT} \right) \cdot \exp \left(0.5 \frac{F}{RT} (\Delta \phi_{0,2}(T) - \Delta \phi_0(T)) \right) \\ &= k_2^0 \cdot \exp \left(\frac{1}{RT} (-E_{A,2} + 0.5 \cdot (\Delta \phi_{0,2}(T) - \Delta \phi_0(T))) \right) \\ &\approx k_2^0 \cdot \exp \left(\frac{1}{RT} (-\tilde{E}_{A,2}) \right) \end{aligned} \quad (A.122)$$

This is the overall reaction rate expression for the first mentioned reaction mechanism, the peroxide mechanism. The expressions for all other reaction paths can be derived analogously. While the general shape of the results is always similar, the exponents and the apparent transition factors are different for each mechanism. The results for all five reaction paths are given in the section 2.1.3.8 "Reaction kinetics". The reaction rate expression for the modified superoxide mechanism by Bednarz is identical to that of the original superoxide mechanism.

A.6 Parameter values of the base case configuration

The base case is frequently referred to within this work. Therefore the complete set of parameters used in this case is given here. The parameters are grouped according to their interpretation in system theory and their physical meaning in Table A.4. All parameter values of the reduced model model which differ from their counterparts in the reference model are given in Table A.5.

Table A.4: System and input parameter values of the base case configuration.

System parameters: Reaction kinetics					
	ref1	ref2	ox1	ox2	red
Da_j	25.0	100.0	5.0	5.0	0.3
Arr_j	84.4	6.2	21.6	21.6	31.2
ϑ_j^0	2.93	2.93	2.93	2.93	2.93
System parameters: Thermodynamics					
$A_{i,1..4}$		$A_{i,1}$	$A_{i,2}$	$A_{i,3}$	$A_{i,4}$
	CH_4	1.4353	2.7831	0.1923	-0.1967
	H_2O	4.1347	0.2810	-0.5743	0.0
	H_2	3.2333	0.1285	0.1422	0.0
	CO	3.7241	0.0874	-0.3792	0.0
	CO_2	6.1496	0.1566	-1.9897	0.0
	O_2	3.5066	0.2322	-0.2492	0.0
	N_2	3.6586	0.0912	-0.3224	0.0
$s_{f,i}(1)$	CH_4	22.4021			
	H_2O	22.7116			
	H_2	15.7179			
	CO	23.7729			
	CO_2	25.7149			
	O_2	24.6748			
	N_2	23.0647			
$h_{f,i}(1)$	CH_4	-30.2199			
	H_2O	-97.6182			
	H_2	0.0			
	CO	-44.6114			
	CO_2	-158.8333			
	O_2	0.0			
	N_2	0.0			
$h_{f,carbon}$	0.0				
$s_{f,carbon}$	0.6904				
$c_{p,carbon}$	1.2845				
g_{f,CO_3^2}	-300.0				

Table A.4 (continued): System and input parameter values of the base case configuration.

System parameters: Stoichiometry								
$v_{i,j}$		ref1	ref2	ox1	ox2	red		
	CH_4	-1	0	0	0	0		
	H_2O	-1	-1	1	0	0		
	H_2	3	1	-1	0	0		
	CO	1	-1	0	-1	0		
	CO_2	0	1	1	2	-1		
	O_2	0	0	0	0	-1/2		
	N_2	0	0	0	0	0		
$v_{i,Cj}$		C_{CH_4}	C_{H_2O}	C_{H_2}	C_{CO}	C_{CO_2}	C_{O_2}	C_{N_2}
	CH_4	-1	0	0	0	0	0	0
	H_2O	2	0	1	0	0	0	0
	H_2	0	0	-1	0	0	0	0
	CO	0	0	0	-1	0	0	0
	CO_2	1	0	0	1	0	0	0
	O_2	-2	0	-1/2	-1/2	0	0	0
	N_2	0	0	0	0	0	0	0
$v_{i,carbon}$		carbon1	carbon2	carbon3				
	CH_4	0	-1	0				
	H_2O	0	0	1				
	H_2	0	2	-1				
	CO	-2	0	-1				
	CO_2	1	0	0				
	O_2	0	0	0				
	N_2	0	0	0				
n_j		ref1	ref2	ox1	ox2	red		
		-	-	2	2	2		
F		3.5/8.0						
System parameters: Heat transfer kinetics								
ϑ_u		1.0						
Pe_s		2.5						
St_{as}		80.0						
St_{cs}		120.0						
St_m		1.0						

Table A.4 (continued): System and input parameter values of the base case configuration.

System parameters: Accumulation capacities		
$c_{p,s}$	10000.0	
V_a	1.0	
V_c	1.0	
V_m	5.0	
c_a	$1.0 \cdot 10^{-5}$	
c_e	$1.0 \cdot 10^{-5}$	
c_c	$1.0 \cdot 10^{-5}$	
V_{ac}	0.01	
V_{cc}	0.01	
System parameters: Mass transfer kinetics		
$D_{i,as}$	100.0	
$D_{i,cs}$	100.0	
κ_e	1.0	
System parameters: Others		
f_{blower}	0.1	
l_2	0.666	
Input parameters		
$X_{i,a,in}$	CH_4	1.0/3.5
	H_2O	2.5/3.5
	H_2	0.0
	CO	0.0
	CO_2	0.0
	O_2	0.0
	N_2	0.0
$\Gamma_{a,in}$	1.0	
$\vartheta_{a,in}$	3.0	
$X_{i,air}$	CH_4	0.0
	H_2O	0.0
	H_2	0.0
	CO	0.0
	CO_2	0.0
	O_2	0.21
	N_2	0.79
λ_{air}	2.2	
ϑ_{air}	1.5	
f_{back}	0.5	
I_{cell}	0.7	

Table A.5: Default parameter values of reduced model deviating from reference model.

$\Delta_r h_j^0$	ref1	ref2	ox1	ox2	red
	90.5	-14.5	56.0	42.0	156.0
c_p	4.5				
$K_{ref1}(\vartheta)$	$\exp\left(30.19 - \frac{90.41}{\vartheta}\right)$				
$K_{ref2}(\vartheta)$	$\exp\left(-3.97 + \frac{14.57}{\vartheta}\right)$				
$\Delta \phi_{ox1,0}(\vartheta)$	$28.26 - 19.84 \cdot \vartheta$				
$\Delta \phi_{ox2,0}(\vartheta)$	$20.98 - 17.86 \cdot \vartheta$				
$\Delta \phi_{red,0}(\vartheta)$	$78.00 - 23.06 \cdot \vartheta$				
$\Delta_R g_{carbon1}^0(\vartheta)$	$-51.91 + 12.95 \cdot \vartheta$				
$\Delta_R g_{carbon2}^0(\vartheta)$	$+53.12 - 21.24 \cdot \vartheta$				
$\Delta_R g_{carbon3}^0(\vartheta)$	$-37.53 + 9.04 \cdot \vartheta$				
V_m	0.0				

A.7 Cited literature

(in order of appearance)

- [1] D. Oertel, T. Fleischer, Arbeitsbericht Nr. 67 des Büros für Technikfolgen-Abschätzung beim Deutschen Bundestag (TAB): "Brennstoffzellen-Technologie", Dezember 2000.
- [2] M. Bischoff, G. Huppman, *Operating experience with a 250 kW_{el} molten carbonate fuel cell (MCFC) power plant*, Journal of Power Sources 105, 2002, 216-221.
- [3] MTU CFC Solutions GmbH, www.mtu-cfc-solutions.de
- [4] T.L. Wolf, G. Wilemski, *Molten Carbonate Fuel Cell Performance Model*, Journal of The Electrochemical Society: Electrochemical Science and Technology 130 (1), 1983, 48-55.
- [5] F. Yoshiba, N. Ono, Y. Izaki, T. Watanabe, T. Abe, *Numerical analyses of the internal conditions of a molten carbonate fuel cell stack: comparison of stack performances for various gas flow types*, Journal of Power Sources 71, 1998, 328-336.
- [6] B. Bosio, P. Costamagna, F. Parodi, *Modeling and experimentation of molten carbonate fuel cell reactors in a scale-up process*, Chemical Engineering Science 54, 1999, 2907-2916.
- [7] J.-H. Koh, B.S. Kang, H.C. Lim, *Analysis of Temperature and Pressure Fields in Molten Carbonate Fuel Cell Stacks*, AIChE Journal Vol. 47, No. 9, 2001, 1941-1956.
- [8] H.-K. Park, Y.-R. Lee, M.-H. Kim, G.-Y. Chung, S.-W. Nam, S.-A. Hong, T.-H. Lim, H.-C. Lim, *Studies of the effects of the reformer in an internal-reforming molten carbonate fuel cell by mathematical modeling*, Journal of Power Sources 104, 2002, 140-147.
- [9] M.D. Lukas, K.Y. Lee, H. Ghezal-Ayagh, *Development of a Stack Simulation Model for Control Study on Direct Reforming Molten Carbonate Fuel Cell Power Plant*, IEEE Transactions on Energy Conversion, Vol. 14, No. 4, 1999, 1651-1657.
- [10] M.D. Lukas, K.Y. Lee, H. Ghezal-Ayagh, *Modeling and cycling control of carbonate fuel cell power plants*, Control Engineering Practice 10, 2002, 197-206.
- [11] C. Shen, G.-Y. Cao, X.-J. Zhu, *Nonlinear modeling of MCFC stack based on RBF neural networks identification*, Simulation Modelling Practice and Theory 10, 2002, 109-119.
- [12] E. Achenbach, *Three-dimensional and time-dependent simulation of a planar solid oxide fuel cell stack*, Journal of Power Sources 49, 1994, 333-348.
- [13] J.R. Ferguson, J.M. Fiard, R. Herbin, *Three-dimensional numerical simulation for various geometries of solid oxide fuel cells*, Journal of Power Sources 58, 1996, 109-122.
- [14] M. Iwata, T. Hikosaka, M. Morita, T. Iwanari, K. Ito, K. Onda, Y. Esaki, Y. Sakaki, S. Nagata, *Performance analysis of planar-type unit SOFC considering current and temperature distributions*, Solid State Ionics 132, 2000, 297-308.

- [15] S. Nagata, A. Momma, T. Kato, Y. Kasuga, *Numerical analysis of output characteristics of tubular SOFC with internal reformer*, Journal of Power Sources 101, 2001, 60-71.
- [16] P. Aguiar, D. Chadwick, L. Kershenbaum, *Modelling of an indirect internal reforming solid oxide fuel cell*, Chemical Engineering Science 57, 2002, 1665-1677.
- [17] L. Petruzzi, S. Cocchi, F. Fineschi, *A global thermo-electrochemical model for SOFC systems design and engineering*, Journal of Power Sources 118, 2003, 96-107.
- [18] M. Mangold, A. Kienle, M. Sheng, P. Heidebrecht, K. Sundmacher, *Development of physical models for the process control of a molten carbonate fuel cell system*, Chemical Engineering Science, 2004, submitted.
- [19] M. Zlokarnik, *Dimensional Analysis and Scale-up in Chemical Engineering*, Springer-Verlag, Heidelberg, 1991.
- [20] P. Heidebrecht, K. Sundmacher, *Dynamic Modelling and Simulation of a counter current Molten Carbonate Fuel Cell (MCFC) with Internal Reforming*, Fuel Cells No. 3-4, 2002, 166-180.
- [21] P. Heidebrecht, K., Sundmacher, *Molten Carbonate Fuel Cells (MCFC) with Internal Reforming: Model-based Analysis of Cell Dynamics*, Chem. Eng. Sci. 58, 2003, 1029-1036.
- [22] K. Sundmacher, *Reaktionstechnische Grundlagen der elektrochemischen Absorption mit Gasdiffusionselektroden*, Fortschritt-Berichte VDI, 1998, ISBN 3-18-356403-3.
- [23] J.O.S. Bockris, S. Srinivasan, *Fuel Cells: Their Electrochemistry*, McGraw-Huill, New York (1967)
- [24] P.S. Christensen, H. Livbjerg, *A New Model for Gas Diffusion Electrodes: Application to Molten Carbonate Fuel Cells*, Chemical Engineering Science 47 (9-11), 1992, 2933-2938.
- [25] C.Y. Yuh, J.R. Selman, *The polarization of molten carbonate fuel cell electrodes, I. Analysis of steady-state polarization data*, Journal of The Electrochemical Society 138, 1991, 3642-3648.
- [26] J.A. Prins-Jansen, K. Hemmes, J.H.W. de Wit, *An extensive treatment of the agglomerate model for porous electrodes in molten carbonate fuel cells – I. Qualitative analysis of the steady-state model*, Electrochimica Acta 42, 1997, 3585-3600.
- [27] J.A. Prins-Jansen, K. Hemmes, J.H.W. de Wit, *An extensive treatment of the agglomerate model for porous electrodes in molten carbonate fuel cells – II. Quantitative analysis of time-dependent and steady-state model*, Electrochimica Acta 42, 1997, 3585-3600.
- [28] M. Bednarz, *Mechanistische Untersuchung und Modellierung der Kathodenreaktion in Karbonatbrennstoffzellen (MCFC)*, Dissertation, IPCH Universität Hamburg, 2002.

- [29] K. Hou, R. Hughes, *The kinetics of methane steam reforming over a Ni/a-Al₂O catalyst*, Chemical Engineering Journal 82, 2001, 311-328.
- [30] J. Xu, G.F. Froment, *Methane-steam reforming, methanation and water gas shift- I. Intrinsic kinetics*, AIChE Journal 35, 1989, 88-96.
- [31] G. Wilemski, *Simple Porous Electrode Models for Molten Carbonate Fuel Cells*, Journal of The Electrochemical Society: Electrochemical Science and Technology 130 (1), 1983, 117-121.
- [32] K. Janowitz, M. Kah, H. Wendt, *Molten carbonate fuel cell research Part I. Comparing cathodic oxygen reduction in lithium/potassium and lithium/sodium carbonate melts*, Electrochimica Acta 45, 1999, 1025-1037.
- [33] NIST Chemistry WebBook, National Institute of Standards and Technology, webbook.nist.gov
- [34] M. Mangold, M. Sheng, *Nonlinear model reduction of a two-dimensional MCFC model with internal reforming*. Fuel Cells 4, 2004, 68-77.
- [35] R. Fellows, E. W. Sloetjes, R. Ottervanger, *Stack networking for system optimisation: an engineering approach*, Journal of Power Sources 71, 1998, 138-143.
- [36] R. Fellows, *A novel configuration for direct internal reforming stacks*, Journal of Power Sources 71, 1998, 281-287.
- [37] F. Tränkle, M. Zeitz, M. Ginkel, E.D. Gilles, *PROMOT: A Modeling Tool for Chemical Processes*, Mathematical and Computer Modelling of Dynamical Systems 6 (3), 2000, 283-307.
- [38] R. Köhler, K. Mohl, H. Schramm, M. Zeitz, A. Kienle, M. Mangold, E. Stein, E.D. Gilles, in A. Vande Wouwer, P. Saucez and W. Schiesser (Eds.), *Adaptive Method of Lines*, Chapman & Hall/CRC Press, Boca Raton, 2001.
- [39] M. Mangold, S. Motz, E.D. Gilles, *A network theory for the structured modelling of chemical processes*, Chemical Engineering Science 57 (19), 2002, 4099-4116.
- [40] Hanke, R., Mangold, M. and Sundmacher, K., *Modellierung und dynamische Simulation von Brennstoffzellen* (Plenary), ASIM 2003, 16-19 September 2003, Magdeburg, Germany, invited.
- [41] NAG Ltd., *NAG Fortran Library Document*, 1993, Oxford, England.

Lebenslauf

Persönliche Angaben

Name, Vorname	Heidebrecht, Peter
Geburtsdatum	05.05.1975
Geburtsort	Frunse
Familienstand	verheiratet

Ausbildung und Studium

Mai 1994	Abitur am Gymnasium Leopoldinum in Detmold (Bewertung: 1,7)
Nov. 1994 – Dez. 1995	Zivildienst
April 1996 – Okt. 2000	Studium der Umweltprozeßtechnik an der TU Clausthal (Gesamtbewertung: sehr gut) Diplomarbeit "Experimentelle Ermittlung von Diffusionskoeffizienten des ternären Stoffgemisches 1,4-Butandiol/ Tetrahydrofuran/ Wasser in Nafionmembranen" am Institut für Chemische Verfahrenstechnik der TU Clausthal (Bewertung: 1,0)
Jan. 2001 – Dez. 2004	Wissenschaftlicher Mitarbeiter am Lehrstuhl für Systemverfahrens- technik der Otto-von-Guericke-Universität Magdeburg. Thema: "Modelling, Analysis and Optimisation of a Molten Carbonate Fuel Cell with Direct Internal Reforming (DIR-MCFC)"

Weitere Tätigkeiten

1998 – 2000	Nebentätigkeit im Ingenieurbüro "IDV-Systeme" in Clausthal (Prof. Zimmermann). Simulationen mit der FE-Methode.
-------------	--